CERN–2006–011
15 September 2006

ORGANISATION EUROPÉENNE POUR LA RECHERCHE NUCLÉAIRE
CERN EUROPEAN ORGANIZATION FOR NUCLEAR RESEARCH

The CERN PS multi-turn extraction based on beam splitting in stable islands of transverse phase space

Design Report

The PS Multi-Turn Extraction Study Group

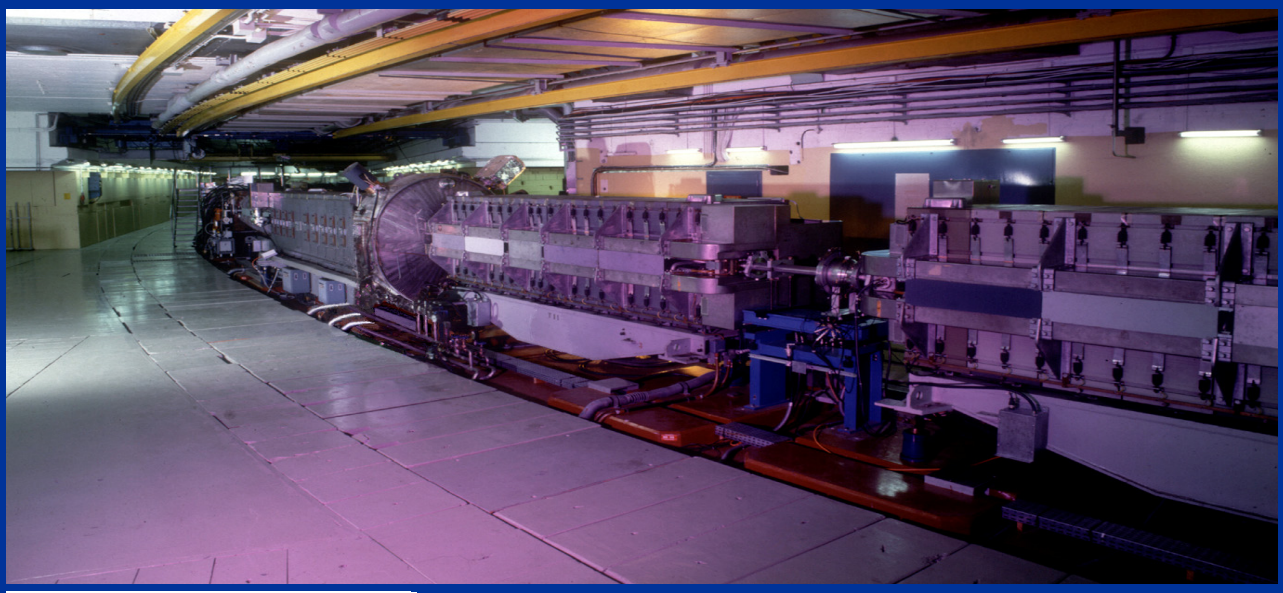

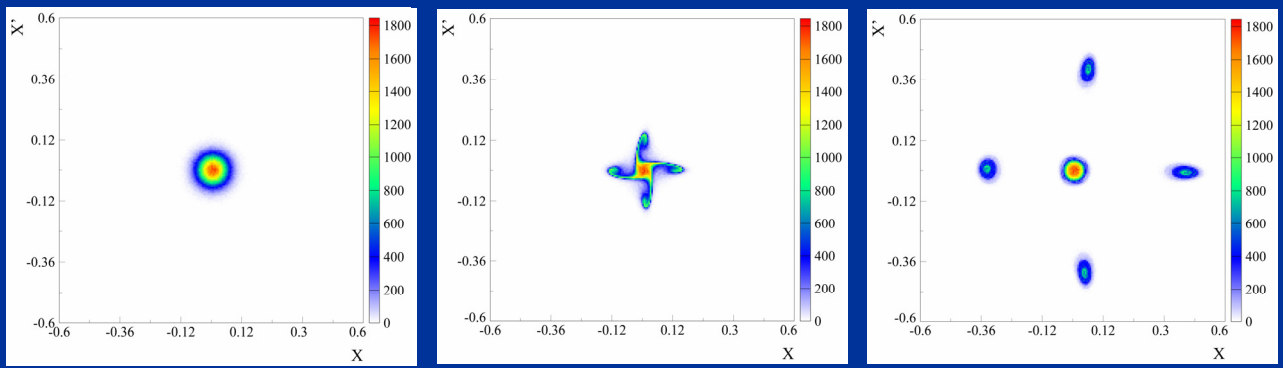

Editor: M. Giovannozzi

GENEVA
2006

CERN–2006–011
15 September 2006

ORGANISATION EUROPÉENNE POUR LA RECHERCHE NUCLÉAIRE
CERN *EUROPEAN ORGANIZATION FOR NUCLEAR RESEARCH*

The CERN PS multi-turn extraction based on beam splitting in stable islands of transverse phase space

Design Report

The PS Multi-Turn Extraction Study Group

M. J. Barnes*, O. E. Berrig, A. Beuret, J. Borburgh, P. Bourquin, R. Brown, J.-P. Burnet, F. Caspers, J.-M. Cravero, T. Dobers, T. Fowler, S. Gilardoni, M. Giovannozzi (Study Group Leader), M. Hourican, W. Kalbreier, T. Kroyer, F. di Maio, M. Martini, V. Mertens, E. Métral, K.-D. Metzmacher, C. Rossi, J.-P. Royer, L. Sermeus, R. Steerenberg, G. Villiger, T. Zickler

* On leave from TRIUMF, Canada.

GENEVA
2006

Abstract

Since 2001 considerable effort has been devoted to the study of a possible replacement of the continuous-transfer extraction mode from the PS to the SPS. Such an approach, called Multi-Turn Extraction (MTE), is based on capture of the beam inside stable islands of transverse phase space, generated by sextupoles and octupoles, thanks to a properly chosen tune variation. Both numerical simulations and measurements with beam were performed to understand the properties of this new extraction mode. The experimental study was completed at the end of 2004 and by the end of 2005 a scheme to implement this novel approach in the PS machine was defined and its performance assessed. This design report presents the outcome of the studies undertaken both in terms of technical issues as well as of resources necessary to implement the proposed scheme.

Contents

List of figures

List of tables

1 Introduction

In the framework of the activities to prepare the future high-intensity proton beam for the CERN Neutrino to Gran Sasso (CNGS) Project [1], a critical review of the key processes used to generate such a beam was carried out [2], in view of a possible upgrade beyond the present nominal intensity value of about 3.3×10^{13} protons per PS batch. Among other issues, efforts were devoted to the improvement of the present extraction scheme from the PS to the SPS, the so-called Continuous Transfer (CT). Such an extraction mode was developed in the mid-1970s [3] with the aim of delivering a beam at 14 GeV/*c* to the Super Proton Synchrotron (SPS), five Proton Synchrotron (PS) turns long, and with a reduced horizontal beam emittance to overcome the SPS aperture limitation in the vertical plane: a special optics in the transfer line joining the PS and SPS allows the two transverse planes to be exchanged (in particular the emittance values) [4]. This approach consists in slicing the beam by means of an electrostatic septum: with the horizontal tune set to 6.25 this method allows the generation of one continuous ribbon four turns long plus an additional slice, representing the beam core, for a total beam length of five PS turns. Although this extraction mode is certainly adapted to the present performance, in the event of an intensity increase, a number of potential weak points appear, such as the intrinsic beam losses related to the underlying principle of this extraction mode, and also the properties of phase space matching of the different slices.

In the framework of the High Intensity Protons Working Group (HIP-WG) [5] a detailed analysis of the losses for the beam for CNGS was performed [6]. The outcome is rather striking: for an overall intensity of about 4.5×10^{19} protons/year required by the neutrino experiments, approximately 1.7×10^{19} are lost in the accelerator chain, corresponding to about 40% of the total intensity. A large fraction of beam losses, namely 0.7×10^{19}, or 40% of the total intensity lost occurs in the electrostatic septum of the PS ring used to slice the beam.

In the quest for an improved extraction mode, a novel approach was proposed. In the new scenario the beam will be separated in transverse phase space by generating stable islands inside the region where the beam sits and by slowly (adiabatically) moving them towards higher amplitudes. By doing this, particles may get trapped inside islands thus generating well-separated beamlets [7,8]. This method is potentially superior to the present one as no intercepting device is used to split the beam; hence particle losses are limited to the fraction of the beam improperly deflected during the kicker rise time. Furthermore, the extracted beam should better match the phase space structure. Following the encouraging results of numerical simulations, a measurement campaign on the PS machine was launched in 2002 and continued throughout the whole of 2003. To co-ordinate these activities, a Study Group was set up [9] with the following mandate:

- Demonstrate the feasibility of the scheme.
- Investigate the various technical issues.
- Evaluate the resources required to define and specify a possible project to replace the present continuous transfer scheme.

The results of the studies performed were collected in a report [10]. Subsequently, the mandate of the Study Group was extended to continue the experimental studies in view of reducing the losses observed during the capture process with the high-intensity, single-bunch proton beam. This goal was achieved in summer 2004, when beam splitting without any measurable losses was observed [11–13]. Efforts continued in order to increase the fraction of trapped particles [12,13]. In parallel, the study of the implementation of the proposed scheme in the CERN PS machine was pursued [14–16]. This activity dominated the studies performed

during 2005, when no experimental activity could take place due to the long shutdown of the CERN accelerators, namely the PS and the SPS.

The progress was reported at the AB Management Board on three occasions [9,17,18]. The study for the Multi-turn Extraction (MTE) was also part of the activities covered by the Beam Losses and Radiation Working Group (BLRWG) [19].

By the beginning of 2006, the conclusions of the Study Group were considered worthy of publication in a Design Report to allow moving from the study stage to that of official project with the mandate of implementing the proposed scheme within the level of resources identified by the Study Group during its activity.

The plan of this report is the following: in Section 2 the present CT is presented and its performance reviewed. In Section 3 the principle of the novel MTE is presented together with the analysis of its theoretical performance and the results of the long experimental campaign carried out on the PS machine. In Section 4 the proposed scheme to implement the MTE in place of the CT is discussed in detail, together with the hardware modifications required to allow the realization of this extraction. In Section 5 an analysis of the resources necessary to implement the MTE is presented including also a proposal for the schedule. An executive summary, Section 6, concludes the core of this report.

2 The present continuous transfer

2.1 Principle

Just prior to extraction the horizontal tune of the PS machine is set to the value 6.25. At the same time the closed-orbit is modified by means of two dipoles that generate a closed bump around the electrostatic septum located in section 31 of the PS circumference. In addition, a second bump around the electrostatic septum is generated by two kickers so that by selecting its amplitude, a different portion of the beam is cut off the central core. Because of the value of the horizontal tune, four slices are shaved off and extracted as a continuous ribbon over four turns. Therefore, only a fraction of the beam core remains in the machine and is extracted last, during the fifth turn, by changing the beam trajectory, so as to jump over the septum blade. The shaved beam receives a horizontal kick by the electrostatic septum that produces the necessary displacement to jump over the thicker blade of the extraction magnetic septum located in section 16 of the PS ring (see Fig. 1). To amplify the effect on the beam trajectory of the kickers and septa, the optics of the machine is perturbed by means of the so-called kick enhancement quadrupoles (QKE16), namely two quadrupoles located in Straight Sections (SS) 5 and 25, as can be seen in Fig. 2. They increase the horizontal beta-function at the location of the electrostatic septum so as to reduce the local beam density and hence the losses on the device. At the same time, the value of the horizontal dispersion function is reduced at the electrostatic septum, thus making the whole extraction process less sensitive to the intrinsic momentum spread of the beam. From the very principle it is clear that the five extracted slices have different extraction conditions, i.e., positions and angles at extraction, as well as equivalent optical parameters and emittances. During normal operation, the difference in extraction trajectories is corrected by means of dedicated kickers installed in the TT2 transfer line, the DFAs, also called Emittance Reduction Dipoles (ERDs).

Another interesting property of such an approach is that the horizontal emittance of the extracted beam is decreased with respect to that of the circulating one. However, a number of drawbacks are present, namely: i) beam losses, especially at the electrostatic septum, are unavoidable. They amount to about 15% of the total beam intensity [20]; ii) the extracted slices do not match the natural structure (circles) of phase space, thus generating a betatronic mismatch. This, in turn, induces emittance blow-up in the receiving machine; iii) the

extracted slices have different transverse emittance. A detailed analysis of the properties of the extracted slices can be found in Ref. [21], where computation of the mismatch parameters for the CT as a function of the slicing was performed.

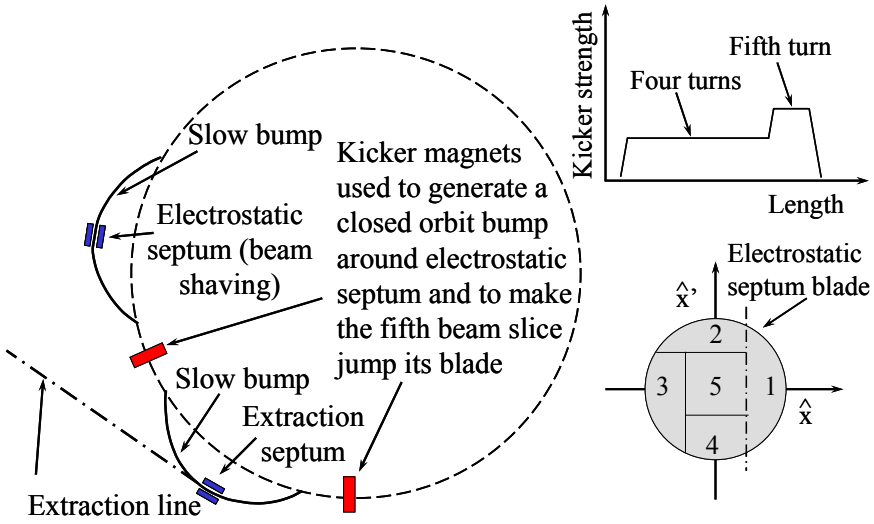

Fig. 1: Principle of the CT extraction from the PS machine: the extraction scheme (left), the kicker strength as a function of time (upper right), the normalized phase space (lower right)

For the CT extraction, the optical parameters and the beam emittance are different for the five slices, thus generating different emittance blow-up at SPS injection. Furthermore, because of the fancy shape of the slices, the mismatch can be rather large. A summary of the outcome of the analysis presented in Ref. [21] is reported in the next section.

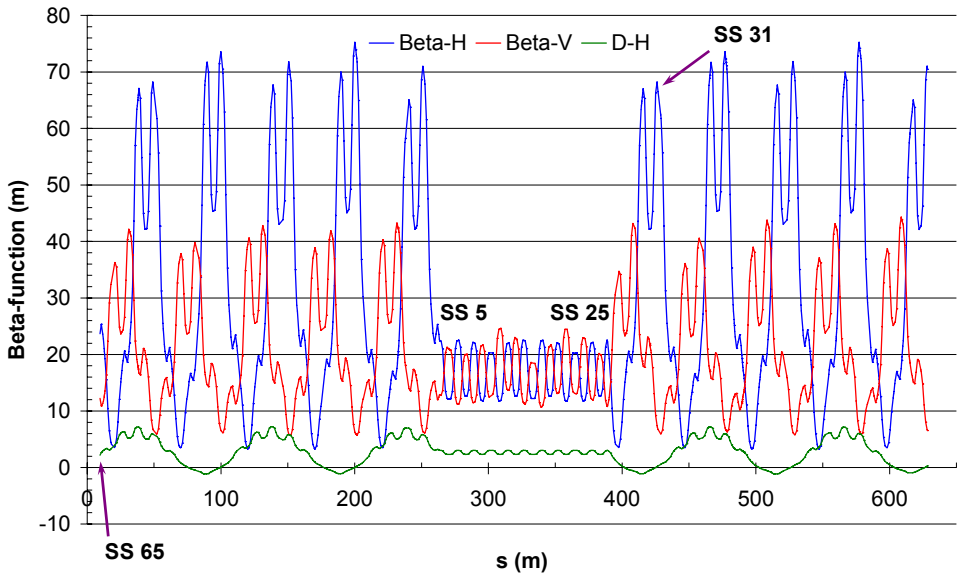

Fig. 2: Optical parameters for the PS ring when the beam is sliced for the CT. The standard optics is perturbed by means of special quadrupoles, the QKE16.

2.2 Performance

When a beam is injected into a circular machine, it may experience emittance blow-up due to a number of different phenomena. In this paper we focus on the betatron mismatch [22,23],

which occurs when the beam optical parameters at injection do not fit those of the circular machine. In this case, tails may grow at the expense of the beam core, thus increasing the overall beam emittance. Of course, such behaviour is particularly harmful for high-intensity beams as they usually completely fill the machine acceptance. To quantify the betatron mismatch, it is customary to start from the statistical definition of the beam emittance ε and optical parameters $\overline{\alpha},\overline{\beta},\overline{\gamma}$ [24] in terms of the second-order moments of the beam distribution [25]. By using the notation $(\hat{x},\hat{x}')$ for the physical phase space coordinates, while (x,x') represent normalized Courant–Snyder coordinates [24], the following holds:

$$\begin{aligned} \langle x^2 \rangle &= \overline{\beta}\,\varepsilon \\ \langle x x' \rangle &= -\overline{\alpha}\,\varepsilon \\ \langle x'^2 \rangle &= \overline{\gamma}\,\varepsilon. \end{aligned} \tag{1}$$

In the equations quoted above the symbol $\langle\cdot\rangle$ stands for the average over the beam distribution of the specified variable. It is worth while mentioning that whenever the beam distribution is not centred at the origin, the second-order moments in Eq. (1) are the central ones, i.e., referred to the mean value of the beam distribution. This approach is equivalent to fitting an ellipse to the phase space distribution, where the fit parameters are its surface, amplitude, and orientation.

If the nominal Twiss parameters α,β,γ, i.e., those relative to the nominal optics, are used to transform Eq. (1) into normalized phase space via the well-known transformation rules [24]

$$x=\frac{\hat{x}}{\sqrt{\beta}}, \qquad x'=\frac{\alpha}{\sqrt{\beta}}\hat{x}+\sqrt{\beta}\,\hat{x}', \tag{2}$$

the key relations

$$\begin{aligned} \langle x^2 \rangle &= \frac{\overline{\beta}}{\beta}\varepsilon \\ \langle x x' \rangle &= \left(\alpha\frac{\overline{\beta}}{\beta}-\overline{\alpha}\right)\varepsilon \\ \langle x'^2 \rangle &= \left(\alpha^2\frac{\overline{\beta}}{\beta}-2\alpha\overline{\alpha}+\beta\overline{\gamma}\right)\varepsilon \end{aligned} \tag{3}$$

are obtained. The value of the rms emittance can be computed by solving Eqs. (3), namely

$$\varepsilon=\sqrt{\langle x^2\rangle\langle x'^2\rangle-\langle x\,x'\rangle^2}\ . \tag{4}$$

The meaning of the coefficients $\overline{\beta}/\beta, \alpha\overline{\beta}/\beta-\overline{\alpha}$ is clear: they measure the deviation of the 1σ contour of the beam distribution from the circular shape it should have in normalized phase space. In case of perfect matching one would have $\overline{\beta}/\beta=1$ and $\alpha\overline{\beta}/\beta-\overline{\alpha}=0$

implying the trivial relation $\overline{\beta} = \beta$, $\overline{\alpha} = \alpha$. Furthermore, it turns out that the emittance after filamentation, $\varepsilon_{\text{after fil.}}$, i.e., when the circular symmetry has been restored in the receiving machine, is expressed as [23]

$$\varepsilon_{\text{after fil.}} = H\varepsilon \quad \text{with} \qquad H = \frac{1}{2}\left[\frac{\overline{\beta}}{\beta} + \frac{\beta}{\overline{\beta}} + \left(\alpha\sqrt{\frac{\overline{\beta}}{\beta}} - \overline{\alpha}\sqrt{\frac{\beta}{\overline{\beta}}}\right)^2\right] \tag{5}$$

where ε is the initial value of the beam emittance.

It is customary to assume that the transverse beam distribution is a Gaussian function. However, because of the presence of long, and strictly speaking infinite, tails sometimes a different beam distribution is considered, namely a so-called quasi-parabolic distribution (see, for example, Ref. [26] and references therein for more details). Such a distribution does not have tails, though it is not a truncated Gaussian. It is represented by a smooth function

$$\rho(x, x', m) = \begin{cases} \dfrac{m+1}{2\pi\varepsilon(m+2)}\left[1 - \dfrac{x^2 + x'^2}{2\varepsilon(m+2)}\right]^m & \text{if } x^2 + x'^2 \le 2\varepsilon(m+2) \\ 0 & \text{if } x^2 + x'^2 > 2\varepsilon(m+2) \end{cases} \tag{6}$$

where m is a parameter and ε the rms beam emittance. The results discussed in Ref. [21] and reported here refer to the case $m = 5$.

The computation of the optical properties of the five extracted slices of the CT can be derived by performing integration over the beam distribution taking into account the shape of the slice due to the interaction with the electrostatic septum. Knowing that the relative position between the septum and the beam can be controlled on a turn-by-turn basis, it is rather straightforward to compute all relevant quantities for each slice (in some cases it is even possible to derive analytical expressions of the optical parameters vs. the septum position). Two approaches have been followed, corresponding to the equalization of the beam intensity or of the extracted emittance. The first approach corresponds to what done in reality when tuning the beam. The second one cannot be applied in practice on account of lack of an appropriate instrument to measure the beam emittance of each extracted slice.

Interestingly enough, it turns out that the two approaches are not compatible with each other. In other words, making the intensity equal generates very unequal emittances and vice-versa. This fact is visualized in Fig. 3, where the shape of the five slices is shown for the two approaches. The difference is clearly visible.

The numerical results are summarized in Table 1 where the optical parameters and the emittance for each slice are reported for the two approaches considered.

A clear feature is apparent: by equalizing one quantity (intensity or emittance) the other shows huge variations between the different slices. The most stable case seems to be the one where equal intensity is imposed as the extracted beam emittance differs by only a factor of three between the first and the last slice. Of course, by slightly reducing the intensity of the first slice and increasing that of the last two slices, more balance may be found. Finally, it is worth while pointing out that the emittance ratio of the order of 0.3 obtained for equal intensities is in rather good agreement with experimental measurements [27].

The considerations reported here refer to the beam at extraction from the PS machine. Obviously, the most relevant quantity in the performance evaluation is the emittance after filamentation, i.e., after injection into the SPS. Different physical effects may contribute to emittance dilution, such as steering errors, dispersion mismatch and betatron mismatch [22,23].

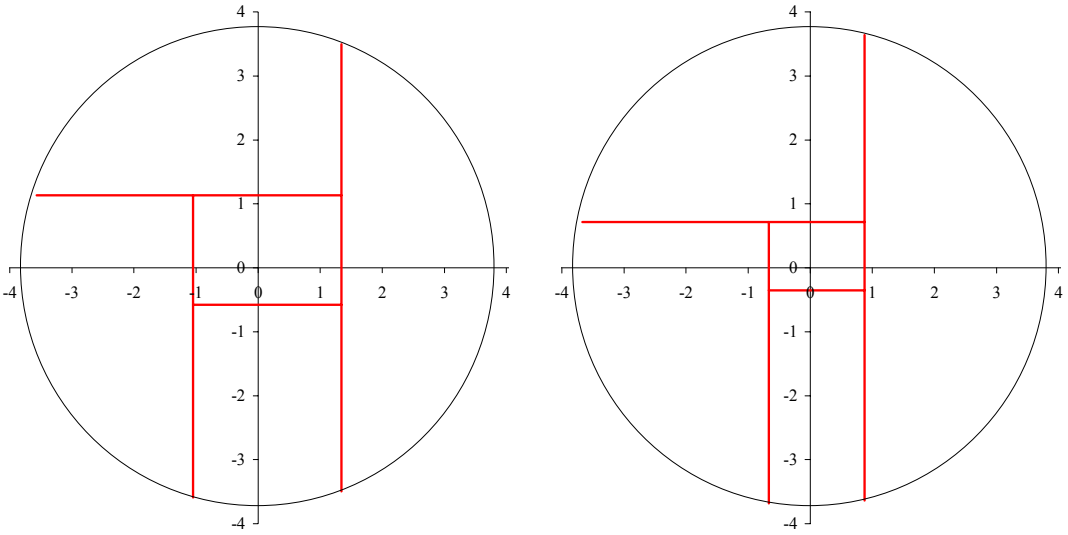

Fig. 3: Shape of the five slices for the present CT in normalized phase space (x,x') according to whether intensities (left) or emittances (right) have been equalized. The solid circle represents the locus where the quasi-parabolic distribution reaches zero, which occurs at $\sqrt{14\varepsilon}$.

From the previous analysis, it turns out that the five slices have different position and angle at PS extraction. However, fast correction dipoles are installed in the TT2 transfer line to compensate, at least partially, for these small differences. Therefore, this source of emittance blow-up can be neglected as well as the dispersion mismatch and only the betatron mismatch will be taken into account.

Table 1: Summary of the beam parameters $\varepsilon_i / \varepsilon$, $\overline{\beta}_i / \beta$, $\alpha\ \overline{\beta}_i / \beta - \overline{\alpha}_i$ and intensity for the five slices of the present CT extraction. For the case of equal emittances, the common value for a quasi-parabolic distribution is $\varepsilon_i / \varepsilon \approx 0.303$.

Approach	Beam parameter	Slice				
		1	2	3	4	5
Equal I	$\varepsilon_i / \varepsilon$	0.394	0.337	0.327	0.227	0.132
	$\overline{\beta}_i / \beta$	0.432	1.674	0.639	0.817	1.419
	$\alpha\ \overline{\beta}_i / \beta - \overline{\alpha}_i$	0	0.053	1.570	0.005	0
Equal $\varepsilon_i / \varepsilon$	I_i / I	9.475	12.576	13.734	22.210	42.005
	$\overline{\beta}_i / \beta$	0.370	2.206	0.494	1.321	1.350
	$\alpha\ \overline{\beta}_i / \beta - \overline{\alpha}_i$	0.370	2.206	0.494	1.321	1.350

As already stressed in the previous sections, the results are qualitatively the same for both distributions. Rather large values (up to a factor of two) for H_i are obtained. The same type of analysis described in the previous section allows one to obtain the mismatch factors H_i in the case of four independent parameters and for two different approaches, namely same intensities or same extracted beam emittances for the five slices. The numerical values of H_i are reported in Table 2 together with the value of $\varepsilon_{\text{after fil.}}/\varepsilon$ for each slice.

Table 2: Summary of the mismatch factor H_i and emittance after filamentation for the different slices of the present CT extraction

Approach	Beam parameter	Slice 1	2	3	4	5
Equal I	H_i	1.373	1.137	1.105	1.021	1.062
	$\varepsilon_{\text{after fil.}}/\varepsilon$	0.541	0.381	0.361	0.232	0.240
Equal $\varepsilon_i/\varepsilon$	H_i	9.475	1.556	1.330	1.262	1.040
	$\varepsilon_{\text{after fil.}}/\varepsilon$	0.370	0.471	0.402	0.382	0.315

Both approaches generate quite large blow-up factors (between 30% and 50%). However, the overall ratio between $\varepsilon_{\text{after fil.}}/\varepsilon$ and beam emittance before extraction is at maximum of the order of 0.5–0.6 depending on the approach used. Equalizing the intensity of the five extracted slices generates a better situation than having equal emittances.

2.3 Beam losses

Another result of the analysis presented in the previous section is that the relative position between the electrostatic septum and the beam can be derived, thus allowing the evaluation of the losses intrinsic to the slicing process. The results are reported in Table 3, together with the ratio of the emittance of the extracted slice with respect to that of the circulating unsliced beam. The relative beam–electrostatic septum position is the position of the blade of the septum relative to the beam centre, which is measured in terms of the local beam width.

Table 3: Relative beam–electrostatic septum position, as computed in Ref. [21], assuming equal intensity for the five extracted turns. The fifth turn is not sliced; hence no value for the septum position is given. The relative beam emittance $\varepsilon_i/\varepsilon$ of each slice is also reported, as well as the angle for each extracted slice at the location of the electrostatic septum as computed using the PS model and the operational settings.

Parameter	Slice 1	2	3	4	5
Relative beam–electrostatic septum position (σ)	0.878	0.716	0.665	0.356	–
$\varepsilon_i/\varepsilon$	0.394	0.337	0.327	0.227	0.132
Slice angle (mrad)	–0.335	–0.336	–0.376	–0.421	–0.529

It is worth mentioning that for the computation of the losses, the transverse beam distribution has been considered to be Gaussian in all four phase space dimensions. However, as the slicing process takes place only in the horizontal phase space, a bi-Gaussian

distribution function in the two horizontal phase space variables is used. As far as the longitudinal beam distribution is concerned, it was assumed to be uniform, as the beam is debunched before extraction and only partially recaptured using the PS 200 MHz cavities.

To perform the estimate of the beam losses for the CT [28,29] the analytical computations concerning the properties of the five slices reported in Ref. [21] have been assumed. Furthermore, the geometry of the electrostatic septum was taken from the values used during normal operation, i.e., the septum angle is taken as –0.216 mrad with respect to the nominal beam trajectory. As far as the width of the electrostatic septum is concerned, the nominal value is 0.1 mm. However, the energy deposited by the beam induces heat deposition and consequent deformation of the surface (warping), so that the final value is of the order of 0.2–0.3 mm [30]. Such a value is measured after one or two years of operation. The most realistic value of 0.2 mm was assumed in the computations presented here. In the computation of the beam losses for each extracted slice, the relative angle between beam and electrostatic septum is a crucial parameter. In the past, the septum angle was carefully adjusted to minimize the losses for the operational beam [31]. By using the MAD model of the PS ring measured for the CT operation [32] together with the operational values of the kickers' strength for generating the closed bump around the electrostatic septum, it was possible to estimate the relative angle, which is reported in Table 3.

Finally, to complete the overview of the optical parameters used in the computations presented in Refs. [28,29], the beam divergence across the long straight section where the electrostatic septum is located has been neglected. This assumption holds true for the nominal optics. Whenever the QKE16 is switched on, this is true only to a first approximation: the horizontal beta-function changes from 68 m to 63 m between the entry and the exit of the septum, corresponding to a variation of 7%. This has been considered negligible with respect to the uncertainties intrinsic with the other beam parameters used in the estimate.

As far as the horizontal rms normalized beam emittance is concerned, a value of ε_H^* of 9.3 μm was assumed, corresponding to the value quoted in Ref. [33] for the 2004 operation during the high-intensity MD period. Parenthetically, it is worth mentioning that during the last year of high-intensity proton operation for the neutrino experiments, the horizontal rms normalized emittance was much larger, being about 16.6 μm. It is clear that although a larger emittance implies possible aperture bottlenecks, it also implies smaller local beam densities, hence smaller losses on the electrostatic septum during the extraction process.

In the case of the first four turns, the losses have been estimated by integrating the beam distribution over the septum width at the amplitude given by the analytical computations for the option with same intensity for the various slices. In the case of the last slice, the extraction losses are mainly given by the finite rise time of the kickers, which is of the order of 820 ns[†] corresponding to the rise time between 5% and 95% of the kick amplitude. The rise of the kick amplitude $x(t)$ is modelled by a sinusoidal function according to

$$x(t)=\frac{A}{2}\left\{\sin\left[2\left(t-\frac{\pi}{4}\frac{\tau_{1-\alpha,\alpha}}{\arcsin(2\alpha-1)}\right)\frac{\arcsin(2\alpha-1)}{\tau_{1-\alpha,\alpha}}\right]+1\right\} \quad 0\le t\le\frac{\pi}{2}\frac{\tau_{1-\alpha,\alpha}}{\arcsin(2\alpha-1)} \tag{7}$$

where $\tau_{1-\alpha,\alpha}$ represents the time required to increase the kick amplitude from $(1-\alpha)\%$ to $\alpha\%$ of the nominal value. Parenthetically, to link the value of the rise time for two values of the parameter α the following relationship applies:

[†] In Refs. [5, 6] the value of 260 ns was used. Such a value was extracted from the official web site of the BT Group http://ab-div-bt.web.cern.ch/ab-div-bt/Sections/KPS/Systems/PSPARAM.asp. However, it turned out that it does not correspond to the actual rise time, but only to the time constant τ.

$$\tau_{1-\beta,\beta} = \tau_{1-\alpha,\alpha} \frac{\arcsin(2\beta - 1)}{\arcsin(2\alpha - 1)}. \tag{8}$$

In particular, the following holds:

$$\frac{\tau_{5,95}}{\tau_{10,90}} = \frac{\arcsin(0.9)}{\arcsin(0.8)} \approx 1.2076. \tag{9}$$

In all the computations presented here, it is assumed that the losses onto the magnetic septum can be neglected, as the slices are meant to jump beyond the magnetic septum thanks to the kick imparted by the electrostatic septum.

Under these assumptions, the dependence of the beam losses on the three key quantities, like the septum angle relative to the beam, the septum thickness, and the beam emittance have been derived. The results are shown in Figs. 4 to 6.

According to the results concerning the dependence of the beam losses on the septum angle, it is clear that the optimum is reached for a value different from the one used in normal operation. During the next run it will be worth dedicating some MD studies to the optimization of the septum angle. Of course, it is worth while mentioning that the knowledge of the beam trajectory is probably not accurate enough to be used for quantitative predictions.

The total losses depend linearly on the electrostatic septum thickness (see Fig. 5). The two curves refer to two values of the septum angle: of course the minimum value differs for the two situations, but the conclusions are the same. It is worth stressing that the losses do not tend to zero with the septum thickness. This is an artefact of the numerical simulations. Indeed, on account of the non-vanishing relative angle between slices and septum, the integral used to compute the value of the total beam losses is never zero.

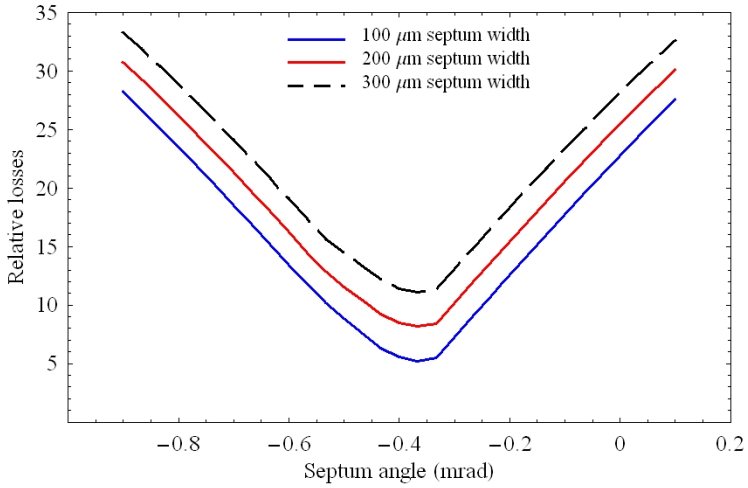

Fig. 4: Dependence of the total relative beam losses (%) at extraction for the CT as a function of the electrostatic septum angle. The three curves refer to three values of the septum thickness.

This plot deserves more comments, as one possible option to reduce the losses would be to decrease the septum thickness. From a technological point of view, thinner electrostatic septa are already in operation in the SPS ring. Such a device is made of thin wires of 0.06 mm diameter. However, the alignment of the overall structure imposes a lower limit on the effective thickness to about 0.1 mm [34]. A slight improvement could be envisaged for a PS

electrostatic septum made of thin wires, as the overall length is about 2 m against the 3 m of the SPS structure. Hence a reasonable value for the thickness is of the order of 0.080 mm. Such a target would be already rather challenging for the present technology. Whenever the value used in operation of the septum angle is used, such a septum improvement would induce a reduction in the losses from about 14.6% (corresponding to 0.2 mm) to 11.2% (corresponding to 0.08 mm): hence only 23%, which seems not to be worth the effort in developing such a challenging septum structure.

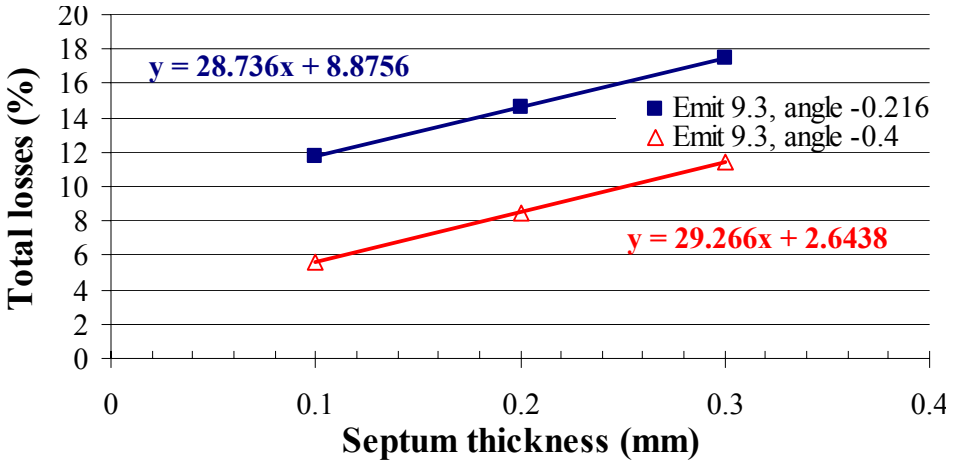

Fig. 5: Dependence of the total beam losses on the electrostatic septum thickness. The two curves correspond to two values of the septum angle.

The dependence of the losses on the value of the circulating beam emittance is shown in Fig. 6. As can be expected, the total beam losses decrease when increasing the beam emittance, as the local beam density is lower. The values of the beam emittance measured during the last high-intensity run in 1997 and the recent high-intensity MD period in 2004 are also reported. The main point here is that there is a trade-off between emittance minimization, to overcome possible aperture bottlenecks and hence beam losses in the SPS, and emittance increase to reduce extraction losses in the PS machine: this study might be a first step towards such an approach for the future runs with CT.

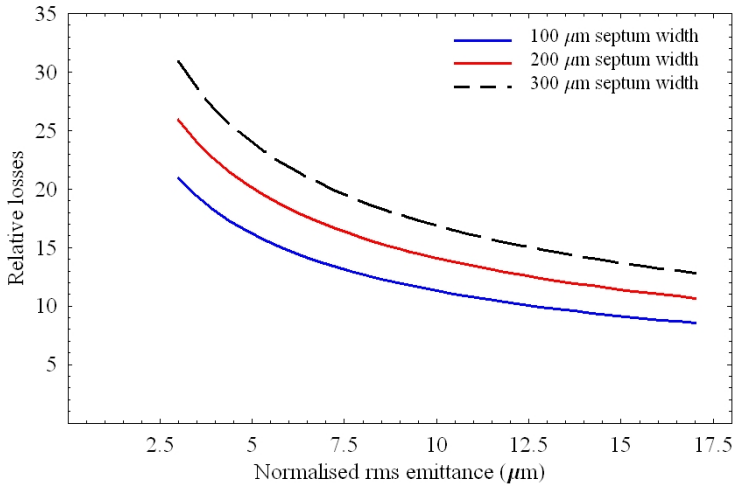

Fig. 6: Dependence of the total beam losses (%) on the horizontal rms normalized beam emittance. The three curves refer to different values of the septum thickness.

As the parameters' space is rather large, the minimization of the losses for the CT extraction should be performed after having evaluated the impact of the various parameters in the reduction of the losses. In the previous analysis, the numerical computations focused on the impact of electrostatic septum thickness, relative angle between electrostatic septum and beam and transverse horizontal beam emittance, but the impact of the rise time of the extraction kickers was not considered. Additional numerical simulations were performed and the results are presented in Fig. 7, with the dependence of the total beam losses as a function of the normalized emittance and the septum angle for the three longitudinal bunch structures (columns).

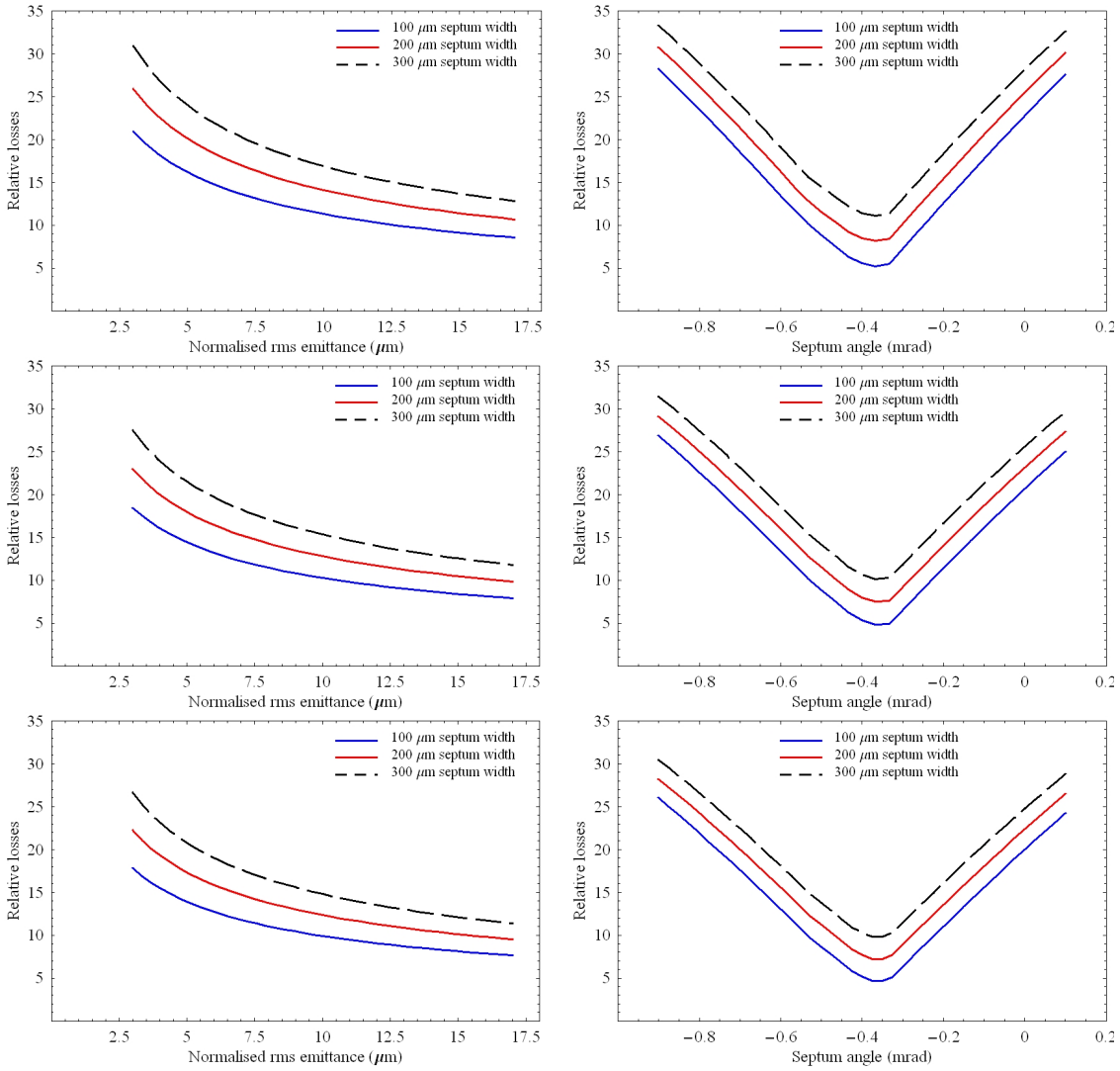

Fig. 7: Dependence of the total beam losses (%) for the present CT as a function of the horizontal emittance (first column), beam-septum angle (second column). Various longitudinal structures are considered, continuous (first row), bunched on h = 16 (second row), bunched on h = 8 (third row).

The dependence of the losses on the longitudinal structure is rather mild and the qualitative behaviour found in the previous plots is confirmed, with a slight reduction of the losses whenever the harmonic number is reduced. The dependence of the beam losses on the rise time is shown in Fig. 8, where the losses due to beam slicing for the three longitudinal structures are presented together with the extraction losses for the fifth turn. The dependence

on the kickers' rise time is a bit more striking, as almost no improvement is found by shortening the rise time, no matter what the longitudinal structure of the beam. It is clear that, in the case of a continuous beam, this result is quite natural. However, for bunched beams, this simply means that the losses due to beam slicing largely dominate the overall losses, so that a reduction in the rise time does not significantly improve the amount of beam lost. Of course, this is true for the first four turns, but the situation is different for the fifth one. In fact, in this case the last turn does not have to be sliced and, indeed, the losses in this case are generated by the kickers' rise time. This is clearly seen in the right part of Fig. 8, where the dependence of the beam losses for extracting the fifth turn only are shown as a function of the kickers' rise time.

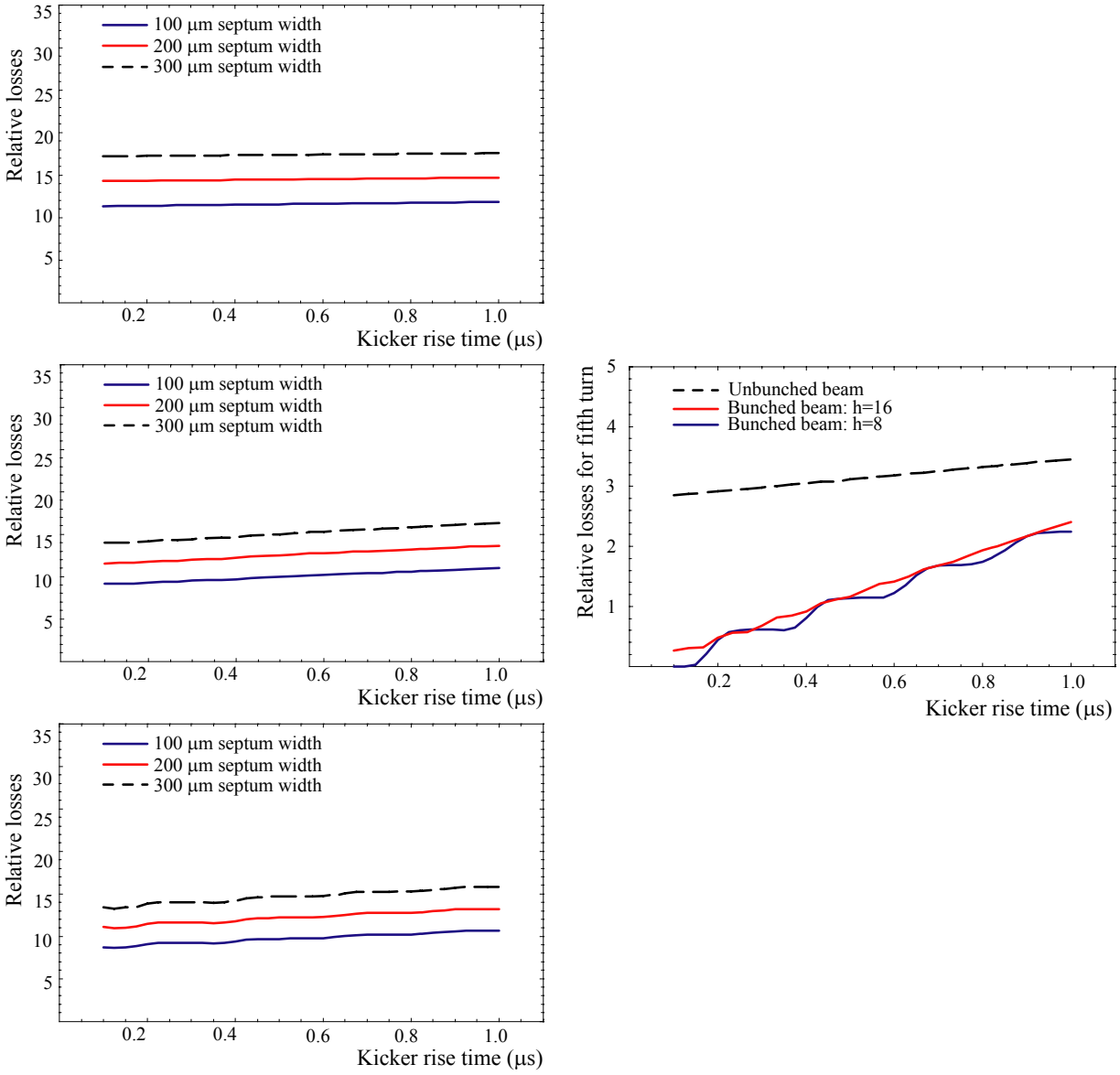

Fig. 8: Dependence of the total beam losses (%) for the present CT as a function of the kickers' rise time $\tau_{5,95}$ (first column). Various longitudinal structures are considered, continuous (first row), bunched on h = 16 (second row), bunched on h = 8 (third row). The dependence of the losses for the fifth extracted turn is shown in the second column.

Almost no dependence on the rise time is found in the case of a continuous beam, while a strong dependence is found in the case of bunched beams, as expected. The steps in the graphs are due to the bunch structure of the beam. All in all, this suggests that no efforts should be devoted to improving the performance of the kickers, but resources should be devoted to other activities.

To find which is the most effective parameter to reduce the losses, the Jacobian of the function expressing the total losses has been computed numerically, more precisely, given $L = L(p_1, p_2, \cdots p_n)$, the function giving the total relative losses, then the quantities $\Delta L_i = \left| \left(\partial L / \partial p_i \right)_{p_{io}} p_{io} \right|$, where p_{io} represents the nominal value of the *i*-th parameter, are computed. The ΔL_i's are normalized so that they can be compared to give an indication of the relative effectiveness of each free parameter. The results are reported in Table 4.

Table 4: Effectiveness of the free parameters in reducing the total losses at extraction for the CT

Longitudinal structure	ΔL_1 p_1 = emittance	ΔL_2 p_2 = septum angle	ΔL_3 p_3 = kickers' rise time	ΔL_4 p_4 = septum width
Continuous	7.51	12.18	0.38	2.88
Bunched h = 16	6.52	11.24	2.02	2.63
Bunched h = 8	6.27	10.86	2.59	2.05

From the values quoted in Table 4, it is clear that the most efficient parameter is the relative angle between the electrostatic septum and the beam. The second most efficient is then the horizontal emittance and finally the electrostatic septum width. As far as the rise time of the extraction kickers is concerned, losses are somewhat affected only in the case of bunched beams: then its relative importance as a loss reduction parameter is equivalent to the septum of the electrostatic septum.

3 The novel multi-turn extraction

3.1 Principle

The novel technique relies on the use of non-linear magnetic fields (sextupolar and octupolar) to generate stable islands in the horizontal phase space. By means of an appropriate tune variation, a specific resonance is crossed, the fourth-order in the case under study, and the beam is split by trapping inside the stable islands moving from the origin of the phase space towards higher amplitudes [7,8,35,36]. A good model consists in choosing a simple FODO cell with a sextupole and an octupole located at the same longitudinal position, both represented in the single-kick approximation [37]. For the application under study, only the horizontal plane is relevant. Hence, the dynamics of such a system is generated by a 2D one-turn transfer map, which can be computed and it turns out to be a polynomial map of the form:

$$\begin{pmatrix} X_{n+1} \\ X'_{n+1} \end{pmatrix} = R(\omega_n) \begin{pmatrix} X_n \\ X'_n + X_n^2 + \kappa X_n^3 \end{pmatrix}, \tag{10}$$

where the coordinates (X, X') are adimensional normalized coordinates [37], $R(\omega)$ represents a rotation matrix of an angle $\omega = 2\pi\nu$ and κ depends on the ratio between the strength of the sextupole and the octupole with a weight given by the value of the optical beta-function at the location of the non-linear magnetic elements [36,38], namely

$$\kappa = \frac{2}{3}\frac{K_3}{K_2^2}\frac{1}{\beta_x} \qquad (X,\ X') = \lambda(x,\ x') \qquad \lambda = \frac{1}{2}K_2\,\beta_x^{3/2}, \tag{11}$$

where $(X,\ X'), (x,\ x')$ stand for adimensional normalized coordinates and normalized Courant–Snyder coordinates, respectively. It is important to stress that the angle ω is indeed a function of the turn number. In all the plots shown in this report, as well in the numerical and analytical computations reported here, the special adimensional normalized coordinates are used.

An example of the change of the phase space topology during resonance crossing is shown in Fig. 9.

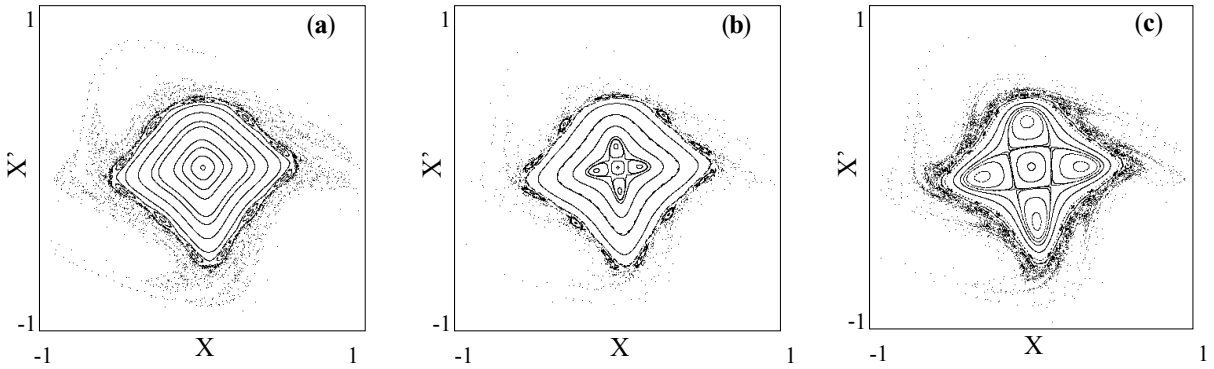

Fig. 9: Topology of the normalized phase space during resonance crossing

The evolution of the beam distribution during the resonance crossing is shown in Fig. 10.

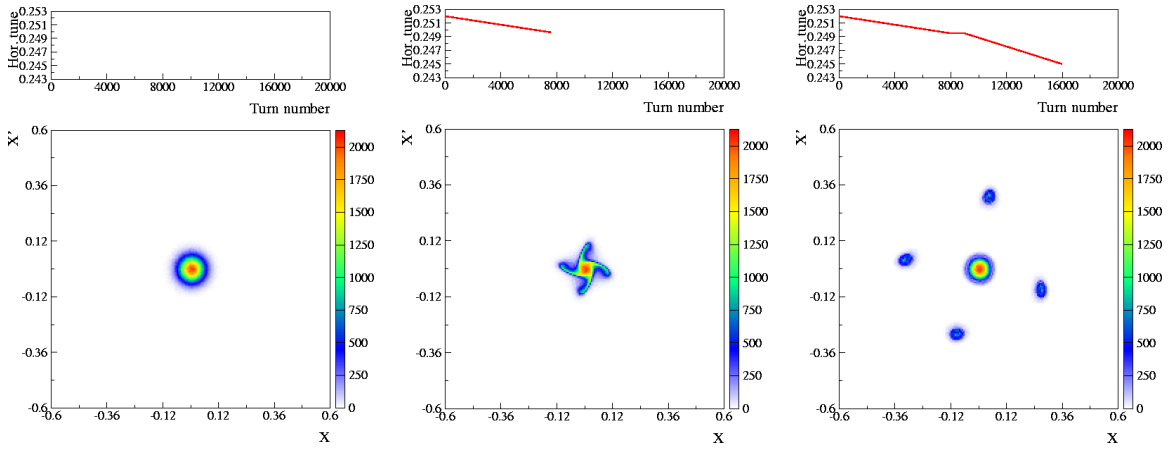

Fig. 10: Evolution of the beam distribution during resonance crossing. The initial state is represented by a bi-Gaussian beam (left), at resonance crossing some particles are trapped inside the moving islands (centre), at the end of the process, the particles trapped in the islands are moved towards higher amplitudes (right).

When the tune is changed, the islands move through the phase space region where the charged particles sit and some are trapped inside the islands. At some stage a complete separation between the beamlets and the central core occurs and the distance between the beamlets can be increased at will by simply acting on the tune. It is worth while stressing that the beam after trapping has a peculiar structure, i.e., it is made of two disconnected parts: the beamlets, which are indeed one single structure closing up after four turns around the machine (see Fig. 11), and the central core.

The idea behind this process is that such a beam splitting in the transverse phase space can be used to perform multi-turn extraction. In fact, once the various beamlets are separated, the whole structure can be pushed towards an extraction septum by means of a closed slow bump. Then, kicker magnets generate a fast closed bump and one island jumps beyond the septum blade so that the beamlets are extracted out of the machine in four turns. The fifth beamlet, i.e., the beam core, is extracted using a classical single-turn extraction. The advantage of this approach is that, at least for the first four turns, the optical parameters are, by definition, the same. This is intrinsic to the method, as the same stable island is used to extract the beam.

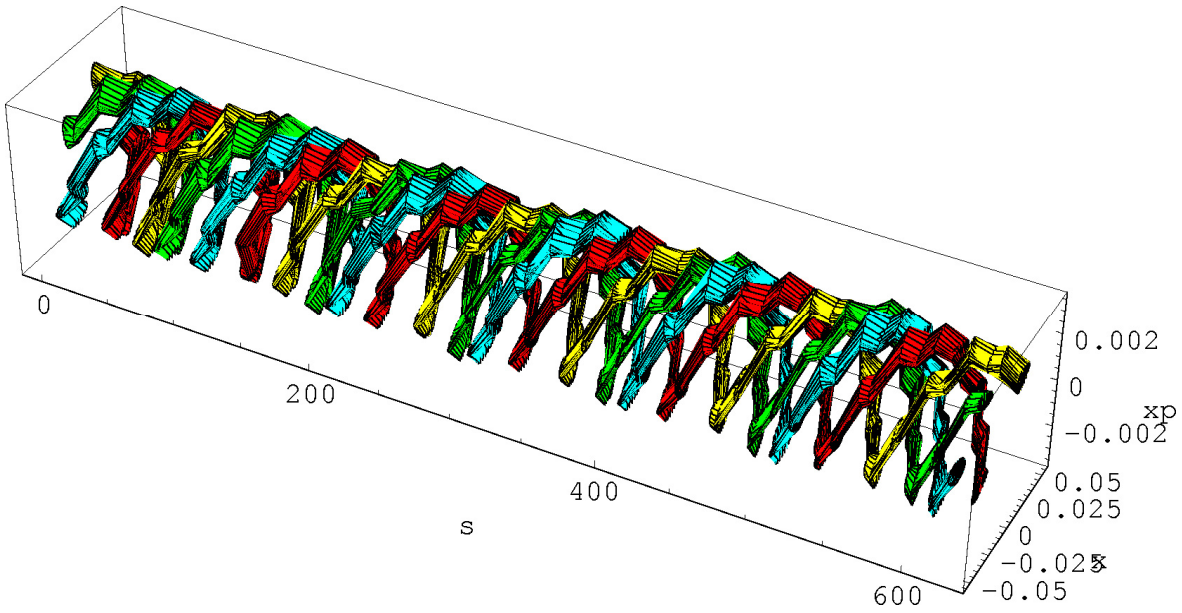

Fig. 11: 3D view of the beamlets along the circumference of the PS machine. The fifth beamlet, i.e., the beam core, is not shown here.

It is worth stressing that numerical simulations are performed by crossing the resonance from above: this is the opposite of what is done in the experimental tests, where the resonance is crossed from below. The choice of the resonance to be crossed is completely arbitrary: the use of a fourth-order resonance is dictated by the CERN-specific application.

The islands' phase at two key PS sections, namely the extraction septum location and the one where the wire scanner to measure the horizontal beam profile is installed, is shown in Fig. 12.

3.1.1 Analysis of the capture process for the fourth-order resonance

Following the first encouraging results [7,8], a series of studies were launched to analyse in more detail the capture and trapping process with a view to improving the control of the parameters of the beamlets. This goal was tackled using two complementary approaches: a numerical one and an analytical one. In the first case, the simple model described in Eq. (10)

was used to perform numerical simulations by varying a number of key parameters such as the functional dependence of the linear tune on the number of turns, the strength of the non-linear elements, and the parameters of the initial distribution, e.g., form of the distribution—Gaussian or uniform—and its emittance. As far as the tune-dependence on the number of turns is concerned, two models were used, i.e., a linear dependence or a polynomial one. No major differences were found for the two options and in all the simulations reported here a linear dependence is used.

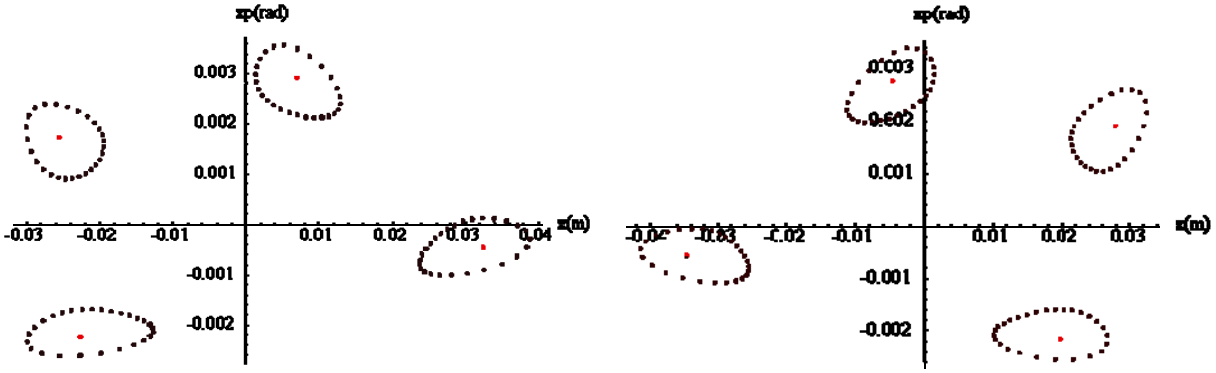

Fig. 12: Shape of the stable islands at two straight sections of the PS machine, namely the extraction section (left) and the section where the wire scanner used for profile measurements (see next sections) is located (right)

In Fig. 13 an example of the simulation results is reported. In the real application of this method, it is important to have a uniform sharing of initial intensity and emittance among the five beamlets after the trapping process. Hence ideally one aims at having 20% of the initial intensity in each beamlet as well as 20% of the initial emittance. In the simulations discussed here, the fraction of trapped particles and the emittance of each beamlet are computed as a function of the sigma of the initial Gaussian distribution. All the other parameters are kept fixed for this study. The different markers refer to the five beamlets (the one marked Isl#5 is indeed the central core).

It is apparent that increasing the sigma of the initial beam distribution has a positive impact on both intensity and emittance sharing. This is a consequence of the fact that the islands have a small size near the origin, hence they tend to capture fewer particles in the region with the highest density. Therefore, increasing the sigma means increasing the particles' density at larger amplitude, where the islands are bigger. An important point is that the ideal value of 20% sharing among the beamlets seems to be within reach by properly tuning the appropriate parameters.

On the theoretical side intense efforts were devoted to computing the islands' parameters, e.g., width, position, and secondary frequency, as a function of the linear tune and the strength of the non-linear elements (sextupoles and octupoles) [39]. This was achieved by using the normal forms approach [37].

Analytical formulae linking the islands' parameters, see Fig. 14, to the linear tune $\omega=2\pi\nu$, the detuning term Ω_2, the resonant term $u_{0,3}$, the strength of the non-linear elements κ, and the distance from the resonance ε are reported in the following.

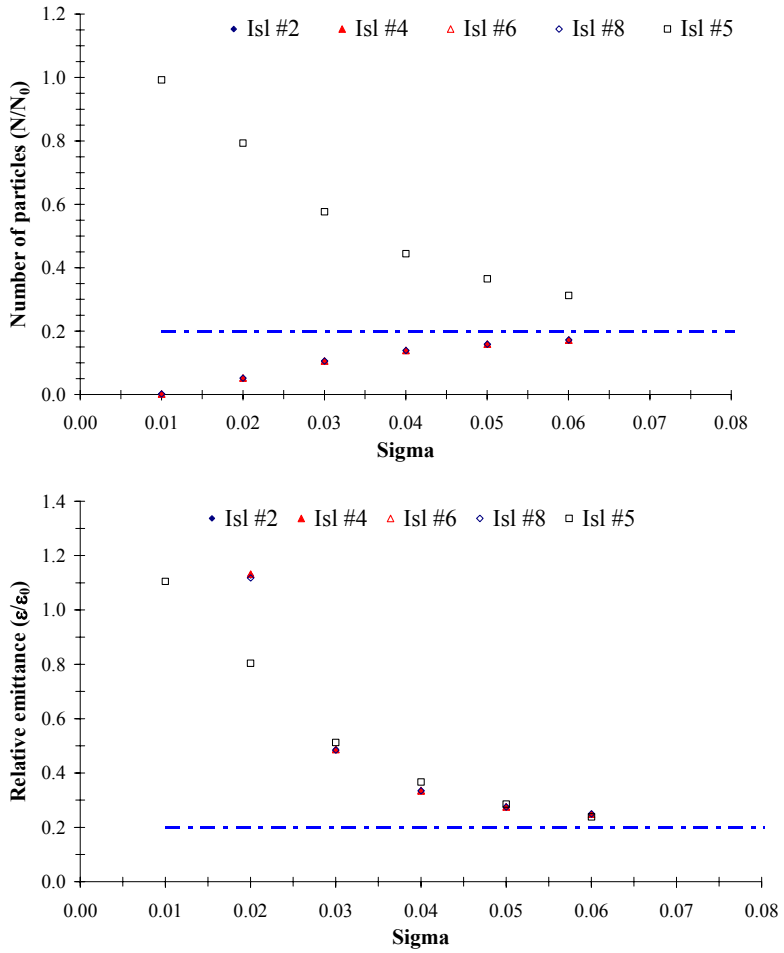

Fig. 13: Results of numerical simulations to evaluate the intensity trapped in each island vs. the sigma of the initial bi-Gaussian distribution (upper) and the emittance of each beamlet vs. the sigma (adimensional) of the initial bi-Gaussian distribution (lower). The dot-dashed line represents the goal of perfect splitting, i.e., equal intensity and emittance among the five resulting beamlets.

The distance of the fixed point from the origin ρ_+ and the maximum distance between separatrices Δ can be expressed as:

$$\rho_+ = -\frac{\varepsilon}{\Omega_2 + 2\varepsilon|u_{03}|}, \qquad \Delta = 4\sqrt{\left|\frac{\varepsilon}{\Omega_2}\right| \cdot |u_{0,3}|\rho_+^2} \tag{12}$$

where

$$u_{0,3} = \frac{i}{16} e^{i\omega}\left(\cot\frac{\omega}{2} - \cot\frac{3\omega}{2} - 2k\right) \qquad \Omega_2 = -\frac{1}{16}\left(3\cot\frac{\omega}{2} + \cot\frac{3\omega}{2}\right) - \frac{3}{8}\kappa\,. \tag{13}$$

The island surface and the secondary frequency are, respectively,

$$\Sigma = 16\sqrt{\left|\frac{\varepsilon}{\Omega_2}\right| \cdot |u_{0,3}|\rho_+^2} \qquad \omega_{\text{sec}} = 4\sqrt{|\Omega_2\varepsilon| \cdot |u_{0,3}|\rho_+^2}\,. \tag{14}$$

A first application of these formulae is the control of the islands' size during the transport towards higher amplitudes. A crucial point in the proposed technique is that, once the beamlets are created, they should be separated to leave enough space for the blade of the extraction septum, which should not intercept any particle. This goal is achieved by changing

the tune so that the islands move towards higher amplitudes: if this is performed slowly enough, the particles trapped inside move with the islands. The key issue is that the islands' size increases with the value of the linear tune. Hence the final value of the emittance of the beamlets would increase too.

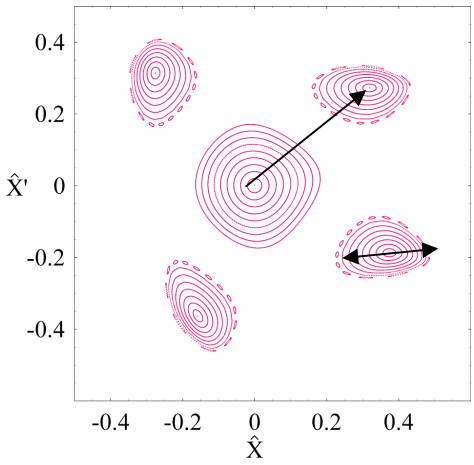

Fig. 14: Example of islands and their characteristic parameters

The knowledge of the analytical dependence of the islands' size on the tune and on the strength of the non-linear elements allows one to find a way to move the beamlets while keeping the surface constant. An example is shown in Fig. 15. To achieve the optimal control it is now necessary to vary the strength of the sextupoles and octupoles at the end of the capture process just before the transport towards higher amplitudes starts (upper).

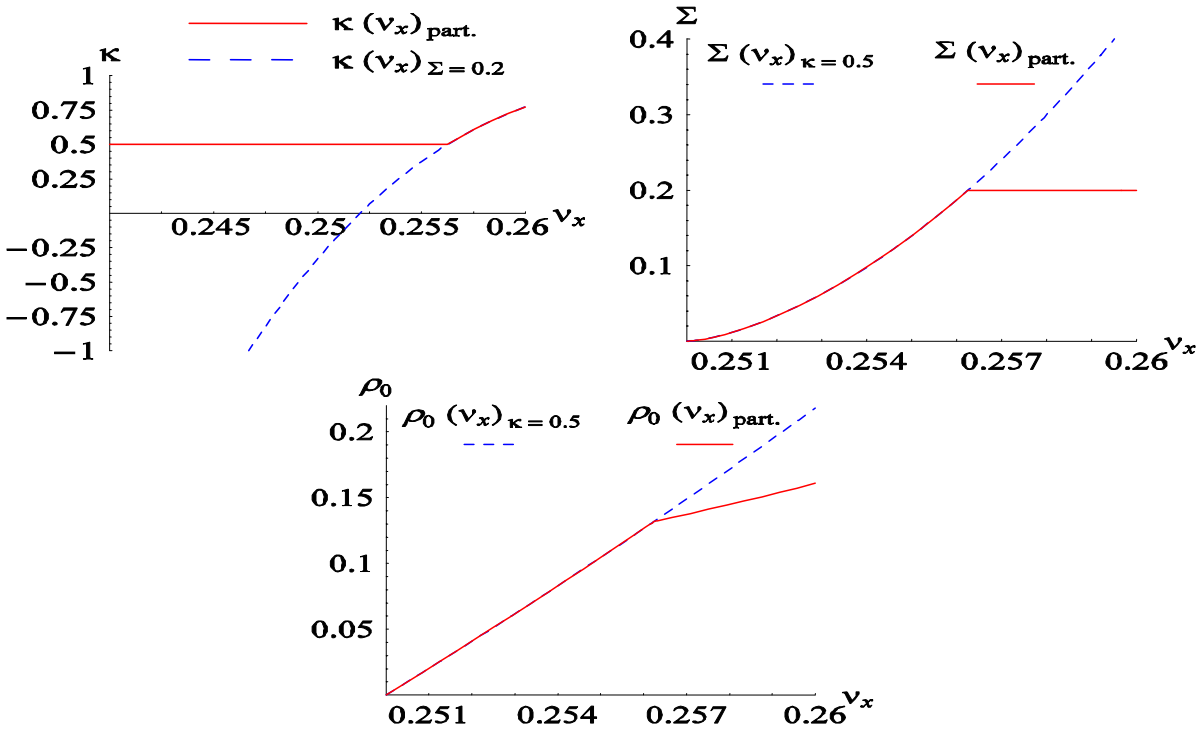

Fig. 15: Example of control of the islands' size while moving them towards higher amplitudes. The solid line represents a solution with constant island surface, while the dashed line corresponds to a constant value of the strength of the non-linearities.

In all the plots the quantities with subscript 'part' refer to a special solution where the islands' surface is left free to vary until the tune reaches the value 0.256 and then it is kept constant to 0.2.

In the upper right part, the islands' surface is shown and it is clearly kept constant once the fractional part of the linear tune is higher than 0.256. Correspondingly (lower) the islands' centre continues to move, although at a lower speed, when the surface is kept constant. It is planned to test these results by means of numerical simulations to evaluate the impact on the properties of the generated beamlets.

3.1.2 Extension to other resonances

Indeed, a rather straightforward extension of the proposed method to perform multi-turn extraction from a circular accelerator consists in crossing a different resonance, hence generating a different number of beamlets at the end of the splitting process [39]. The most natural alternative to the fourth-order resonance is to use the third-order one. This has another important consequence. In fact, the fourth-order is a stable resonance, which means that particles sitting near the origin of phase space will not be trapped by the moving islands. Therefore, for a stable resonance of order n, n+1 beamlets will be generated. On the other hand, when the resonance is unstable, particles will be pushed away from the origin and will fill the islands. Thus, for an unstable resonance of order n, n beamlets will be generated.

The results of numerical simulations performed using an initial Gaussian distribution and crossing the third-order resonance are shown in Fig. 16.

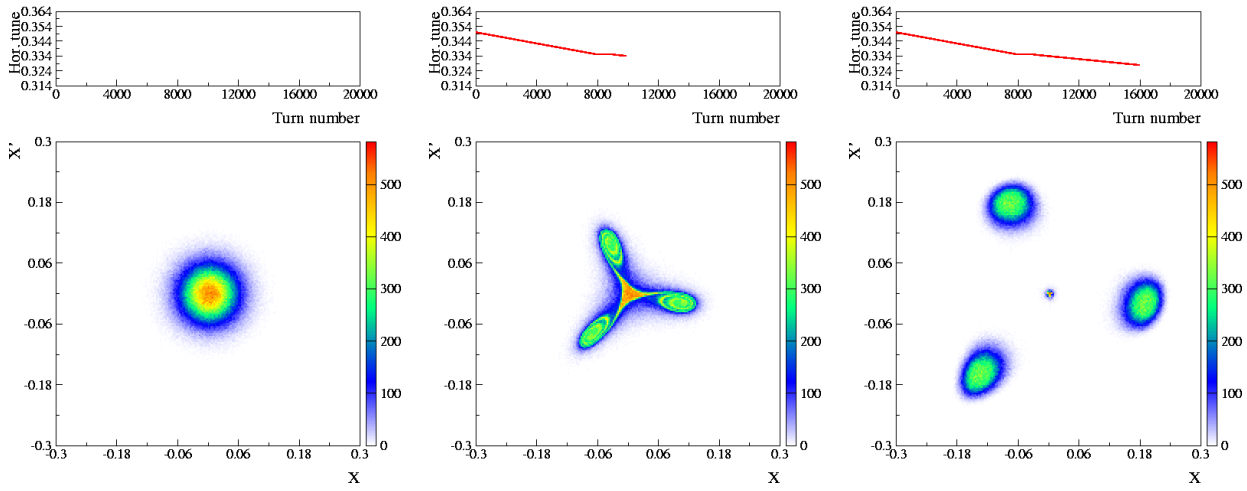

Fig. 16: Evolution of the beam distribution during resonance crossing: the initial state is represented by a bi-Gaussian beam (left); at resonance crossing some particles are trapped inside the moving islands (centre); at the end of the process, the particles trapped in the islands are moved towards higher amplitudes (right)

In contrast to the previous case, almost no particle is left at the origin. Furthermore, another interesting side effect is that the potential difference in terms of particle sharing and emittance between the central and the other beamlets is not present in this case.

Of course, the method can be generalized to other resonances: two examples are shown in Fig. 17.

It is worth while stressing that when the resonance order is increased, the islands' size tends to become smaller, thus implying that there will be fewer and fewer particles trapped in the islands. Furthermore, there will be less room for locating the blade of an extraction septum without intercepting any particle.

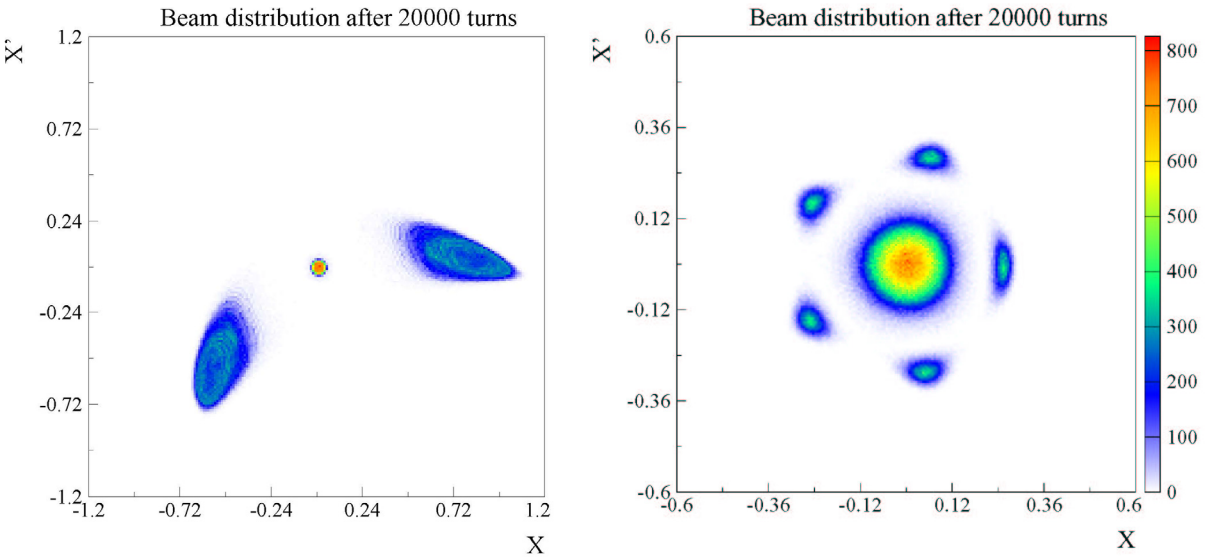

Fig. 17: Final stage of the splitting process after crossing the half-integer resonance (left) and the fifth-order resonance (right)

3.1.3 Multi-turn injection using stable islands

The most recent development is the application of the proposed technique to multi-turn injection [40]. This is a sort of natural consequence of the time-reversal property of the phenomena under consideration. However, there are interesting implications, which might be relevant for situations where the space charge forces are dominant. An example of multi-turn injection based on the use of stable islands in the transverse phase space is shown in Fig. 18.

In the case presented here, the fourth-order resonance is used: four turns are injected into the outermost island, which should be beyond the injection septum blade. Then, the tune is changed to merge the four beamlets back into one single structure. The fact that the islands have a size approaching zero near the origin implies that the beamlets will not be merged into a perfect Gaussian beam, but the final result is, instead, a hollow beam. Of course, this could be extremely important for high-intensity beams, as the hollow structure in the transverse phase space allows the tune spread to be reduced. It important to stress that the simulations presented here do not take into account the Coulomb interaction between the particles, hence the observation made should be confirmed by more detailed simulations also taking into account space charge effects. Another important point is that a fifth turn could also be injected: in this case instead of a hollow beam the final distribution would be the superposition of a hollow one plus a Gaussian at the centre: this opens up the possibility of performing a sort of painting in the transverse phase space [40].

3.2 Performance

A key issue is the robustness of the novel method against variation of the strength of non-linear elements. In fact, small deviations of K_2, K_3 from their nominal values might change the islands' parameters, thus modifying the extracted beam emittance and the capture efficiency [21]. Numerical simulations allowed this point to be tested. By using the nominal model, the value of the parameter κ, defined in terms of sextupolar and octupolar strength, has been changed, without varying any other parameter (functional dependence of the tune variation on the turn number and initial beam emittance). The results are shown in Fig. 19.

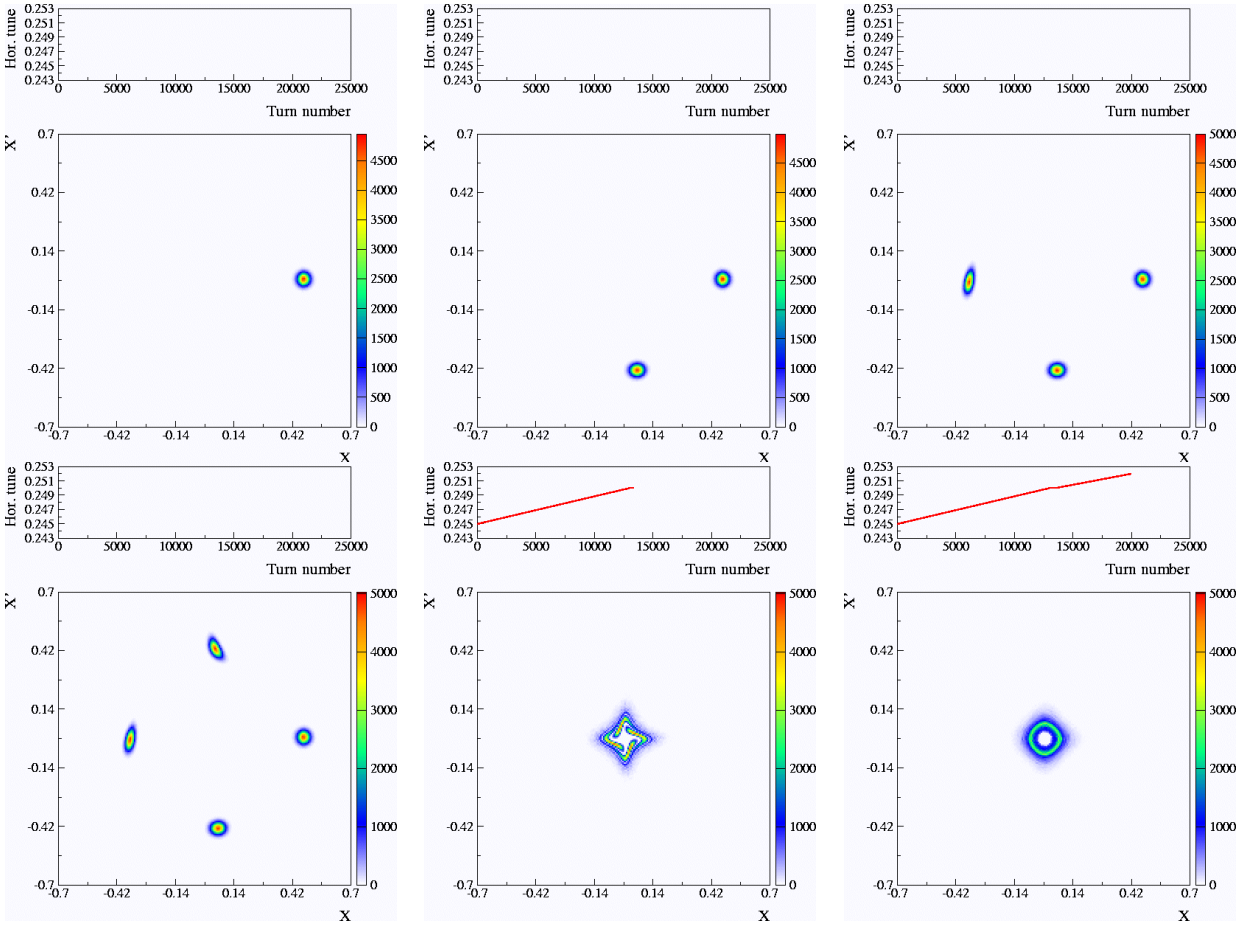

Fig. 18: Multi-turn injection by means of trapping in stable islands of transverse phase space. Four turns are injected and the beamlets merged by crossing the fourth-order resonance. As a result a hollow beam in the transverse phase space is generated.

The data concerning all four islands are shown to illustrate the differences between the various phase space structures. However, it should be emphasized that for the actual beam extraction, only one island will be used which will make the first four beamlets exactly equivalent as far as the optical and beam parameters are concerned. Both $\overline{\beta}_i / \beta_i$ and $\alpha \overline{\beta}_i / \beta - \overline{\alpha}_i$ do not deviate considerably from the perfectly matched values: only the fourth island seems to differ from the others. Also the dependence on κ is mild and smooth. As far as the relative emittance is concerned, the four islands have the same behaviour, showing a high dependence on the value of κ. However, this fact is not at all surprising, as κ dictates the island size [37]. It is important to stress that even for this novel approach, the extracted beam emittance is about 0.4–0.45 times smaller than that of the circulating beam (for the last beamlet, a more favourable value is obtained for the first four beamlets), comparable with the value for the present CT extraction obtained by the computations presented in the previous sections.

In contrast to the present CT, the proposed technique might suffer from tune ripple during the delicate phase of adiabatic capture. In fact, a periodic modulation of the nominal tune may generate particle diffusion resulting in emittance blow-up (see Refs. [41–43] as an example of some accelerators physics issues related with modulational diffusion and Ref. [44] for a general review of the problem). The effect of tune ripple consists in periodically displacing the islands and, at a smaller level, also varying their size. Numerical simulations were

performed to test this issue. The model in Eq. (10) has been modified by adding a periodic tune modulation to the necessary linear tune variation

$$\nu_n = \overline{\nu}_n \left[1+\Delta\nu\cos\left(2\pi n f_{\text{ripple}}+\varphi\right)\right] \tag{15}$$

where $\overline{\nu}_n$ represents the nominal time-dependence of the tune, $\Delta\nu$, f_{ripple}, φ are amplitude, frequency (properly converted from Hertz into turns), and phase of the ripple, respectively. Different values of the frequency f_{ripple} and of $\Delta\nu$ have been used in the simulations.

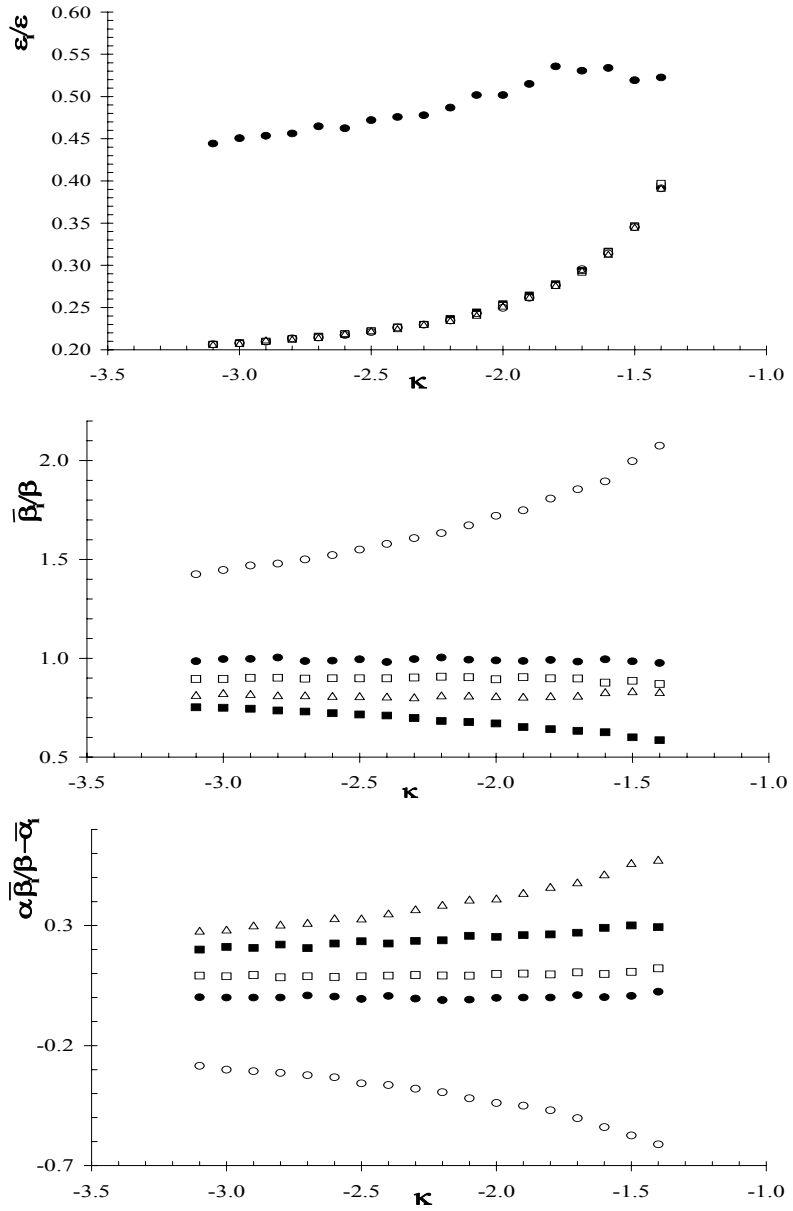

Fig. 19: Properties of the five beamlets vs. κ for the novel extraction mode based on adiabatic capture: relative beam emittance $\varepsilon_i / \varepsilon$ (upper); mismatch factor $\overline{\beta}_i / \beta_i$ (centre); and mismatch factor (lower) (black square first, open square second, open triangle third, open circle fourth, black circle fifth beamlet)

In Fig. 20 the final result of the adiabatic capture is shown, together with the tune curve. It is clearly seen that the higher-frequency ripple has a bigger effect on the five beamlets: in these cases their shape is almost unchanged, but the size is increased. Furthermore, the density is proportionally decreased as evidenced by the lighter colour. Detailed numerical simulations confirmed that the optical parameters do not depend strongly on the presence of ripple and the value of its characteristics parameters. Furthermore, the four beamlets corresponding to the four stable islands experience a rather similar emittance blow-up, higher than that of the beam core. As an example, $\varepsilon_1/\varepsilon$ and $\varepsilon_5/\varepsilon$ as a function of the ripple amplitude are shown in Fig. 21. Different ripple frequencies have been tested.

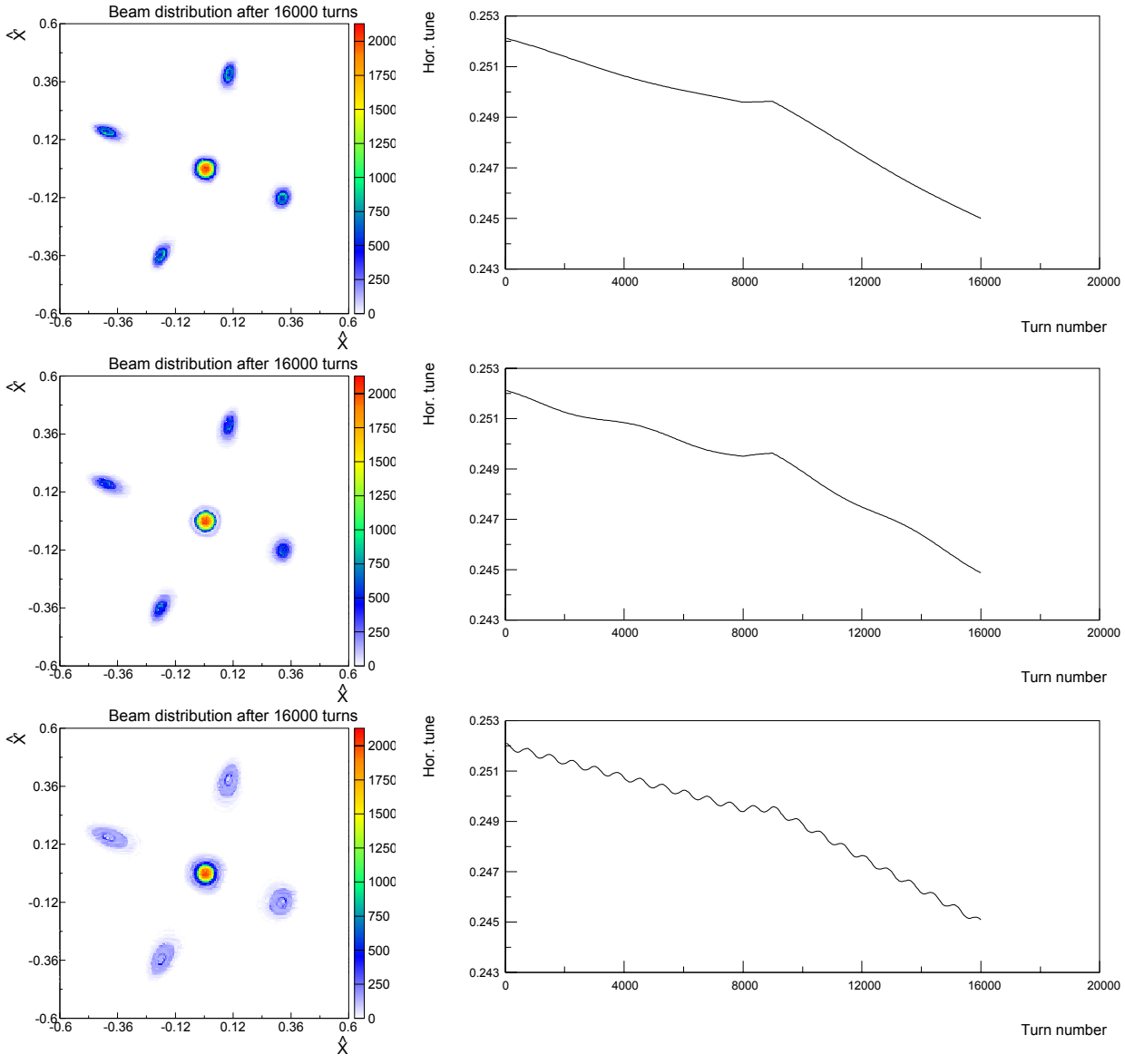

Fig. 20: The generated beamlets at the end of the capture process (left) for three different ripple frequencies: 50 Hz (upper), 100 Hz (centre), and 600 Hz (lower). The tune variation is shown on the right. The tune ripple amplitude $\Delta\nu$ is 5×10^{-4} in all cases.

The case corresponding to the absence of tune ripple is also shown as a reference. It is quite natural to observe that the lower frequencies have a smaller impact on the beam

characteristics, as they act for a shorter time during the adiabatic capture process. Also, for 50 Hz and 100 Hz, the amplitude dependence is quite smooth and regular. On the other hand for 600 Hz, the relative emittance shows a sudden increase even for quite small ripple amplitudes, while it reaches a sort of saturation immediately after.

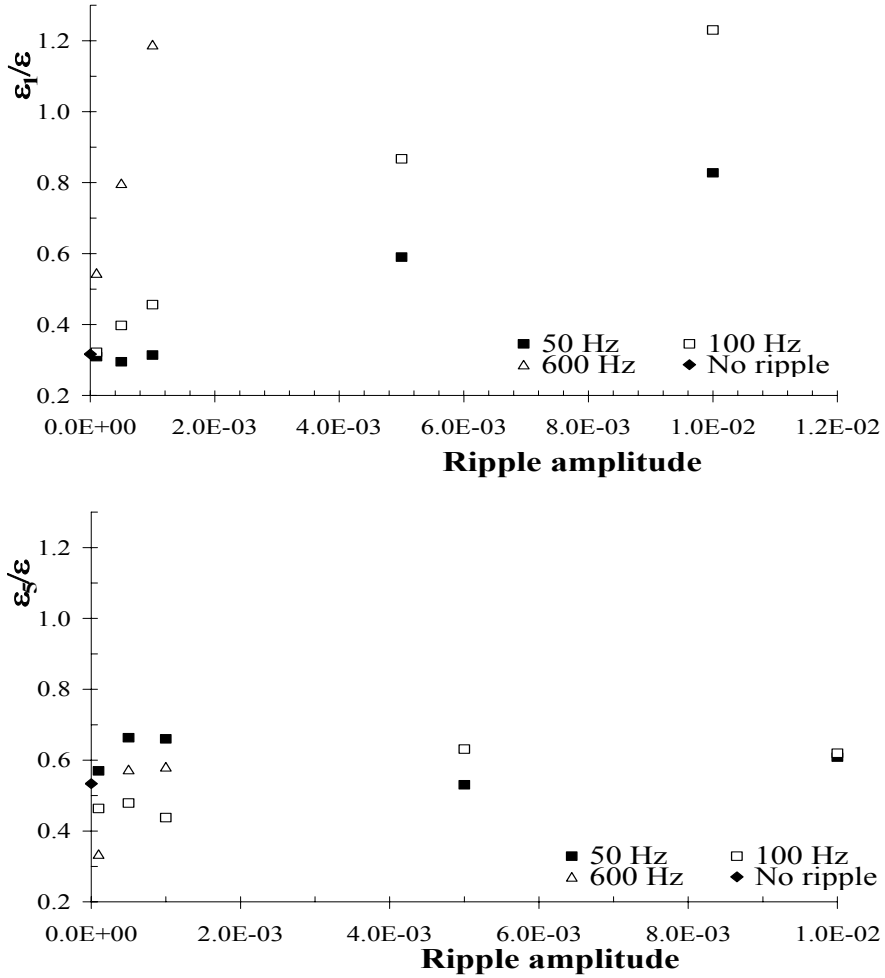

Fig. 21: Relative emittance $\varepsilon_i / \varepsilon$ for the first beamlet (left) and for the core (right), as a function of the ripple amplitude for different ripple frequencies

As was done for the present version of CT extraction, the blow-up after injection in the SPS was also computed for the proposed extraction. In Fig. 22 the factor H_i for the different beamlets is shown as a function of the parameter κ.

Again, the dependence on the strength of the non-linear elements is quite smooth. Furthermore, the absolute value of H_i is much smaller than in the case of the present CT extraction. In this respect, the proposed approach seems to be superior to CT. When tune ripple is taken into account, the fact that it does not much affect the optical beam parameters means that the mismatch at injection will be small too.

3.3 Beam losses

As was done for the present CT, the estimate of the beam losses for the proposed approach was computed using an analytical approach. The relevant parameters for the computation

depend on the performance of the kickers used to extract the beam and on the beam longitudinal structure. The kickers' parameters correspond to the proposed implementation and will be discussed in detail in the next sections. The estimate of the total beam losses was performed by assuming a bi-Gaussian beam distribution in the horizontal phase space, a magnetic septum thickness of 3 mm, which correspond to about 1.5 σ of the measured width of a beamlet, and it is assumed that the septum is located at 4 σ with respect to the beam core. The kicker rise time is of the order of 350 ns for the first four extracted turns and 80 ns for the fifth one (in all the cases, the rise time is expressed for 10%–90% of the amplitude).

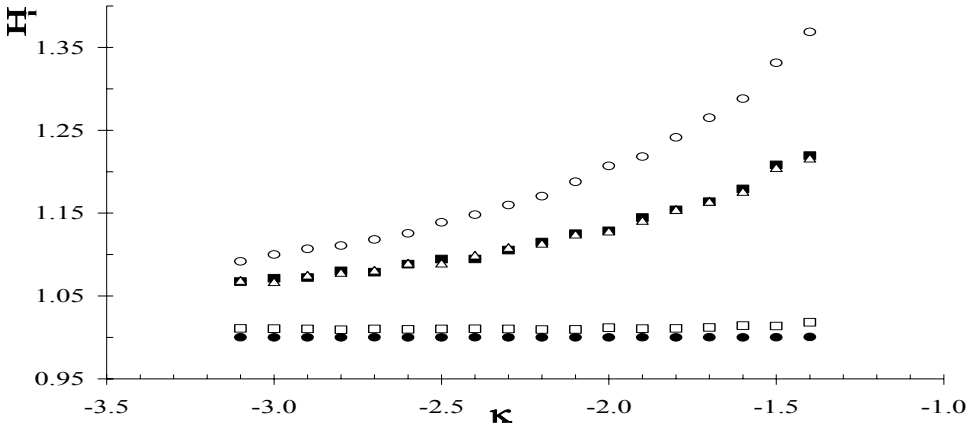

Fig. 22: Emittance blow-up factor H_i for the five beamlets as a function of κ (black square first, open square second, open triangle third, open circle fourth, black circle fifth beamlet)

As far as the longitudinal distribution is concerned, it will be mainly imposed by the SPS. Hence for the time being three cases, namely continuous beam, i.e., recaptured on h = 420, bunched beam on h = 16 or h = 8 have been considered. For the last two cases, the bunch length is fixed to 80 ns and 100 ns, respectively (the first value being an estimate, while the second one represents a realistic value from an MD beam). The longitudinal beam distribution for the two types of bunched structures is parabolic. In Fig. 23 the details of the kicker wave form (left part) and of the longitudinal beam structure in the h = 8 case (right part) are shown.

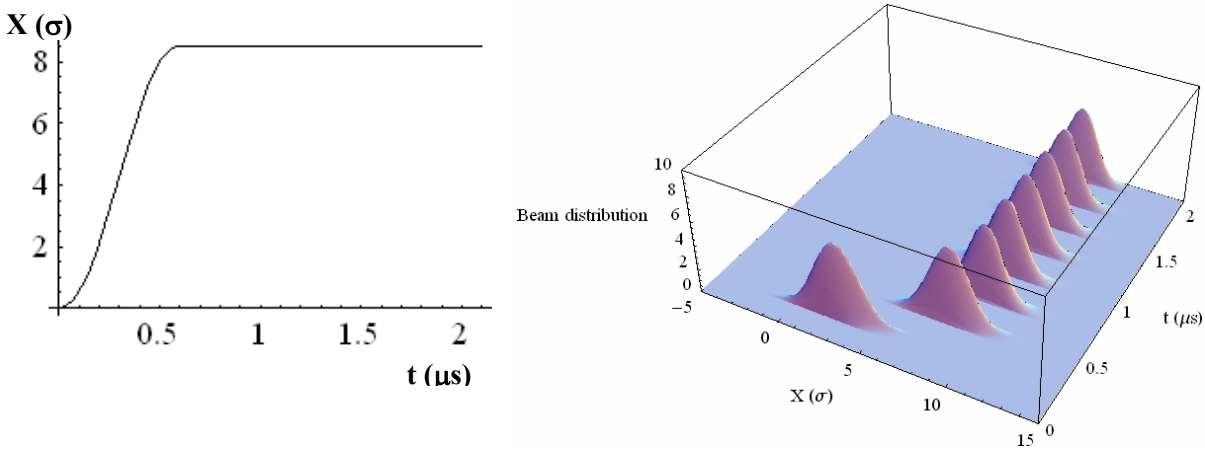

Fig. 23: Kicker wave form (left part) and longitudinal and transverse beam distribution (right part) used in the analytical computations of the total beam losses for the novel multi-turn extraction. In both cases the longitudinal axis corresponds to one single machine circumference at 14 GeV/*c*.

The main results are reported in Fig. 24 where the total relative beam losses as a function of the magnetic septum thickness are shown. The three curves refer to the different longitudinal structures.

The numerical values of the beam losses are also listed in Table 5, where two additional configurations, namely one with reduced kicker rise time (from 350 ns to 150 ns) and one with reduced magnetic septum thickness have been considered. In all the cases 2%–3% beam losses have been added to the computed losses to take into account the observed losses during resonance crossing.

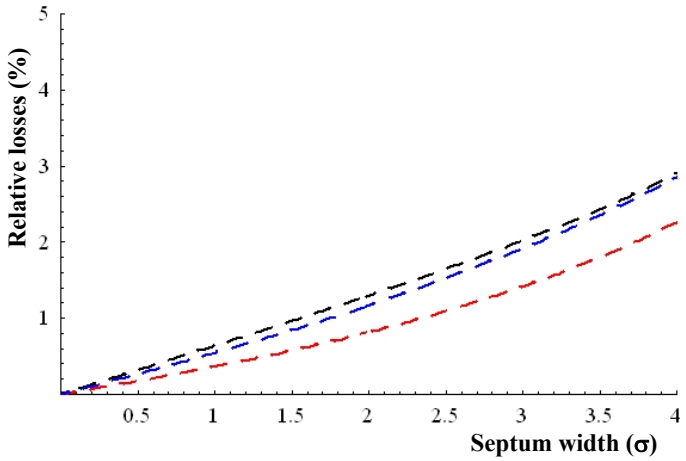

Fig. 24: Total relative beam losses at extraction for the novel multi-turn extraction. The black curve refers to the continuous beam; the blue curve refers to the bunched beam on h=16; the red curve refers to the bunched beam on h=8. The thickness of the magnetic septum corresponds to about 1.5 σ of the measured width of a beamlet.

Table 5: Comparison of the total beam losses for the novel multi-turn extraction as a function of the longitudinal beam distribution for the nominal extraction layout and two improved versions: one with reduced rise time of the kickers, and one with reduced magnetic septum thickness

	Beam losses (%)		
	Continuous	Bunched (h=16)	Bunched (h=8)
Nominal configuration	1	0.9	0.6
Total (capture+extraction)	3–4	2.9–3.9	2.6–3.6
Improved kickers (faster rise time)	0.6	0.5	< 0.1
Total (capture+extraction)	2.6–3.6	2.5–3.5	2.1–3.1
Reduced thickness of magnetic septum	0.6	0.5	0.3
Total (capture+extraction)	2.6–3.6	2.5–3.5	2.3–3.3

The first comment on the results shown in Table 5 is that the capture losses dominate over the extraction losses. Therefore, the beneficial reduction of the extraction losses has a rather modest impact on the overall losses. Furthermore, for the case of continuous beam or bunched on h=16, the improvement induced by the reduction of the kickers' rise time is the same as the one generated by the reduction in the magnetic septum thickness. On the other hand, for the case of bunched beam on h=8, for which the improved kickers' rise time would really fit the bunch spacing, the reduction of the extraction losses is dramatic.

Finally, it is worth mentioning that for the present CT the overall losses were estimated in the previous section to be of the order of 9% to 13%, depending on the assumed electrostatic septum width. Therefore, the novel extraction will reduce the losses by a factor of 3 to 4.

3.4 Measurement results

3.4.1 Overall measurement strategy

In parallel with the computational and theoretical analysis of the problem, an intense experimental campaign was launched at the end of 2001 [11–13,45–48] on the CERN PS. This entailed the development of new measurement systems, such as the turn-by-turn orbit measurement system [49,50], as well as the installation of sextupoles and octupoles to generate the stable islands.

The magnetic elements and the beam instrumentation used in the experimental campaign are shown in Fig. 25. The tune is changed by means of two families of focusing and defocusing quadrupoles, normally used to tune the machine. Sextupoles and octupoles are used to generate the stable islands; the fast-extraction kicker is used to displace the beam and induce betatron oscillations for phase space measurements; a wire scanner [51] is used to measure the horizontal beam profile (see Fig. 26 for details on the installation); two pick-ups are used to record the betatron oscillations.

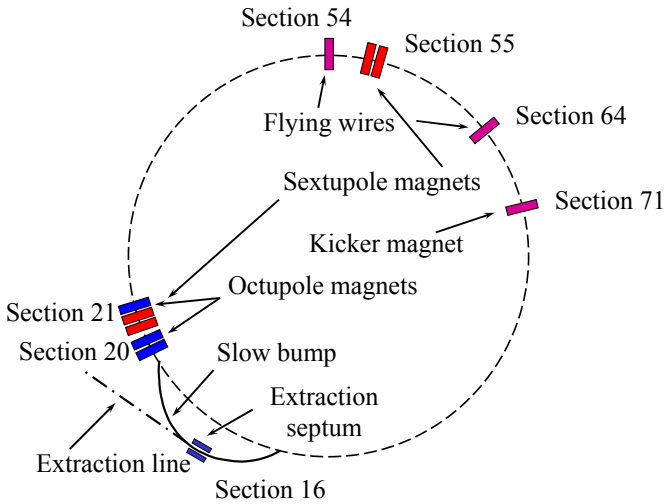

Fig. 25: Schematic layout of the PS machine with the elements used for the experimental study of the novel multi-turn extraction

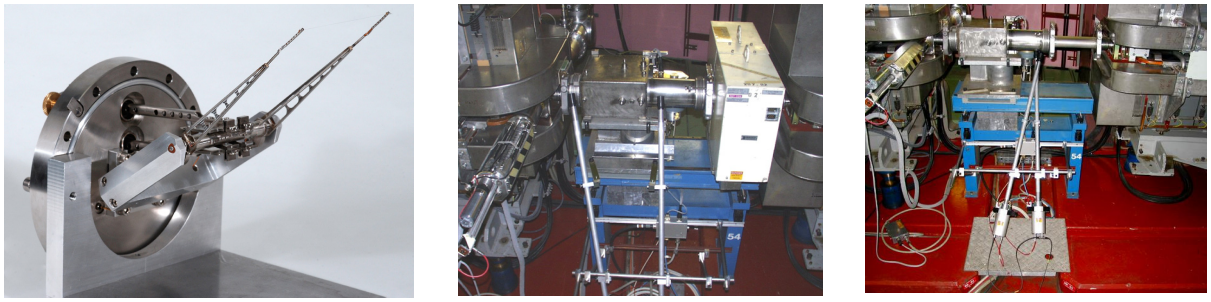

Fig. 26: Schematic layout of the mechanism of the PS wire scanner (left). The installation of the scintillators on one side of the vacuum chamber used during the experimental campaign and the new layout with symmetric scintillators are shown on the centre and right part, respectively.

The overall strategy for the experimental campaign was based on three stages:

1. Measurement of the phase space topology. This is performed by displacing a low-intensity, single-bunch, pencil beam by means of the fast extraction kicker. The betatron oscillations measured by two pick-ups are then recorded on a turn-by-turn basis and analysed to detect the presence of stable islands. Normally the position signal features a decoherence due to beam filamentation induced by non-linear effects and chromaticity. Whenever the beam is displaced inside one island, natural decoherence is almost completely suppressed. An example of the measurement results is shown in Fig. 27 [39]. The position signal as a function of the number of turns is shown in the upper part: no sign of decoherence is visible. Damped oscillations are visible in the first part of the time-series. These indicate that the beam is rotating around the island's centre. From the first part of the time-series it is possible to measure the so-called secondary frequency [37] or island tune [52]. Furthermore, it is possible to scan over the amplitude inside the island to evaluate a sort of detuning curve [39]. The result of such a measurement is shown in the lower left part. Finally, the information from the two pick-ups is combined to reconstruct the transverse phase space topology (lower right). A clear signature of the presence of four islands is visible.

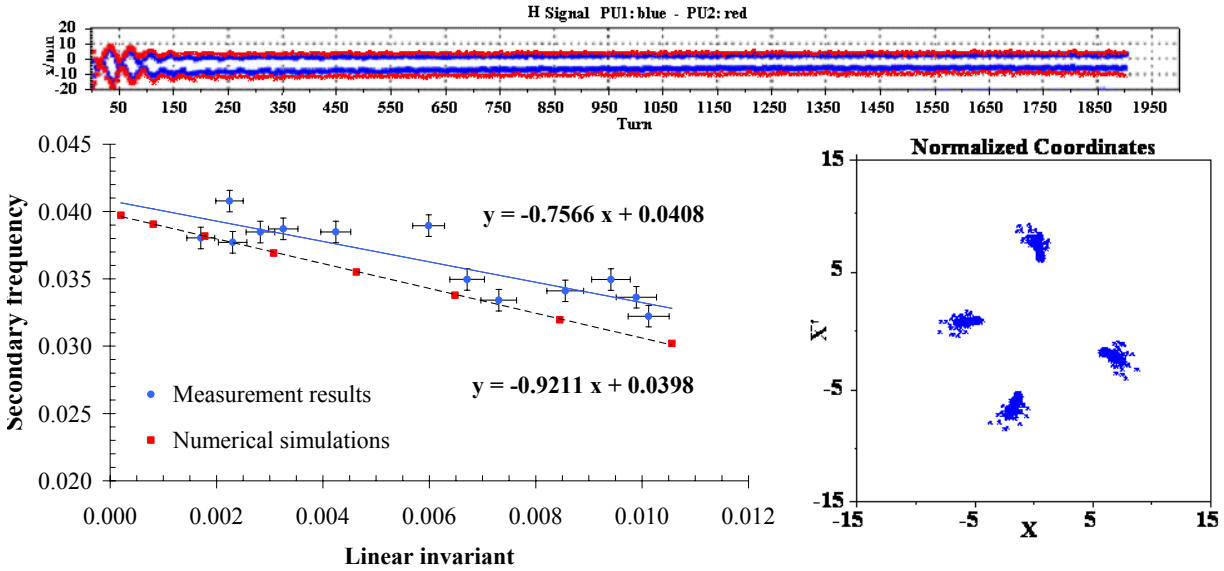

Fig. 27: Results of the phase space measurements in presence of stable islands generated by means of sextupoles and octupoles. The beam position vs. the number of turns is shown in the upper part, while the reconstructed phase space is shown in the lower right part. The secondary frequency vs. the amplitude inside the island is shown in the lower left part.

2. Trapping measurement with a low-intensity beam. The key measurement, i.e., the verification of the splitting due to resonance crossing is usually performed first with a low-intensity, single-bunch beam. This has the advantage of suppressing any possible effect due to Coulomb interaction between the protons in the bunch. Furthermore, a special care is devoted at the level of the PS Booster, i.e., the PS injector, when generating this special beam. In fact, as already mentioned, the larger the horizontal emittance of the initial beam, the more efficient the trapping. Therefore, the beam is artificially blown up in the horizontal plane, while keeping the vertical emittance as small as possible. Ideally, the horizontal emittance should have as much as possible a value similar to that of the high-intensity beam, while the vertical one should be similar to that of the pencil beam used for the phase space measurement. The first requirement

allows the reproduction of the conditions achieved when operating with an intense beam, while the second one allows the reduction of the non-linear horizontal/vertical coupling, thus facilitating the setting up during the first attempts. During this stage of the measurements the key instrument is the wire scanner. It allows the horizontal beam profile to be recorded, thus showing the details of the splitting. Examples of profile measurements can be seen in Figs. 28, 29, 31, 32. The raw data are fitted using five Gaussian distributions whose parameters, mean, sigma, integral, are assumed to reflect the properties of the beamlets.

3. Trapping measurement with a high-intensity beam. This represents the most important test for this novel approach. A sequence of transverse beam profiles during the splitting process is shown in Fig. 28 (upper part) together with the best result achieved (lower part). The intensity as a function of time is shown (lower left) together with the measured horizontal beam profile at the end of the capture process (lower right). The injected intensity is slightly above 6×10^{12} protons and small losses are visible up to transition crossing (second vertical red line). Then, the intensity stays remarkably constant up to extraction, which is performed by means of a kicker in a single turn after having merged back the beamlets in order to reduce the beam size in the horizontal plane to match the septum acceptance.

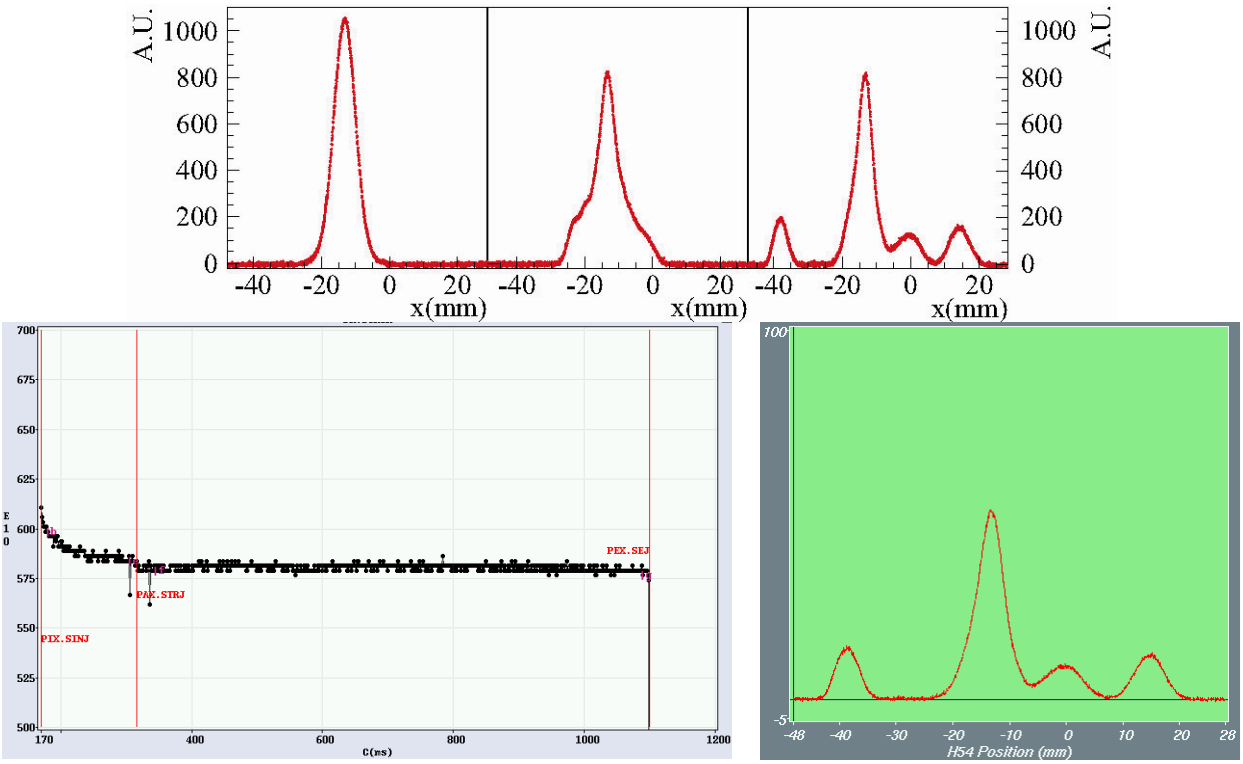

Fig. 28: Sequence of beam profile during splitting (upper) and best result achieved with a high-intensity beam, whose intensity as a function of time (lower left) and horizontal beam profile at the end of the capture process (lower right) is shown. The fact that the profile is not centred at zero is due to an instrumental offset of the wire scanner position.

In the right part of Fig. 28 the beam profile after the splitting is shown. A number of peaks are visible; in particular the central one features rather large tails. Indeed, the left tail is due to the projection of the beamlet behind (see Fig. 27, right). Another important point is that the left-most beamlet is very well-separated and the region between it and

the central core is depleted. This feature is crucial for having small or no losses at all at extraction, as it guarantees no interaction between the extraction septum blade and the beam.

The control of the tune is a crucial ingredient during the whole process. Detailed measurements were made in order to perform a scan in the horizontal tune keeping the vertical one constant. The results of the measurements are shown in Fig. 29 (left) where the evolution of the horizontal and vertical tune is shown as a function of time along the cycle. In the upper part, the tune change is compared to the magnetic cycle, while in the lower part a detailed view of the tune change around the resonance-crossing gymnastics is plotted. It is worth stressing that, unlike in the numerical simulation where the fourth-order resonance was crossed from above, in the experimental tests the resonance was crossed from below. The tune was measured every millisecond and each experimental point represents the average over five measurements. Interestingly enough, the vertical tune is shifted down during the first stage of the resonance crossing, perhaps due to non-linear coupling between the two transverse planes.

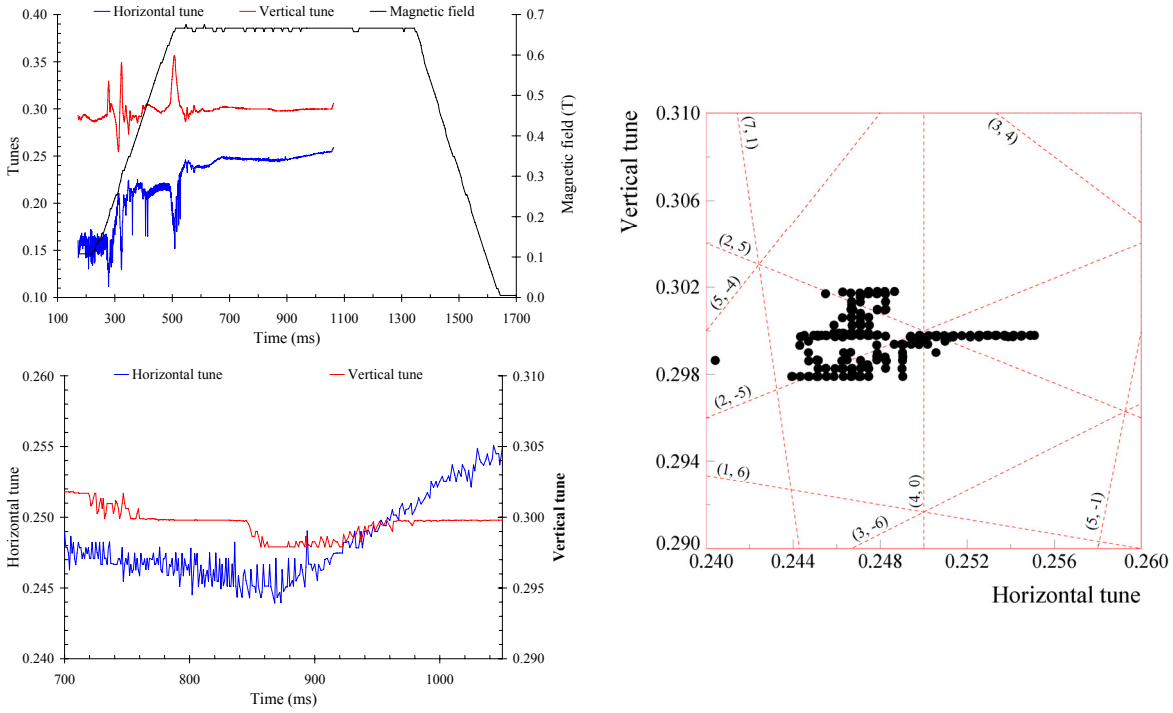

Fig. 29: Time evolution of the horizontal and vertical tunes (left) and representation of the tune in the resonance diagram (right)

In the right part of Fig. 29 the tunes are represented in the resonance diagram. Resonance lines from third to ninth order are represented. Even though the value of the vertical tune is such that the fourth-order resonance is crossed where also two seventh-order ones are present, namely the (2, ±5), such a working point turned out to be the best in terms of losses.

A final test was performed to increase the fraction of particles trapped inside the islands. For this study, a special setting of the octupoles was programmed: instead of keeping their strength constant all along the resonance-crossing phase, the current was suddenly increased just before resonance crossing and then gradually reduced. This should generate large islands at small amplitudes thus trapping more particles from the

region where the density is high, and then keeping almost constant the island's size. The results are shown in Fig. 30, where the current as a function of time for both the sextupoles and the octupoles is shown (left) as well as the measured horizontal beam profile (right).

Under these new conditions it was indeed possible to increase the fraction of particles inside the islands, achieving a value of 18% against a previous value of about 13%. It is worth while mentioning that for the optimal performance of the SPS machine, the allowed fraction of particles inside each beamlets is limited to (20±5)%: if this holds for the central core the limit for the other beamlets is instead (20±1)%. However, the price to pay was the presence of slightly higher losses during resonance crossing up to the level of 2%–3% of the total beam intensity.

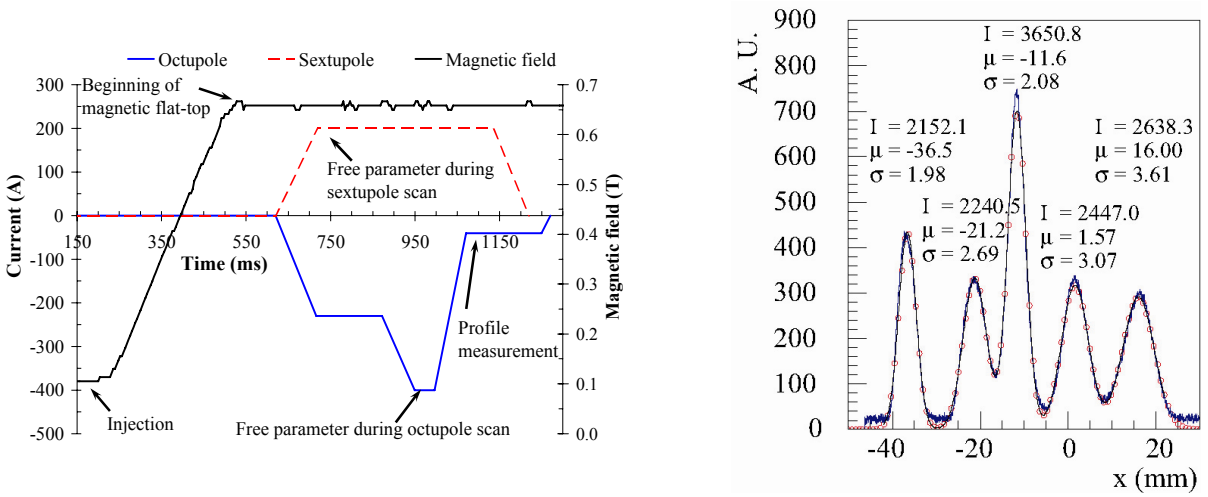

Fig. 30: Current as a function of time for the sextupoles and octupoles as used in the special test to increase the fraction of particles trapped in the beamlets (left). The resulting horizontal beam profile after splitting is also shown (right). The profile is not centred at zero due to an instrumental offset of the wire position.

The measured beam profile shown in Fig. 30 is used as the basis for the subsequent analysis of the required mechanical aperture. The beam parameters of the five beamlets, i.e., intensity, mean position and sigma, are derived by fitting appropriate Gaussian functions. The approach used deserves some comments. The underlying physical process imposes a constraint on the measured intensity of the four outermost beamlets. As they represent a single structure closing up around the machine after four turns, the measured intensity has to be the same for all of them. In addition, the experimental set-up used to detect the particles generated by the beam-wire interaction adds another feature. In fact, the scintillator is located on one side of the vacuum chamber, so that the solid angle under which the five beamlets are seen is not the same. This can be seen clearly in Fig. 26 (centre) where the positions of the two pipes containing the scintillators on the same side of the wire scanner tank are clearly visible. This configuration is a consequence of the former operation with negatively charged particles, i.e., electrons for LEP and antiprotons for the SPS, when the appropriate scintillator was selected based on the direction of the particle motion. This introduces a left/right asymmetry in the measured profile, which has to be considered in the analysis. To this end, instead of fitting the profile using five Gaussians, out of which four feature the same intensity, the leftmost beamlet (see Fig. 30) is fitted without imposing any constraint on the intensity, while the

other three have the same intensity (the centre core being independent in any case). The results of the analysis are reported in Table 6: they will be used in the next sections to simulate the beam envelope with a view to estimating the aperture requirements.

Table 6: Values of the fit parameters of the best result shown in Fig. 30, namely intensity, mean value μ and σ. The shift of the position of the centre core is due to an instrumentation issue.

Beamlet	Intensity (Arb. units)	μ (mm)	σ (mm)
Centre core	3618	–11.63	2.05
Leftmost beamlet	2152	–36.57	1.98
Left beamlet	2428	–21.14	2.75
Right beamlet	2428	1.60	3.13
Rightmost beamlet	2428	15.98	3.49

Parenthetically, the set-up was improved so that for the 2006 run a symmetric, namely one on each side of the vacuum pipe, configuration of the two scintillators will be used (see Fig. 26 right).

As a final result the beam distribution as measured in the transfer line downstream the extraction point form the PS machine is shown in Fig. 31. An Optical Transition Radiation (OTR) [53] is used to record the two-dimensional beam distribution in physical space.

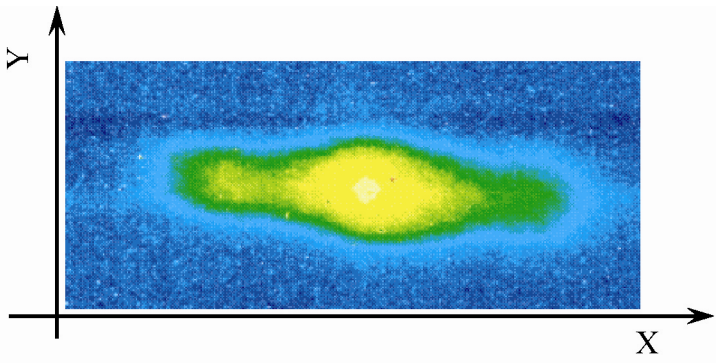

Fig. 31: Two-dimensional beam distribution in physical space of the beam in the transfer line downstream of the PS extraction point

The peculiar shape of the beam distribution is clearly visible: the two lateral peaks represent the projection in physical space of the beamlets.

The main parameters of the single-bunch beams used in the experimental campaign are summarized in Table 7.

Table 7: Parameters of the three single-bunch beams used for the experimental tests of the novel multi-turn extraction. The emittance is the normalized, one–sigma value.

Parameter	Intensity (protons/bunch)	$\varepsilon^*_H(\sigma)$ (μm)	$\varepsilon^*_V(\sigma)$ (μm)	$\Delta p/p(\sigma)$ 10^{-3}
Low-intensity, pencil beam	5×10^{11}	2.3	1.3	0.25
Low-intensity, large horizontal emittance	5×10^{11}	6.2	1.6	0.25
High-intensity beam	6×10^{12}	9.4	6.4	0.60

3.4.2 Special measurements

In addition to the measurements performed to establish the feasibility of the proposed method, a number of detailed measurements were performed to study the dependence of the beamlet parameters, such as the fraction of captured particles, position, and width on the non-linear parameters and, even more important, on the way the resonance in crossed. Although in the numerical simulations the influence of a polynomial dependence on the turn number of the linear tune was tested, in the real experiments only a linear tune variation was tested. However, the influence on the resonance crossing speed was assessed.

During such a test the resonance was crossed twice with the aim of bringing back the beamlets towards the centre core. When the resonance crossing is slow enough, one could argue that it should be possible to end up in a state not too different from the initial one. The crossing speed was the same in both directions and after the first resonance crossing, the tune was kept constant for a period of 20 ms or 180 ms. The horizontal beam profile was measured at three different moments: before the first resonance crossing, after the first resonance crossing when the tune was constant and the beam split, and after the second resonance crossing (see Fig. 32). The crossing speed was changed and the profiles for many values of the crossing speed recorded.

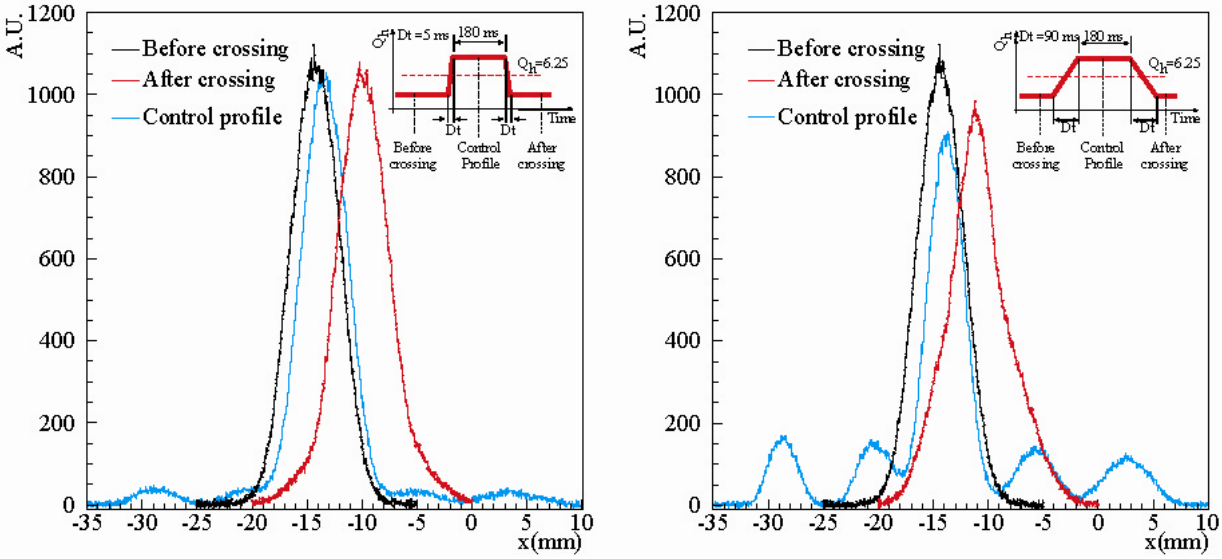

Fig. 32: Results of the dependence of the beamlets parameters on the resonance crossing speed. The sketch of the measurement principle is shown in each plot (upper right part). The horizontal profiles for a fast crossing (5 ms) are shown in the left part, corresponding to the three moments, while the profiles on the right correspond to a slow crossing (90 ms). The profiles are not centred at zero due to an instrumental offset of the wire scanner position.

When a fast crossing occurs, almost no particles are trapped inside the moving islands and the final profile is very similar to the initial one. On the other hand, when a slow crossing occurs, many more particles are trapped inside the islands, but the final beam profile is no longer Gaussian and differs from the initial one. The hypothesis is that tails are generated by the beamlets when they are put back into the central core. As long as the crossing time is longer than 50–70 ms the fraction of particles trapped inside the beamlets stays constant and the final profile features non-Gaussian tails. The situation does not change quantitatively when the period when the tune is kept constant is reduced drastically: the process seems to be always non-reversible.

The influence of the octupole strength on the number of particles captured in the islands is the last example of detailed measurement presented in this paper. The maximum negative current corresponding to the second plateau shown in Fig. 30 (left) is changed. The influence of the octupole is twofold: it changes the islands' size and it varies the detuning with amplitude, thus moving the islands' centres. The results are shown in Fig. 33.

The increase in the number of particles trapped when the strength of the octupole is reduced (in a relative sense) is clearly visible (left). At the same time, the fraction of particles remaining in the central core is reduced. Two points are clearly outliers: the fit procedure failed for those two cases because of the too low intensity captured in the islands. The horizontal beam profile measured at the end of the splitting process is shown in Fig. 33 (right). The impact of the octupole on the fraction of particles trapped, as well as on the position of the beamlets, is clearly visible.

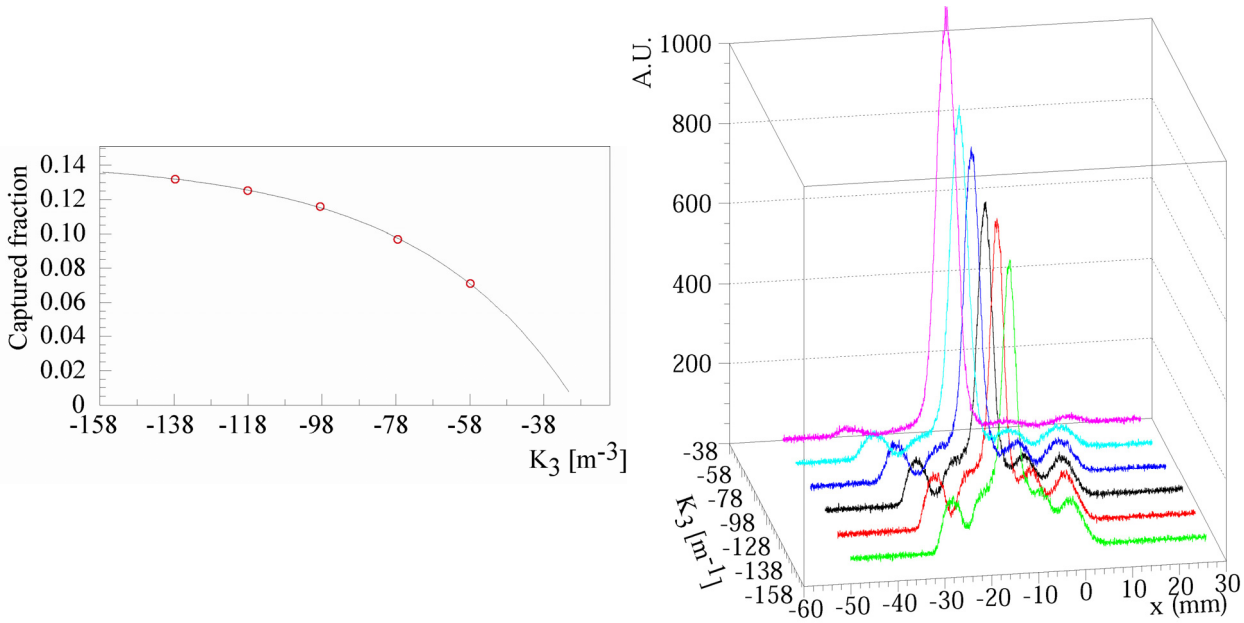

Fig. 33: Results of the influence of the octupolar strength on the fraction of particles trapped in the beamlets (left). A series of horizontal beam profiles measured for different values of the octupolar strength are also shown (right).

4 Proposed scheme for MTE at the CERN PS

4.1 Principle

The experimental campaign was completed at the end of the 2004. The analysis of the required modifications to implement the proposed multi-turn extraction took place during the 2005/2006 long shutdown of the PS machine. The conceptual design of the proposed multi-turn extraction can be sketched as follows:

- Beam splitting: two pairs of two sextupoles and one octupole each will be used to separate the initial single beam into the five beamlets prior to extraction. Contrary to the experimental set-up, where only one set of two sextupoles and one octupole was used, the choice of two pairs is mainly dictated by the need to control and adjust the phase of the islands at the extraction point.

- Extraction: the extraction point is in SS16, where the magnetic septum for the beam extraction towards the SPS is located. In the proposed scheme, the electrostatic septum, currently used to slice the beam in the context of the CT extraction in SS31, is not required, thus simplifying the overall scheme. Moreover, this will have the added benefit of maintaining less highly-radioactive material. Two bumps will be used to displace the beam towards the magnetic septum blade (slow bump) and to extract the beamlets over five turns (fast bump).
- Slow bump: a set of dipole magnets (bumpers) will be used to generate the slow bump around the magnetic septum. Currently, four bumps powered with a series/parallel circuit are used to extract the beams towards the SPS. In the proposed scheme, six independently powered magnets are foreseen. The large number of bumpers is imposed by the aperture constraints, i.e., it will allow a careful shaping of the bump to overcome the potential aperture bottlenecks.
- Fast bump: three new kickers will be used to generate the fast bump used to displace the beam beyond the blade of the magnetic septum. The pulse length should correspond to five PS turns. Since the centre core of the beam needs to be ejected, an additional kick will have to be imparted at the fifth turn. For this the fast extraction kicker will be used.
- Trajectory correction in the transfer line towards the SPS: even though, in principle, the extraction conditions for the novel multi-turn extraction do not change from turn to turn, as one single island is used to extract the beam, the feed-down effects of the machine non-linearities (particularly from the pole face windings in the main magnets) due to the extraction bumps could generate turn-by-turn variation of the beamlet position at PS extraction. Such an effect could have a negative impact on the emittance after filamentation in the SPS. Hence two kickers capable of generating deflection changing from turn to turn will be used in the TT2 transfer line to correct for the variation in the extraction conditions (position and angle). These two devices are already being used for the present CT extraction mode.

The challenge consists in implementing the proposed scheme within the tight boundary conditions given by the PS ring layout in such a way that new elements can be installed without having a domino effect, where consequences of the change propagate far away from the original straight section.

4.2 Implementation

4.2.1 Slow bump

The present version of the slow bump in section 16 is made of four magnets (two of type 206, and two of type 210, whose parameters can be found at the end of this report in Appendix A) located in straight sections 12, 14, 20, and 22. The elements in sections 12 and 22 are in series (magnets of type 206 and 210, respectively) and the same holds for those in sections 14 and 20 (magnets of type 210 and 206, respectively). The two groups 12–22 and 14–20 are then connected in parallel to a single power converter, also called PR.BSW16. The power converter is a capacitor discharge type, which is also used for the slow bump in section 31 (BSW31), the one used to approach the beam to the electrostatic septum prior to slicing during CT extraction. It is also used for the two quadrupole kick enhancement systems for extraction in straight section 16 (QKE16) and 58 (QKE58), the former fast extraction of antiprotons towards the SPS. Parenthetically, both QKEs are made of two quadrupoles of type 414 (see Appendix B for the details concerning their magnetic and electrical properties)

installed in straight sections 5 and 25 (QKE16) and 49 and 69 (QKE58). Typical operational settings are reported in Table 8 for the CT extraction (14 GeV/*c*), the fast extraction for the nTOF facility (20 GeV/*c*), and LHC-like fast extraction (26 GeV/*c*).

Table 8: Values of the current for the magnetic elements powered with capacitor discharge converters with the present layout of slow bump 16

Element	Straight section	Magnet type	14 GeV/*c* (CT)	20 GeV/*c*	26 GeV/*c*
BSW16.1 (A)	12	206	315	360	465
BSW16.2 (A)	14	210	315	360	465
BSW16.3 (A)	20	206	315	360	465
BSW16.4 (A)	22	210	315	360	465
QKE16 (A)	5/25	414	1940	960	1250
QKE58 (A)	49/69	414	–	960	1250
BSW31 (A)	27/35	205	275	–	–
Beam length [a] (μs)			10.5	2.1	2.1

[a] While for the 14 GeV/*c* extraction this parameters corresponds to the actual pulse length, in the case of the 20 GeV/*c* and 26 GeV/*c* extraction this parameter corresponds to the machine circumference.

For the future multi-turn extraction, it is planned to modify the layout of the slow bump 16 in the following way:

- Each magnet will be powered by a dedicated power converter.
- One additional magnet will be added in straight section 18.
- The magnet currently installed in straight section 15, which is used for the correction of the high-energy closed-orbit distortion together with a similar element installed in straight section 60, will also be used to generate the slow bump for the novel extraction scheme.
- All the magnets will be of type 205 compatible with enlarged vacuum chamber to overcome possible issues with the available mechanical aperture. This will impose the replacement of one magnet of type 205 for bump 31 with one of type 206. Furthermore, this will have a beneficial effect for the power converters, which will be of standard type and will not require any specific adjustment for the magnet type.

According to the results of the numerical simulations used to design the new version of the slow bump, the required current values are reported in Table 9, while the shape of the bump in its present configuration and in the proposed one is shown in Fig. 34.

The shape of the present version of the slow bump for extraction in SS16 features a non-negligible oscillation outside the required bump region. This is a consequence of having the four dipoles powered by a single power converter and the fact that the betatronic phase advance between them is only roughly adapted to the need to have a closed bump. On the other hand, the new version features a perfect closure of the bump, which is an improvement generated by the choice of independently powered dipoles. In this respect, the implementation of the new layout of the bump will have a positive impact also on all the various beams produced by the PS.

The difference in amplitude between the two bumps is due to the fact that for the new layout only the outermost beamlet has to be pushed towards the extraction septum blade: such a beamlet is already rather far away from the centre of the phase space; hence the bump amplitude is reduced.

Table 9: Values of the current for the magnetic elements powered with capacitor discharge converters, including the magnets for the new layout of slow bump 16

Element	Power converter	Straight section	Magnet type	Current settings (A)			
				14 GeV/*c* (CT)	20 GeV/*c*	26 GeV/*c*	14 GeV/*c* (MTE)
BSW16.12	Pulsed	12	205	315	360	465	120
BSW16.14	Pulsed	14	205	315	360	465	341
BSW16.15	Programmable	15	205	0	140	180	–371
BSW16.18	Pulsed	18	205	0	0	0	196
BSW16.20	Pulsed	20	205	315	360	465	56
BSW16.22	Pulsed	22	205	315	360	465	–79
QKE16	Pulsed	5/25	414	1940	960	1250	–
QKE58	Pulsed	49/69	414	–	960	1250	–
BSW31	Pulsed	27/35	205/206	275	–	–	–
Beam length [a] (μs)				10.5	2.1	2.1	10.5

[a] While for the 14 GeV/*c* extraction this parameter corresponds to the actual pulse length, in the case of the 20 GeV/*c* and 26 GeV/*c* extraction this parameter corresponds to the machine circumference.

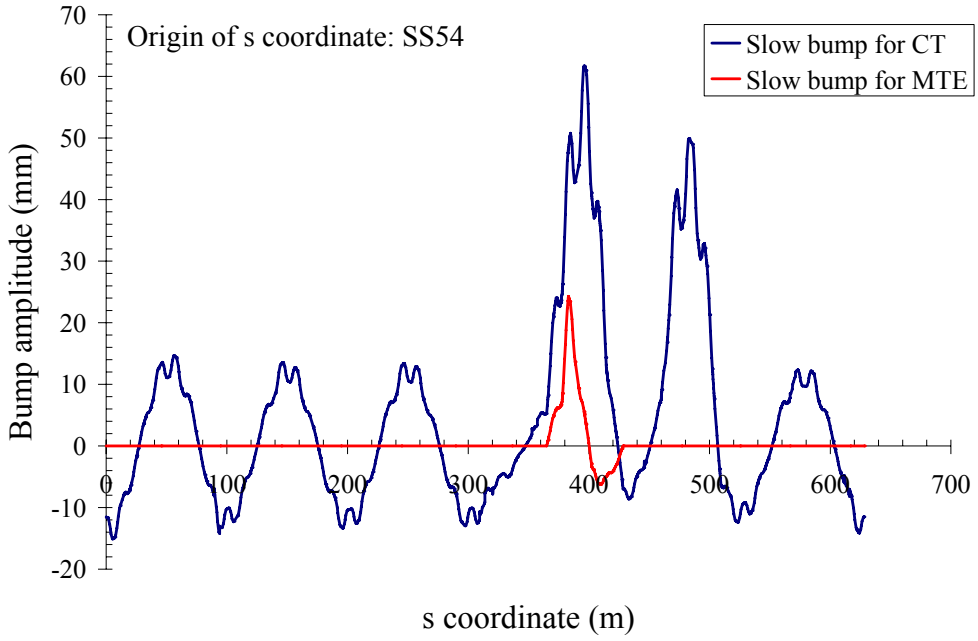

Fig. 34: Amplitude of closed bump 16 all along the circumference of the PS machine for both the present version based on the use of four dipoles and the proposed one based on six dipoles

The proposal for a new version of the slow bump entails a number of changes at the level of the power converters. To study a solution, the following assumptions are made:

- The rise time can be reduced from the present value of 7.4 ms to 5.3 ms.
- The power converters should be capable of changing polarity from one cycle to another (pulse-to-pulse modulation, PPM).

- Basic period of 900 ms should be assumed in order to be compatible with the option of running the PS-Booster at a faster repetition rate.
- The same accuracy as for the present power converter is required.

Furthermore, special considerations are required for the element in straight section 15 and its power converter. As already mentioned, this dipole is normally used to compensate for the closed orbit distortion due to the saturation effects in the main magnets of the PS machine at high energy, i.e., starting at 20 GeV/*c*, together with the device installed in straight section 60. The current has to follow a special function, thus requiring the possibility of programming the power converter. For this reason a TEKELEC type power converter is used. An example of the current as a function of time is given in Fig. 35.

New power converters are under development in the framework of the study to replace TEKELEC and they could easily match our needs, that is use the programmable power converter to simulate the behaviour of the capacitor discharge devices so that the dipole in straight section 15 could be use for two purposes, namely closed orbit distortion correction for all beam operations beyond 20 GeV/*c*, like the present situation, and as an active element in the new slow bump 16 for the novel multi-turn extraction.

As far as the capacitor discharge power converters are concerned, it is worth mentioning that since 1993 many capacitor discharge power converters were installed for the slow bumpers in section 16 and 58, the QKE16 and the QKE58. Some power converters were specified to produce two current pulses delayed by 30 ms in order to be used for the ejection of the electrons for LEP. The characteristics of the various converters are reported in Table 10.

As already mentioned, the need to correct the closed-orbit distortion with the dipole in straight sections 15 and 60 imposed the change of the power converter from capacitor discharge (as from specifications in 1993) to a programmable one. Furthermore, it is worth stressing that the power converters PR.DHZ73 and PR.BSW58 are no longer used (the latter since the stop of lepton operation following the definitive shutdown of LEP in 2000). Of course, the double-pulse option is no longer used either. Finally, a spare power converter for each type (type 1 and type 2) is available.

Given these considerations it is possible to find an optimized solution for the power converters required by the new bump. In total five power converters will be needed. As the current rise time is changed for the new bump 16, the QKE16 and QKE58 power converters have to be modified in order to deliver a discharge current with a similar rise time. The shortening of the rise time is meant to make available some capacitors, hence allowing the building of more power converters using the same original number of components. The converter specifications to cope with these requirements are presented in Table 11.

It appears that all the power converter capacitor banks have to be re-arranged and the electronic crate regulation cards have to be adjusted accordingly. Four new DCCTs have to be ordered on account of the increase of the discharge current. The power converter for bump 16 in section 22 must allow polarity reversal of its output current. A new system, with thyristors and appropriate electronic control, has to be implemented on this converter and its spare device.

With this new layout, no additional capacitor discharge power converter has to be ordered. However, it must be noted that the actual type 2 spare power converter is used to supply the PR.BSW16.20 magnet. As a consequence, only one spare will be available for all converters. This spare will have to be configured with the larger capacitor bank and a polarity inverter. Before replacing a defective converter, this spare will need to be configured and adjusted. It is foreseen to study carefully whether the QKE58 is indeed required for the fast extractions.

This point will be studied by means of dedicated Machine Development (MD) time during the 2006 run of the PS machine. In case this element is confirmed to be unnecessary for the routine operation, then the corresponding power converter PR.QKE58 will be configured as a dedicated type 2 spare immediately available for the BSW16 converters.

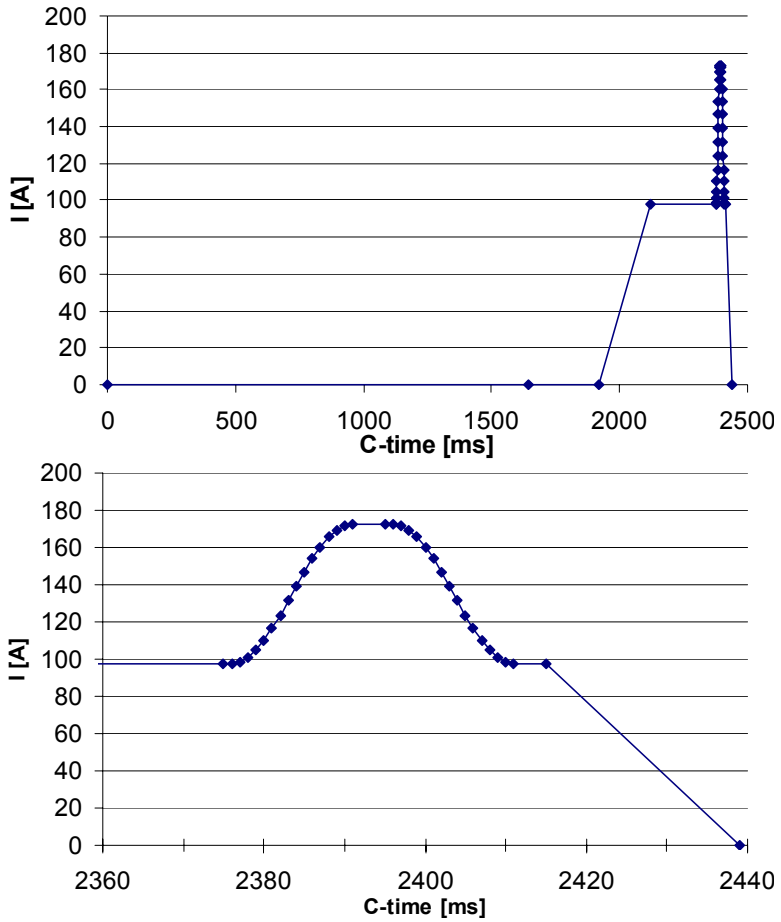

Fig. 35: Typical powering of the dipole in straight section 15, powered by a TEKELEC power converter, when used to correct the closed-orbit distortion for a 26 GeV/*c* operation. The complete function is shown in the upper part, while a zoom is reported in the lower part. Similar functions apply also to the 20 GeV/*c* operation, where a linear re-scaling is applied (see the value quoted in Table 9). The last spike corresponds to the ramping of the slow bump prior to beam extraction.

4.2.2 Fast bump

The MTE scheme is based on a fast bump around the magnetic septum SMH16 (for an overview of the situation and the equipment involved see Fig. 36). Fast pulsed magnets (kickers), to be located in straight sections 13 and 21, will create a nearly closed bump for the beamlets in the first four turns. To close it perfectly, an existing kicker in SS9 will be used. The core beam needs to be moved out by more than twice the distance of the other four beamlets. One additional kicker, to be located in SS4, in conjunction with the existing KFA71-79 system will kick out the remaining beam in the fifth turn. Two existing emittance reduction fast dipoles in the TT2 transfer line will be used to correct the trajectory of the beamlets. As an example, the fast bump generated by the kickers for the extraction of the fifth turn, i.e., the beam core left at the centre of the phase space after the resonance crossing, is shown in Fig. 37.

Table 10: Specification of the capacitor discharge power converters as given in 1993

Power converter		PR.BSW16	PR.BSW58	PR.QKE16	PR.QKE58	PR.BSW31	PR.DHZ15	PR.DHZ73
Capacitors	Total (μF)	5120	12 800	12 800	12 800	1280	2560	2560
		8×640	20×640	20×640	20×640	2×640	4×640	4×640
L (magnet) (mH)		5	2.1	2.1	2.2	17.2	8.9	9
R (magnet) (mΩ)		200	115	112	100	225	175	115
Pulse period (ms)	Single pulse	31.9	33	32	33	29.5	30	30
	Double pulse	22.5	23	23	23			
Time for I_{peak} (ms)	Single pulse	7.5	7.5	7.5	7.6	7.2	7.3	7.4
	Double pulse	5.4	5.4	5.5	5.5			
I_{peak} (A)		1200	2000	1880	1400	360	250	100
U_c (charging voltage) (V)		1377	994	930	692	1383	500	196
Transformer type (kVA)		63	63	63	63	20	20	20
Converter type		1	1	1	1	2	2	2

Table 11: Specifications of the power converters for the new version of slow bump 16 for multi-turn extraction

Power converter		PR.BSW16.12	PR.BSW16.14	PR.BSW16.18	PR.BSW16.20	PR.BSW16.22	PR.QKE16	PR.QKE58	PR.BSW31
Capacitors	(μF)	2560	2560	2560	2560	2560	7860	12 800	1280
		4×640	4×640	4×640	4×640	4×640	12×640	20×640	2×640
L (magnet) (mH)		6.3	6.3	6.3	6.3	6.3	2.1	2.2	12.4
R (magnet) (mΩ)		100	100	100	100	100	112	100	160
Pulse period (ms)		25.7	25.7	25.7	25.7	25.7	27.5	28	25.2
Time for I_{peak} (ms)		6	6	6	6	6	5.7	5.8	6.2
I_{peak} (A)		850	850	850	850	850	2000	1350	360
U_c (charging voltage) (V)		1550	1550	1550	1550	1550	1600	1100	1200
Polarity reversal		No	No	No	No	Yes	No	No	No
Transformer type (kVA)		63	63	20	20	20	63	63	20
Converter type		1	1	2	2	2	1	1	2

The optical design of the new fast bump was undertaken by using the measured optical model of the PS ring [32]. Two approaches have been used to cope with the need to correct the extraction trajectory on a turn-by-turn basis, namely: i) using a staircase kicker in the PS ring; ii) using the staircase kickers in the TT2 transfer line. In the first option, the kicker located in SS9 is assumed to be capable of delivering a variable kick, thus keeping constant the extraction conditions over the four turns.

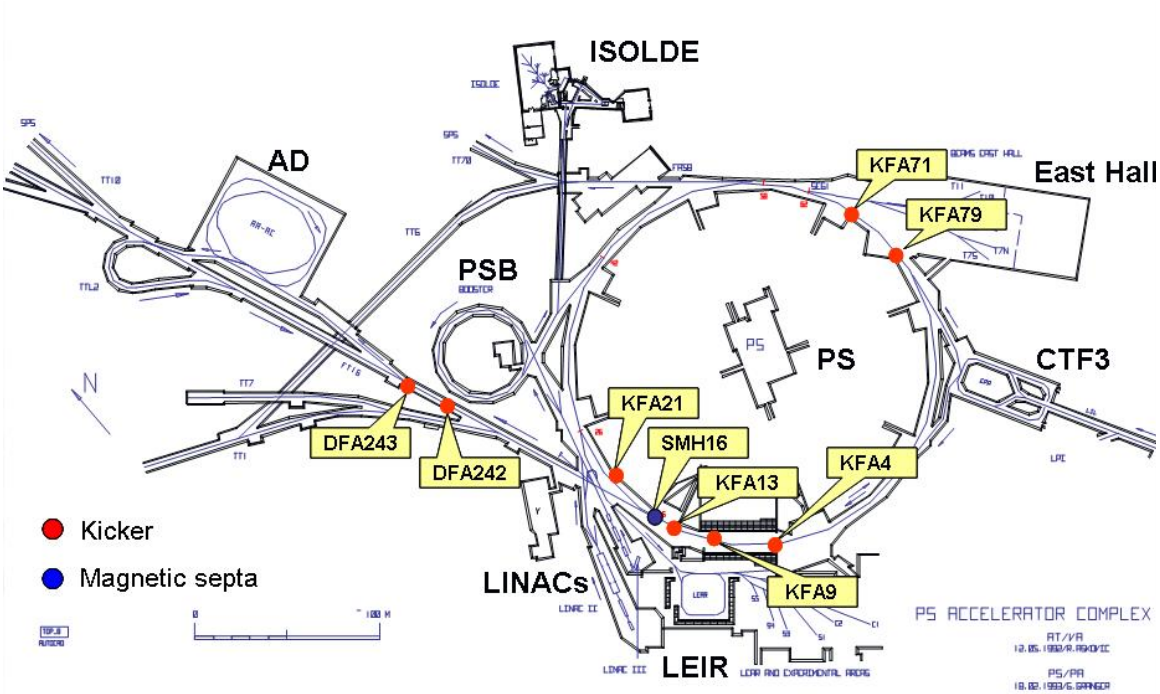

Fig. 36: PS complex layout, indicating the location of the fast pulsed magnets (red dots) and the magnetic septum SMH16 (blue dot) implied in the new PS multi-turn extraction scheme. The elements named DFA correspond to the devices called ERD.

The situation for the fifth turn is different, as its position will be set equal to the first four extracted beamlets by an appropriate setting of the kickers in SS4 and KFA71-79. In the second option the kickers in the PS ring are assumed to deliver a constant kick, apart from the additional kick given to the centre core, and the difference in extraction condition will be corrected using the ERDs in TT2, located in position 242 and 243. For these computations, it is assumed that the position between the two kickers will be changed so as to have exactly 90 degrees of betatronic phase advance in order to optimize the situation. Furthermore, as the details of the optics in the transfer line are not yet known, it is assumed that the matching section of the transfer line TT2 will be used to keep the periodic structure equal to that used so far for the CT extraction, which was also used to compute the corrections. The results of the computations were used to generate the specifications for the hardware. A summary is reported in Table 12.

In the same table, the results concerning the emittance blow-up at injection in the SPS are reported, based on the computed trajectories in the transfer line and the formula [22]

$$\frac{\Delta\varepsilon}{\varepsilon_{\mathrm{inj}}} = \frac{1}{2}\frac{\Delta x^2 + \left(\beta_{\mathrm{inj}}\,\Delta x' + \alpha_{\mathrm{inj}}\,\Delta x\right)^2}{\beta_{\mathrm{inj}}\,\varepsilon_{\mathrm{inj}}} \tag{16}$$

where the values of the optical parameters and the emittance at SPS injection are used. Concerning ε_{inj}, the measured value of $\sigma_\beta = 1.5$ mm (see Section 4.3) is used giving $\varepsilon_{\text{inj}} \approx 0.19$ μm (where it is assumed a value of $\beta \approx 12$ m). It is worth noting that in all the cases the beam emittance after filamentation stays well below the SPS acceptance value of 0.5 μm.

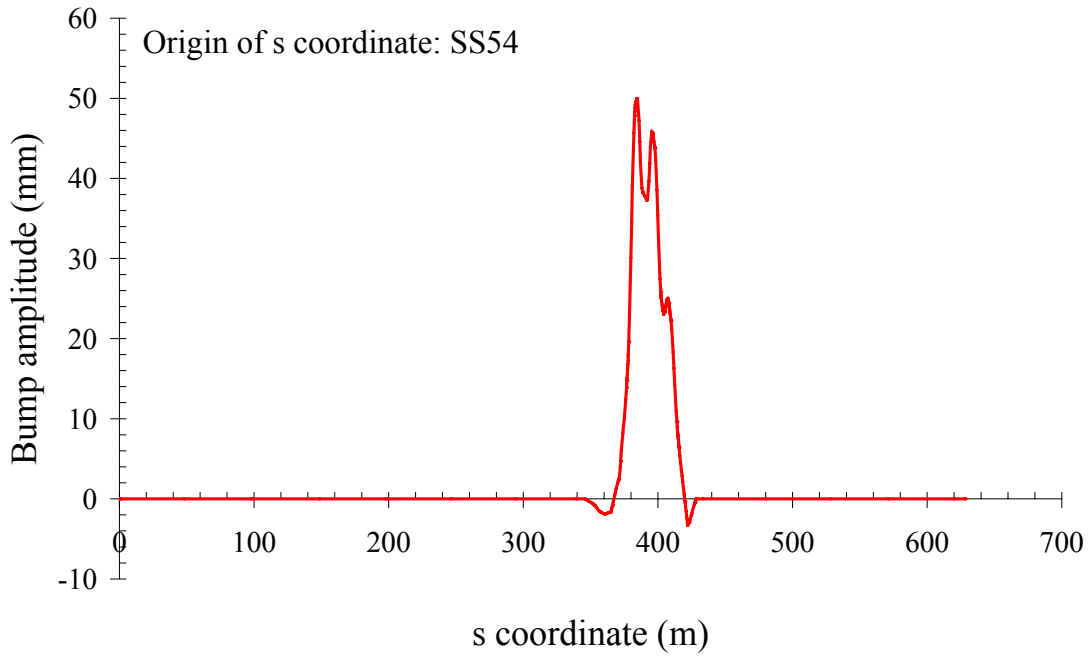

Fig. 37: Example of the bump generated by the proposed kickers for the extraction of the fifth turn, i.e., the beam core

Given the results of the computations, the choice was made to implement the second method. Indeed, this generates a smaller emittance blow-up at SPS injection. Furthermore, it has the advantage of being more flexible than the first one. In fact, even though the kicker in SS9 cannot deliver a variable kick, nevertheless the standard extraction kicker KFA71-79 is, by default, capable of changing the kick on a turn-by-turn basis, which means one can keep a sort of simplified correction capability in addition to the one granted in the transfer line.

The system will be implemented in two phases. The first phase will use the KFA13/21 and KFA4 sub-systems to validate the new multi-turn extraction method in the PS machine, whilst maintaining the existing CT system operational. Once the new scheme is validated, the existing CT will be dismantled and the second phase sub-systems, KFA9 and DFA242/243, needed for trajectory correction, will be installed.

The new system will re-use a maximum of existing de-commissioned and reserve equipment to minimize delays and reduce the cost. The use, in SS13, of the spare KFA79 magnet tank will render fast PS beam extraction vulnerable to failure of the operational KFA79 magnet tank with possible downtime of many months. Construction of a new spare KFA79 magnet tank should therefore be regarded as part of the baseline project.

Table 12: Required strength for the kickers in the PS machine and in the TT2 transfer line for the two approaches used. The value of the rise time is given between 10% and 90%. The strength is computed assuming a magnetic rigidity of 46.68 T·m

		Kickers in the PS ring					Kickers in TT2 (pedestal)			Kickers in TT2 (staircase)		
	Turn no.	KFA9	KFA13	KFA21	KFA71 /79	KFA4	DFA242	DFA243	Δ ε/ε (%)	DFA242	DFA243	Δ ε/ε (%)
First method	1	–0.114	1.839	1.887	0	0	0	0	0	0	0	0
	2	–0.249	1.841	1.897	–0.101	0	0	0	0	0	0	0
	3	–0.343	1.841	1.897	–0.049	0	0	0	0	0	0	0
	4	–0.542	1.841	1.897	–0.188	0	0	0	0	0	0	0
	5	–0.542	1.841	1.897	–1.567	–0.400	0	0	64	0	0	64
Second method	1	–0.114	1.839	1.887	0	0	0	0	0	0	0	0
	2	–0.114	1.839	1.887	0	0	0.105	0.195	30	0.047	0.057	0
	3	–0.114	1.839	1.887	0	0	0.105	0.195	36	0.074	0.138	0
	4	–0.114	1.839	1.887	0	0	0.105	0.195	25	0.140	0.186	13
	5	–0.114	1.839	1.887	–1.834	–0.400	0.105	0.195	36	0.140	0.186	13
Max. strength (mrad)		0.640	2.100	2.100	3.582	0.536	0.167	0.381		0.167	0.381	
Achievable rise time (ns)		350	350	350	70	80	350	350		350	350	

Schematic circuit diagrams and main parameters of the kicker systems mentioned below are given in Appendix F.

4.2.2.1 Bump between SS13 and 21

The spare vacuum tank of the PS full aperture kicker KFA79, which contains three 15 Ω delay line magnets, will be installed in SS13. To minimize the cost the magnets will be connected in series, requiring only one high-voltage pulse generator to excite them. The combined magnet will have to operate in short-circuit mode to provide the required kick, to the detriment of the pulse rise time. Modifications inside the tank are required to connect the magnets in series. New vacuum feedthroughs and magnet connectors are also required to cope with the increased pulsed current.

Another spare vacuum tank containing three similar magnets (formerly used in the PS multi-pulsing extraction system) will be installed in SS21.

Two new pulse generators plus one spare are required, each containing an artificial Pulse Forming Network (PFN) of 12.5 Ω / 80 kV / 10.5 μs. No CERN design exists for such a high-voltage; however an upgrade of an existing lower voltage, shorter pulse length design is currently being studied in detail. The PFN characteristic impedance deliberately mismatches that of the magnet to achieve the required kick whilst keeping undesirable side-effects on kick rise time and flat-top within acceptable limits.

Ten 222 m lengths of new RG220 high-voltage cable will be used as transmission from the pulse generators to the magnets. The expected rise time (10% to 90%) is 350 ns. The nominal required kick will be achieved at 88% of the maximum PFN voltage. The pulse generators and auxiliary equipment will be located in building 367 adjacent to the KFA4 equipment.

These magnets, together with the magnet proposed for SS4, will present a certain shunt impedance to the circulating beams in the PS. Measurements have been made to estimate the impact of this and to validate the usability of the existing magnets. The results indicate that an increase in the total PS longitudinal impedance at the most critical harmonic frequencies of approximately 10% is to be expected. It must be noted that the magnets cannot be substantially improved impedance-wise without reducing their vertical aperture which is not acceptable due to the present PS beam sizes; only minor improvements can be made by implementing beam transition structures between the magnet end-plates and the vacuum chambers.

4.2.2.2 Additional deflection in SS9

The existing pedestal magnet of the present CT kicker system will be used, together with its dedicated high-voltage pulse generator. The electronic controls and low-voltage chassis for this system will need rejuvenation or replacement to provide a standard and homogeneous solution for the control of all kickers implicated in the new scheme.

The expected rise time (10% to 90%) is 305 ns. However, an additional inductance of 0.3 μH in series with the magnet will allow matching to the 350 ns rise time of the kicker system in SS13/21. The maximum required kick will be achieved at 26% of the maximum PFN voltage.

4.2.2.3 Kick in SS4

An existing magnet tank, previously used for injection of leptons in the PS during the LEP era, will be installed in SS4. The tank contains a 15.7 Ω delay line magnet under vacuum. It will be operated in terminated mode to provide the necessary kick and comply with the rise time constraints. New SF_6-filled high-voltage feedthroughs will replace the existing oil-filled ones on the tank to handle the increased current load and avoid severe contamination of the

vacuum chamber in case of leak. New high-voltage transmission cables will be required between building 367 and SS4.

An existing 80 kV pulse generator, using an SF_6 gas-filled PFN cable of 2.2 μs pulse length, will be refurbished to power the magnet. The expected rise time (10% to 90%) is 80 ns. The full required kick will be achieved at 70% of the maximum PFN voltage.

The pulse generators (one operational plus one spare) and auxiliary equipment will be located in building 367 adjacent to the KFA13/21 equipment.

4.2.2.4 Kick in SS71 and 79

The existing PS full-aperture kicker magnets in SS71 and SS79 will be used to optimize the extraction conditions for the five turns. Modifications to the controls and timing equipment will be necessary to permit the fine delays needed on individual modules to effectively reduce the kick rise time so as to match that of SS4.

4.2.2.5 Kick in theTT2 transfer line

Two existing fast dipoles (‘emittance reduction dipoles’ DFA242 and 243) will be used to correct the trajectory of the extracted beamlets. In DFA242 the magnet coil must be reduced from two turns to one. DFA243 will be moved 21 m downstream of its present position.

Both magnets will be excited using individual 4-step staircase pulse generators. The expected rise time (10% to 90%) is 114 ns. However, an additional inductance of 5.5 μH in series with the magnet will allow matching to the 350 ns rise time of the kicker system in SS13/21. The maximum required kick will be achieved at 63% of the maximum PFN voltage for DFA242 and at 60% of the maximum PFN voltage for DFA243 for a staircase correction. Eight 222 m lengths of new RG220 high-voltage cable will be used as PFN cables for the pulse generators.

The pulse generators and auxiliary equipment will be located in building 359 in space curently occupied by the de-commissioned SMH57 power converter equipment. High-voltage switch assemblies will be recovered from the EPA ejection kicker generators that are currently available, however, new high-voltage cable PFNs and charging systems will be required.

It must be noted that the trajectory correction sub-systems (in SS9 and TT2) described above will not be available during the first period of operation of the MTE as the magnets will still be in service in the existing CT system.

4.2.3 Sextupoles and octupoles

During the experimental tests for the novel extraction, the configuration of the non-linear elements used to generate the stable islands of the transverse phase space was not optimal in terms of the islands’ phase at the location of the extraction septum. Nonetheless, this was not a serious limitation as extraction was in any case impossible due to hardware limitation at the level of the installed devices. Unlike the sextupoles, which were always standard PS sextupole during the whole experimental campaign (see Appendix D for details concerning their characteristics), the original PS octupoles (see Appendix E for more details) were replaced by one single SPS octupole (see Appendix E for more details) in the last part of the experimental campaign. This choice was mainly dictated by the need to install the octupoles in a straight section with small vertical beta-function, but the standard PS octupoles are limited in horizontal aperture and cannot fulfil the constraint.

When starting the design of the MTE, the search for suitable locations in the PS ring had the following constraints:

- Two pairs of sextupoles/octupoles are required to allow the tuning of the extraction conditions.

– Possibly each pair should be located in the same straight section to avoid high-order effects.
– The non-linear elements should be outside the extraction bumps, both slow and fast, to avoid feed-down effects.

Of course, availability of space in the PS straight section is also a critical issue.

The outcome of the studies was that only two straight sections would be good candidates for installing the non-linear elements, namely SS39 and SS55. When the values of the currents used in the experimental tests are used for the computation of the topology of the horizontal phase space, the island's phase at extraction is the correct one as can be seen in Fig. 38.

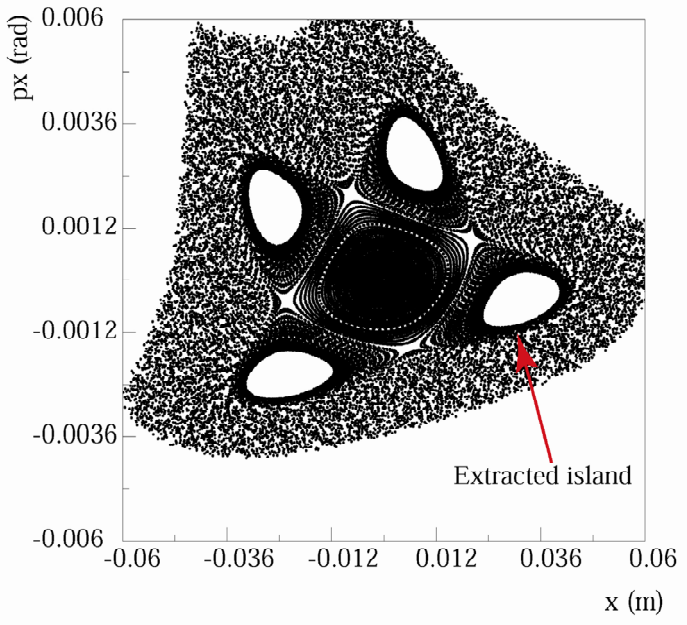

Fig. 38: Phase space topology obtained by using the values of the currents for the sextupoles and the octupole as obtained from the experimental measurements and assigned to the two sets of non-linear elements in SS39 and SS55

This observation ruled out the possibility of using SPS octupoles for the design of the MTE, as they are too long to be accommodated in a standard PS straight section, which is 1 m long, together with the standard PS sextupoles. Therefore, it was decided to build new octupoles based on the specification and the design presented in Ref. [54].

As far as the power converters are concerned, the two circuits for the two sextupoles and the octupole used during the experimental tests were powered by two TEKELEC converters. In the design of the new octupole the electrical parameters were specified to be similar to those of the SPS. Therefore, for the final implementation, four TEKELEC power converters, or the replacements under study in the framework of the consolidation activities, will be well adapted to our needs.

4.2.4 Beam instrumentation

In terms of beam instrumentation, the proposed MTE relies heavily on the wire scanners, as mentioned already in the section concerning the experimental results obtained in the past years. The horizontal wire scanners are the best-suited instruments to monitor and to record the evolution of the transverse beam distribution during the splitting process. It is extremely important to solve the issue of left/right asymmetry, especially in view of precise

measurements to maximize the fraction of trapped particles. To the single scintillator currently located on one side of the vacuum chamber a second one should be added to restore the broken symmetry.

Then, in order to improve the reconstruction of the position of the beamlets in view of tuning the splitting process prior to extraction, a tomographic reconstruction of the 2D beam distribution would be extremely useful. To this aim, the addition of a third wire scanner could turn out to be a crucial step. Two possibilities were found concerning a possible straight section in which to install the additional wire scanner, namely SS74 or SS75. This choice is mainly dictated by the horizontal betatronic phase advance between the instruments and the space available in the straight sections. Figure 39 plots the topology of the phase space at the various sections where the horizontal wire scanners are located. The final choice between the two options will be made in a later stage of this study.

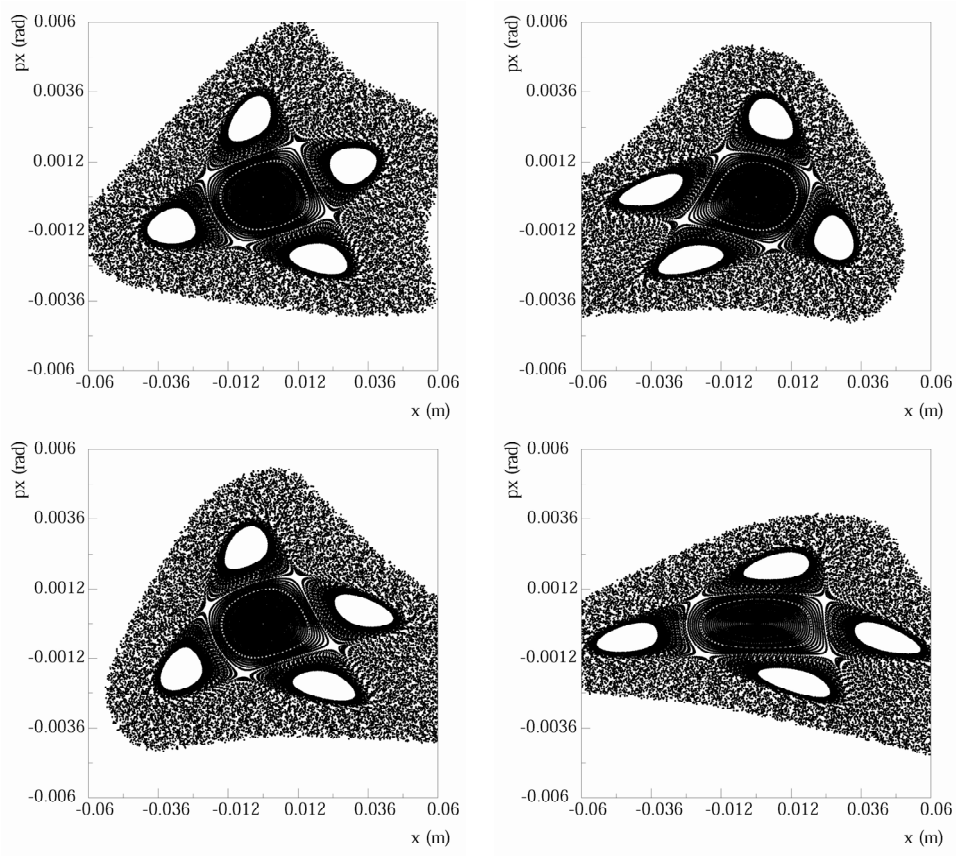

Fig. 39: Phase space topology at SS54 (upper left), SS64 (upper right), SS74 (lower left) and SS75 (lower right) for the settings of the sextupoles and octupoles determined in the experimental studies

4.2.5 New ring layout

One of the main challenges in the study for the design of the MTE was the implementation of the scheme found on paper on the existing PS ring. Many hardware constraints made this task rather difficult. In the following, the complete list of the modifications to be performed to the present layout of the PS machine will be presented. In Fig. 40 a schematic view of the straight section involved in this process is shown.

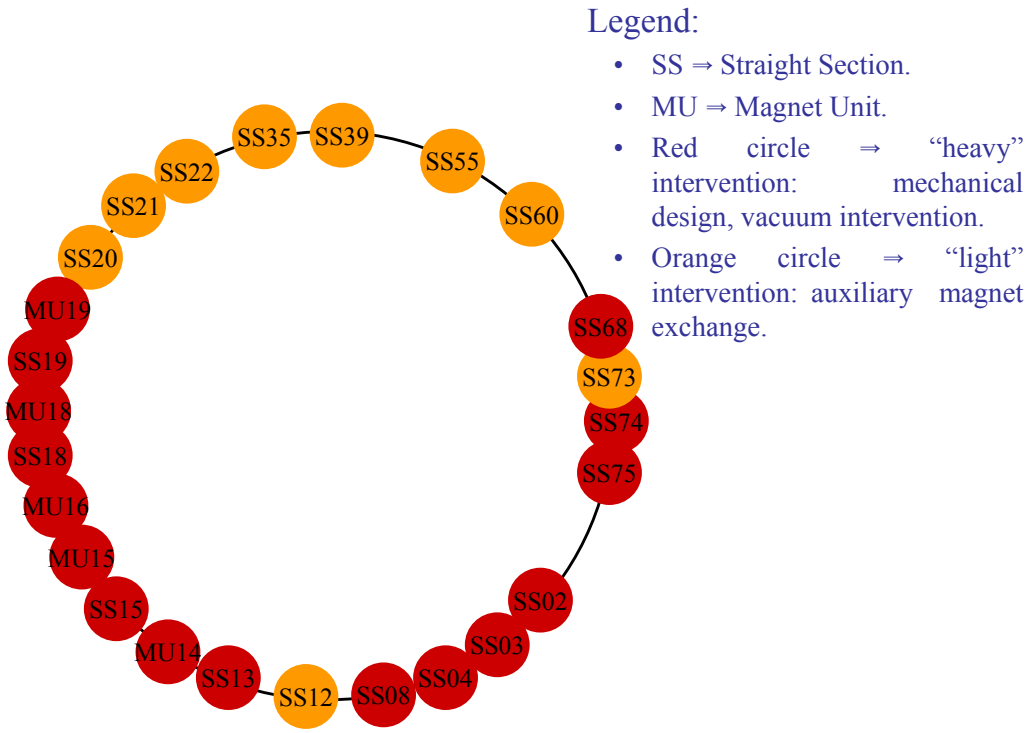

Fig. 40: Summary of the changes required to implement the MTE

The list of the straight sections affected by the necessary modifications to the PS layout follows, together with the description of the required changes.

– Straight section 2

The computation of the available aperture indicates that the cross section of the vacuum chamber is too small. This choice is indeed imposed by the presence of the standard PS octupole, which is part of the string used to combat beam instabilities. Such a magnet does not fit around a standard PS vacuum chamber. To install a vacuum pipe of standard cross section the octupole should be removed as well as the injection sextupole, which is no longer used during standard operation.

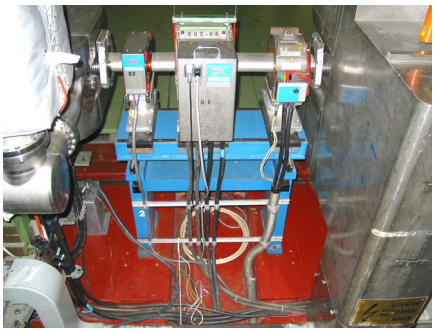

– Straight section 3

Currently, two sextupoles are installed in SS19 to generate the appropriate phase space structures required to perform the slow extraction towards the East Hall [55, 56]. However, SS19 will still be in the bump region, thus requiring an enlarged vacuum chamber to accommodate for the split beam. The standard PS sextupoles are not compatible with an enlarged vacuum chamber. Hence it is proposed to move them by 2π in horizontal betatronic phase advance, which corresponds to SS3. Two sextupoles will be

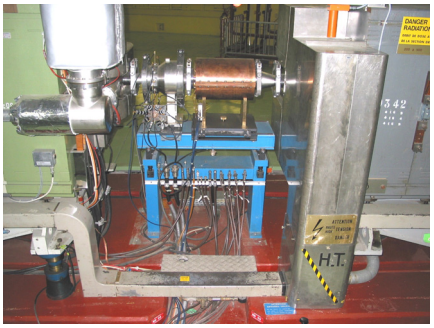

installed in SS3, for this the first quadrupolar pick-up [57–61] will have to be dismantled. Numerical simulations were performed to determine whether the proposed solution is compatible with the present configuration. The horizontal phase space was computed for the present and the proposed configuration, showing a substantial similarity in the phase space topology (see Fig. 41).

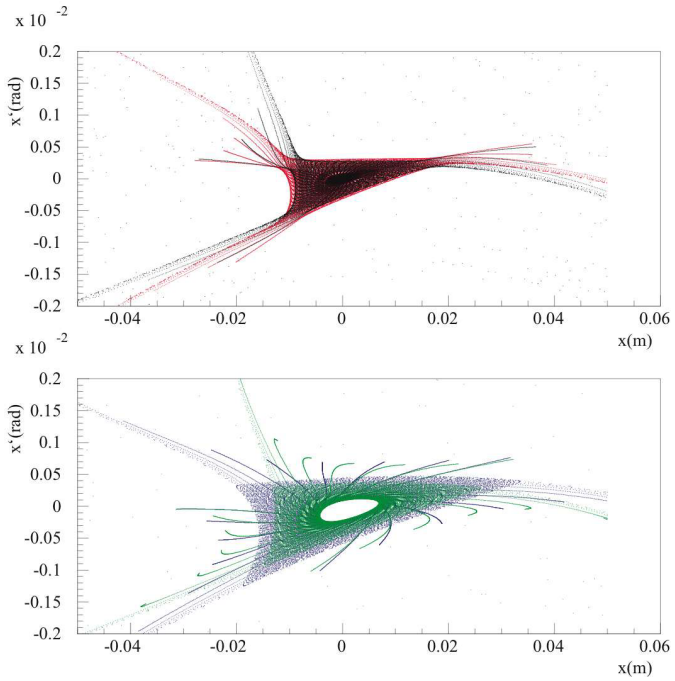

Fig. 41: Phase space portrait for the slow-extraction settings for the present configuration of sextupoles (black) and the proposed one (red) for $\Delta p / p = 0$ (upper part) and for the present configuration (green) and the proposed one (blue) for $\Delta p / p = 1 \times 10^{-3}$ (lower part).

During the year 2006 tests will be performed to assess the performance of the new layout for the slow extraction. In case of positive results the two sextupoles in SS19 will be removed thus allowing the cross section of the vacuum chamber to be increased. Otherwise, new sextupoles with an increased aperture will have to be designed and built.

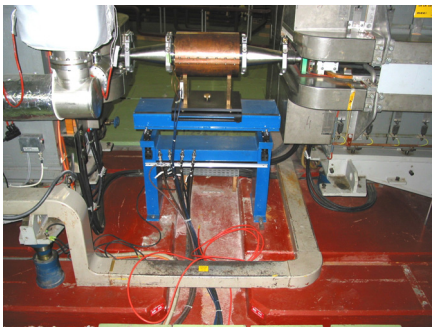

– Straight section 4

This straight section is foreseen for the installation of the extraction kicker KFA4, used to deflect the fifth turn. The hardware currently installed there, namely the second quadrupole pick-up, should be removed prior to the kicker installation.

– Straight section 8

Two 200 MHz cavities are installed in this straight section. They are part of the group of eight cavities used to generate longitudinal blow-up in the PS machine or to capture the proton beam prior to the CT extraction in order to match the longitudinal bunch structure of the SPS. Following the outcome of the studies for the high-intensity in the SPS, the decision to remove these two cavities was taken, thus leaving the straight section empty [62]. At the same time, the layout of the fast bump for the MTE foresees a kicker to be installed in SS13, where an 80 MHz cavity is located. Following analysis of the available space and infrastructure, it is proposed to move the 80 MHz cavity to SS8.

The vacuum valve will have to be moved elsewhere.

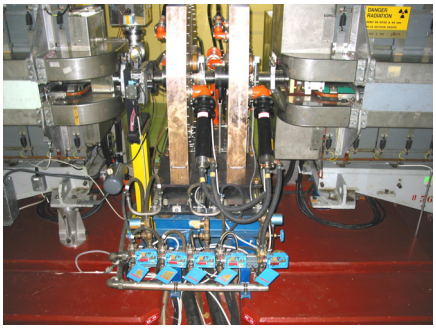

– Straight section 12

In this section the first element of the slow bump used to extract the beam towards the SPS is installed. In its present version the dipole is of type 206. To have a slow bump made of similar magnets, thus making easier the adjustment of the individual power converters, the dipole will have to be replaced with one of type 205.

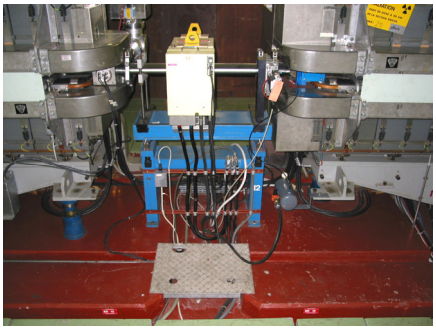

– Straight section 13

The 80 MHz cavity used to generate the appropriate longitudinal bunch structure required by the LHC [63–65] is installed in this section. It is part of the system that splits the beam in the longitudinal plane so that, for each PS-Booster bunch, up to 12 bunches can be generated at PS extraction. In the layout of the fast bump for the MTE, one kicker is foreseen to be installed in this section. Therefore the cavity will have to be moved elsewhere. According to the analysis carried out, the best choice is SS8.

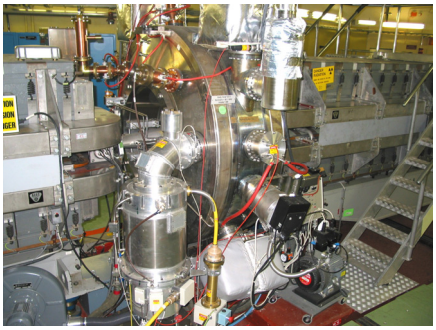

– Straight section 14 and magnet unit 14

The second bumper for the slow bump is installed in this section. Currently it is a dipole of type 210 and will have to be replaced by one of type 205. The injection sextupole will be removed. To increase the mechanical aperture, the vacuum chamber will be replaced with a special enlarged one. The situation of aperture is particularly critical also in the magnet unit 14, thus requiring a change of the vacuum chamber. In this case, the special enlarged vacuum chamber for main

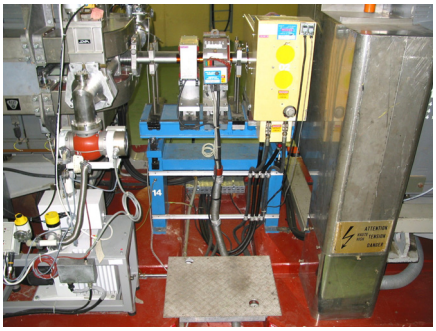

dipoles does not provide enough clearance for the beam. Hence a new chamber type has been designed (see next section).

– Straight section 15 and magnet unit 15

The dipole of type 205 normally used to correct the closed-orbit distortion at high energy is located in this straight section (DHZ15). In the proposed layout of the slow bump for the MTE this magnet will be the third element of the slow bump. In the same section a high-energy sextupole (type 602) which has not been used for years is also installed: it will then be removed. Furthermore, as the slow bump is approaching its maximum, the aperture requirements become more and more demanding in this area. Therefore the vacuum chambers of both the straight section and the downstream magnet unit will have to be replaced with special pipes. In the case of the straight section a new design is available, while the same chamber developed for the magnet unit 14 will also equip magnet unit 15.

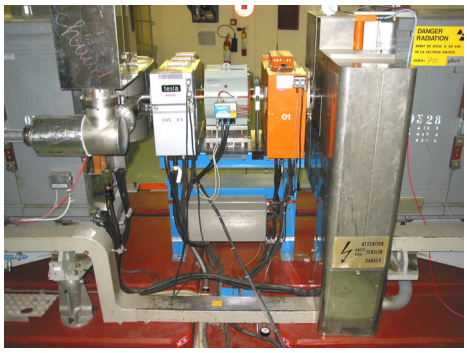

– Magnet unit 16

This magnet is located just downstream of the extraction septum (SS16) and the vacuum chamber is y-shaped in order to accommodate both the circulating and the extracted beam. In the second half of the main magnet, magnetic shims are installed to shield the extracted beam from the influence of the unavoidable stray fields. Also in this case the mechanical aperture is rather tight, thus calling for the design of a special chamber.

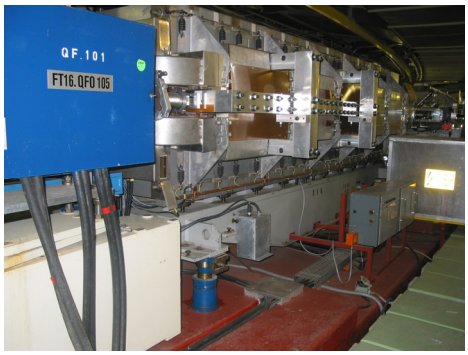

– Straight section 18 and magnet unit 18

The only piece of hardware installed in this straight section is the so-called measurement target. It is a device used to scraped the beam and capable of deriving the beam profile, and hence its emittance, from the beam intensity as a function of the scraper position. According to the new layout of the slow bump, a new dipole of type 205 should be installed in SS18. This straight section is located just downstream of the peak of the bump amplitude and the residual bump is still rather large. Therefore, a new enlarged vacuum chamber will replace the one currently installed. Such a vacuum chamber will be compatible with the aperture of the bumper, but not with that of the

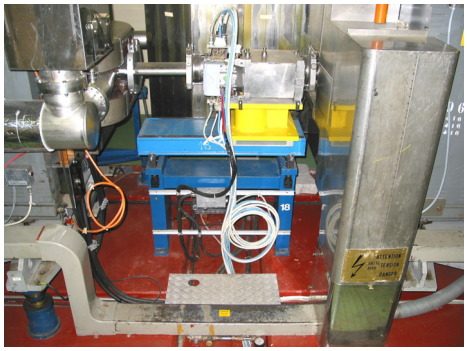

measurement target. Therefore such a device will have to be moved elsewhere. The proposed location is SS68. In addition, also in the downstream magnet unit, the vacuum pipe should be replaced by means of an enlarged one. In this case the main magnet is equipped with a tuning quadrupole of type 401, which is incompatible with an enlarged vacuum chamber. A quadrupole of type 402 should be installed. Availability of two spares was guaranteed, even though their actual status will have to be assessed.

– Straight section 19 and magnet unit 19

This straight section is completely filled with magnets, namely two sextupoles of type 608 used for the slow extraction towards the East Hall; one dipole of type 205 used to generate the slow bump in SS23 (where an electrostatic septum for the slow extraction is located); one quadrupole of type 408 used for the gamma-jump scheme [66–72]. Once more, the aperture in both the straight section of the magnet unit needs to be increased and the vacuum chambers should be replaced with similar objects with increased cross section. At the level of the magnet unit, this change is rather straightforward: the tuning quadrupole of type 403 should be exchanged with one of type 404 taken, for example, from one of the magnet units 12, 47 or 48. On the other hand, none of the magnets installed in SS19, except the dipole 205, are compatible with enlarged vacuum chambers and hence they need to be moved elsewhere. As far as the two sextupoles are concerned, it is proposed to move them to SS3. Detailed tests will have to be carried out during the PS run in 2006, with both sextupoles in the original location and two additional ones in the new sections will be available. In case of success those in SS19 will be removed in the 2006/2007 shutdown. Even more crucial is the situation concerning the quadrupole used for the gamma-jump scheme. The simplest solution would consist of replacing the magnet of type 408 with the spare quadrupole of type 406, which is compatible with the larger aperture. However, this would exhaust the stock of spare magnets of type 406, thus imposing the building of a new element. An alternative would be to move the quadrupole into another section. The solutions studied so far (see next sections) did not give fully satisfactory results. Further studies are

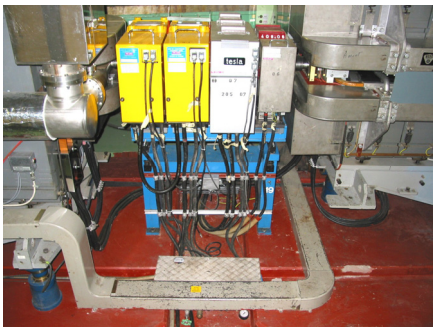

ongoing and their outcome will be crucial to define the most appropriate strategy to deal with this issue.

– Straight section 20

The fifth bumper of the new slow bump is installed in this section. Currently, a dipole of type 206 is located in SS20 and it should be replaced by another magnet of type 205. Two standard PS octupoles are installed in this section: originally, only one was there and it was part of the string of eight octupoles used to combat beam instabilities. At the beginning of the experimental studies for the novel extraction it was removed from the string and powered by an independent power converter. In a second stage, an additional octupole was installed in order to increase the available strength for generating the stable islands. In the final implementation these elements are no longer used and should be removed. This choice is also imposed by the reduced horizontal aperture of these magnets, which imposes a vacuum chamber with a reduced cross section. Given the aperture requirements, the present vacuum chamber is no longer compatible with the novel extraction and it should be replaced by an enlarged one.

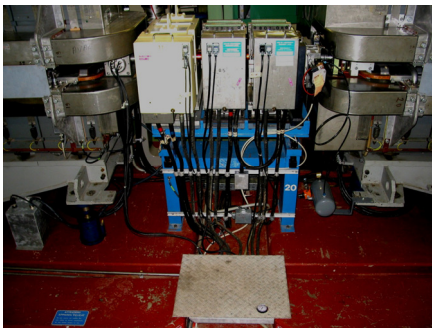

– Straight section 21

This straight section played a key role in the last experimental campaign as the two sextupoles of type 608 and the single SPS octupole of type LOE (see Appendix E) were located here. In the final implementation of the MTE this section is reserved for one of the kickers used to generate the fast bump. Hence it is foreseen to remove all three magnets: the octupole will be put back in the pool of spare SPS magnets, while the two sextupoles will be moved to SS39.

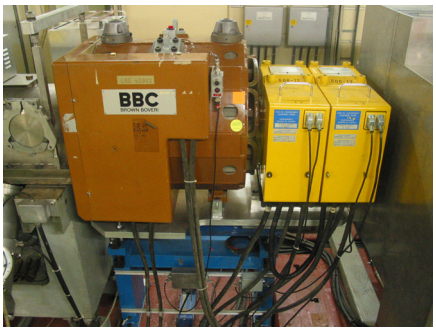

– Straight section 22

This straight section is planned to host the sixth and last dipole of the new slow bump. Currently, there is the fourth dipole of the slow bump and, as it is of type 210, it will be replaced with another one of type 205. It is worth noting that because of the limited number of dipoles of type 205, it will be necessary to change the composition of the magnets used to generate the slow bump in SS31, i.e., the one used to push the beam towards the electrostatic septum prior to slicing for the CT extraction. In fact, such a bump is made of two

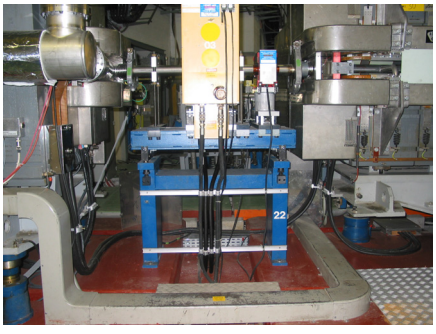

dipoles of type 205 and one will be exchanged with the dipole currently installed in SS22. The fact that the two dipoles of bump 31 are of different types should have a minor impact on the bump properties, as such a difference in the excitation curve is only of the order of 3%.

– Straight section 35

The dipole of type 205 will be exchanged with the one of type 210 currently located in SS22. As already mentioned, the difference in magnetic properties is negligible. Furthermore, in the PS machine there is another bump made of two different dipoles, namely bump 57 that is used for the slow extraction in SS61. This bump is actually made of dipoles of type 205 and 206, respectively, and the difference in magnetic properties is twice as much as that for the proposed layout of bump 31. As a last point, it is worth stressing that this configuration of slow bump 31 is only a short-term solution as in the long term it is planned to decommission the present CT extraction mode following the running-in of the new MTE.

– Straight section 39

At the moment this section hosts one of the three wigglers that were used for the lepton beams during the LEP era (the other two were installed in SS41). In the proposed scheme, the wiggler will be removed to leave space for the set of two standard PS sextupoles (type 608) and the new octupole under design, for the generation of the stable islands.

– Straight section 55

Two sextupoles of type 608 are installed in this section together with a dipole of type 212. The two sextupoles were used during the first stage of tests for the experimental studies of the novel multi-turn extraction in conjunction with the octupoles in SS20. The bumper was part of the slow bump for extraction in SS58, which was used for delivering negatively charged particles to the SPS (the other three elements were installed in SS52, SS60 and SS63). Since the dismantling of the LEP machine such an extraction is no longer in operation: even though the magnet is still in the PS ring the power converter is no longer connected to it. Therefore it is proposed to remove it. This will leave enough space to install

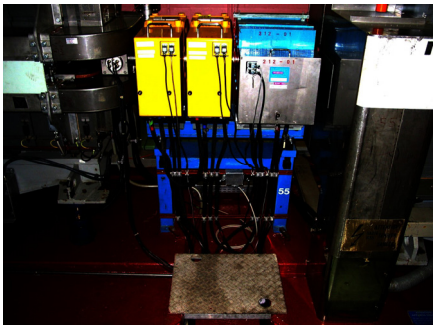

another special octupole. After the proposed modifications this section will host the second set of sextupoles and octupole used to generate the stable islands and to split the beam. The horizontal betatron phase difference between SS39 and SS55 is about 2π so that at first order the non-linear effects add up linearly.

– Straight section 60
In addition to the bumper magnet used for the former slow bump 58, a dipole corrector of type 205 is installed and powered by a TEKELEC converter. It is used together with a similar element in SS15 to perform the correction of the closed-orbit distortion due to field saturation in the PS main magnet at high energy. This magnet will be exchanged with the dipole of type 206 currently installed in SS20 in order to have six magnets of the same type for the new slow bump 16.

– Straight section 68
This section hosts the unused vertical dipole DVT68. It is proposed to remove it in order to make space for the measurement target that should be displaced from SS18 to this section.

– Straight section 73
The unused horizontal dipole DHZ73 of type 205 should be removed and installed in SS18 as part of the new slow bump 16.

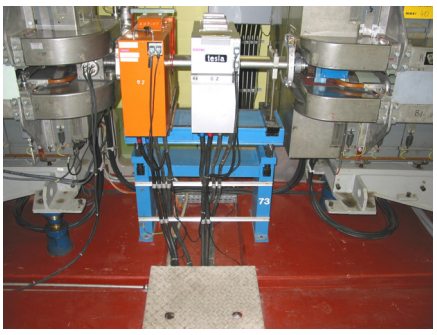

– Straight section 74
In order to perform some tomographic reconstruction of the beamlets after splitting, it is proposed to install an additional wire scanner in this section. As mentioned in the section concerning the experimental results, this device is the most useful instrument to monitor the splitting process and to derive physical parameters of the split beam. Currently, two horizontal wire scanners are installed in SS54 and SS64, while two vertical ones are located in SS75 and SS85. Some attempts have already been made to reconstruct the horizontal beam distribution starting from the information of the measured profiles at the two locations and folding in the information derived from the PS model concerning the position of the fixed points. Of course, the use of only two profiles makes the analysis rather difficult and at the limit of the physical significance. The addition of a third instrument would improve the situation. The three

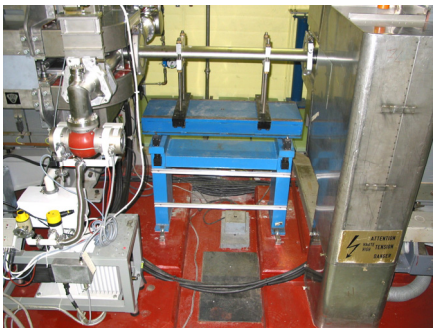

instruments will be separated by about $5/4\pi$ and $10/4\pi$ phase advance in the horizontal plane, thus providing independent sections of the 2D beam distribution. Hence a third profile will allow a more accurate reconstruction of the islands' position and hence could be used as a guideline to tune the extraction, e.g., to set the horizontal tune and/or the octupole current so as to change the beamlets separation.

– Straight section 75

A wire scanner to measure the beam profile in the vertical plane is installed in this section.

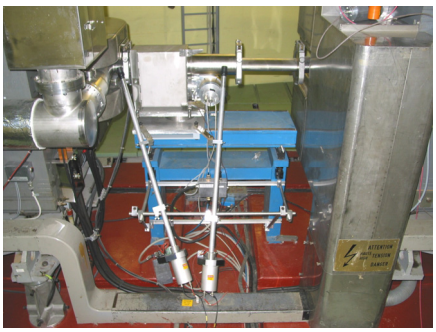

According to the nominal optics of the PS machine, straight sections with even number feature a small horizontal and a large vertical beta-function, respectively. The contrary holds for odd straight sections. Using this straight section to perform horizontal beam profile measurement and to use the data in conjunction with the wire scanners currently installed in SS54 and SS64 would give the same quality of reconstruction as the proposed solution with instruments in SS54, SS64 and SS74. However, SS75 would grant higher resolution to the measured profile. Furthermore, this would also be advantageous for the high-brilliance beams, such as the one for the LHC, featuring a small transverse size. If the wire scanner in SS75 is rotated to become a horizontal device, then the one foreseen in SS74 will have to be installed so as to measure the vertical beam profile. This decision concerning the orientation of the wire scanner can be delayed until further analysis is performed.

– TT2 transfer line

As already mentioned, the proposed scheme relies on the adjustment of the trajectory of the extracted beamlets in the TT2 transfer line, i.e., the transfer line joining the PS and the SPS ring. At present, two kickers are installed in position ERD242 and ERD243, corresponding to the FODO part of the transfer line. In order to have an optimal correction scheme, the two elements should be separated by $\pi/2$ in betatronic phase advance, which is not the case for the nominal optics used for the CT extraction [73,74]. It is therefore, necessary to displace the ERD243 about 21 m downstream of its present location. The detailed location will be defined once the optics of the transfer line is matched to the optical conditions at PS extraction (see Fig. 42).

4.3 Aperture issues

The main modifications to the PS ring will involve a new layout of the slow bump used to approach the beam to the extraction magnetic septum and a new, fast, closed bump around the

extraction septum. A crucial issue is the available aperture, as the situation is particularly critical in the extraction region. On account of the very principle of the novel multi-turn extraction, once the beam is split, there will be five beamlets circulating in the ring with different closed orbits (see Fig. 43, where the trajectory for the four beamlets is shown).

Detailed computations of the available aperture allowed a number of critical locations in the ring to be identified and the design of special vacuum chambers to be started (the straight sections involved in the aperture modifications have been listed in the previous section).

The first step in this analysis was the collection of information concerning the aperture of the present PS layout. This was a difficult and painful task as most of the drawings available from the official CERN repositories are out of date. The outcome of this activity is the model of the PS aperture used for our studies and presented in Figs. 44 (upper part) and 45 (upper part). In the former the horizontal aperture is shown, while in the latter the vertical one is reported.

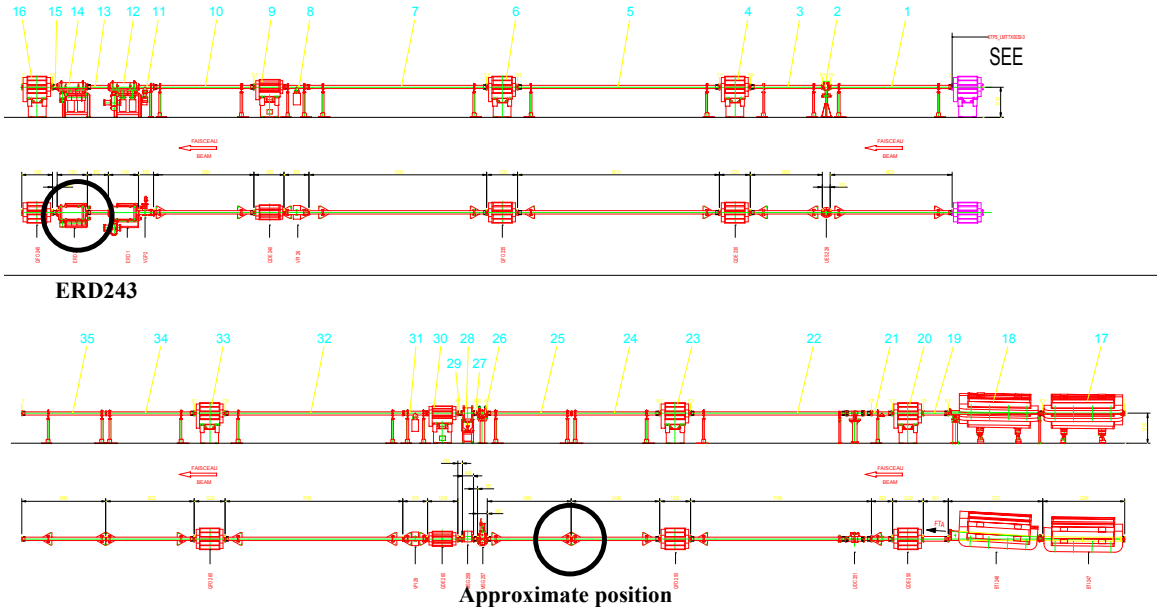

Fig. 42: Layout of the TT2 transfer line including the ERD243 with its present and proposed position

The available aperture is shown as a function of the *s*-coordinate and the corresponding straight section number is also quoted. The vacuum chambers have a complex shape, usually made of four arcs of circumference making a cross-section that is symmetric with respect to the median plane. The horizontal aperture is represented as the size of the vacuum chamber corresponding to the horizontal symmetry plane, while in the case of the vertical aperture, the size reported in the plots corresponds to the chamber size at the position of the nominal closed-orbit.

It is clear that in the present version of the installed aperture, the extraction region is enlarged already to guarantee enough aperture for the displaced beam: three regions are clearly visible, namely the one around SS16 corresponding to the fast extraction towards the SPS, the one around SS31, corresponding to the injection of ions from LEIR (SS28) and the slicing on the electrostatic septum in SS31 for the CT, and the region around SS42 corresponding to the injection point. In the vertical plane no clear pattern is visible. The spikes at localized points where the aperture is considerably increased correspond to the position of vacuum valves.

In the lower part of Figs. 44 and 45, the proposed layout of the aperture model for the implementation of the MTE is shown. The changes are concentrated in straight sections in the

neighbourhood of SS16 and they are aimed at accommodating the five beamlets without any beam losses. These changes represent the outcome of complex computations devoted to the evaluation of the beam envelope after beam splitting and during the stage when the new slow bump is switched on and the fast bump is used to displace the beam.

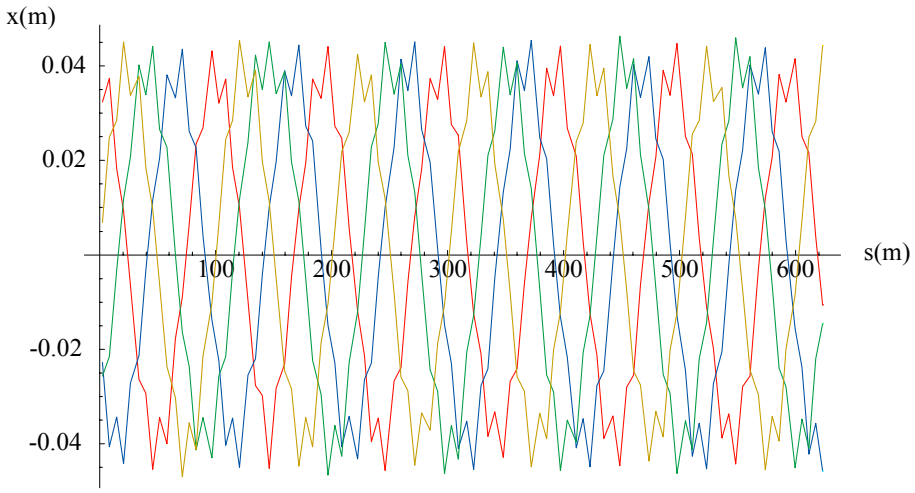

Fig. 43: Closed orbit for the four beamlets along the circumference of the PS machine. The closed orbit of the central core is the origin of phase space.

The numerical simulations were performed by means of the MAD computer program and using a number of tools developed for these studies. The model of the PS machine is used to track a set of initial conditions chosen within the islands where the beamlets are trapped. The initial conditions are selected to identify an invariant curve corresponding to a given number of sigmas of the measured (see Table 6) beam profiles.

The tracking is performed by assuming that the momentum off-set is zero. Then, to determine the actual beam envelope, the contribution from the momentum off-set has to be taken into account. This requires the computation of the dispersion function within the islands. It is worth noting that equivalent optical parameters, i.e., beta-, alpha-functions and dispersions, can be computed for the linearized motion inside the islands: of course, these parameters will in general be different with respect to the corresponding values around the centre of the phase space.

As far as the dispersion function is concerned, it is computed using its very definition, namely the position of the fixed points (the centres of the islands) is computed setting the momentum off-set to zero. Then, the position of the fixed points is computed for a different, but small, value of the momentum off-set, the difference in the fixed points' positions gives the local value of the dispersion. Of course, in this case the dispersion function is no longer periodic over one single machine turn, but over four. An example is shown in Fig. 46.

The results of the tracking were used to define the minimum and maximum extension of the beam envelope for each beamlet as a function of the *s*-coordinate. Then, these values are added quadratically with the contribution from the dispersion according to the standard formula

$$\sigma^2 = \sigma_\beta^2 + \sigma_p^2 D^2 \tag{17}$$

where σ_β represents the betatronic sigma of the beam, σ_p represents the sigma of the momentum distribution, and D stands for the local value of the dispersion function.

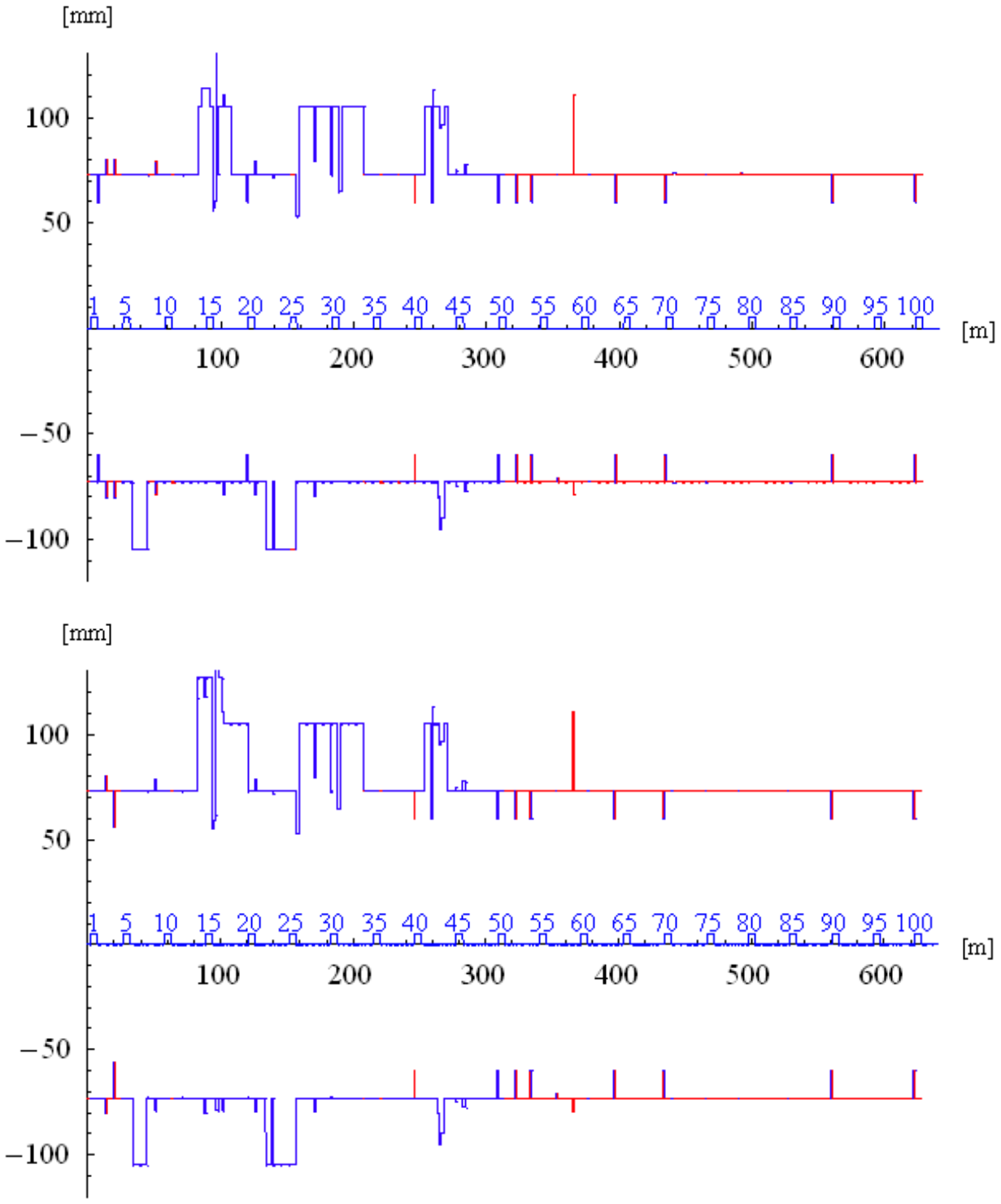

Fig. 44: Horizontal PS aperture model currently installed (upper part) and proposed changes for the implementation of the MTE (lower part). The blue lines correspond to the part for which the aperture model has been completely cross-checked and found in agreement with what is installed in the machine. The red lines correspond to the sections that have still to be cross-checked. In the horizontal axis both the *s*-coordinate and the main magnet number are reported.

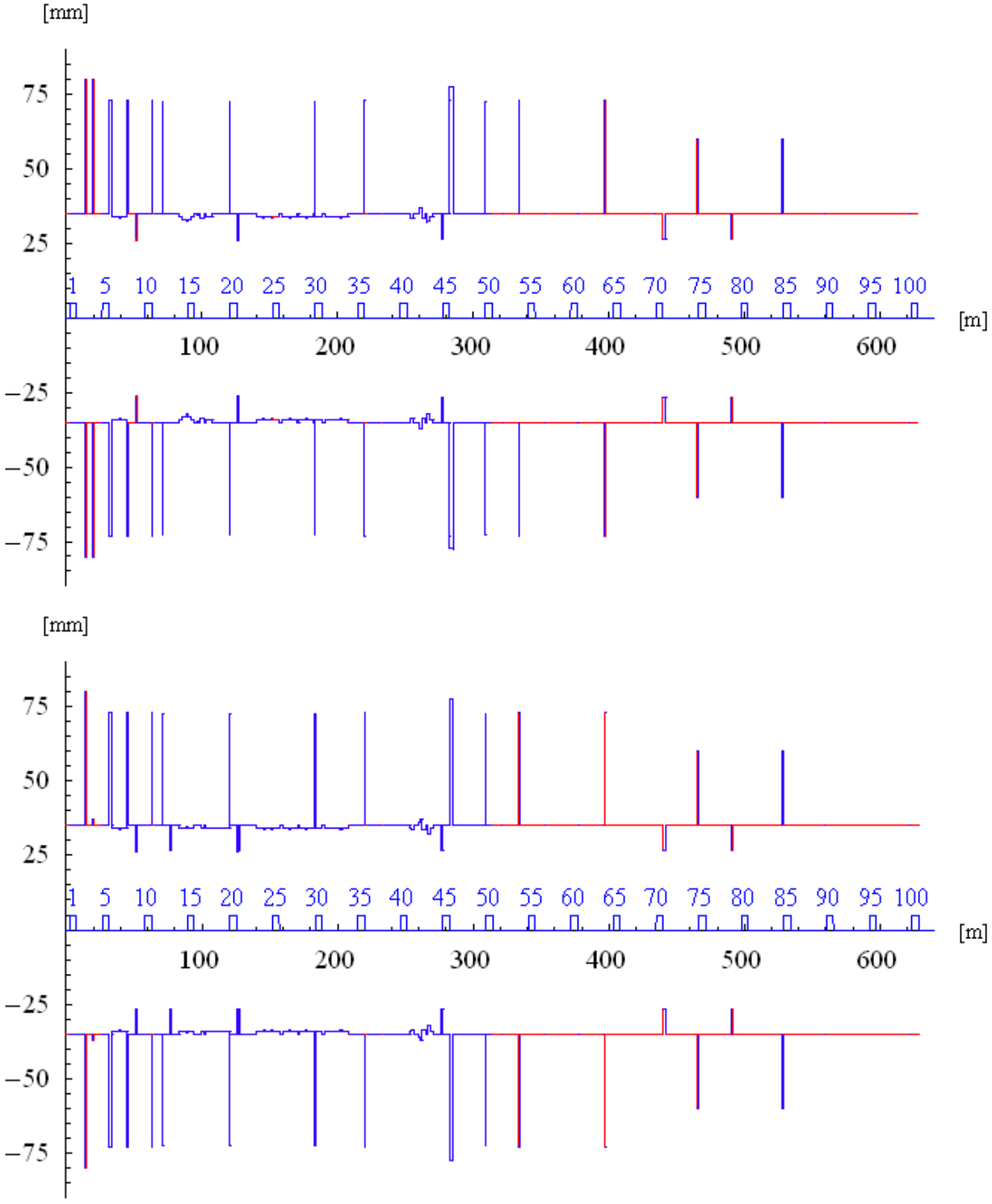

Fig. 45: Vertical PS aperture model currently installed (upper part) and proposed changes for the implementation of the MTE (lower part). The blue lines correspond to the part for which the aperture model has been completely cross-checked and found in agreement with what is installed in the machine. The red lines correspond to the sections that have still to be cross-checked. In the horizontal axis both the *s*-coordinate and the main magnet number are reported.

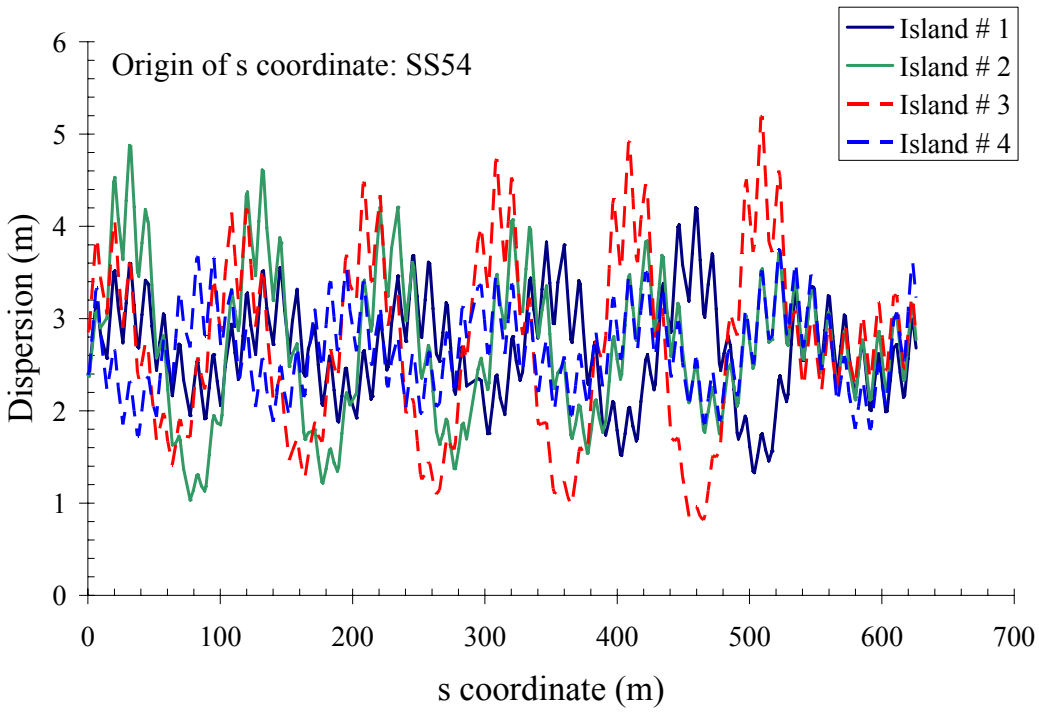

Fig. 46: Dispersion function for the linearized motion inside the four islands where the beamlets are trapped

This complex approach is required in the horizontal plane because of the non-linear effects introduced to generate the stable islands. On the other hand, in the vertical plane it is customary to neglect the non-linear coupling between the two transverse planes and to assume a pure linear dynamics. Therefore, when checking the available aperture in the physical space (x, y) the beam is assumed to be represented by a rectangle of sides given by the envelope computations. In the analysis made, the envelope was computed using a five-sigma value in the transverse space and two-sigma in the longitudinal one, which is justified by the fact that in the longitudinal distribution for protons is usually parabolic. The numerical values used are $\sigma_\beta = 1.5\,\text{mm}$ and $\sigma_p = 0.5\times10^{-3}$ for the horizontal plane and $\sigma_\beta = 2.89\,\text{mm}$ for the vertical plane.

All three values are derived from measurements results. This analysis emphasized that the critical points in terms of aperture are the magnet units 14, 15, 16, 18, 19. As far as the last two magnet units are concerned, the replacement of the standard vacuum chamber with a standard enlarged one represents a suitable solution. On the other hand, for the remaining three units the situation is more complicated. A special cross section had to be designed to optimize the aperture, requiring also a thorough study of the mechanical properties and magnetic properties. The proposed layouts are shown in Fig. 47 for magnet units 14 and 15 and Fig. 48 for magnet unit 16. Also, in Fig. 49 the cross sections for the proposed chamber for magnet unit 16 are reported.

All these chambers will be made of Inconel 625 on account of its excellent mechanical properties, making it possible to reduce the chamber thickness, combined with good magnetic properties. To ease the production process, the chambers for magnet units 14 and 15 share the same profile and differ only for the extremities. The one to be installed in magnet unit 16 is also based on the same cross section as the other two for the second piece, where only the circulating beam is accommodated.

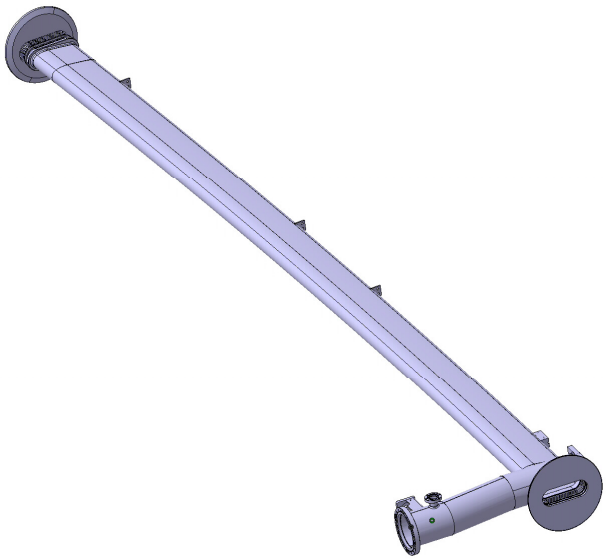

Fig. 47: Layout of the new vacuum chambers for magnet units 14 and 15

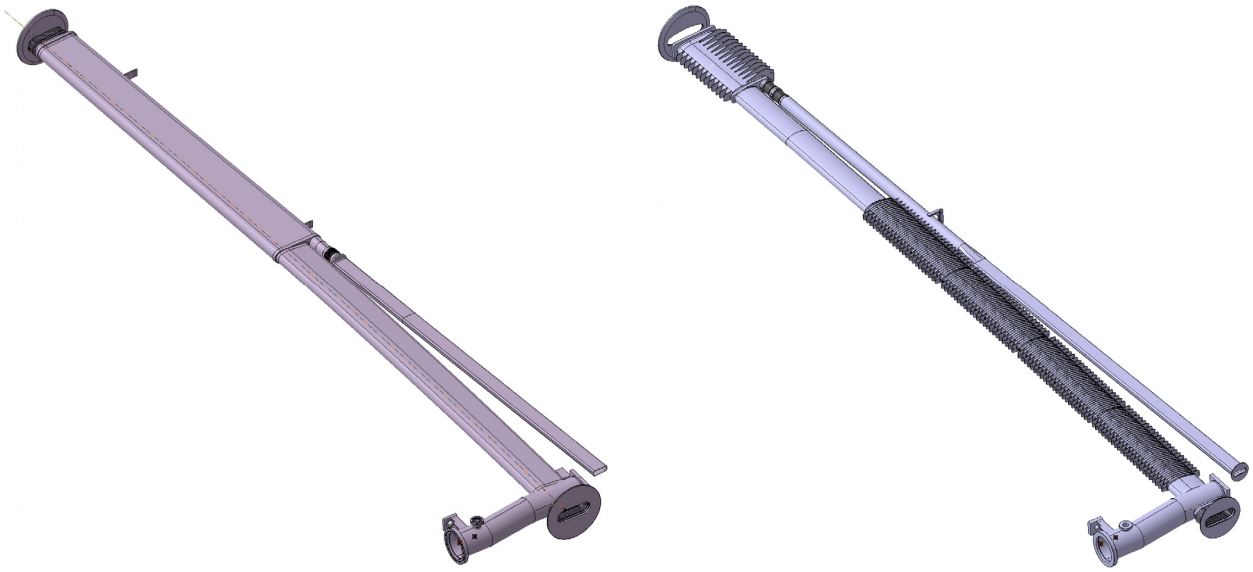

Fig. 48: Proposed layout of the vacuum chamber in magnet unit 16 (left part). The chamber currently installed is also shown (right part). This vacuum chamber accommodates both the circulating and the extracted beam.

The results of this study in terms of change of cross section of the vacuum chambers installed in the PS ring are reported in Appendix K where the list of changes (proposed and installed) vacuum chambers is found.

If the proposed layout for the vacuum chambers is used in the numerical simulations, then the results seem to indicate that the aperture available for the beam is enough, with a safety margin of about 1 σ_β whenever the beam envelope is computed at the 5 σ_β level.

The results of the numerical simulations are presented in Figs. 50 and 51, where the beam envelope —horizontal and vertical, respectively— for the four beamlets is shown for the case when the slow bump is switched on. For this situation no aperture limitations are visible,

apart from one in the horizontal plane in magnet unit 16 concerning the first beamlet, which is produced by the extraction septum and hence unavoidable.

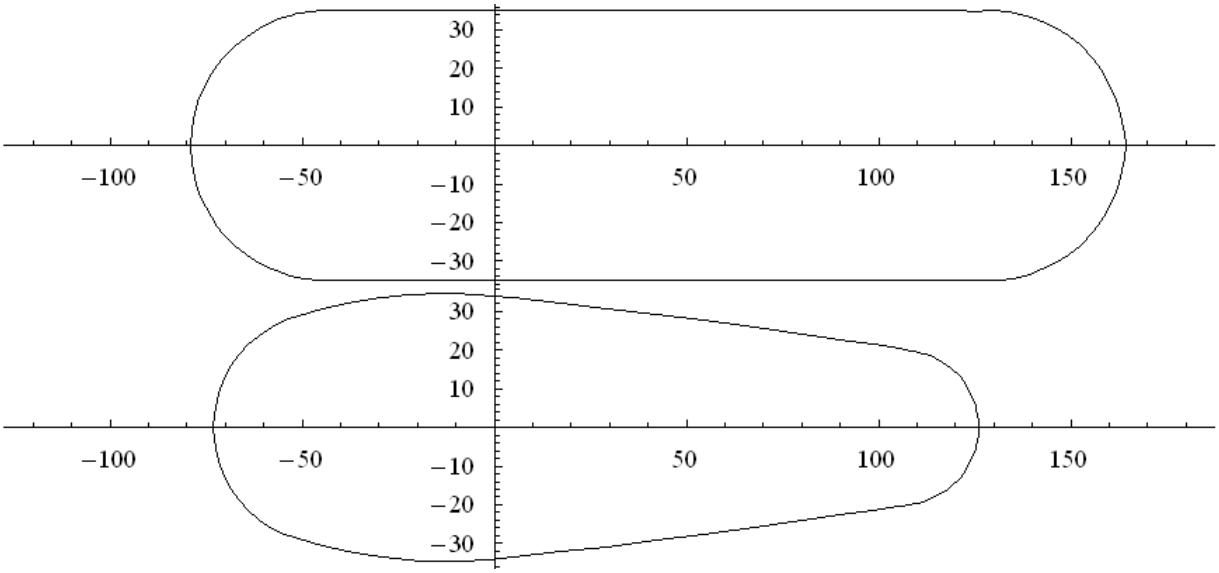

Fig. 49: Cross sections of the proposed vacuum chamber for magnet unit 16. The upper part represents the first part of the vacuum chamber, where both the circulating and the extracted beams are accommodated, while the lower part represents the second piece of the chamber downstream of the extraction point. The units for both axes are millimetres.

In Fig. 52 the situation at extraction, i.e., when both the slow and the fast bumps are switched on, is plotted for the first beamlets and the centre core, both in the horizontal and in the vertical planes. In contrast with the previous situation where the aperture limitation was in the horizontal plane, now it is in the vertical one at the level of magnet unit 15 and for the first extracted beamlet. However, it is worth mentioning that this restriction corresponds to a safety margin of more than one sigma in the case of a beam envelope computed at five times the value of the betatronic sigma, which corresponds to nearly zero beam losses. As far as the other beamlets are concerned, the situation is rather safe, as no aperture restriction appears even though the fast bump is switched on, until the beamlet is extracted and in this case the point of minimum distance between beamlet and vacuum chamber is always the magnet unit 15 in the vertical plane.

Such a situation is visualized in Fig. 53, where the cross section of the vacuum chamber designed for both magnet units 14 and 15 is plotted together with the cross section of the beamlets at extraction. As already mentioned, the beam cross section is approximated by rectangles instead of ellipses, thus introducing an additional safety margin in the numerical computations concerning the available aperture. The fact that the restriction occurs in the vertical plane is clearly visible.

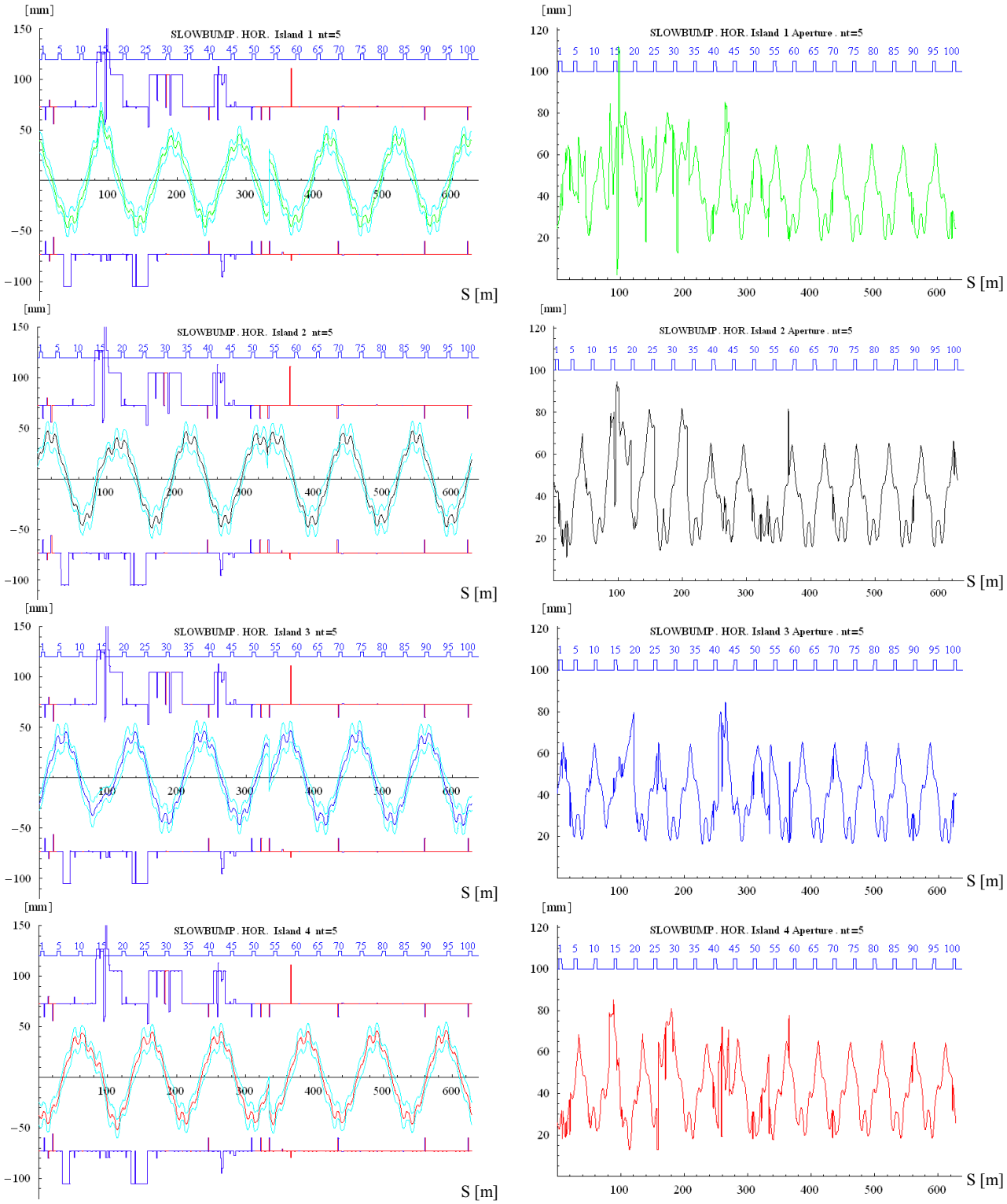

Fig. 50: Horizontal beam envelope along the PS circumference for the four beamlets (left) and clearance (right) when the slow bump is switched on. The centre core is not shown as it cannot pose any problems in terms of aperture. The minimum distance for the first beamlet is achieved at the extraction septum blade. The upper numbers stand for the main magnet identification number.

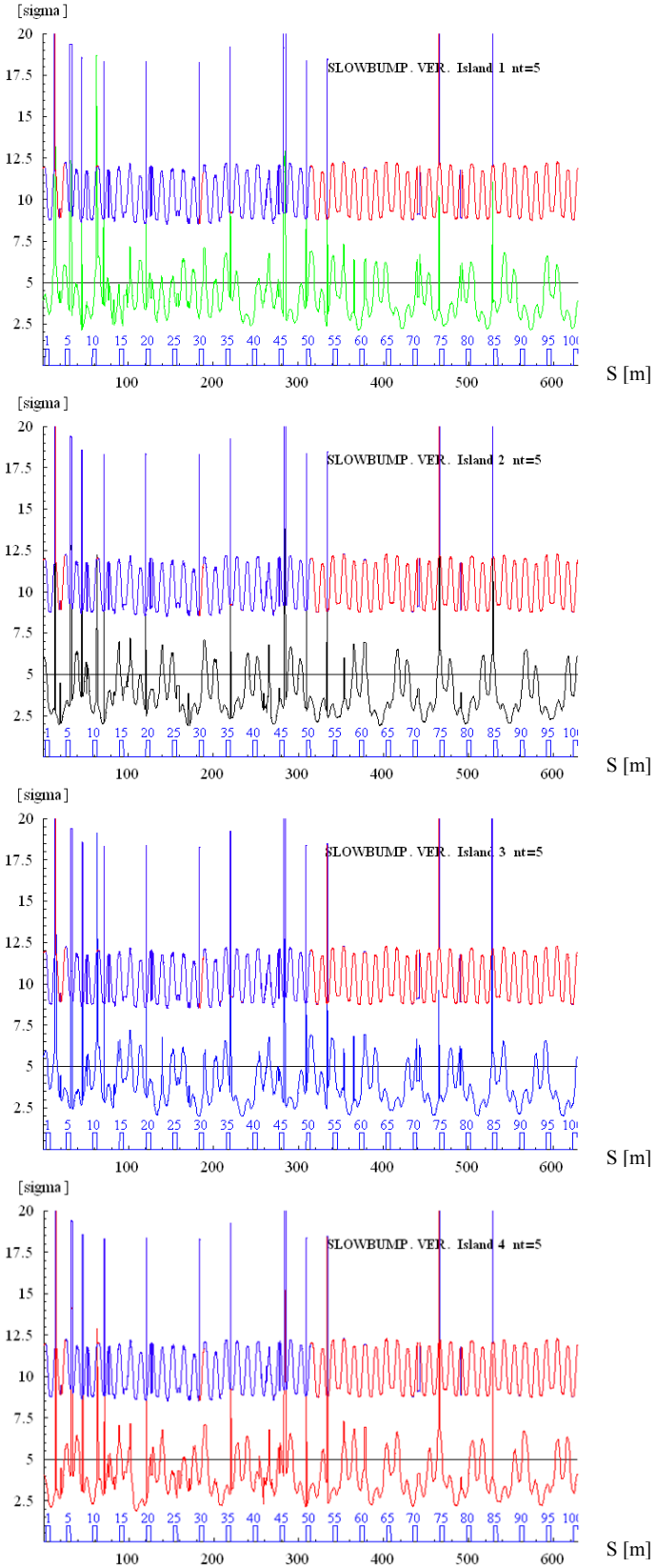

Fig. 51: Beam clearance in units of betatronic sigma for the vertical beam envelope for the four outermost beamlets for the case when the slow bump is switched on. The numbers in the lower part stand for the main magnet identification number.

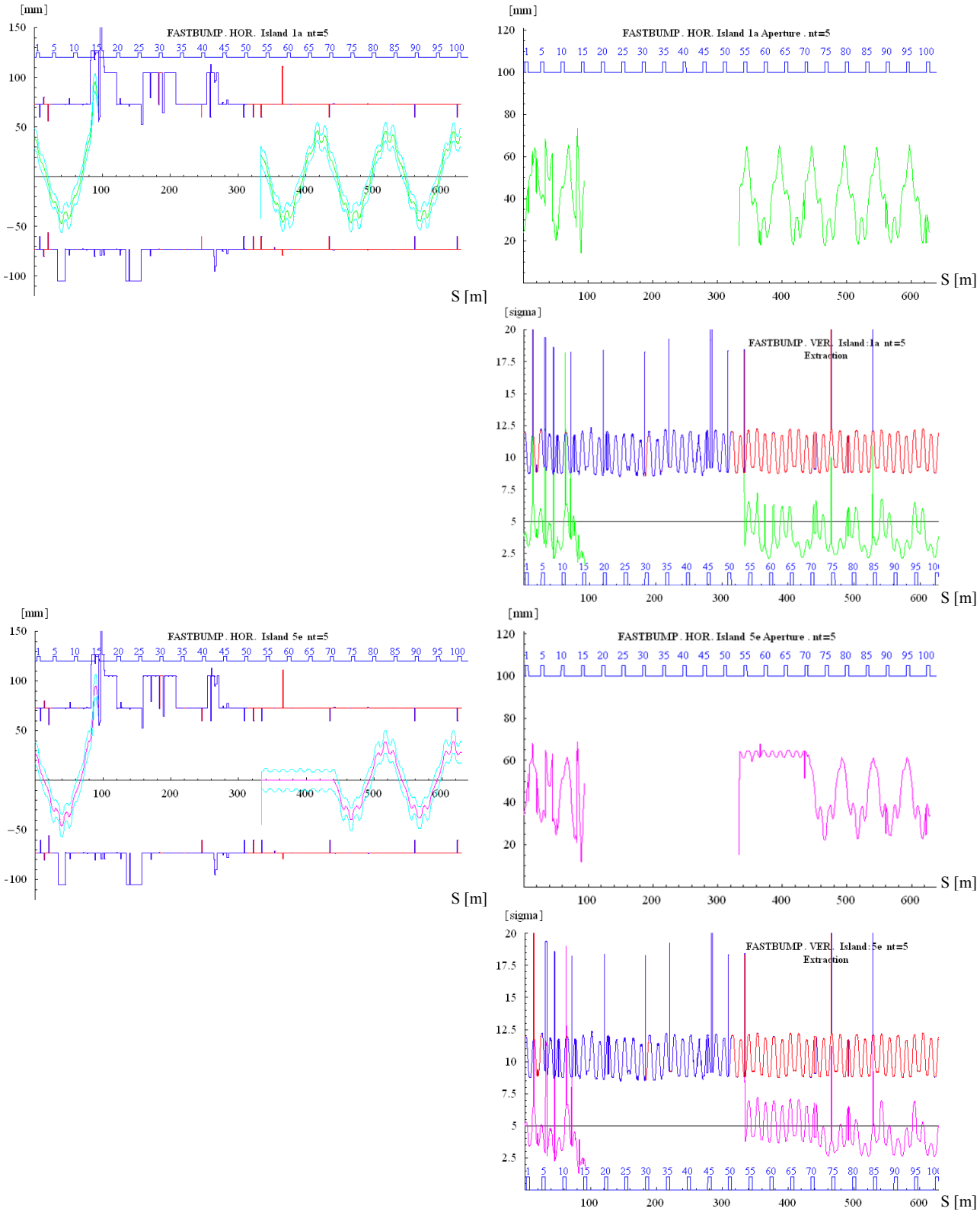

Fig. 52: Evolution of the horizontal beam envelope (left) and beam clearance (right) along the PS circumference for the first beamlet when both the slow and fast bumps are switched on (first row), and the centre core (third row). In the second and fourth rows the vertical beam clearance is shown for the first beamlet and the centre core, respectively. The upper numbers stand for the main magnet identification number.

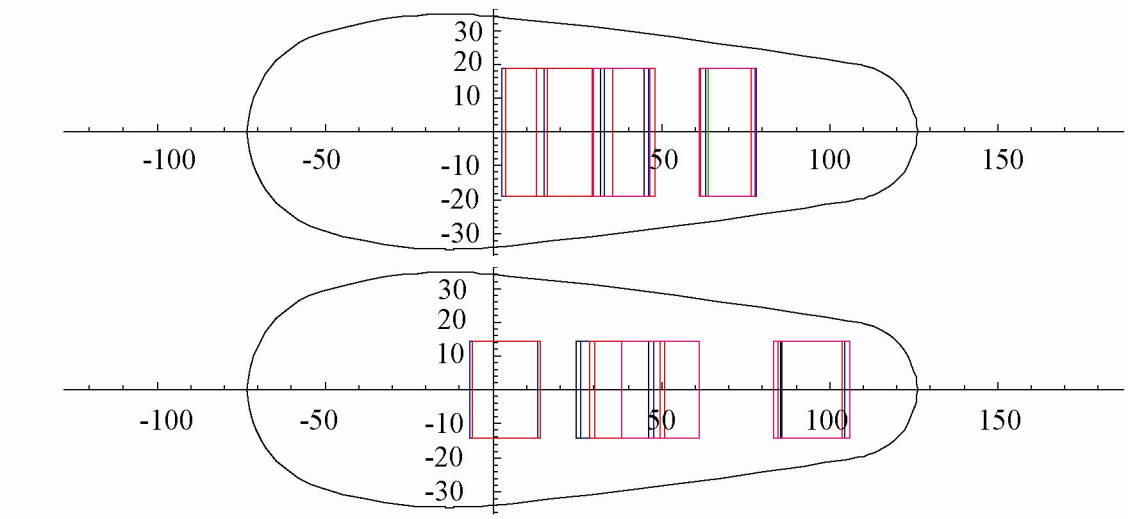

Fig. 53: Proposed cross section of the vacuum chamber in magnet unit 15 together with the transverse sections of the beamlets at extraction. The units for both axes are millimetres.

Finally, in Fig. 54 the superposition of the horizontal beamlets in the neighbourhood of the extraction point is reported. This case corresponds to the situation when both the slow and the fast bumps are switched on. The last five turns are plotted.

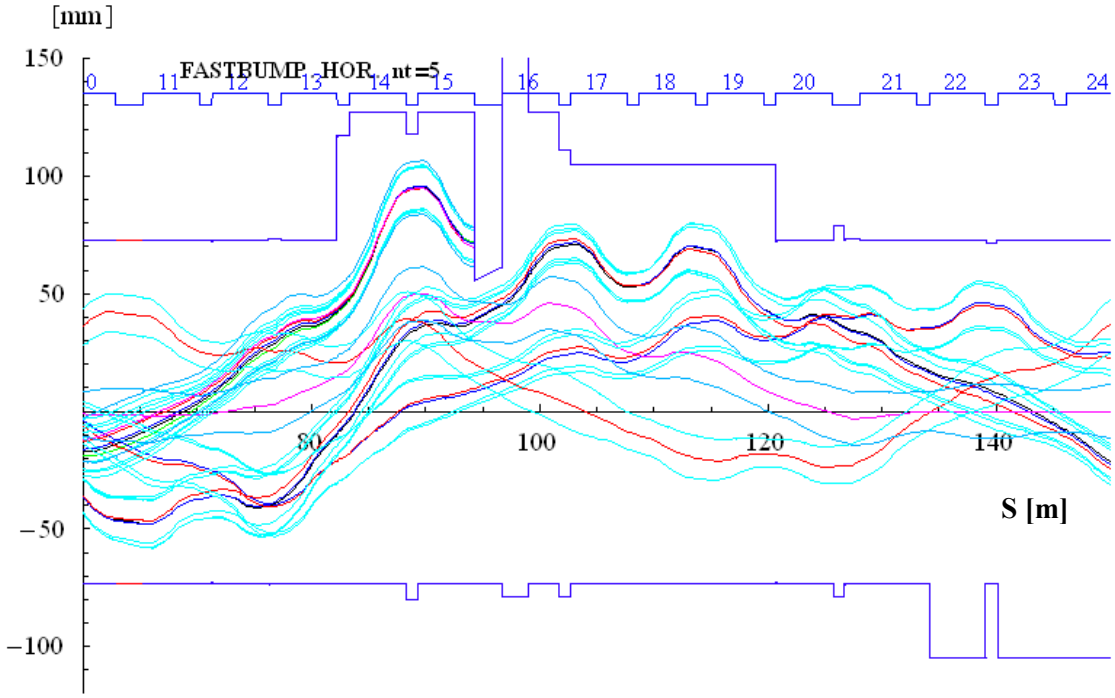

Fig. 54: Superposition of the horizontal beam envelope for the five beamlets at extraction, i.e., when both the slow and fast bumps are switched on. Only a subset of the PS circumference in the neighbourhood of the extraction point is shown. The upper numbers stand for the main magnet identification number.

Two potential issues were considered during this study and a third one will be investigated in the near future. As can be seen from the list of chambers' cross section reported in Appendix K, in all cases the proposed aperture is increased with respect to what is currently

installed in the machine, except in SS4, where a reduction in the horizontal aperture is foreseen, due to the kicker aperture. In principle, this should not be an issue, as the horizontal beta-function reaches its minimum value in even straight sections. However, detailed simulations have been carried out for fast extracted beams, i.e., for those beams passing through SS4 after being displaced by the kicker in SS71–79, hence with the most stringent aperture requirements in SS4. The cases considered are the nTOF beam, on account of its large size, and the LHC beam.

The evolution of the horizontal beam envelope is shown in Fig. 55 for both beams, while the parameters used in the numerical simulations are reported in Table 13.

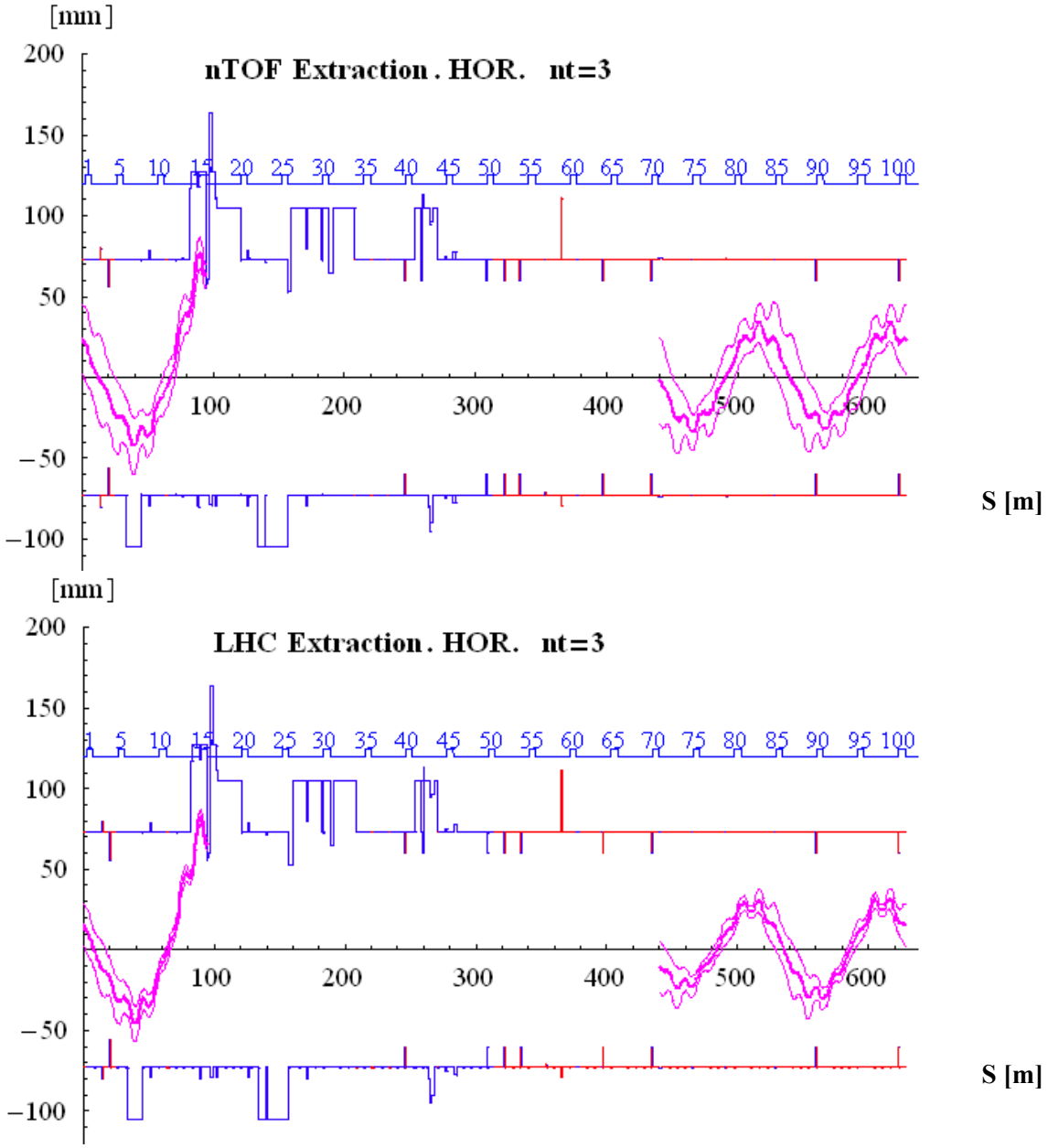

Fig. 55: Evolution of the horizontal beam envelope for the nTOF beam (upper part) and for the LHC beam (lower part). The envelope is computed considering $3\sigma_\beta$ and $2\sigma_p$. No aperture limit is visible in SS4 on account of the restriction introduced by the new kicker. The upper numbers stand for the main magnet identification number.

Table 13: Parameters of the nTOF and LHC beams used for the numerical simulations of the horizontal envelope

Parameter	$\varepsilon^*_H(\sigma)$ (μm)	$\varepsilon^*_V(\sigma)$ (μm)	$\Delta p/p(\sigma)$ 10^{-3}
nTOF beam (20 GeV/*c*)	12	6	1.5
LHC beam (26 GeV/*c*)	2.5	2.5	1.0

The second point to mention concerns the eddy current effects in the vacuum chambers and their compensation using passive circuits (see Refs. [75,76] and the presentation [77] for an overview on the subject). The passive circuits currently installed in the PS main magnets are adapted to the shape of the installed vacuum chambers so that the eddy current effects are compensated. With the proposed modifications the passive circuits will also have to be changed. In particular, for the vacuum chambers in magnet units 18 and 19 that are enlarged but standard, the appropriate spare circuits are already available. On the other hand, for the special chambers in magnet units 14, 15 and 16, a study should be launched to evaluate the electrical characteristics of the required circuits.

The last point that should be analysed refers to the estimate of the variation of the machine impedance due to the change in the cross section of the installed vacuum chambers. It is believed that the impact should be irrelevant, but accurate estimates will be carried out to confirm this point quantitatively.

To summarize, it seems correct to state that, with the present knowledge of the beam splitting process and with the proposed changes in the PS machine layout, the aperture available for the beam should be sufficient to avoid any measurable losses.

4.4 Gamma transition jump issues

The lattice of the PS machine features a real transition located at about 6.1 GeV. A number of special manipulations are performed at the level of the transverse optics in order to increase the speed with which the transition is crossed. The details can be found in Refs. [67–72,78–82].The basic principle relies on a number of quadrupoles that are pulsed in correspondence with the time corresponding to the crossing of the natural value of the transition.

The quadrupoles are grouped into two periodic structures, as a sort of cell, each made of a sequence of doublet-like, triplet-like and doublet-like quadrupole groups [83]. Subsequent quadrupoles are separated by π in betatronic phase, while the phase advance between the doublets and the triplets is a free parameter of the scheme and in the specific case of the PS machine is fixed to $\pi/2$ (see Fig. 56 for a sketch of the layout). Because of the presence of the electrostatic septum used for the slow extraction towards the East Hall, the nominal symmetry of the triplet of the second cell is broken and the quadrupole, which should have been located in SS57, is displaced further downstream by 2π, i.e., to SS73.

The quadrupoles are powered via two power converters: one for the doublets and one for the triplets. The doublets circuit is configured as a series-parallel circuit: the quadrupoles in SS61, SS69, SS87 and SS95 are connected in series, as well as those in SS19, SS27, SS29 and SS37. The two branches are then powered in parallel. The functional dependence of the current upon time is shown in Fig. 57. The transition crossing occurs once the current of the doublets crosses zero.

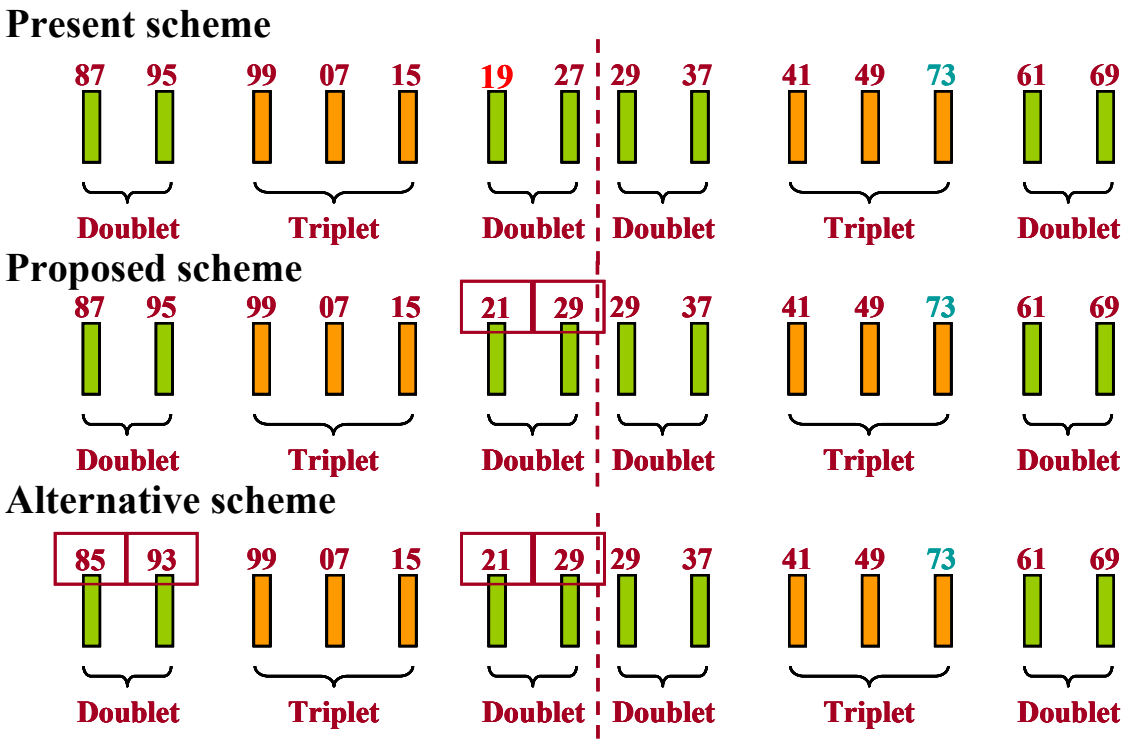

Fig. 56: Layout of the quadrupoles used for the present version of the gamma-jump scheme (upper) together with a new proposed scheme (centre) and an alternative one (lower). The structure with doublets and triplets is clearly visible, as well as the broken symmetry due to the quadrupole in SS73.

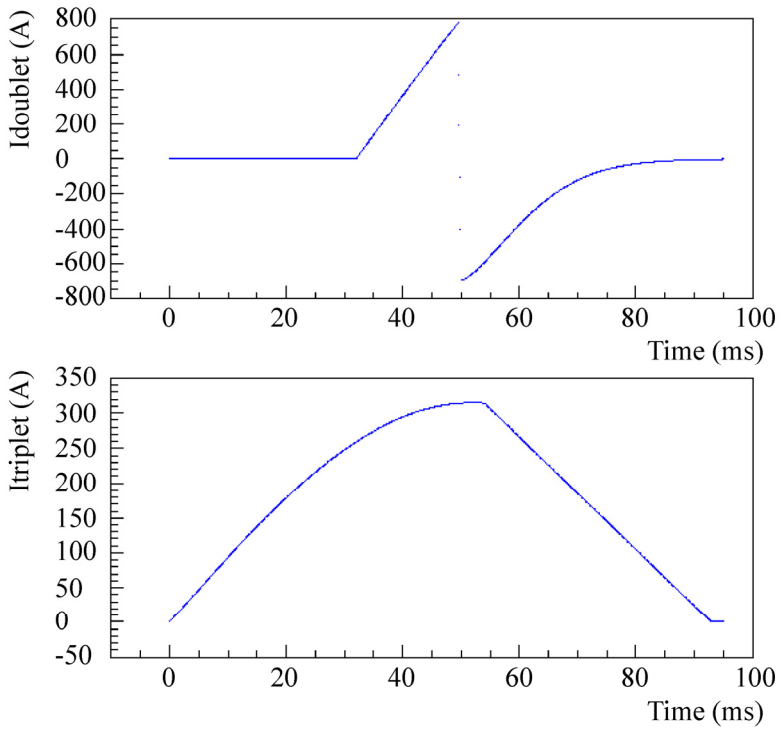

Fig. 57: Functional dependence of the current upon time for the doublets (upper) and the triplets (lower). The timing corresponding to the transition crossing is given by the zero crossing of the current powering the doublets.

A second violation of the theoretical scheme comes from the hardware properties of the quadrupoles themselves. In fact, the doublet and the triplet quadrupoles are split into two families each according to their mechanical aperture, namely one fitting around a standard vacuum chamber and a second one fitting around an enlarged vacuum chamber. Furthermore, the electric and magnetic properties are slightly different for the various families. Hence the actual gradient generated by each element is not exactly the nominal one. The slight mismatch induced does not seem to have a serious impact on the overall performance of the system [83].

During routine operation with high-intensity beams some losses are observed during transition crossing, corresponding to a few per cent of the total beam intensity. It is also known that a careful adjustment of the machine tune is important in minimizing these losses. As far the loss pattern around the machine circumference is concerned, it is worth noting that a peak is found in SS63.

In the framework of the studies for the novel multi-turn extraction, the decision to increase the dimensions of the vacuum pipe installed in SS19 was taken. This implies that the quadrupole installed in the same section as a part of the doublet for the gamma-jump gymnastics has to be moved elsewhere. Two schemes were proposed and they can be found in Fig. 56 (centre and lower) [84]. The first one features a displacement by two straight sections of one of the doublets of the first cell, namely from SS19/SS27 to SS21/SS29. The second scheme foresees to also move the other doublet of the first cell so as to restore the symmetry with respect to the triplet.

A number of numerical simulations were performed to assess the performance of the various schemes and to allow comparisons between them. The results are shown in Figs. 58 and 59. In Fig. 58 the key optical parameters, i.e., beta-functions, horizontal dispersions, tunes, and η are shown as a function of time during the transition-crossing gymnastics. A large peak in the value of the horizontal beta-function is visible, reaching more than 60 m.

Whenever the beta-functions and the dispersion are considered, the differences between the three layouts are not too large. However, the tunes feature much larger variations, which are reflected in the slower variation of η. The horizontal line represents the threshold for the development of microwave instability for the nTOF beam [85]. Whenever $|\eta| \leq 0.004$ the instability develops with a growth time of about 1 ms. Hence while the nominal scheme allows staying in the instability regime for a time shorter than the growth time, in the proposed schemes the beam will certainly become unstable on account of the slower transition crossing.

Indeed, if the evolution of the optical parameters is shown as a function of the position inside the machine circumference (see Fig. 59), then a peak in SS63 is clearly found for the horizontal beta-function.

This corresponds to the broken symmetry in the triplet of the second cell, which had to be moved by 2π of phase advance downstream of the nominal position because of the presence of the electrostatic septum in SS57. This means that the origin of the beam losses observed during routine operation is fully understood. Also, the results of the numerical simulations indicate clearly that the gamma-jump gymnastics entails a non-zero tune change, which explains why in operation the machine working point has to be carefully adjusted.

Following the outcome of these studies it is planned to have a closer look at the time evolution of the currents used for the doublets and the triplets. In fact, it is planned to have new power converters for both circuits, with the capability of driving the power converter by a function generator. This means that a study on the way to optimize the functional dependence of the currents has to be undertaken to exploit the new capabilities provided by the power converters. It is hoped that this could improve the performance of the alternative

schemes proposed. Whether this approach can improve the aperture bottleneck in SS63 has still to be proven.

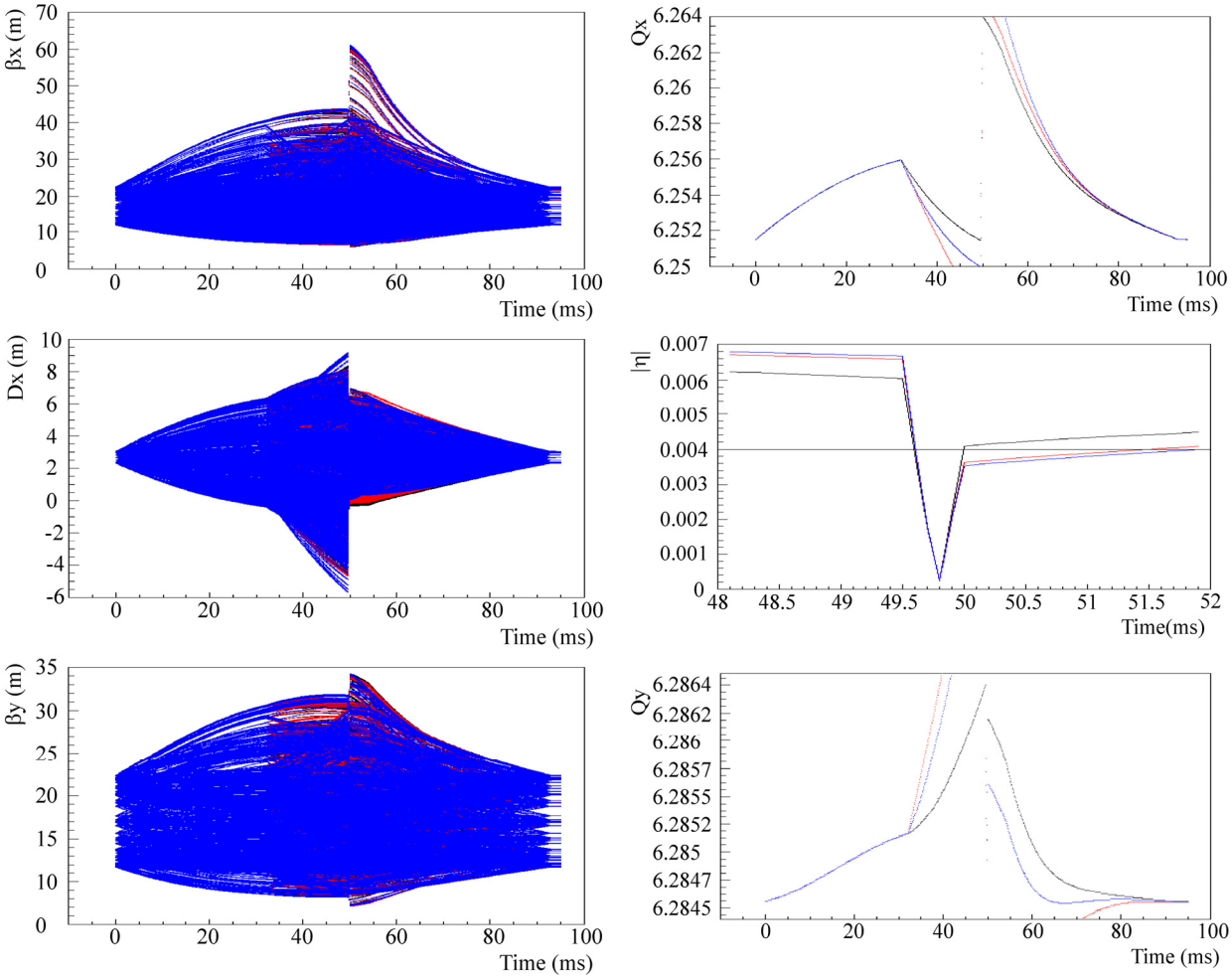

Fig. 58: Optical functions for the three layouts presented in Fig. 55 (black – nominal scheme; red – only one doublet displaced; blue – two doublets displaced) vs. time. The horizontal line in the plot showing the time dependence of η gives the threshold for the development of microwave instability for the nTOF beam.

4.5 Impedance issues

The scenario under study foresees the installation of three kickers in the PS ring with both vacuum tanks and magnet recuperated from existing hardware. This implies that no means to reduce the impedance of the devices can be foreseen. Therefore, before installing these new kickers into the machine, it is important to evaluate the impedance of the set of kickers currently installed in the PS machine and to estimate the increase of impedance due to the installation of the additional devices.

A measurement campaign was launched in 2005 to evaluate the impedance of the new devices and compare it to the PS machine impedance, which is believed to be dominated by the present kickers. At the same time theoretical studies were undertaken to analyse the experimental data and the measurement technique.

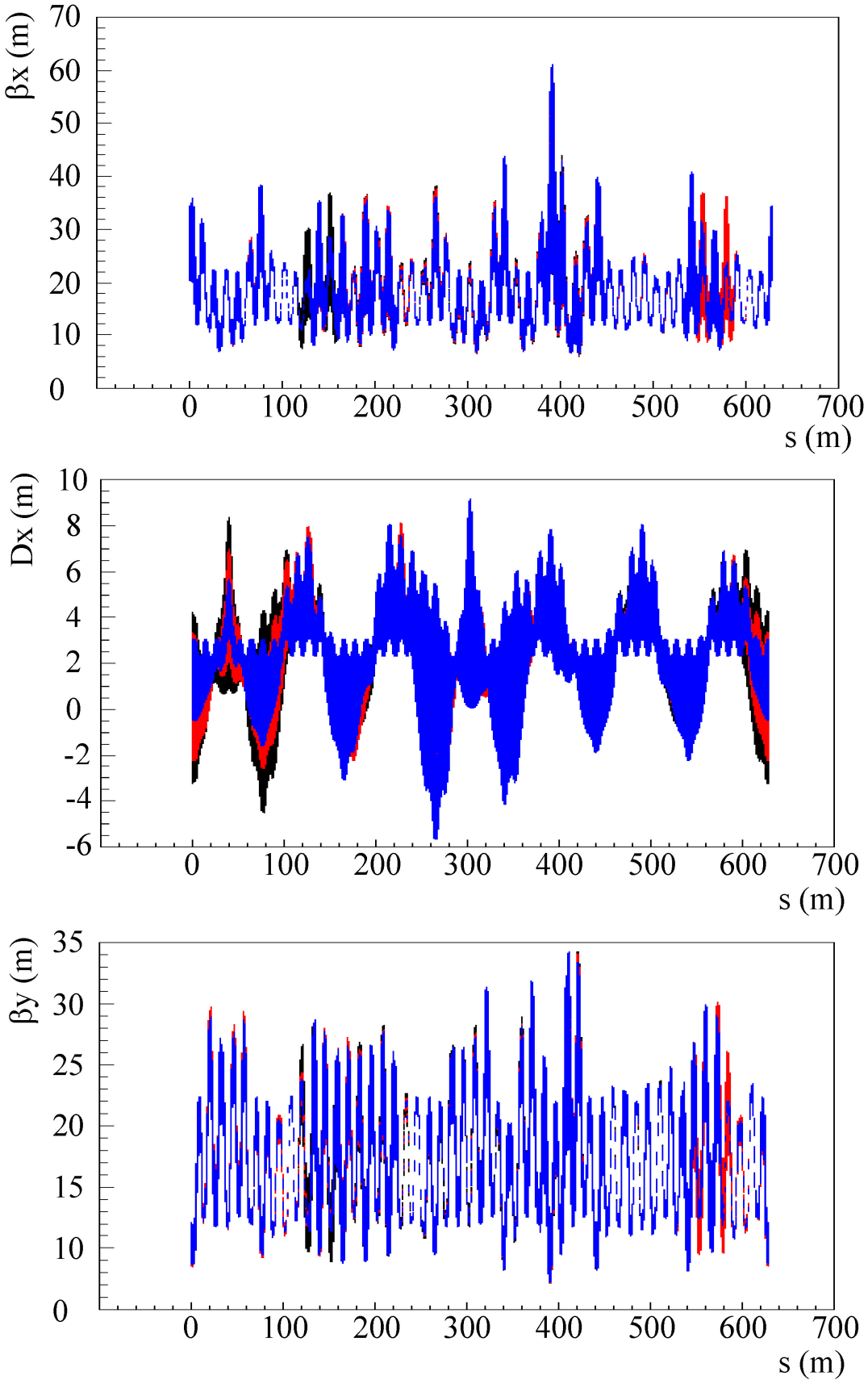

Fig. 59: Time evolution of the optical parameters represented along the PS machine circumference

4.5.1 Properties of kickers

1. The following kickers are currently installed in the PS machine:

   - injection kicker KFA45 in SS45;
   - extraction kicker KFA71/79 in SS71 and SS79;
   - BFA9/21 (pedestal and staircase) in SS9 and SS21 used for the CT extraction;
   - injection kicker for ions KFA28 in SS28.

2. The following kickers will be installed for the novel multi-turn extraction:

   - two identical new kickers KFA13 and KFA21 in SS13 and SS21. The modules are similar to those of the extraction kicker KFA71/79;
   - one new kicker KFA4 in SS4. The modules are recuperated from the extraction kickers for leptons;
   - all the kickers mentioned under point 1 will be also present.

As far as the electrical properties of the ferrite are concerned, all kickers are made from Philips material 8C11 (see also Ref. [86] for technical data sheets). The plot of the complex permeability of the 8C11 ferrite vs. frequency is shown in Fig. 60, while the numerical data are listed in Appendix G.

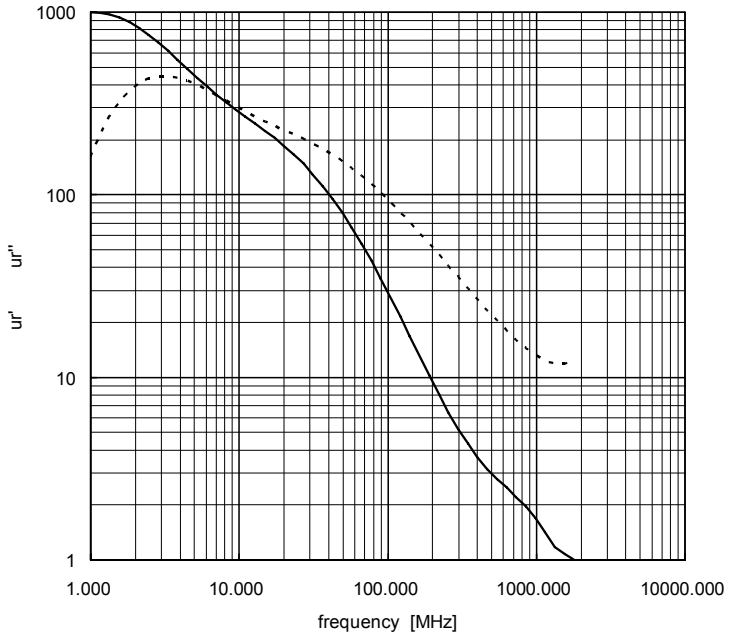

Fig. 60: Complex permeability of the 8C11 ferrite vs. frequency

The geometrical data for the various types of kickers are listed below:

- Kicker in SS9 (BFA, pedestal and staircase): it is a lumped magnet, i.e., the ferrite is not split longitudinally in many cells. The cross sections of pedestal and staircase kickers are shown in Fig. 61.
- Kicker in SS13: it is made of modules of the same type as those of the extraction kicker KFA71/79 (see below). In the second stage, a new design (increased gap, coating or beam screen) might be envisaged.

– Kicker in SS21 (BFA, pedestal and staircase); it is of the same type as the hardware installed in SS9.

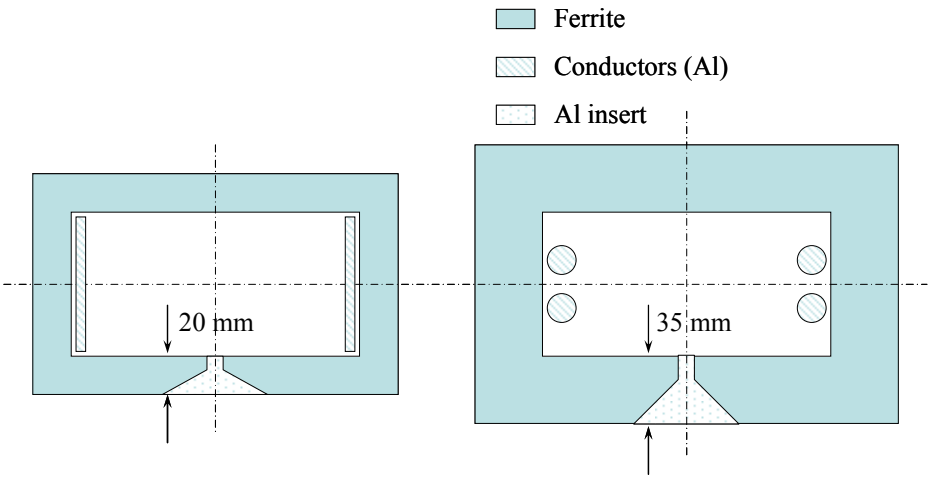

Fig. 61: Cross section of the BFA magnets installed in SS9 and SS21. The design of the pedestal and staircase are shown on the left- and right-hand side, respectively.

– Kicker in SS21 (new element): it is made of modules of the same type as those of the extraction kicker KFA71/79 (see below). In the second stage, a new design (increased gap, coating or beam screen) might be envisaged.
– Kicker in SS28: it is a lumped magnet, i.e., the ferrite is not split longitudinally in many cells. Its cross section is shown in Fig. 62. An aluminium insert is added to reduce the impedance seen by the beam.

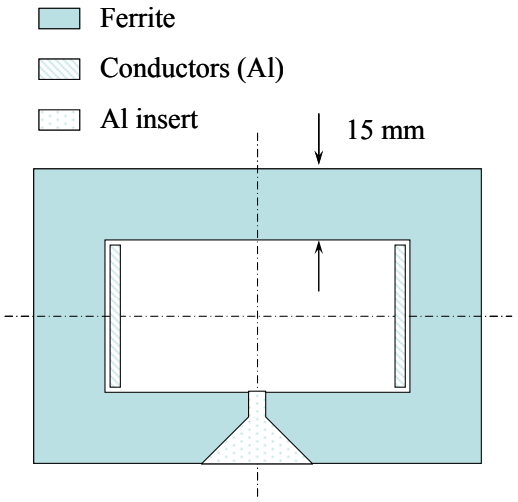

Fig. 62: Cross section of the injection kicker in SS28

– Kicker in SS45: it is a delay line, i.e., the ferrite is split longitudinally in eight cells. Each cell is 25 mm long: 20 mm of ferrite and 5 mm of aluminium. Its cross section is shown in Fig. 63.

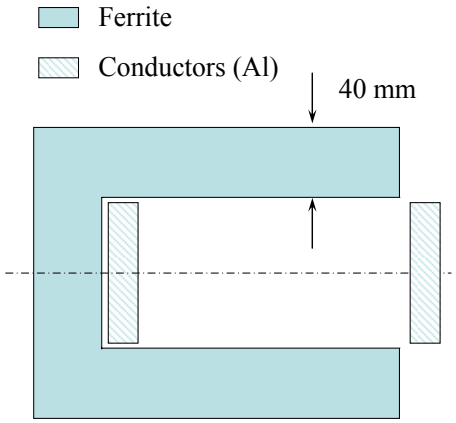

Fig. 63: Cross section of the injection kicker in SS45

– Kickers in SS71 and SS79: they are based on a delay line design, i.e., the ferrite is split longitudinally in many (nine for each magnet) cells. Each cell is 24 mm long: 19 mm of ferrite and 5 mm of aluminium. The cross section is shown in Fig. 64.

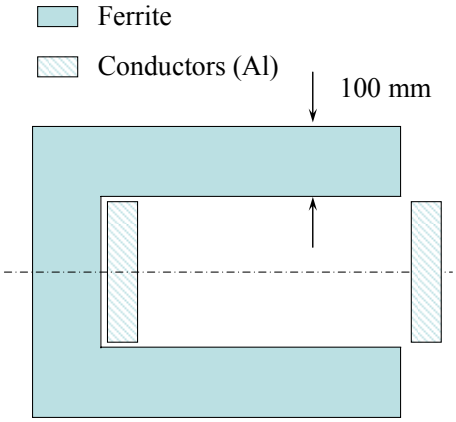

Fig. 64: Cross section of the extraction kicker installed in SS71 and SS79

– Kicker in SS4: it is based on a delay line design, i.e., the ferrite is split longitudinally in twenty-four cells. Each cell is 24 mm long: 19 mm of ferrite and 5 mm of aluminium. The cross section is shown in Fig. 65.

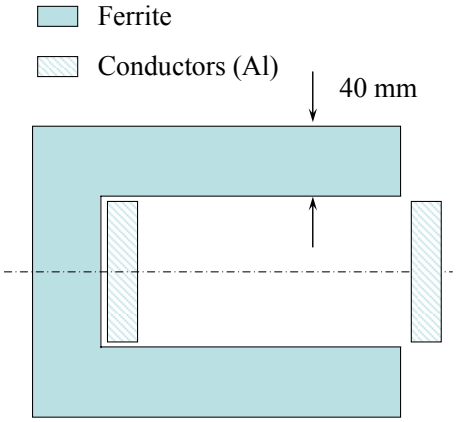

Fig. 65: Cross section of the extraction kicker installed in SS4

The transverse betatron functions, which are important for the kicker strength and the effective impedance seen by the beam, are given in Table 14. A summary of geometrical data is listed in Table 15 (see also Ref. [87] for a list of parameters).

Table 14: Transverse betatron functions for the existing kickers in SS45, SS71 and SS79, as well as for the future kickers in SS13, SS21 and SS4. The kicker in SS79 works in series with the kicker in SS71. The kicker in SS79 consists of three KFA modules, whereas the kicker in SS71 consists of nine KFA modules.

Betatron functions	KFA45	KFA71	KFA79	KFA13	KFA21	KFA4
Horizontal (m)	22.8	20.4	21.9	22.1	20.4	12.6
Vertical (m)	11.8	11.8	12.5	12.5	11.9	20.0

4.5.2 Measurements

Two measurement techniques were used to try to disentangle the transverse driving (also called classical or dipolar) and detuning (also called quadrupolar) impedances [88], which are both important for the beam dynamics. The first consists in measuring the longitudinal impedance for different transverse offsets using a single displaced wire. The sum of the transverse driving and detuning impedances is then deduced applying the Panofsky–Wenzel theorem [89]. The second uses two wires excited in opposite phase (to simulate a dipole), which yields the transverse driving impedance only. Simulations with Ansoft HFSS^{TM}, a finite-element electromagnetic simulator [90], are being performed to cross-check the measurement results, and study the effect of the finite kicker's length. The results will be presented in Ref. [91].

The measured longitudinal impedance vs. transverse offset, using a single displaced wire in a symmetric structure, is given by [88,92]

$$Z_{||}^{\text{measured}}(f) = Z_{||,0}(f) + Z_{||,1x}(f)\,x_0^2 + Z_{||,1y}(f)\,y_0^2\,, \tag{18}$$

where x_0 and y_0 are the transverse offsets of the wire from the centre of the chamber. The first term is the classical longitudinal impedance (in the centre of the vacuum chamber). The frequency-dependent coefficients $Z_{||,1x}(f)$ and $Z_{||,1y}(f)$ are linked to the 'generalized' transverse impedances Z_x and Z_y through the Panofsky–Wenzel theorem by

$$Z_x = Z_x^{\text{driving}} - Z^{\text{detuning}} = \frac{c}{2\pi f} Z_{||,1x}(f), \tag{19}$$

$$Z_y = Z_y^{\text{driving}} + Z^{\text{detuning}} = \frac{c}{2\pi f} Z_{||,1y}(f). \tag{20}$$

Table 15: Summary of PS kicker magnet parameters

Name	Magnet type No. of cells × L (mm)	Element	Mechanical aperture hor.×vert. (cm)	Magnet Aperture w×h (cm²)	Air field (Gauss)	L_{eff} (cm)	Integral Bdl (Gauss m) in SS	Rise/fall time (ns) (5–95)%	Flat-top length (μs)
Pedestal	Lumped	BFA 9/21 P	15.8 × 5.25	15.8 × 5.25	478.5	54	239.2	131	12.6
Staircase	Lumped	BFA 9/21 S	15.8 × 5.25	15.8 × 5.25	765.6	43	298.6	260	12.6
Kicker 28	Lumped	KFA 28	15.9 × 7.0	15.9 × 7.0	251.2	92.5	232.4	255	0.6–6.8
TIK proton	Delay line 8 × 25	KFA 45	15.0 × 5.3	15.0 × 5.3	355.5	22.1 × 4	314.2	39	2.6
FAK71/79	Delay line 9 × 24	KFA 71/79	14.7 × 5.3	14.7 × 5.3	628.0	22.2 × 12	1671.9	68–70	0.1–2.1
PS e^+/e^- inj.	Delay line 24 × 24	KFA 72/94	11.2 × 7.4	11.2 × 7.4	424.3	61.5	261.0	87–90	0.1–2.1

Therefore only the sum (or difference) of the driving and detuning impedances is measured with a single displaced wire. Note that there is no detuning impedance for chambers invariant over a 90º rotation and that for some asymmetric structures the detuning impedance can be larger than the driving one [88]. As can be seen from Eqs. (19) and (20), the detuning impedance can be removed by adding the two equations, leading to

$$Z_x + Z_y = Z_x^{\text{driving}} + Z_y^{\text{driving}} \,. \tag{21}$$

In the following, the measured longitudinal and transverse impedances are given for kicker KFA13, which is equal to KFA21, and kicker KFA4 of the future multi-turn extraction. The results are compared with analytical predictions by Tsutsui [93,94] and Burov–Lebedev [95–97] using 2D models, i.e., assuming an infinitely long kicker. The model of Burov–Lebedev used here is two parallel ferrite plates. It is expected to give a good approximation in the vertical plane as the kicker is much wider than high. The model of Tsutsui is shown in Fig. 66, where it can be seen that, in addition to the two parallel ferrite plates considered by Burov [97], a perfect conductor is assumed outside. This model is closer to the real cases (see Figs. 64 and 65). The results of the measurements, compared with those of Tsutsui and Burov–Lebedev, are given in Figs. 67 and 68. The longitudinal impedance is normalized by $n = f / f_{\text{rev}}$, as it is the quantity of interest for beam dynamics considerations.

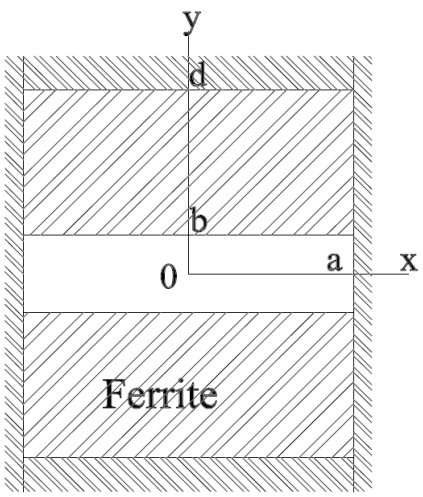

Fig. 66: Tsutsui's 2D model to compute the longitudinal and transverse driving impedances. The two parallel ferrite plates are surrounded by a perfect conductor. The length in the *z*-direction is assumed to be infinite.

As said above, the transverse impedances are deduced using Eqs. (18–20). Examples of the parabolas measured at some frequencies are given in Fig. 69 for the horizontal plane (left part). The sign of the parabola changes with frequency, which indicates that the sign of the horizontal impedance will also change (see Fig. 67). The same parabolas are shown for the vertical plane in Fig. 69 (right part), where no change of sign is observed (see also Fig. 67).

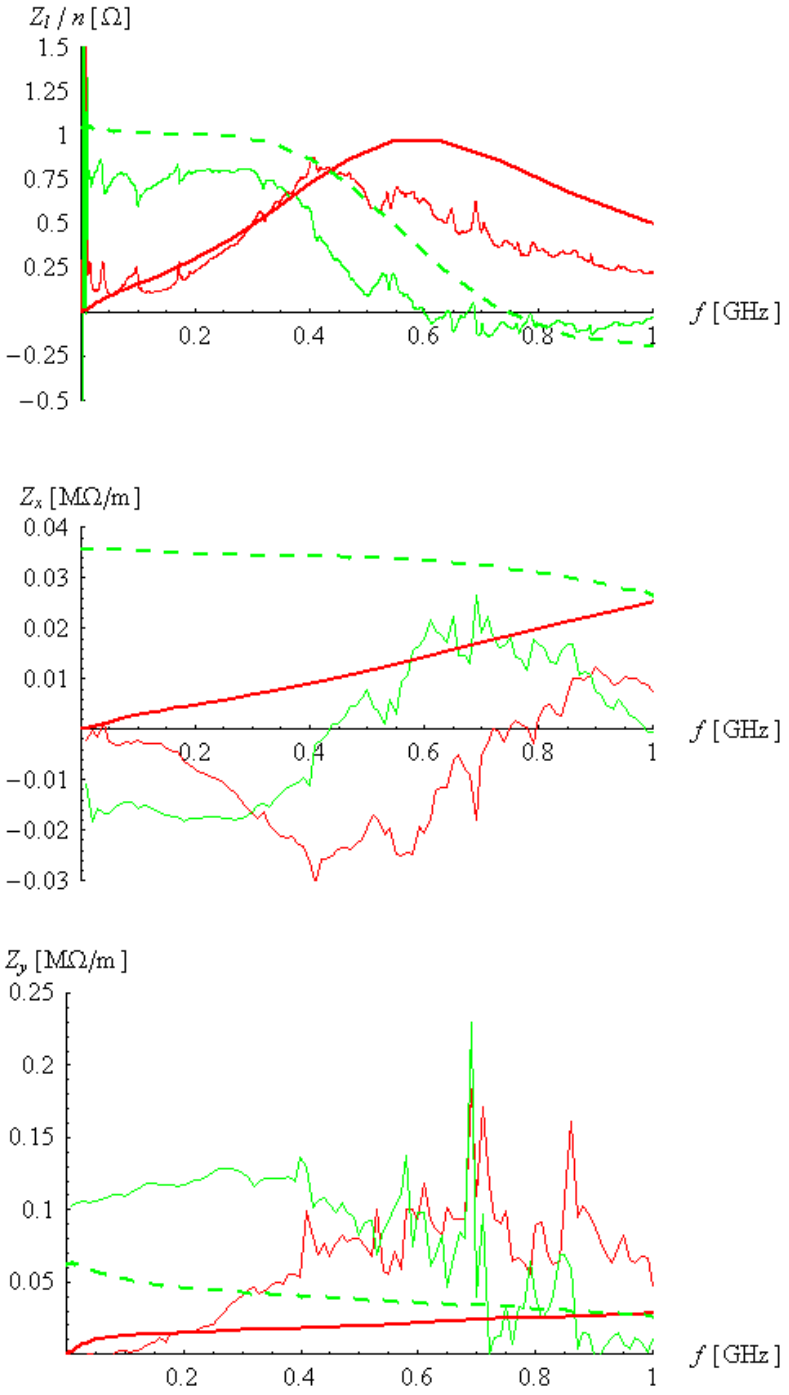

Fig. 67: Measured longitudinal (top), horizontal (middle) and vertical (bottom) impedances vs. frequency, using a single displaced wire. The real part is in red, whereas the imaginary part is in green. The thick, full, red line gives the real part of the driving impedance from the analytical result of Tsutsui (using the 2D model shown in Fig. 66) [93,94], and the thick dashed green line gives the imaginary part.

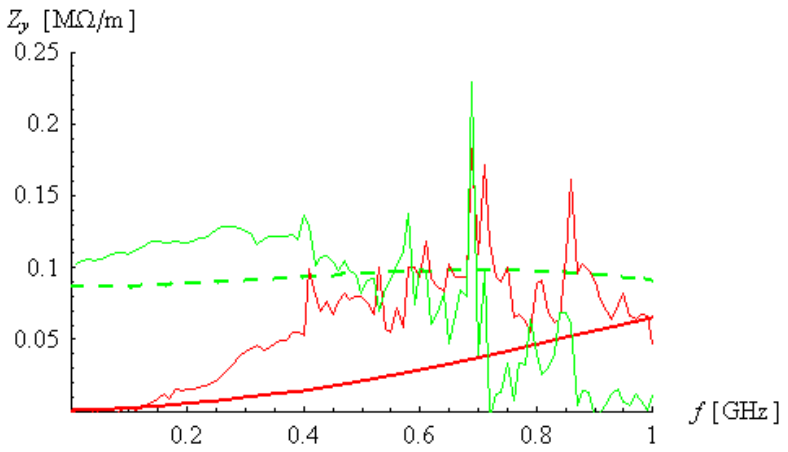

Fig. 68: Measured vertical impedance vs. frequency, using a single displaced wire (cf. the last plot of Fig. 67). The real part is in red, whereas the imaginary part is in green. The thick, full, red line gives the real part of the driving impedance from the analytical result of Burov–Lebedev (using a 2D model of two parallel ferrite plates) [97], and the thick, dashed, green line gives the imaginary part.

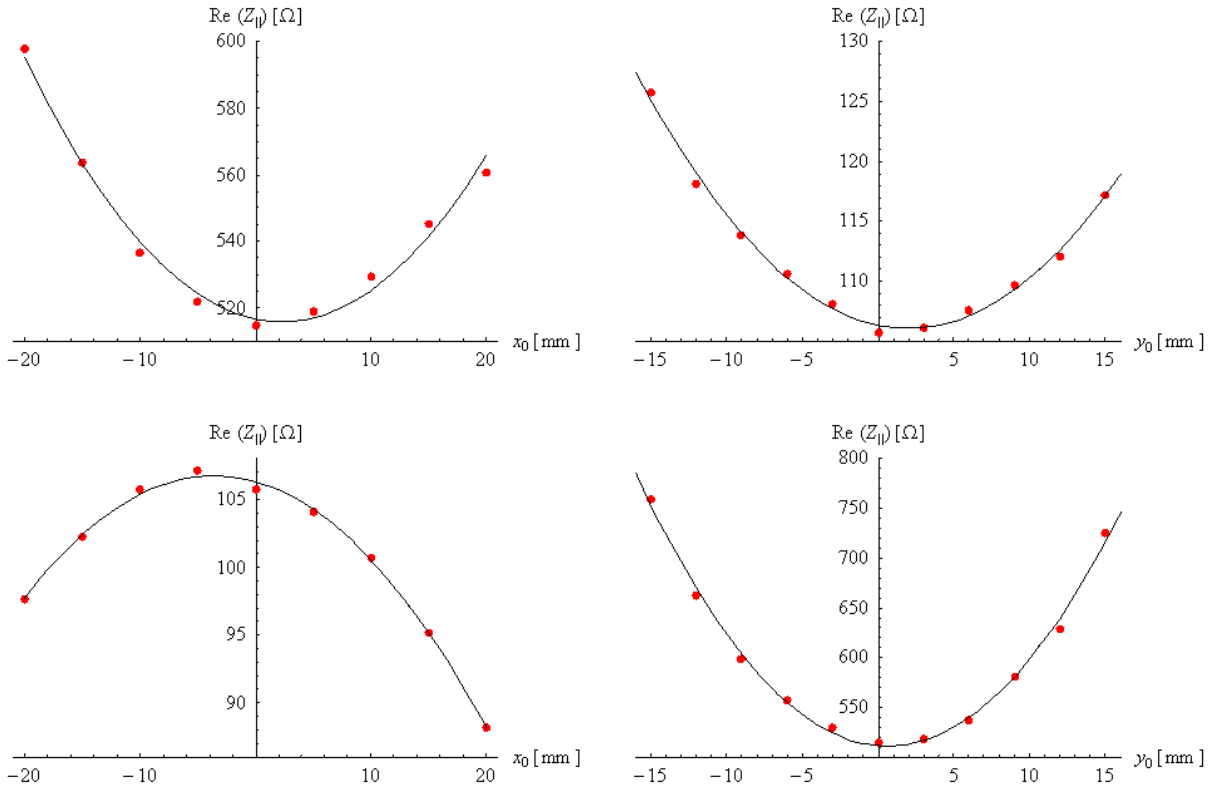

Fig. 69: Measured real part of the longitudinal impedance (red dots) vs. horizontal offset at 200 MHz (above) and 1 GHz (below). The full, black line is the parabolic fit used to deduce the horizontal impedance (left part) or the vertical impedance (right part).

Using Eq. (21), the sum of the horizontal and vertical driving impedances can be deduced from the measurements (see Fig. 70). This gives an upper limit for the transverse driving impedance, which can be used to estimate the impact of the new kickers on the PS beam dynamics (see the following sections).

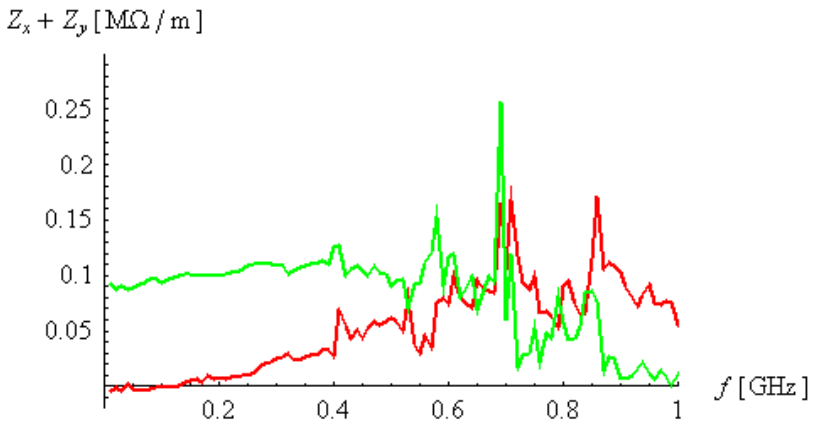

Fig. 70: Measured horizontal plus vertical driving impedances. The real part is in red, whereas the imaginary part is in green

Using the two-wire method, the transverse driving impedances were also measured. The comparison between the two methods for the real part of the sum of the transverse impedances is shown in Fig. 71, where it can be seen that a good agreement is reached for the frequencies between ~ 400 MHz and 1 GHz. The oscillation observed on the blue curve (two-wire method) is due to the residual mismatch. The low-frequency part still has to be analysed in detail.

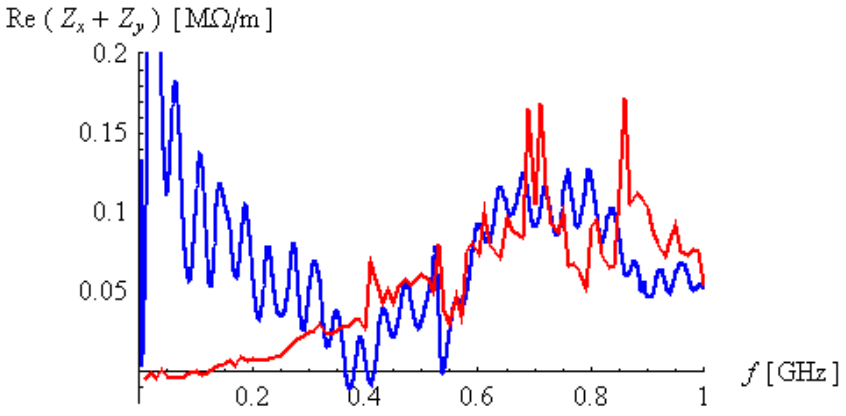

Fig. 71: Comparison between the measured horizontal plus vertical driving real impedances using the single-wire (in red) and two-wire (in blue) methods

The same type of results are obtained for the kicker KFA4, as shown in Figs. 72 to 75.

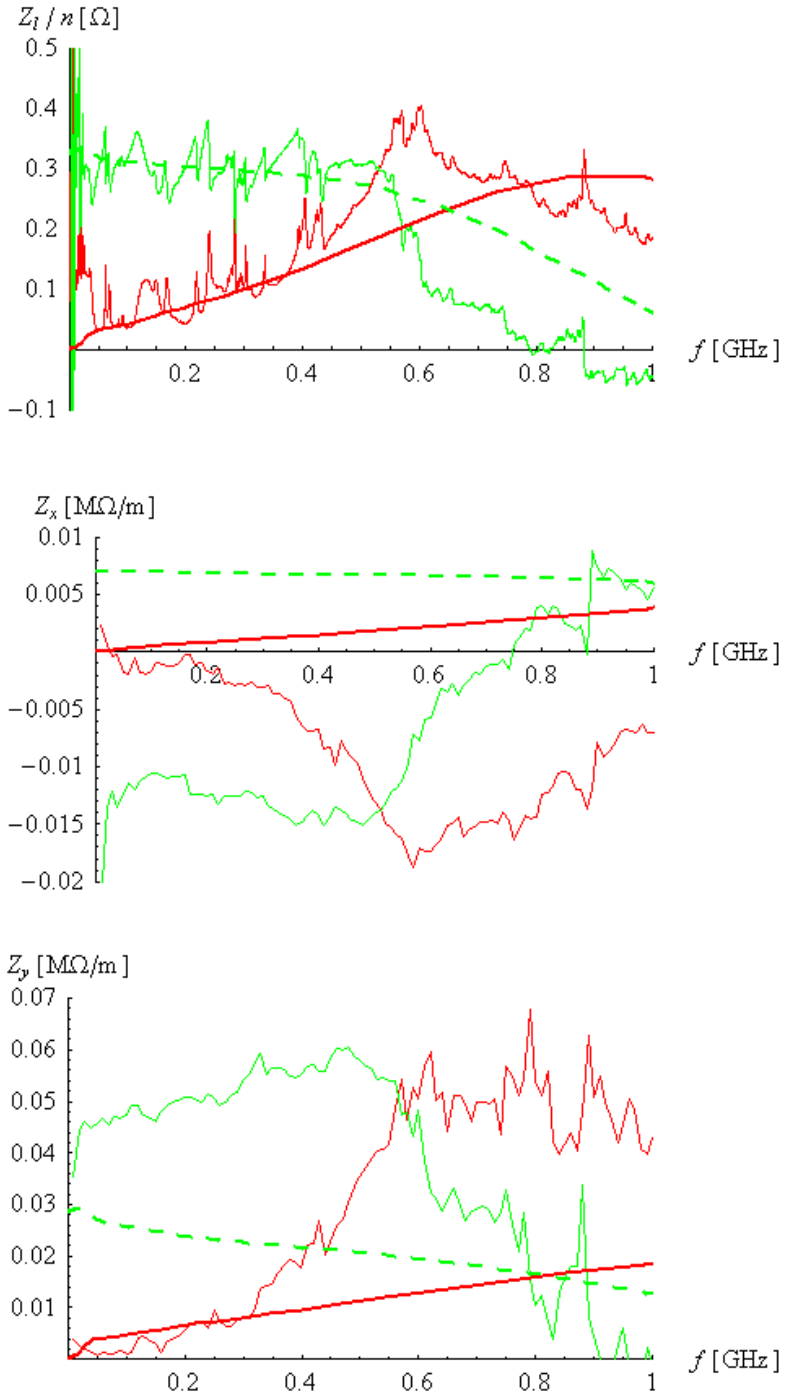

Fig. 72: Measured longitudinal (top), horizontal (middle) and vertical (bottom) impedances vs. frequency, using a single displaced wire. The real part is in red, whereas the imaginary part is in green. The thick, full, red line gives the real part of the driving impedance from the analytical result of Tsutsui (using the 2D model shown in Fig. 70) [93, 94], and the thick, dashed, green line gives the imaginary part.

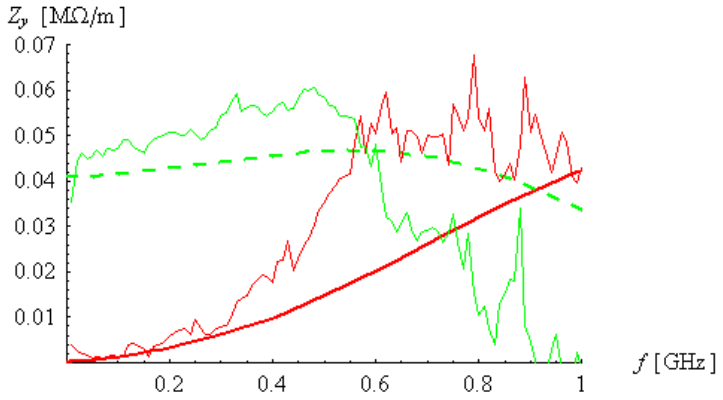

Fig. 73: Measured vertical impedance vs. frequency, using a single displaced wire (cf. the last plot of Fig. 72). The real part is in red, whereas the imaginary part is in green. The thick, full, red line gives the real part of the driving impedance from the analytical result of Burov–Lebedev (using a 2D model of two parallel ferrite plates) [97], and the thick, dashed, green line gives the imaginary part.

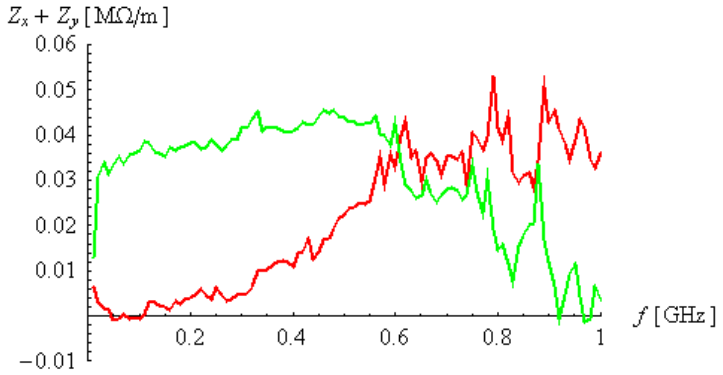

Fig. 74: Measured horizontal plus vertical driving impedances. The real part is in red, whereas the imaginary part is in green.

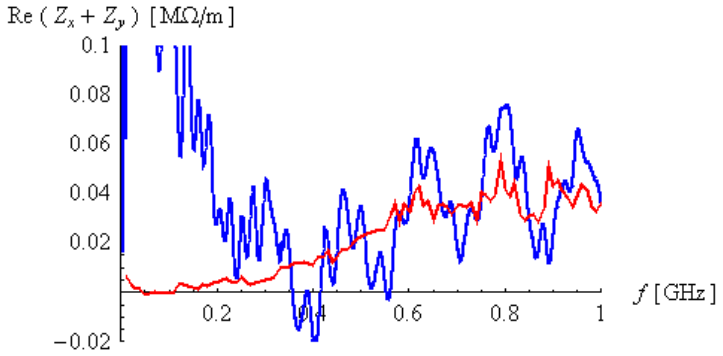

Fig. 75: Comparison between the measured horizontal plus vertical driving real impedances using the single-wire (in red) and two-wire (in blue) methods.

The conclusions from the measurements are that installing the three new kickers (KFA13, KFA21 and KFA4) will add to the PS machine:

- A longitudinal broad-band impedance of ~ 2 Ω, with a resonance frequency near ~ 400–500 MHz (see Figs. 67 and 72),
- A maximum (upper limit) transverse broad-band driving impedance of ~ 0.25 MΩ/m, with a resonance frequency near ~ 700 MHz (see Figs. 71 and 74). Taking into account the values of the optical β functions (see Table 15) leads to a normalized impedance of ~ 0.2 MΩ/m. The normalization is done by multiplying the impedance by the weighting factor $\beta / \langle\beta\rangle$, where β is the local betatron function in the relevant transverse plane and $\langle\beta\rangle$ the average β-function defined as the ratio of the average machine radius to the betatron tune.

4.5.3 Present PS machine impedance

The usual broad-band impedances measured in the PS machine in the past using several classical methods such as quadrupolar synchrotron frequency shift, potential-well bunch lengthening and coherent tune shifts, are given in Ref. [98]:

- a longitudinal broad-band impedance of ~ 20 Ω, with a resonance frequency near ~ 1.4 GHz (which is the cut-off frequency of the vacuum chamber),
- a horizontal broad-band impedance of ~ 1 MΩ/m, with a resonance frequency near ~ 1.4 GHz,
- a vertical broad-band impedance of ~ 3 MΩ/m, with a resonance frequency near ~ 1.4 GHz.

Therefore, based on these numbers, the installation of the three new kickers should increase the longitudinal and transverse broad-band impedances by ~ 10%.

A new estimate of the PS machine impedance is ongoing, starting with the measurements of the kickers' impedance. For the moment only two kickers have been measured, namely the extraction kicker KFA71/79, which is the same as the kicker KFA13 or KFA21, but four times longer, and the injection kicker KFA45. The measured longitudinal and transverse impedances for the two kickers are shown in Fig. 76.

As can be seen from Fig. 76, the longitudinal impedance of the two installed kickers, KFA71/79 and KFA45, is equivalent to a broad-band impedance of ~ 5 Ω, with a resonance frequency near 400 MHz. It is worth noting that there is also a resonance near 100 MHz, which may be quite harmful. For the transverse planes, the sum of the horizontal and vertical driving impedances is more complicated. The imaginary part is almost constant and equal to ~ 0.6 MΩ/m until ~ 500 MHz, and then it increases with frequency, reaching ~ 3.5 MΩ/m near 1 GHz. The real part has a mild maximum near ~ 700 MHz.

4.5.4 Beam dynamics considerations

The longitudinal stability of the different beams which have to be provided by the PS machine (and in particular the different flavours of the LHC beam) has to be checked, and this will only be possible with beams [99].

As far as the transverse planes are concerned, the vertical one is the most critical due to the fast single-bunch instability (i.e., due to a broad-band impedance) observed since 2000 at transition with high-intensity beams (see Fig. 77). This instability is suppressed by increasing the longitudinal emittance up to ~ 2.2 eVs for the more critical beam, which is the nTOF beam, where more than 7×10^{12} protons are accelerated in a single bunch [100]. The longitudinal emittance will thus have to be slightly increased. Note that the resonance frequency of the broad-band impedance responsible for the fast instability of Fig. 77 is

~ 700 MHz, which is consistent with the peak of the vertical impedance of Fig. 76: the kickers KFA45 and KFA71/79 may be the culprits of this instability. More beam dynamics studies have been started, using the HEADTAIL simulation code [101].

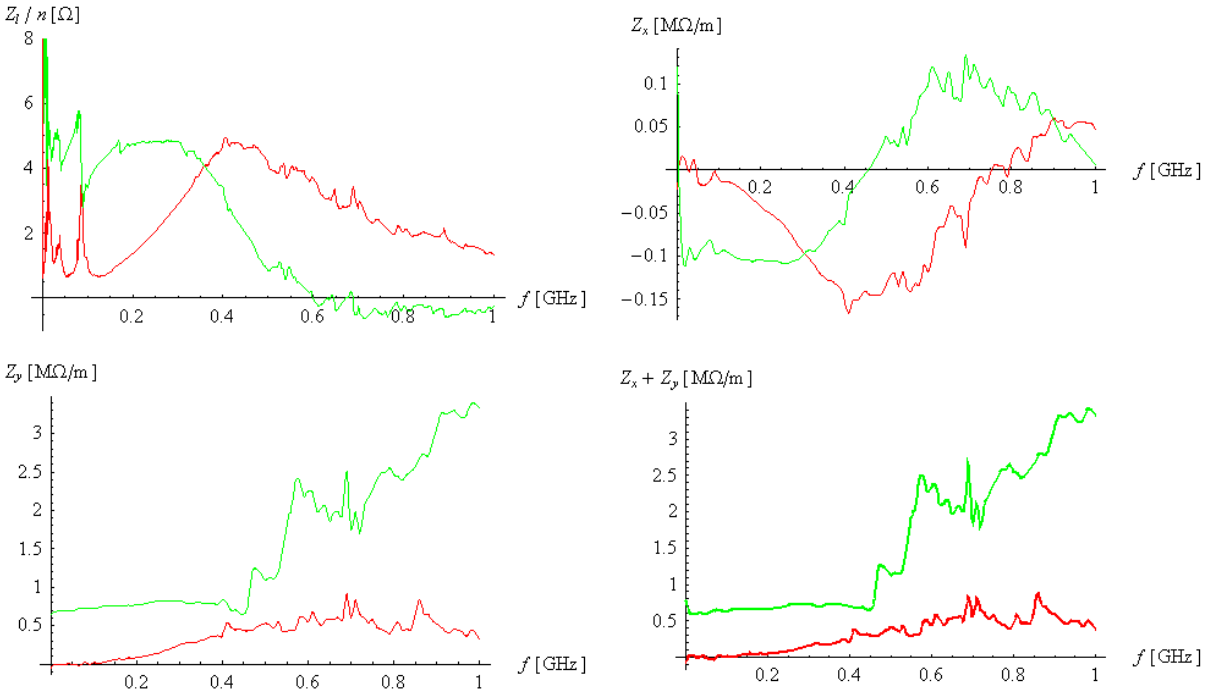

Fig. 76: Measured longitudinal and transverse impedances for the sum of the injection and extraction kickers KFA45 and KFA71/79 currently installed in the PS machine. The real part is in red, whereas the imaginary part is in green.

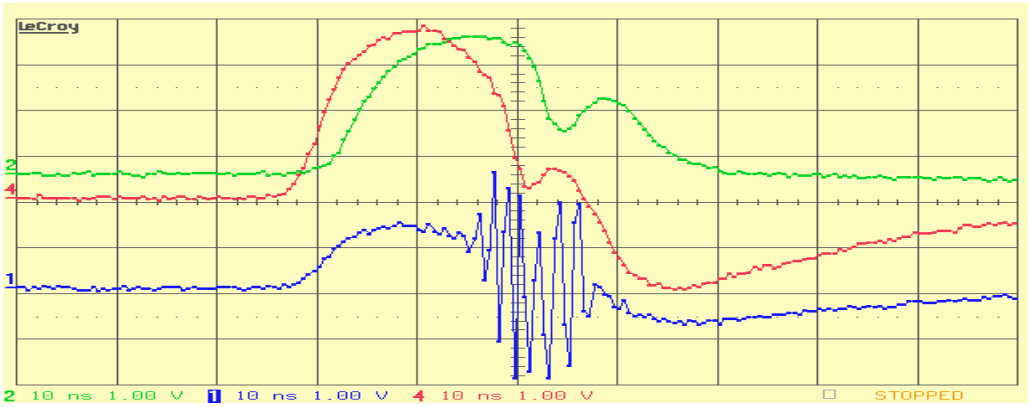

Fig. 77: Fast instability observed in the CERN PS near transition (~6 GeV total energy) in the year 2000. Single-turn signals from a wide-band pick-up. From top to bottom: Σ, Δ*x*, and Δ*y*. Time scale: 10 ns/div. The head of the bunch is stable and only the tail is unstable in the vertical plane. The particles lost at the tail of the bunch can be seen from the hollow in the bunch profile. The frequency of the vertical oscillation at the tail of the bunch is ~ 700 MHz.

It is worth noting that the 114 MHz RF cavities, which were for the leptons, were removed from the PS machine during the 2000/2001 shutdown, and that beam-based impedance estimates made in 2001 [102] were still consistent with those made in 1989 and reported in

Ref. [98]. Furthermore, the kicker tanks in SS72 and SS94, which were used for extracting the leptons, were only removed from the PS machine in January 2003, i.e., after the production of the fully nominal LHC beam [103]. Therefore it is justified to assume that these kickers were not too harmful for the beam quality, at least not for the production of the nominal LHC beam. Finally, two 200 MHZ RF cavities have been removed from the machine during the 2004/2006 long shutdown and the impedance reduction due to this change still has to be evaluated.

In conclusion, the foreseen increase of the PS machine impedance by ~ 10%, due to the installation of the three new kickers required for the future multi-turn extraction, is not believed to be a critical issue for beam stability in the PS machine.

4.6 Digression: A new extraction septum?

In the course of the studies for the new PS multi-turn extraction the need for (or benefit from) a thinner extraction septum in SS16, with half the septum thickness of the present system, was recognized. This would help to reduce the losses even further and, unlike the option of reducing the rise time of the kickers used to generate the fast bump, this improvement would be beneficial not only for the 14 GeV/*c* operations, but for all extractions towards the SPS. Although the new multi-turn extraction will not be operated at the PS top energy, such a septum must be compatible with the other extraction cycles where beam leaves the PS in SS16, in particular nTOF, i.e., a beam extracted at 20 GeV/*c*, AD, and all the flavours of the LHC beam, corresponding to a momentum of 26 GeV/*c*.

4.6.1 Technical considerations

The present magnetic extraction septum SMH16 contains two magnets installed under vacuum in one common vacuum vessel. Both coils are electrically operated in series. A layout of the assembly is given in Appendix H, together with the main parameters. The current septum type has a relatively short operational history; no precise forecast can therefore be given about its lifetime. However, failures in 1999 and 2004 have shown that the coils are currently the most fragile part of the equipment. Their lifetime is estimated, under the present operating conditions, i.e., 1.2 s magnetic cycle, to range between 5 and 10 years.

The maximum stress $\sigma_{\max}$ in the septum conductor scales with the septum thickness d, the gap height h, and the electromagnetic force F as follows:

$$\sigma_{\max} \propto \frac{F.h}{d^2}. \tag{22}$$

When reducing the thickness of the septum blade it is important not to increase the mechanical stresses further. If this limit is not respected the impact on the fatigue will be rather dramatic and the lifetime becomes totally irregular.

A rather cost-effective solution would consist of replacing the two identical magnets by two different, individually powered magnets, one with a thin septum blade and one with a thicker blade. The first, thin septum, would only displace the beam enough to enter the gap of the thick septum. While fitting into the available space, such a set-up could re-use a maximum of infrastructure and ancillary equipment, such as remote displacement systems, vacuum equipment and bake-out system.

For a given gap height, the electromagnetic force scales with the square of the electrical current I, yielding

$$\sigma_{\max} \propto \frac{I^2}{d^2}. \tag{23}$$

To keep the stresses at the present level, dividing the septum thickness by two would mean limiting the current density to half of the present one. This, however, would yield a long thin magnet, leaving insufficient space for the thick magnet to obtain the required total integrated field of 2.6 T·m. Therefore an alternative technology needs to be applied to make the septum conductor mechanically more resistant. Several options are available such as using a stainless steel reinforcement brazed onto the septum conductor. This solution comes at the cost of a reduced copper section for the septum conductor, hence an increase in the total power dissipation, and therefore higher cooling needs. Another solution would be to shape the septum conductor differently, making it more rigid. The inner profile of the thin septum, close to the ejected beam, would be designed in such a way as to enable the septum to be placed as close as possible to the ejected beam whilst reducing the losses on the septum itself (Fig. 78). This solution comes at the cost of deteriorated field homogeneity in the gap close to the septum conductor. The impact on the beam quality still needs to be quantified.

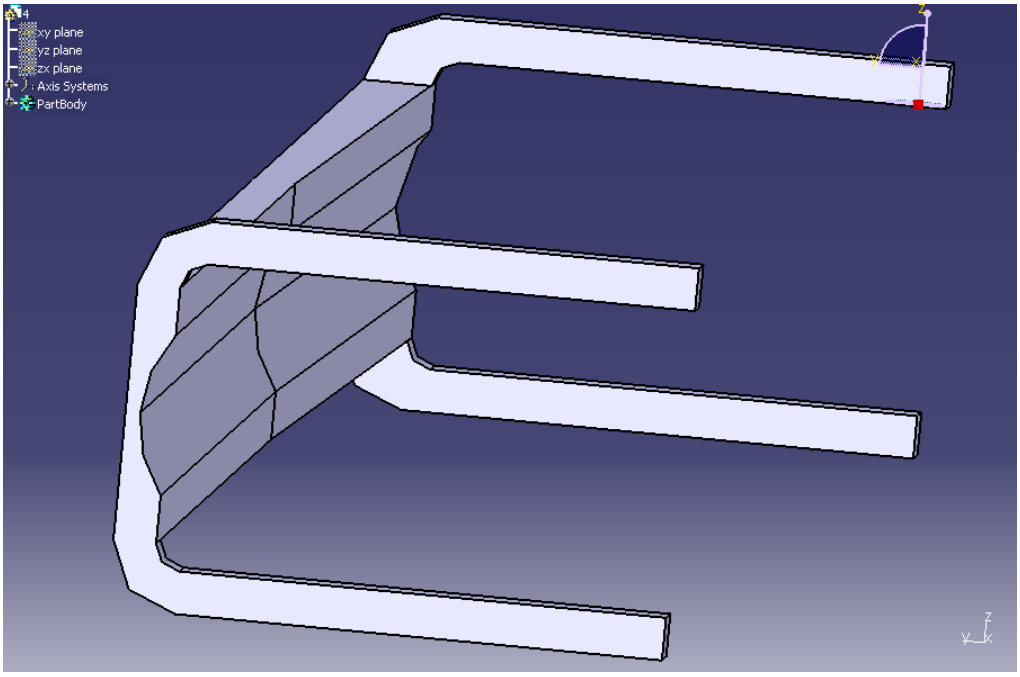

Fig. 78: Non-uniform cross section septum conductor

4.6.2 Implementation

Using one of the techniques mentioned above, the new septum could consist of a thin septum with 1.7 mm thickness that displaces the beam at its exit by 3.3 mm, enough for the beam to jump a 3.3 + 1.7 mm = 5 mm thick septum downstream. A computer-generated view of the thin septum using a non-uniform septum cross section is given in Fig. 79. The layout of the overall assembly and the main parameters are given in Appendix H. Such a new extraction septum will be compatible with all beams using this extraction channel.

4.6.3 Open issues

The proposed design still requires a number of crucial issues to be tackled. In the following a list of the main points is presented:

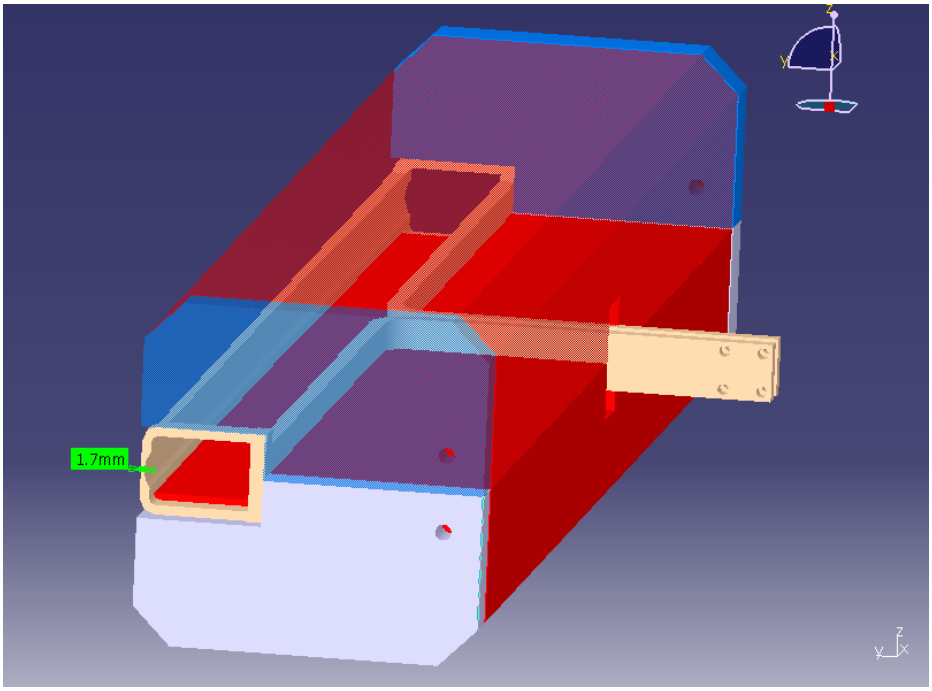

Fig. 79: Computer-generated model of the thin septum magnet

- The proposed new septum displaces the bending centre of the extracted beam by approximately 121 mm in the downstream direction. More investigations are needed to confirm that the geometry of the downstream extraction line can cope with this modification.
- The technical feasibility of the construction of a profiled septum needs to be further assessed, considering the dimensions and difficulty of machining and brazing operations involved. In this respect it is worth while noting that a thinner septum will have the side-effect that the septum will be less activated by the beam, hence reducing the amount of radiation taken by the personnel maintaining it.
- Size constraints, imposed by the coil length and the capacity of the brazing furnace, might require splitting the thick septum magnet into two magnets of half the length, electrically connected in series.
- The thin and the thick magnet must be powered by two independent power converters. Modifications to the present vacuum vessel are required to fit two high-current feedthroughs. Alternatively, new vacuum vessels could be constructed, which would increase the cost, but, at the same time, it would lower the radiation dose to the personnel during machining operations: the cost estimate is based on this observation.
- At present, the strategy would be to recover the existing SMH16 power converter to excite the thin septum magnet, and to add a more powerful one for the thick magnet. More time is needed to study the powering requirements.
- A septum of such demanding characteristics, using new techniques, normally requires an extensive prototyping phase to identify and remove potential design flaws as early as possible. Likewise, an extensive testing period should normally be foreseen to shake out weak points in the manufacturing and assembly of the components and to arrive at a reliable lifetime estimate. If sufficient time is not available for testing, there are inherent risks which can not easily be quantified, but often have serious consequences. It should be noted that the new septum

would be one-to-one compatible with the existing system, except possibly for the power converters and power connections. Therefore the old set-up may serve as a fall-back system.

Once more, it is important to stress that the option of building a new magnetic septum to replace the existing SMH16 is not part of the present proposal. However, it is clear that, in the framework of the renewed efforts of reducing the irradiation of the CERN machines, see, for example, the activity co-ordinated by the Beam Losses and Radiation Working Group, this option is rather interesting and very efficient in achieving the goal of overall reduction of beam losses and irradiation of material, which, in turn, is responsible for the dose delivered to the personnel. Hence it would be important that an appropriate body be charged with the follow-up of this proposal.

4.6.4 Cost estimate

The resources for a new power converter are not included in the estimates below. However, the material cost would be about 250 kCHF.

The material cost for three magnets (one installed system plus two spares), including new vacuum vessels, is estimated at 1.0 MCHF, including industrial support and services in various domains (design office, mechanical, electrical, vacuum, transport, etc.). A detailed cost breakdown is contained in Appendix H.3. The estimate does not include a contingency, which is proposed to be of the order of 100 kCHF.

The supply of a new septum SMH16 will require in total 3.0 man-years (1.0 man-year design and engineering, and 2.0 man-years technical construction and installation work). The total CERN staff manpower cost in terms of personnel budget is estimated at 320 kCHF.

Provided the required services, namely design office, workshop, etc., are readily available when needed, the minimum time to complete the new septum is estimated at about two years, from the launch of the design to the commissioning, including a short test period for the prototype.

Without strengthening the team, the required resources can only be made available if some of the planned consolidation work is postponed. As an example, deferring the consolidation of the BISMH (PS Booster injection septum) would make it possible to have the new SMH16 available for the start–up in 2008.

5 Resources and planning

5.1 New ring layout

The modifications of the layout of the PS ring will require the co-ordinated efforts of many specialists in different domains, namely:

- Drawing office: it will be responsible for the design of the new vacuum chambers, the modifications to the PS layout so that the drawings are always up to date and the follow-up of the production at the CERN workshops for the equipment that will be built on site. The strategy consists in producing the vacuum chambers for the straight section at CERN, while those for the main magnet units will have to be produced elsewhere. A contract for the production of vacuum chamber for the PS magnets in the framework of the activities for the renovation of the pole face windings circuits with an Italian firm has already been signed. It is then assumed that an extension of such a contract could be signed to produce the additional chambers required for the implementation of the MTE. Under this hypothesis, it is

also assumed that the follow-up of the production will be ensured by the AT/VAC Group as is the case for the present contract. Alternative strategies have been defined in order to have back-up solutions. Such a scenario would entail producing a straight chamber in the CERN workshops with the appropriate cross section and to deliver it to an outside firm to bend the chamber to fit the PS main magnet curvature.

The preferred solution will be defined in a second stage. Given these uncertainties, it was not possible to give an accurate cost estimate for the special chambers for the magnet units 14, 15 and 16. However, it is proposed to use a guess cost estimate of 100 kCHF per chamber.

As far as the enlarged, but standard vacuum chambers, for magnet units 18 and 19 are concerned, based on the price from the present contract with the Italian firm, it is possible to estimate their cost at 30 kCHF per chamber [104].

- Installation: the installation of the proposed layout would require the intervention of experienced mechanics. Of course, specific competence in the domain of vacuum would be an advantage and, in some cases, it will be mandatory. Even though it was not possible to evaluate accurately enough the resources required, a rough estimate gives two men over one complete shutdown [105], based on experience gained on the past shutdown activities. These tasks are normally under the responsibility of the AT/VAC Group.

  In order to ease the existing constraints, the proposed installation schedule for the MTE was prepared so as to fit with the LHC installation schedule, which foresees that the resources from AT/VAC should be available by the 2007/2008 shutdown.

A summary of the resources required is presented in Table 16.

Table 16: Cost estimate for the activities related to the implementation of the new layout for the PS ring. The cost of the special vacuum chambers for the magnet units 14, 15 and 16 is only a guesstimate.

	Cost (kCHF)
Drawings (design and documentation)	130.00
CERN workshops	30.00
Vacuum chambers for magnet units 18 and 19	60.00
Vacuum chambers for magnet units 14, 15 and 16	300.00
Total	520.00

5.2 Slow bump

The estimated cost to modify the converters is 115 kCHF. The cabling cost for the magnets is estimated at 60 kCHF. The magnet fault interlock system has to be modified. In case the power converter for the QKE58 could not be used as a spare converter in 2007, the cost of a new spare is 120 kCHF. Total budget details are given in Table 17.

The resources for the polarity inverters study and the complete re-arrangement of the converters is estimated to be 0.5 man-year. The additional manpower for the manufacturing of a new spare converter is 0.5 man-year.

The effective modification of the converters will take place during the 2006/2007 shutdown to allow the PS start-up in 2007 with this new configuration. We should know

whether the PR.QKE58 is needed in operation following the necessary beam studies in July 2006.

Table 17: Cost estimate for the converter modification and associated cabling

	Cost (kCHF)
Power converter modifications (FSU)	30.00
Material and documentation	25.00
DCCTs	20.00
Polarity inverter and electronics	40.00
Optional spare converter	120.00
Cabling (power converters. The estimate to be confirmed by TS)	60.00
Cabling (timing and interlocks. The estimate to be confirmed by AB/CO)	10.00
Total	305.00

5.3 Fast bump

The total material cost of the new MTE kicker system is estimated at 5.5 MCHF. A detailed cost breakdown is contained in Appendix F.5.

Items included in this estimate are

- Industrial support and services in various domains
  - design office, corresponding to 1.5 man-years;
  - mechanical;
  - electrical;
  - vacuum;
  - transport.
- Collaboration of a Project Associate (0.5 man-year).
- Dismantling and disposal of the existing SMH57 power converter in building 359 to make space for the installation of the HV power supplies for the trajectory correction system.
- A contingency of the order of 10%.

Items included, providing opportunities for savings are

- A new spare KFA79 magnet tank to replace the one used in SS13. If not implemented, then savings of 725 kCHF are available. Failure of the operational KFA79 magnet tank could result in the inability to fast-extract from the PS for LHC operation. Repairs could require up to many months if the full rebuild of magnets or vacuum tank is required. The possibility to re-use the KFA13 magnet tank in SS79 to enable fast PS extraction is feasible. However, it would still require many weeks of intervention and would render the MTE system inoperative.
- One spare pulse generator for each of the subsystems KFA13/21, KFA4, BFA9 and DFA242/243, which would allow rapid recovery (typically less than one hour) from operational failures. If longer downtime due to faults is acceptable (several days per failure) then savings up to 950 kCHF could be realized, depending on the chosen level of spare back-up.

Other cost-related considerations are

- The new MTE system is foreseen to replace the existing CT system after a period of up to one year of parallel PPM operation, after which the CT will be decommissioned. In the event that the MTE is approved, it is proposed not to carry out the otherwise planned consolidation of the existing system. Its material cost is estimated at 400 kCHF. Note that this will entail maintaining the present level of downtime and manpower-intensive maintenance of the existing CT until this system becomes obsolete. This will also require continued support from the AB/CO group of the present controls infrastructure until the system is fully decommissioned.
- An alternative, less flexible trajectory correction scheme using additional elements in the PS ring instead of TT2, would allow economies of the order of 300 kCHF.

The experienced workforce required to implement the new MTE kicker system is estimated at 11.7 man-years:

- 2.15 man-years electrical engineering
- 6.1 man-years electrical and mechanical technical work
- 3.45 man-years of other qualified mechanical and cabling work.

This does not include items like industrial support, design office work and other services as well as support from a Project Associate, which are all accounted for under material. The total CERN staff manpower cost in terms of personnel budget is estimated at about 1.2 MCHF.

By dropping the planned CT consolidation part, the manpower foreseen for this activity could be recuperated and re-allocated to the construction of the new MTE system, to an extent of about 2.5 man-years.

By delaying other consolidation activities, currently planned to start in 2007, another 1 to 1.5 man-years can be made available.

The kicker system implies an extensive engineering and design phase that needs to be terminated before the procurement of components with long lead-time (6–9 months) can be launched. To alleviate the crucial shortage of experienced electrical engineers, preventing rapid short-term progress, a kicker expert from an outside laboratory joined CERN in August 2005 as Project Associate. Unfortunately, even higher-priority work on LHC kicker magnets has limited the time he has been able to devote to the MTE study. A further three months of engineering study, in parallel with ongoing design office work, remains before long-lead procurement can begin. Together with procurement, construction, testing, installation and commissioning stages, this results in an overall minimum delay for the first phase of the project of two years; the trajectory correction phase will require a further six months implementation after validation of the first phase. This very optimistic estimate is based on the assumption that all required services (mechanical, electrical, vacuum, transport, survey, etc.) can always respond immediately when needed, which is of course not obvious because of the involvement of the same services in the LHC and other projects.

The recently approved recruitment of three technicians (two in the BT/KPS section, one in the BT/EC section) will strengthen the teams to the required level; however, the demand to bring the first phase of the system into operation in mid-2008 will stretch resources to their maximum and allows no slack in a very demanding schedule.

The results of the cost estimate and manpower requirement are listed in Table 18, while in Table 19 some additional details concerning the splitting of the manpower among various staff categories are given.

Table 18: Cost estimate for the kickers used for the fast bump around the extraction septum

	Cost (kCHF)
Kickers (material and contingency)	5500.00
CERN staff	1200.00
Total	6700.00

Table 19: Estimate of the required manpower split according to the various staff categories as a function of time

	2006	2007	2008	2009	Total
Engineer, cat. 2	0.90	0.95	0.30	0.0	2.15
Technician, cat. 3	1.60	2.15	2.15	0.2	6.10
Technician, cat. 4	0.35	1.50	1.30	0.3	3.45
Total	2.85	4.6	3.75	0.8	11.7

5.4 Auxiliary magnets

For the implementation of the MTE a number of magnets are required, namely:

- One spare quadrupole of type 406: this magnet will be required in case the scenarios with displaced magnets do not provide the same performance as the present one.
- Two special sextupoles: in case the proposed solution of moving the sextupoles used for the slow extraction is not performing well, then new sextupoles will have to be built so as to be compatible with the increased aperture foreseen for SS19. In this case, the specifications will be taken as for the present version of the PS sextupoles of type 608, but with an increased mechanical aperture in order to fit around an enlarged vacuum chamber and twice as long as the standard sextupoles. Two elements will be required, one for installation and a spare element.
- Three special octupoles: the SPS octupole used during the experimental tests performed in the past years is not adapted to the needs of the new MTE. Therefore, three new octupoles will have to be built, two for installation in SS39 and SS55 and one spare magnet. The specifications are found in Ref. [54].

For all the three magnet types the construction will require about 18 months. Hence the production of the octupoles should be launched by mid-2006, while the tests to assess the need for special sextupoles should be performed during the PS machine start-up in 2006 to allow for a fast reaction in case of need.

The configuration used in the tests of the beam splitting is based on one power converter for the octupole magnet (LOE type from the SPS machine) and one power converter for the two standard PS sextupoles placed in series. These two power converters are from the standard PS TEKELEC family. These power converters are thirty years old and are included in the CERN consolidation programme. Furthermore, two additional sextupoles and one

octupole will be installed for the MTE, thus implying that two additional power converters will be needed to supply these circuits.

DC cabling must be done between the power converters and the magnets. The cost is estimated at 40 kCHF. Re-use of existing PS cables is under investigation.

The consolidation of the TEKELEC power converters is included in the CERN consolidation programme. The design of the new power converters will be done in 2006 and the production in 2007. The replacement of the old TEKELEC will be done for the 2008 start-up, when the two additional power supplies of the new type will also be installed.

Two power converters out of the four will be charged to the consolidation project. The two new power converters will be charged to the MTE project. The cost of one power converter is 100 kCHF. The infrastructure cost is estimated at 30 kCHF per converter and the cost of the cabling from the new location (Bldg. 365) is estimated at 20 kCHF per power converter. Hence the total cost is 300 kCHF.

The resources for the design of the power converters are in the consolidation project, while 0.5 man-year will be necessary for the production, installation, and tests of the power converters.

In order to match the requirements of the slow-bump, in particular the dipole installed in SS15 and powered by a programmable device, the present TEKELEC converter can not be improved. Therefore the consolidation programmme will focus on this particular element. It is expected that with the new converter topology, the converter will follow the required pulse current waveform. The first tests, with the prototype converter, will be done during the 2007 run. The DC cabling will be renewed because it gives an extra inductance of 3 mH.

The required resources are summarized in Table 20.

Table 20: Cost estimate for the auxiliary magnets and power converters used for the new octupoles

	Cost (kCHF)
Spare quadrupole of type 406	95.00
New sextupoles	75.00
New octupoles	97.50
Power converters for new octupoles (including cables and infrastructure)	300.00
Survey	7.00
Total	574.50

5.5 RF

In the framework of the preparation of the PS ring to operate with the MTE, the AB/RF/SR section will be responsible for moving the 80 MHz cavity from SS13 to SS8. In order to accomplish this move, 33 cables that currently connect the cavity in SS13 to Bldg. 151 and Bldg. 353 must be extended to SS8, while 4 HV cables must be replaced. The special 30 kV HV cables will be fabricated specially for this purpose, so that a minimum quantity of 350 m must be bought, out of which 160 m will be used, for a total amount of 4.5 kCHF. The total cost for cables is estimated at 11.0 + 4.5 kCHF, not including the cables for the vacuum system and vacuum control.

The cost for moving the water cooling distribution system from section 13 to section 8 is estimated to be 15 kCHF maximum.

The upstream vacuum chamber flange of size 195 mm must be replaced with one of size 250 mm. In order to assure a smooth transition from the 25 mm diameter of the flange to the size of the vacuum chamber at the cavity input, the fabrication of a new piece of vacuum

chamber is proposed. The cost is estimated to be 5 kCHF. The cost of the possible modification of the cavity support has not been included in this estimate, but should be negligible. Summarizing, the total cost for material and work is estimated to be 35.5 kCHF.

The requirements in terms of additional manpower are estimated as follows:

- work of the drawing office: 20 man-hours (CERN staff);
- cavity dismantling and remounting with tests (RF): 8 man-weeks (CERN staff);
- cavity move (transport): 6 man-days (CERN staff).

This estimate must still be considered as preliminary and a +20% variation is possible when the work is done. The work of the vacuum group has not been considered here.

The required resources are summarized in Table 21.

Table 21: Cost estimate for the displacement of the 80 MHz cavity currently installed in SS13

	Cost (kCHF)
Cables	11.00
Special HV cables	4.50
Modifications of water cooling circuit	15.00
Mechanical modifications	5.00
Total	35.50

5.6 Beam instrumentation

The key modifications at the level of the beam instrumentation will be the installation of an additional wire scanner in the horizontal plane and the displacement of the measurement target from SS18 to SS68. Concerning the wire scanner, it will be operated in a similar way to the others and its control will be multiplexed, so that no simultaneous measurement of the beam profiles at the various locations in the PS ring will be available. This constraint is not felt to be critical for either the commissioning or the operation of the future MTE. Therefore the new scanner will essentially be a copy of the present hardware design [106].

Concerning the movement of the measurement target, no special issues are foreseen and the main item to be considered in the cost estimate is the price for new cables [107].

The required resources are summarized in Table 22.

Table 22: Cost estimate for the displacement of the measurement target and the installation of an additional wire scanner in the horizontal plane

	Cost (kCHF)
Installation of additional wire scanner	25.00
Consolidation of the additional wire scanner	15.00
Displacement of measurement target (cables)	13.80
Total	53.80

5.7 Controls

Some activities are required from the AB/CO Group for the extensions and changes in the control of the power converters and to provide the infrastructure for the control of the fast bump.

The control line for a pulsed power converter is composed of the MIL1553 connection to the PO crate, four timing (fore-warning, warning, start, acquisition), and one analog signal observation channel. In addition, for a programmed power converter, one channel from a function generator (GFAS) is required.

As far as the slow bump is concerned, the requirements for the Controls Group are

- One additional control line in case the power converter used for the QKE58 turns out to be mandatory for PS operation.
- Reconfiguration of the dipole interfaces, hardware and software, according to the new dipole layout. Five knobs should be generated to control the current for the magnets located in SS12, SS14, SS18, SS20, SS22.

As far as the additional elements used to generate the stable islands are concerned, the requirements for the Controls Group are

- A complete control line for the one additional programmed power converter for the sextupoles.
- A complete control line for the one additional programmed power converter for the new octupole.

This will be handled by means of an extension of the existing front-end computers, namely addition of a few interfaces and some re-cabling.

As far as the new systems for the fast bump are concerned, i.e., kickers and ERDs, the requirements for the Controls Group are

- The installation of the controls infrastructure in Bldg. 367, namely the technical network and the timing distribution.
- The installation of an observation system for the kickers' signals (OASIS). A 16-channel at 150 MHz (500 MSamples) is currently planned.

The resources required to implement these elements are under investigation, but they should amount to only few man-weeks.

The required resources are summarized in Table 23.

Table 23: Cost estimate for the controls extension

	Cost (kCHF)
Interfaces for power converters	20.00
Infrastructure in Bldg. 367	30.00
Analog signals observation	70.00
Total	120.00

Concerning the development of the dedicated application programs to control the two bumps, slow and fast, during commissioning and routine operation of the MTE, specifications will be defined by the AB/ABP Group and the implementation will be carried out by the AB/OP Group.

5.8 Beam dynamics studies

Even though the crucial issues concerning the physical process behind the beam splitting have been addressed in the experimental tests performed in the past years, nevertheless, a number of issues remain to be clarified. In particular, it is necessary to choose between the still open options outlined in the previous sections where the implementation of the MTE was described in detail. To freeze all the options, the following studies will be undertaken during the 2006 PS run:

- The proposed configuration for the sextupoles used for the slow extraction should be tested to decide whether new magnets are required.
- The proposal to get rid of the QKE58 for all the fast extractions should be tested by means of a campaign of optics measurements in the TT2/TT10 transfer line. In particular, the optical conditions at PS extraction should be measured and new optics should be computed. These steps will be crucial to deciding whether a spare power converter for the capacitor discharge elements has to be bought.
- The optics of the TT2 transfer line for the MTE should be computed. This will require a number of optics measurements to determine the extraction conditions when the PS machine is configured for the MTE operation. Investigations will be performed to assess when and under what conditions these measurements could be carried out.
- The fraction of particles trapped within the stable islands should be increased and/or the beam losses during the stage of resonance crossing should be reduced. Indeed, one of the results of the experimental campaign is that the maximum fraction of trapped particles is around 18%, but in conjunction with beam losses of 2%–3%. A series of experimental tests are scheduled to tackle this crucial topic.
- Study the gamma-jump scheme to assess whether, by using the new capabilities provided by the programmable power converter, the performance of the scheme can be maintained even when one quadrupole is moved to another straight section. This study is crucial in deciding whether new spare gamma-jump quadrupoles of type 406 (see Appendix C) are needed.

To deal with these subjects, it is estimated that two man-years (one CERN staff and one fellow) over the period 2006/2008 should be enough. It is worth noting that part of the resources will be provided by the AB/OP Group in the context of the general support to this study, while the rest is provided by AB/ABP.

5.9 Planning: installation schedule, budget, resources

An overall planning schedule is available: here are the milestones of the realization of the MTE:

- Shutdown 2004/2006:
  - Install slow extraction sextupoles in SS3, keeping those in SS19.
  - Replace magnets of slow bump 16 with type 205 magnets.
  - General clean-up of the machine.
- PS run 2006:
  - A number of MD studies are foreseen to decide the strategies for the open points outlined in the MTE description.

  - Launch production of the octupoles (May/June).
  - Complete the study of the special vacuum chambers for magnet units 14, 15, 16 and launch the production.
  - Complete the drawings for the new layout of the PS ring.
- Shutdown 2006/2007:
  - Remove slow extraction sextupoles in SS19.
  - Install new power converters for bump 16.
- PS run 2007:
  - Test the new layout of the slow bump 16 in operation.
- Shutdown 2007/2008:
  - Install kickers in the PS ring.
  - Install modified vacuum chambers (straight sections and magnets).
  - Install sextupoles and new octupoles.
  - Move 80 MHz cavity.
  - Install new wire scanner.
  - Displace DFA243 in the TT2 transfer line.
- PS run 2008:
  - Commissioning of the MTE in parallel with the CT.
- Shutdown 2008/2009:
  - Completion of the spare tanks for the KFA71/79 kicker.
  - Upgrade of kickers in TT2 line to achieve nominal performance.

It is worth while mentioning that during the 2006/2007 shutdown a number of activities related to vacuum, e.g., replacement of vacuum chambers, could be undertaken. However, it seems that no resources will be available owing to the LHC activities of the AT/VAC Group. The proposed planning could be revised in case manpower becomes available.

In terms of the required budget to accomplish the installation and commissioning of the MTE, the summary data is given in Table 24 together with the spending profile (the corresponding plot is shown in Fig. 80).

As far as the resources in terms of manpower are concerned, the situation is summarized in Table 25, where the main items are specified together with the information concerning the availability of the resources under discussion.

The situation concerning the resources is rather clear: most of the topics are covered with an appropriate level of resources, except the activity concerning the actual implementation of the new layout and the remaining beam dynamics studies. In both cases the level of support is clearly insufficient and the situation should be resolved. Even though such a situation will have to be discussed with the AT/VAC management to assess whether resources could be found, opening a post of mechanic would be a very efficient step towards improving the situation.

Also, it must be stressed that hiring a fellow to support the beam dynamics study should be considered as a top-priority objective for the forthcoming selection committee.

Table 24: Total budget required for the implementation of the MTE. The cost of the special vacuum chambers is included on the basis of a guesstimate.

Item	2006	2007	2008	2009	kCHF
Kickers: material	880.00	2190.00	2110.00	320.00	5500.00
Kickers: manpower	292.31	471.79	384.62	51.28	1200.00
Power converters (capacitor discharge)	91.50	213.50			305.00
Power converters (TEKELEC)		240.00	60.00		300.00
Drawings	130.00				130.00
Magnets: octupoles	38.50	56.50	2.50		97.50
Magnets: quadrupoles	70.00	22.50	2.50		95.00
Magnets: sextupoles	22.00	50.50	2.50		75.00
Vacuum chambers	108.00	180.00	72.00		360.00
RF		28.40	7.10		35.50
Instrumentation		31.04	7.76		53.80
Controls	24.00	84.00	12.00		120.00
Workshop	15.00	15.00			30.00
Survey		5.60	1.40		7.00
Total	1671.31	3600.83	2665.38	371.28	8308.80

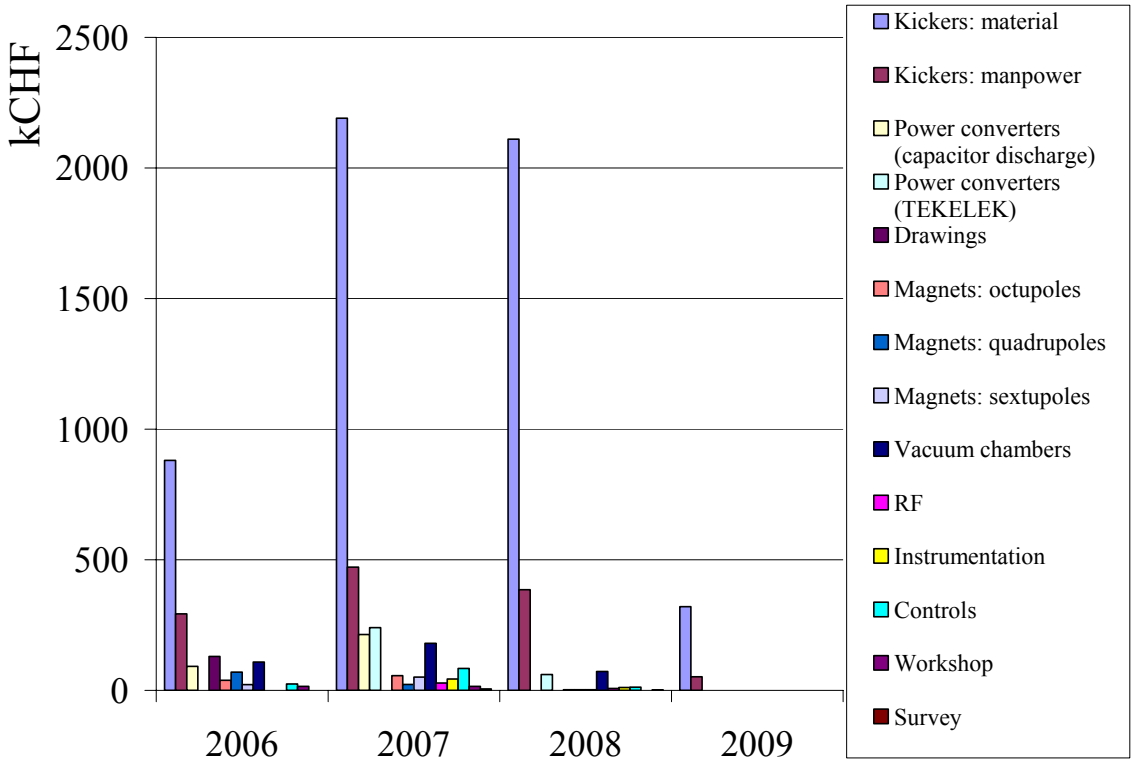

Fig. 80: Plot of the spending profile for the overall budget for MTE implementation

Table 25: Total manpower required for the implementation of the MTE, including information on its availability. The FTEs specified for the beam dynamics activities are equally shared among a CERN staff member and a fellow.

Item	FTE required	2006	2007	2008	2009	Availability
Kickers	11.7	2.85	4.6	3.75	0.8	Yes
Power converters (capacitor discharge)	0.5+0.5 [a]	0.3	0.2+0.5 [a]			Yes
Power converters (TEKELEC)	0.5	0.2	0.3			Yes
Drawings	1.3	1.3				Yes
Magnets: octupoles	0.7	0.3	0.3	0.1		No (unless 2 LD technicians get an indefinite contract in 2007)
Magnets: quadrupoles	0.6	0.3	0.3			No (unless 2 LD technicians get an indefinite contract in 2007)
Magnets: sextupoles	0.7	0.3	0.3	0.1		No (unless 2 LD technicians get an indefinite contract in 2007)
Installation	0.8	0.3	0.5			No
RF	0.2		0.2			Yes
Beam dynamics studies (CERN staff)	3	1	1	1		No (only 50% available)
Beam dynamics studies (fellow)	3	1	1	1		No

[a] Such manpower will be required in case the power converter currently used for the QKE58 cannot be modified into a spare for the elements of the new slow bump.

6 Executive summary

In the framework of the activities to prepare the future high-intensity proton beam for the CERN Neutrino to Gran Sasso (CNGS) Project, a critical review of the key processes used to generate such a beam was carried out, in view of an upgrade beyond the present nominal intensity value of about 3.3×10^{13} protons per PS batch. In this report the efforts devoted to the improvement of the present extraction scheme from PS to SPS, the so-called Continuous Transfer, are reported. Such a method, based on beam slicing onto an electrostatic septum, is affected by unavoidable losses, which have a direct impact on the machine performance (reduced intensity delivered to the experiments) as well as on the hardware integrity (damage due to material irradiation) and on personnel (radiological effects limiting, for example, the hands-on maintenance activities).

In the quest for an improved extraction mode, a novel approach was proposed. In the new scenario the beam will be separated in transverse phase space by generating stable islands inside the region where the beam sits and by slowly (adiabatically) moving them towards higher amplitudes. In this way particles may get trapped inside islands thus generating well-separated beamlets. This method is potentially superior to the present one as no intercepting device is used to split the beam; hence particle losses are limited to the fraction of the beam improperly deflected during the kicker rise time. Furthermore, the extracted beam should better match the phase space structure. Following the encouraging results of the numerical simulations, a measurement campaign on the PS machine was launched in 2002 and continued throughout the whole of 2004, just before the long shutdown of the CERN PS and SPS machines. A Study Group was set up with the following mandate:

- demonstrate the feasibility of the scheme;
- investigate the various technical issues;
- evaluate the resources required to define and specify a possible project to replace the present Continuous Transfer.

Progress was reported at the AB Management Board on three occasions and the study for the Multi-Turn Extraction (MTE) was also part of the activities covered by the Beam Losses and Radiation Working Group (BLRWG).

By the beginning of the year 2006, a coherent scheme for the implementation of the MTE was completed. The proposed layout foresees

- changes in the slow bump around the magnetic septum in straight section 16;
- new kickers installed in straight section 4, 13 and 21 to create a fast bump around the magnetic septum in straight section 16;
- modification of the vacuum chambers, in particular around the extraction region, to remove aperture bottlenecks.

The boundary conditions for these studies were set by the principle of recuperating, as much as possible, existing hardware, to alleviate the need of resources and to fit within the structure of the existing PS ring.

It is worth mentioning that the proposed layout required the verification of the impedance of the new kickers to assess whether this might have an adverse impact on the beam stability.

The analysis of the proposed solution showed that from a technical point of view it is sound and should guarantee a better performance than the present extraction scheme.

In terms of resources, a detailed analysis was undertaken to assess the needs, both in terms of manpower and money.

The main results are reported in the following table, where the estimated cost for the various items required to carry out the modifications to the PS ring are listed. At the same time, the spending profile, which is an important piece of information in the decision-making process, is given.

Item	2006	2007	2008	2009	kCHF
Kickers: material	880.00	2190.00	2110.00	320.00	5500.00
Kickers: manpower	292.31	471.79	384.62	51.28	1200.00
Power converters (capacitor discharge)	91.50	213.50			305.00
Power converters (TEKELEC)		240.00	60.00		300.00
Drawings	130.00				130.00
Magnets: octupoles	38.50	56.50	2.50		97.50
Magnets: quadrupoles	70.00	22.50	2.50		95.00
Magnets: sextupoles	22.00	50.50	2.50		75.00
Vacuum chambers	108.00	180.00	72.00		360.00
RF		28.40	7.10		35.50
Instrumentation		31.04	7.76		53.80
Controls	24.00	84.00	12.00		120.00
Workshop	15.00	15.00			30.00
Survey		5.60	1.40		7.00
Total	1671.31	3600.83	2665.38	371.28	8308.80

The same data are shown in the following figure.

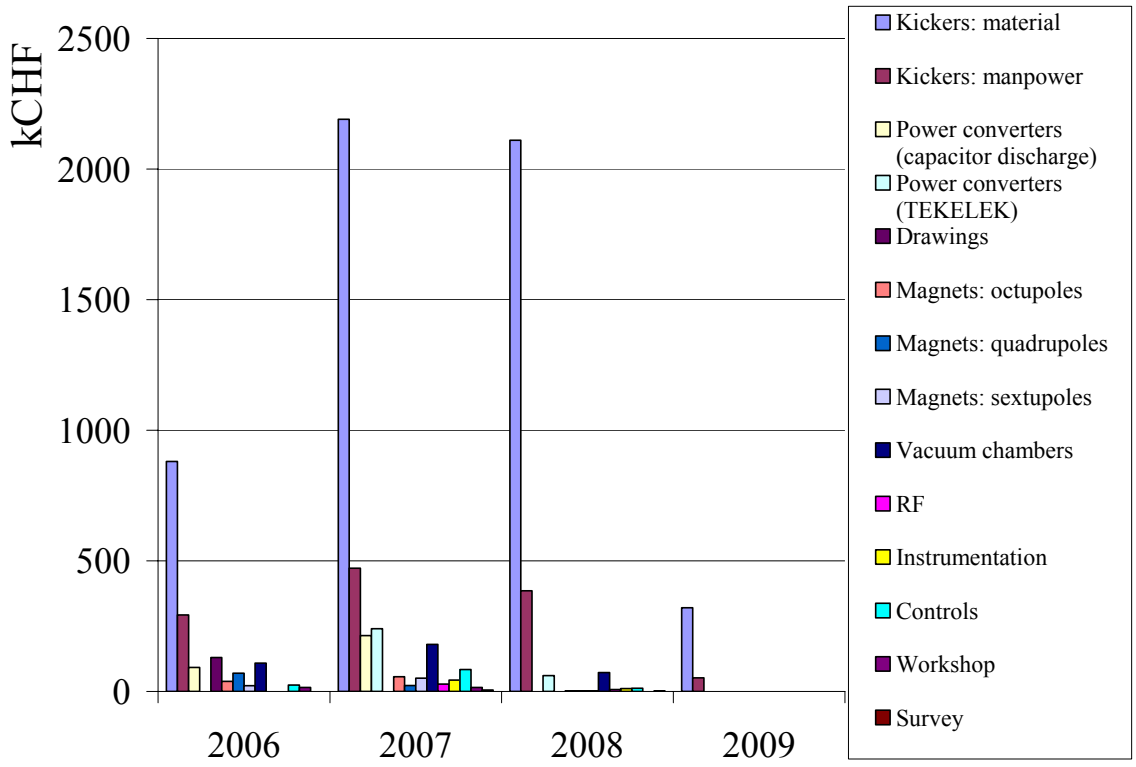

To complete the picture, the situation concerning the required manpower is reported in the next table, where the information concerning the availability of such manpower is also mentioned.

Item	FTE required	2006	2007	2008	2009	Availability
Kickers	11.7	2.85	4.6	3.75	0.8	Yes
Power converters (capacitor discharge)	0.5+0.5 [a]	0.3	0.2+0.5 [a]			Yes
Power converters (TEKELEC)	0.5	0.2	0.3			Yes
Drawings	1.3	1.3				Yes
Magnets: octupoles	0.7	0.3	0.3	0.1		No (unless 2 LD technicians get an indefinite contract in 2007)
Magnets: quadrupoles	0.6	0.3	0.3			No (unless 2 LD technicians get an indefinite contract in 2007)
Magnets: sextupoles	0.7	0.3	0.3	0.1		No (unless 2 LD technicians get an indefinite contract in 2007)
Installation	0.8	0.3	0.5			No
RF	0.2		0.2			Yes
Beam dynamics studies (CERN staff)	3	1	1	1		No (only 50% available)
Beam dynamics studies (fellow)	3	1	1	1		No

[a] Such manpower will be required in case the power converter currently used for the QKE58 cannot be modified into a spare for the elements of the new slow bump.

Some additional comments are necessary:

- The implementation of the MTE will require substantial modifications in a large fraction of the PS circumference. For this activity a strong technical support, in particular in the fields of vacuum and mechanics, will be required.
- A similar issue holds also for the follow-up of the contract for the construction of the special vacuum chamber, which was normally ensured by vacuum specialists.
- As far as the kickers are concerned, these devices make the bulk of the MTE, in particular in terms of resources (money and manpower). The situation, in particular in terms of time scale, seems to be tight, but not impossible to meet, provided that the required resources are made available rather quickly.
- The additional beam dynamics studies will require the contribution from one fellow over a period of three years and there will be still some missing resources.

6.1 Planning: installation schedule, budget, resources

An overall planning schedule is available, while a detailed one will be prepared in the next weeks. Here are the milestones of the realization of the MTE:

- Shutdown 2004/2006:
  - Install slow extraction sextupoles in SS3, keeping those in SS19.
  - Replace magnets of slow bump 16 with type 205 magnets.
  - General clean-up of the machine.
- PS run 2006:
  - A number of MD studies are foreseen to decide the strategies for the open points outlined in the MTE description.
  - Launch production of the octupoles (May/June).
  - Complete the study of the special vacuum chambers for magnet units 14, 15, 16 and launch the production.
  - Complete the drawings for the new layout of the PS ring.
- Shutdown 2006/2007:
  - Remove slow extraction sextupoles in SS19.
  - Install new power converters for bump 16.
- PS run 2007:
  - Test the new layout of the slow bump 16 in operation.
- Shutdown 2007/2008:
  - Install kickers in the PS ring.
  - Install modified vacuum chambers (straight sections and magnets).
  - Install sextupoles and new octupoles.
  - Move 80 MHz cavity.
  - Install new wire scanner.
  - Displace DFA243 in the TT2 transfer line.
- PS run 2008:
  - Commissioning of the MTE in parallel with the CT.
- Shutdown 2008/2009:
  - Completion of the spare tanks for the KFA71/79 kicker.
  - Upgrade of kickers in TT2 line to achieve nominal performance.

It is worth while mentioning that during the 2006/2007 shutdown a number of activities related to vacuum, e.g., replacement of vacuum chamber, could be undertaken. However, it seems that no resources will be available owing to the LHC activities of the AT/VAC Group. The proposed planning schedule could be revised in case manpower becomes available.

Acknowledgements

Many persons were involved in the studies of the novel multi-turn extraction. We are particularly indebted to R. Cappi, who is indeed the originator of the proposal to use stable resonances in the transverse phase space to split the beam. J.-P. Riunaud had a key role in supporting and encouraging the research during the long period of experimental tests and numerical simulations. The numerous fruitful discussions with G. Arduini, R. Garoby and F. Ruggiero were a source of inspiration. We would like to express our gratitude to O. Aberle, S. Baird, C. Bal, D. Cornuet, B. Dehning, J. Hansen, E. Jensen, J. Koopman, and E. Mahner for their help during these years. Last but not least, we would like to acknowledge the support of the OP crew during the many MD sessions on the PS machine as well as the contribution of M. Benedikt and M. Chanel for preparing the PS-Booster beams and S. Hancock for support with the longitudinal beam dynamics in the PS.

References

[1] K. Elsener (Ed.) *et al.*, The CERN Neutrino Beam to Gran Sasso (Conceptual Technical Design), CERN 98-02 (1998).

[2] R. Cappi (Ed.), K. Cornelis, J.-P. Delahaye, R. Garoby, H. Haseroth, K. Hübner, T. Linnecar, S. Myers, K. Schindl, C. Wyss, Increasing proton intensity of PS and SPS, CERN-PS (AE) 2001-041 (2001).

[3] C. Bovet, D. Fiander, L. Henny, A. Krusche, G. Plass, The fast shaving ejection for beam transfer from the CPS to the CERN 300 GeV machine, *in* 1973 Particle Accelerator Conference, edited by D. W. Dupen (IEEE, New York, 1973), p. 438.

[4] L. R. Evans, A phase plane exchange section for the SPS antiproton injection beam line, CERN SPS (DI) 80-2 (1980).

[5] Home page of the High Intensity Protons Working Group, http://ab-div.web.cern.ch/ab-div/Projects/hip/.

[6] M. Benedikt, Estimation of beam losses for nominal CNGS operation, see http://ab-div.web.cern.ch/ab-div/Projects/hip/Presentations/HIP-20Oct03-MBenedikt.pdf.

[7] R. Cappi, M. Giovannozzi, Novel method for multi-turn extraction: trapping charged particles in islands of phase space, Phys. Rev. Lett. **88** (2002) 104801.

[8] R. Cappi and M. Giovannozzi, Novel method for multi-turn extraction: trapping charged particles in islands of phase space, *in* Eighth European Particle Accelerator Conference, edited by J. Poole and C. Petit-Jean-Genaz (Institute of Physics, Bristol, 2002), p. 1250.

[9] Minutes of the AB Management Board meeting held on 30.06.2003, http://ab-div.web.cern.ch/ab-div/Meetings/ABMB/2003/20030630.html.

[10] O. E. Berrig, J Borburgh, J.-P. Burnet, R. Cappi, M. Giovannozzi (Ed.), W. Kalbreier, M. Martini, A.-S. Müller, E. Métral, K.-D. Metzmacher, J.-P. Riunaud, A. Sakumi, P. Scaramuzzi, L. Sermeus, R. Steerenberg, T. Zickler, Report of the Study Group on the new multi-turn extraction in the PS machine, CERN-AB-2004-003-ABP (2004).

[11] M. Giovannozzi, Preliminary results of the MDs on the adiabatic capture of particles in stable islands, APC presentation, August 13 2004, http://ab-div.web.cern.ch/ab-div/Meetings/APC/2004/apc040813/apc040813.html.

[12] M. Giovannozzi, Final results of the studies for the new PS multi-turn extraction, APC presentation, 4 December 2003, http://ab-div.web.cern.ch/ab-div/Meetings/APC/2004/apc041203/apc041203.html.

[13] M. Giovannozzi, R. Cappi, S. Gilardoni, M. Martini, E. Métral, R. Steerenberg, A.-S. Müller, Final results from the novel multiturn extraction studies at CERN proton synchrotron, *in* 2005 Particle Accelerator Conference, edited by C. Horak (IEEE Computer Society Press, Piscataway, 2006), p. 117.

[14] S. Gilardoni and M. Giovannozzi, Additional modifications to the PS for the multi-turn extraction, APC presentation, 12 December 2005, http://ab-div.web.cern.ch/ab-div/Meetings/APC/2005/apc050414/minutes_050414.html.

[15] M. Giovannozzi, Another modification in the PS ring for the multi for the multi-turn extraction turn extraction, APC presentation, 25 August 2005, http://ab-div.web.cern.ch/ab-div/Meetings/APC/2005/apc050825/minutes_050825.html.

[16] M. Giovannozzi, Additional modifications to the PS for the multi-turn extraction, APC presentation, 8 December 2005, http://ab-div.web.cern.ch/ab-div/Meetings/APC/2005/apc051208/minutes_051208.html.

[17] M. Giovannozzi, Summary of studies on PS multiturn extraction, ABMB presentation, 6 December 2004, http://ab-div.web.cern.ch/ab-div/Meetings/ABMB/2004/20041206.html.
[18] M. Giovannozzi, Summary of studies on PS multiturn extraction in the year 2005, ABMB presentation, 30 January 2006, http://ab-div.web.cern.ch/ab-div/Meetings/ABMB/2006/20060130.html.
[19] G. Arduini (Ed.), M. Benedikt, D. Forkel-Wirth, M. Giovannozzi, B. Goddard, C. Hill, E. Métral (Ed.), T. Otto, E. Shaposhnikova, H. Vince, Report of the Beam Losses and Radiation Working Group, in preparation.
[20] D. Manglunki, Various aspects of continuous transfer PS–SPS, http://ab-div.web.cern.ch/ab-div/Projects/hip/Presentations/HIP-07May03-DManglunki.ppt.
[21] R. Cappi and M. Giovannozzi, Computation of betatron mismatch and emittance blow-up for multi-turn extraction, CERN-PS (AE) 2002-083 (2002).
[22] P. J. Bryant, K. Johnsen, *Circular Accelerators and Storage Rin*gs (Cambridge University Press, NY, 1993).
[23] A. W. Chao, M. Tigner, *Handbook of Accelerator Physics and Engineering* (World Scientific, Singapore, 1999), p.253.
[24] E. Courant and H. Snyder, Theory of the alternating-gradient synchrotron, Ann. Phys. (NY) **3** (1958), 1.
[25] J. Buon, Beam phase space and emittance, CERN 94-01 (1994), p. 89.
[26] A. W. Chao, M. Tigner, *Handbook of Accelerator Physics and Engineering* (World Scientific, Singapore, 1999), p. 576.
[27] R. Steerenberg, Transverse emittance as a function of proton beam intensity, CERN PS Note 2000-13 (OP) (2000).
[28] M. Giovannozzi, Comparison of extraction losses for present CT and novel multi-turn extraction, APC meeting 8 February 2005, http://ab-div.web.cern.ch/ab-div/Meetings/APC/2005/apc050407/minutes_050407.html.
[29] M. Giovannozzi, Follow-up of Comparison of extraction losses for present CT and novel multi-turn extraction, APC meeting 14 April 2005, http://ab-div.web.cern.ch/ab-div/Meetings/APC/2005/apc050414/minutes_050414.html.
[30] J. Borbourgh, private communication (2005).
[31] R. Steerenberg, private communication (2005).
[32] R. Cappi, M. Giovannozzi, M. Martini, E. Métral, G. Métral, R. Steerenberg, A.-S. Müller, Optics studies for the CERN proton synchrotron machine: linear and nonlinear modelling using beam based measurements, *in* 2003 Particle Accelerator Conference, edited by J. Chew, P. Lucas and S. Webber (IEEE Computer Society Press, Piscataway, 2003), p. 2913.
[33] E. Métral, Will PS and SPS be ready for CNGS start-up in 2006?, Workshop PS/SPS Days, 2005, http://indico.cern.ch/materialDisplay.py?contribId=12&sessionId=4&materialId=slides&confId=046.
[34] J. Borbourgh, private communication (2005).
[35] R. Cappi, M. Giovannozzi, Adiabatic capture of charged particles in stable islands: a novel approach to multi-turn extraction, *in* 2003 Particle Accelerator Conference, edited by J. Chew, P. Lucas and S. Webber (IEEE Computer Society Press, Piscataway, 2003), p. 2910, 2003.
[36] M. Giovannozzi, R. Cappi, S. Gilardoni, M. Martini, E. Métral, A. S. Müller, P. Scaramuzzi, R. Steerenberg, Multiturn extraction based on trapping in stable islands, CERN-AB-2004-095 (2004).

[37] A. Bazzani, G. Servizi, E. Todesco, G. Turchetti, A normal form approach to the theory of nonlinear betatronic motion, CERN Report, 94-02 (1994).
[38] R. Cappi, M. Giovannozzi, Multi-turn extraction and injection by means of adiabatic capture in stable islands of phase space, Phys. Rev. ST Accel. Beams **7** (2003) 024001.
[39] M. Giovannozzi, P. Scaramuzzi, Nonlinear dynamics studies at the CERN proton synchrotron: precise measurements of islands parameters for the novel multi-turn extraction, *in* Ninth European Particle Accelerator Conference, edited by J. Poole and C. Petit-Jean-Genaz (Institute of Physics, Bristol, 2004), p. 1861.
[40] M. Giovannozzi, J. Morel, A novel technique for multiturn injection in a circular accelerator using stable islands in transverse phase space, in preparation.
[41] O. Brüning, F. Willeke, Diffusion-like processes in proton storage rings due to the combined effect of non-linear fields and modulational effects with more than one frequency, proceedings of 4th European Particle Accelerator Conference, edited by V. Suller and Ch. Petit-Jean-Genaz (World Scientific, Singapore, 1994), p. 991.
[42] F. Zimmermann, Comparison of calculated with measured dynamic aperture, proceedings of 4th European Particle Accelerator Conference, London, UK, edited by V. Suller and Ch. Petit-Jean-Genaz (World Scientific, Singapore, 1994), p. 327.
[43] W. Fischer, M. Giovannozzi and F. Schmidt, Dynamic aperture experiment at a synchrotron, Phys. Rev. E **55** (1997) 3507.
[44] A. J. Lichtenberg, M. A. Lieberman, *Regular and Chaotic Motion* (Springer Verlag, Berlin, 1998).
[45] R. Cappi, M. Giovannozzi, M. Martini, E. Métral, G. Métral, A. S. Müller, R. Steerenberg, Adiabatic beam trapping in stable islands of transverse phase space: measurement results at CERN proton synchrotron, *in* 2003 Particle Accelerator Conference, edited by J. Chew, P. Lucas and S. Webber (IEEE Computer Society Press, Piscataway, 2003), p. 388.
[46] M. Giovannozzi, R. Cappi, S. Gilardoni, M. Martini, E. Métral, A. S. Müller, A. Sakumi, R. Steerenberg, Multiturn extraction based on trapping in stable islands at CERN PS: recent measurement advances, *in* Ninth European Particle Accelerator Conference, edited by J. Poole and C. Petit-Jean-Genaz (Institute of Physics, Bristol, 2004), p. 173.
[47] M. Giovannozzi for the PS Multi-Turn Extraction Study Group, Recent advances on the multi-turn extraction using stable islands of transverse phase space, ICFA Beam Dynamics Newsletter, No. 36 (2005) p. 43.
[48] S. Gilardoni, M. Giovannozzi, M. Martini, E. Métral, A. S. Müller, R. Steerenberg, Experimental evidence of adiabatic splitting of charged particle beams using stable islands of transverse phase space, in preparation.
[49] M. E. Angoletta, A. S. Müller, A multiturn measurement system for the CERN PS, *in* Eighth European Particle Accelerator Conference, edited by J. Poole and C. Petit-Jean-Genaz (Institute of Physics, Bristol, 2002), p. 1948.
[50] M. E. Angoletta, M. Giovannozzi, M. Martini, E. Métral, G. Métral, A. S. Müller, R. Steerenberg, Analysis of multi-turn beam position measurements in the CERN PS, *in* Eighth European Particle Accelerator Conference, edited by J. Poole and C. Petit-Jean-Genaz (Institute of Physics, Bristol, 2002), p. 1273.
[51] C. Steinbach, M. Van Rooij, A scanning wire beam profile monitor, IEEE Trans. Nucl. Sci. **32** (1985) 1920.
[52] T. Satogata, *et al.*, Driven response of a trapped particle beam, Phys. Rev. Lett. **68** (1992) 1838.

[53] C. Bovet, R. Jung, A new diagnostic for betatron phase space matching at injection into a circular accelerator, LHC Project Report 3, June 1996.
[54] B. Langenbeck, Design report of a compact octupole for the Proton Synchrotron, EDMS Document No. 440042 (2004).
[55] C. Steinbach, H. Stucki, M. Thivent, The new slow extraction system of the CERN PS, CERN-PS-93-28-OP (1993).
[56] R. Cappi, L. Durieu, M. Martini, J.-P. Riunaud, C. Steinbach, Fast extracted proton beams at low energies in the CPS east experimental area, CERN-PS-95-18 (1995).
[57] A. Chapman-Hatchett, A. Jansson, D. J. Williams, A magnetic quadrupole pick-up for the CERN PS, CERN-PS-99-030-OP.
[58] A. Jansson, M. Lindroos, L. Søby, D. J. Williams, Measurements with the magnetic quadrupole pick-up in the CERN PS, CERN-PS-2000-020-OP.
[59] A. Jansson, D. J. Williams, A new optimised quadrupole pick-up design using magnetic coupling, Nucl. Instrum. Methods Phys. Res. **A 479** (2002) 233.
[60] A. Jansson, Non-invasive single-bunch matching and emittance monitor, Phys. Rev. Spec. Top. Accel. Beams, **5** (2002) 072803.
[61] A. Jansson, The magnetic quadrupole pick-ups in the CERN PS, CERN-PS-2002-050-OP (2002).
[62] S. Hancock, M. Morvillo and E. Shaposhnikova, APC Presentations, 7 April 2005, http://ab-div.web.cern.ch/ab-div/Meetings/APC/2005/apc050407/minutes_050407.html.
[63] R. Garoby, Bunch merging and splitting techniques in the injectors for high energy hadron colliders, CERN-PS-98-048-RF (1998).
[64] A. Blas *et al.*, The PS complex as proton pre-injector for the LHC: design and implementation report, CERN-2000-003 (2000).
[65] M. Benedikt (Ed.) *et al.*, LHC Design Report v.3: the LHC Injector Chain, CERN-2004-003-V-3 (2003).
[66] O. Barbalat, Specification provisoire pour quadrupoles compacts de haute energie pour sections paires, MPS/DL-Note 68-22 (1968).
[67] W. Hardt, How to pass transition in the CPS at high intensity? Part 1, CERN-MPS-DL 70-16 (1970).
[68] W. Hardt, A. Sørenssen, How to pass transition in the CPS at high intensity? Part 2, CERN-MPS-DL 71-6 (1971).
[69] W. Hardt, A. Sørenssen, How to pass transition in the CPS at high intensity? Part 3, CERN-MPS-DL 71-7 (1971).
[70] H. Schonauer, Lens configurations for the CPS to provide a large and fast gamma transition jump without Q-change, CERN/MPS/DL 72-7 (1972).
[71] A. Sørenssen, Crossing the phase transition in strong focusing proton synchrotrons, CERN-MPS-DL 73-9 (1973).
[72] W. Hardt, Gamma transition jump scheme of the CPS, CERN/MPS DL 74-3 (1974).
[73] G. Arduini, G. Crockford, M. Giovannozzi, K. Hanke, D. Manglunki, M. Martini, G. Métral, C. Niquille, TT2/TT10 transfer line studies for the 14 GeV/*c* continuous transfer, SL-Note-99-013-MD (1999).
[74] G. Arduini, Y. Chao, M. Giovannozzi, J. T. Klem, D. Jacquet, D. Manglunki, M. Martini, G. Métral, F. Roncarolo, Summary of the TT2/TT10 transfer line studies in the years 2001 and 2002, AB-Note-2003-086-ABP (2003).
[75] M. Tardy, Nouvelles corrections des chambres à vide installées dans le PS pendant l'arrêt 1987, PS/PSR/Note 87-7 (1987).

[76] J. Ottaviani, Aimants PS circuits auxiliaires des PFW: utilisation des pick-up et boucles de tours selon les types de corrections, AB-PO-Note 2005-007 (2005).
[77] M. Martini, MD results on passive circuits of PS magnets, APC presentation, 19 September 2003, http://ab-div.web.cern.ch/ab-div/Meetings/APC/2003/apc190903/martini.pdf
[78] H. Hereward and A. Sørenssen, Longitudinal blow up of the bunches at transition caused by coupling between synchrotron oscillations and betatron oscillations, MPS 68-3 (1968).
[79] W. Hardt, G. Merle, A. Sørensen, L. Thorndahl, Experimental verification of the Q-jump method for passing transition with dense beams, CERN-ISR-300-GS-LI-69-26-REV (1969).
[80] W. Hardt and D. Mohl, Q-Jump at transition, CERN-ISR-300/GS/69-16 (1969).
[81] L. Thorndahl, Q-Jump pulser for transition experiment, ISR-300/LI/69-38 (1969).
[82] T. Risselada, Gamma transition jump scheme, *in* CAS - CERN Accelerator School, 5th General Accelerator Physics Course, 1992, CERN-94-01, p. 313.
[83] M. Martini, private communication (2005).
[84] S. Gilardoni and M. Giovannozzi, Additional modifications to the PS for the multi-turn extraction, APC presentation, 12 December 2005.
[85] E. Métral, private communication (2005).
[86] Ferroxcube home page, http://www.ferroxcube.com/.
[87] KPS - Fast Pulsed Magnets, PS Complex home page, http://ab-div-bt.web.cern.ch/ab-div-bt/Sections/KPS/
[88] A. Burov and V. Danilov, Suppression of transverse bunch instabilities by asymmetries in the chamber geometry, Phys. Rev. Lett. **82** (1999) 2286.
[89] A.W. Chao, *Physics of Collective Beam Instabilities in High Energy Accelerators* (Wiley, New York, 1993).
[90] Ansoft home page, www.ansoft.com.
[91] F. Caspers *et al.*, Kicker impedance measurements for the future multi-turn extraction of the CERN Proton Synchrotron, presented at EPAC2006, Edinburgh, UK, 26-30 June 2006.
[92] H. Tsutsui, On single wire technique for transverse coupling impedance measurement, CERN-SL-Note-2002-034 AP (2002).
[93] H. Tsutsui, Some simplified models of ferrite kicker magnet for calculation of longitudinal coupling impedance, CERN-SL-2000-004 AP (2000).
[94] H. Tsutsui and L. Vos, Transverse coupling impedance of a simplified ferrite kicker magnet model, LHC Project Note 234 (2000).
[95] A. Burov and V. Lebedev, Transverse resistive wall impedance for multi-layer round chambers, *in* Eighth European Particle Accelerator Conference, edited by J. Poole and C. Petit-Jean-Genaz (Institute of Physics, Bristol, 2002), p. 1452.
[96] A. Burov and V. Lebedev, Transverse resistive wall impedance for multi-layer flat chambers, *in* Eighth European Particle Accelerator Conference, edited by J. Poole and C. Petit-Jean-Genaz (Institute of Physics, Bristol, 2002), p. 1455.
[97] A. Burov, Transverse impedance of ferrite elements, LHC Project Note 353 (revised) (2004).
[98] R. Cappi, M. Martini, T. Risselada, J.-P. Riunaud, D. Trione, Recent studies on transverse beam behaviour at the CERN PS, CERN/PS 89-39 (PA) (1989).
[99] S. Hancock, private communication (2005).
[100] S. Hancock and E. Métral, Ghost bunches and blow-up losses with high intensity beams, PS/RF Note 2002-198 (2002).

[101] G. Rumolo and F. Zimmermann, Practical User Guide for HEADTAIL, CERN-SL-Note-2002-036 AP (2002).
[102] E. Métral, Impedance measurements in PS, PPC presentation, 14 December 2001, http://psdoc.web.cern.ch/PSdoc/ppc/ppc011214/ppc011214.html.
[103] S. Hancock, LHC Beams in the PS: reliability and reproducibility issues, CERN-AB-2003-008 ADM, p. 38 (2003).
[104] J. Hansen, private communication (2005).
[105] E. Mahner, private communication (2005).
[106] B. Dehning, private communication (2005).
[107] C. Bal, private communication (2005).

Appendix A: Characteristics of the slow bump dipoles

Table A.1: Main parameters of high-energy dipole type 205

Mechanical properties			
	Magnet structure separable in two halves		
	Rectangular aperture h × v	(enlarged)	200 mm × 86 mm
	Overall size		
		Vertical	520 mm
		Horizontal	–
		Longitudinal	249 mm
	Weight		400 kg
	Thickness of laminations		1 mm
	Iron length		137 mm
	No. of windings/pole		48
	Cross section of copper conductor		6 mm × 6 mm
	Diameter of cooling hole		3.5 mm
	Total copper cross section		26 mm^2
Electrical properties			
	Inductance	(0–50 Hz)	6.3 mH
		(1000 Hz)	4.9 mH
	Resistance (20°C)		80 mΩ
	Max. I_{eff} at 25°C and ΔP = 10 bar		215 A
	V_{max} between coils	(test)	70 V
		(nominal)	40 V
	V_{max} between coils and ground	(test)	5 kV (rms)
		(nominal)	3 kV (DC)
Magnetic properties			
	Magnetic length		230 mm
	$\int B dl$ at I = 100 A		30 mT m
	Limit of magnetic linearity		700 A
Cooling			
	Coolant		Demineralized water
	Nominal flow for ΔP = 10 bar		2.8 l/min
	Test pressure		40 bar
References			
	Magnet design		MPS/SM/Spec 74-2
	Magnetic measurements		PS/SM/Note 76-11
	Magnet drawings		64A41.1 (TESLA)
	Support drawings		4C18.400.2

Table A.2: Main parameters of high-energy dipole type 206

Mechanical properties			
	Magnet structure separable in two halves		
	Rectangular aperture h × v	(standard)	162 mm × 82 mm
	Overall size		
		Vertical	418 mm
		Horizontal	–
		Longitudinal	296 mm
	Weight		400 kg
	Thickness of laminations		1 mm
	Iron length		190 mm
	No. of windings/pole		40
	Cross section of copper conductor		7 mm × 7 mm
	Diameter of cooling hole		3.5 mm
	Total copper cross section		38 mm^2
Electrical properties			
	Inductance	(0–50 Hz)	6.1 mH
		(1000 Hz)	5.24 mH
	Resistance (20°C)		136 mΩ
	Max. I_{eff} at 25°C and ΔP = 10 bar		250 A
	V_{max} between coils	(test)	70 V
		(nominal)	40 V
	V_{max} between coils and ground	(test)	5 kV (rms)
		(nominal)	3 kV (DC)
Magnetic properties			
	Magnetic length		270 mm
	$\int B dl$ at I = 100 A		32 mT m
	Limit of magnetic linearity		850 A
Cooling			
	Coolant		Demineralized water
	Nominal flow for ΔP = 10 bar		6.5 l/min
	Test pressure		40 bar
References			
	Magnet design		MPS/SM/Spec 69-2
	Magnetic measurements		–
	Magnet drawings		4A14.004.0
	Support drawings		4A14.600.3

Table A.3: Main parameters of high-energy dipole type 210

Mechanical properties			
	Magnet structure not separable in two halves		
	Rectangular aperture h × v	(standard)	160 mm × 80 mm
	Overall size		
		Vertical	–
		Horizontal	–
		Longitudinal	300 mm
	Weight		390 kg
	Thickness of laminations		1 mm
	Iron length		250 mm
	No. of windings/pole		32
	Cross section of copper conductor		8.5 mm × 8.5 mm
	Diameter of cooling hole		5 mm
	Total copper cross section		50 mm^2
Electrical properties			
	Inductance	(0–50 Hz)	4.3 mH
		(1000 Hz)	3.12 mH
	Resistance (20°C)		29 mΩ
	Max. I_{eff} at 25°C and ΔP = 10 bar		600 A
	V_{max} between coils	(test)	35 V
		(nominal)	40 V
	V_{max} between coils and ground	(test)	5 kV (rms)
		(nominal)	3 kV (DC)
Magnetic properties			
	Magnetic length		300 mm
	$\int B\mathrm{d}l$ at I = 100 A		29 mT m
	Limit of magnetic linearity		850 A
Cooling			
	Coolant		Demineralized water
	Nominal flow for ΔP = 10 bar		7 l/min
	Test pressure		40 bar
References			
	Magnet design		SI/int.MAE/68-9
	Magnetic measurements		–
	Magnet drawings		28.3393.0
	Support drawings		4C02.800.3

Appendix B: Characteristics of quadrupoles of the quadrupole kick enhancement scheme

Table B.1: Main parameters of quadrupole for kick enhancement type 414

Mechanical properties			
	Magnet structure separable in two halves		
	Diameter inscribed circle	(enlarged)	146 mm
	Overall size		
		Vertical	570 mm
		Horizontal	911 mm
		Longitudinal	300 mm
	Weight		–
	Thickness of laminations		1 mm
	Iron length		200 mm
	No. of windings/pole		12
	Cross section of copper conductor		7 mm × 7 mm
	Diameter of cooling hole		4 mm
	Total copper cross section		30.4 mm^2
Electrical properties			
	Inductance	(0–50 Hz)	1.1 mH
		(1000 Hz)	1 mH
	Resistance (20°C)		16 mΩ
	Max. I_{eff} at 25°C and ΔP = 10 bar		–
	V_{max} between coils	(test)	350 V
		(nominal)	100 V
	V_{max} between coils and ground	(test)	5 kV (rms)
		(nominal)	2 kV (max.)
Magnetic properties			
	Magnetic length		–
	$\int G dl$ at I = 100 A		150 mT
	Limit of magnetic linearity		2000 A
Cooling			
	Coolant		Demineralized water
	Nominal flow for ΔP = 10 bar		5.5 l/min
	Test pressure		40 bar
References			
	Magnet design		–
	Magnetic measurements		–
	Magnet drawings		4C19.000.1A
	Support drawings		4C08.100.2

Appendix C: Characteristics of quadrupoles of the gamma-jump scheme

Table C.1: Main parameters of quadrupole for gamma-jump scheme type 406 (doublet)

Mechanical properties			
	Magnet structure separable in two halves		
	Diameter inscribed circle	(enlarged)	146 mm
	Overall size		
		Vertical	566 mm
		Horizontal	845 mm
		Longitudinal	224 mm
	Weight		400 kg
	Thickness of laminations		1 mm
	Iron length		128 mm
	No. of windings/pole		12
	Diameter of copper conductor		3.3 mm
	Diameter of cooling hole		–
	Total copper cross section (7 conductors)		59 mm^2
Electrical properties			
	Inductance	(0–50 Hz)	0.55 mH
		(1000 Hz)	–
	Resistance (20°C)		17 mΩ
	Max. I_{eff} at 25°C and ΔP = 10 bar		60 A
	V_{max} between coils	(test)	100 V
		(nominal)	50 V
	V_{max} between coils and ground	(test)	10 kV (DC)
		(nominal)	4 kV (DC)
Magnetic properties			
	Magnetic length		191 mm
	$\int G\mathrm{d}l$ at I = 100 A		113 mT
	Limit of magnetic linearity		320 A
Cooling			
	Coolant		Air
	Nominal flow for ΔP = 10 bar		–
	Test pressure		–
References			
	Magnet design		–
	Magnetic measurements		–
	Magnet drawings		4C13.000.1
	Support drawings		4C14.200.2

Table C.2: Main parameters of quadrupole for gamma-jump scheme type 407 (triplet)

Mechanical properties			
	Magnet structure separable in two halves		
	Diameter inscribed circle	(enlarged)	146 mm
	Overall size		
		Vertical	570 mm
		Horizontal	960 mm
		Longitudinal	236 mm
	Weight		–
	Thickness of laminations		1 mm
	Iron length		140 mm
	No. of windings/pole		32
	Cross section of copper conductor		6.5 mm × 7 mm
	Diameter of cooling hole		4 mm
	Total copper cross section		32 mm^2
Electrical properties			
	Inductance	(0–50 Hz)	–
		(1000 Hz)	–
	Resistance (20°C)		52 mΩ
	Max. I_{eff} at 25°C and ΔP = 10 bar		244 A
	V_{max} between coils	(test)	50 V
		(nominal)	20 V
	V_{max} between coils and ground	(test)	5 kV (rms)
		(nominal)	2 kV (max.)
Magnetic properties			
	Magnetic length		–
	$\int G dl$ at I = 100 A		307 mT
	Limit of magnetic linearity		700 A
Cooling			
	Coolant		Demineralized water
	Nominal flow for ΔP = 10 bar		10 l/min
	Test pressure		40 bar
References			
	Magnet design		MPS/SR/mem. 73-73
	Magnetic measurements		SPS/EA of 12/3/76
	Magnet drawings		4C09.100.1
	Support drawings		4C14.700.2

Table C.3: Main parameters of quadrupole for gamma-jump scheme type 408 (doublet)

Mechanical properties			
	Magnet structure separable in two halves		
	Diameter inscribed circle	(standard)	122 mm
	Overall size		
		Vertical	440 mm
		Horizontal	577 mm
		Longitudinal	230 mm
	Weight		–
	Thickness of laminations		1 mm
	Iron length		140 mm
	No. of windings/pole		8
	Diameter of copper conductor		3.3 mm
	Diameter of cooling hole		–
	Total copper cross section (7 conductors)		59 mm^2
Electrical properties			
	Inductance	(0–50 Hz)	0.3 mH
		(1000 Hz)	–
	Resistance (20°C)		7.3 mΩ
	Max. I_{eff} at 25°C and ΔP = 10 bar		60 A
	V_{max} between coils	(test)	100 V
		(nominal)	50 V
	V_{max} between coils and ground	(test)	10 kV (rms)
		(nominal)	4 kV (DC)
Magnetic properties			
	Magnetic length		190 mm
	$\int G dl$ at I = 100 A		100 mT
	Limit of magnetic linearity		300 A
Cooling			
	Coolant		Air
	Nominal flow for ΔP = 10 bar		–
	Test pressure		–
References			
	Magnet design		MPS/ML/int. Note 73-12
	Magnetic measurements		MPS/SM/Note of 3/1/74
	Magnet drawings		4C10.000.0
	Support drawings		4C08.400.2

Table C.4: Main parameters of quadrupole for gamma-jump scheme type 409 (triplet)

Mechanical properties			
	Magnet structure separable in two halves		
	Diameter inscribed circle	(enlarged)	146 mm
	Overall size		
		Vertical	570 mm
		Horizontal	960 mm
		Longitudinal	305 mm
	Weight		650 kg
	Thickness of laminations		1 mm
	Iron length		200 mm
	No. of windings/pole		50
	Cross section of copper conductor		6.1 mm × 5.7 mm
	Diameter of cooling hole		3.6 mm
	Total copper cross section		24.3 mm^2
Electrical properties			
	Inductance	(0–50 Hz)	22 mH
		(1000 Hz)	–
	Resistance (20°C)		133 mΩ
	Max. I_{eff} at 25°C and ΔP = 10 bar		500 A
	V_{max} between coils	(test)	70 V
		(nominal)	30 V
	V_{max} between coils and ground	(test)	5 kV (rms)
		(nominal)	2 kV (max.)
Magnetic properties			
	Magnetic length		250 mm
	$\int G dl$ at I = 100 A		640 mT
	Limit of magnetic linearity		600 A
Cooling			
	Coolant		Demineralized water
	Nominal flow for ΔP = 10 bar		13 l/min
	Test pressure		40 bar
References			
	Magnet design		MPS/SI/MAE/int 72-2
	Magnetic measurements		MPS/SI/MAE/int 74-11
	Magnet drawings		4C06.000.0B
	Support drawings		4C08.100.2

Appendix D: Characteristics of sextupoles

Table D.1: Main parameters of high-energy sextupoles type 608

Mechanical properties			
	Magnet structure separable in two halves		
	Diameter inscribed circle	(standard)	134 mm
	Overall size		
		Vertical	500 mm
		Horizontal	730 mm
		Longitudinal	245 mm
	Weight		400 kg
	Thickness of laminations		1 mm
	Iron length		168 mm
	No. of windings/pole		14
	Cross section of copper conductor		7 mm × 6.3 mm
	Diameter of cooling hole		3.4 mm
	Total copper cross section		33 mm^2
Electrical properties			
	Inductance	(0–50 Hz)	1.5 mH
		(1000 Hz)	–
	Resistance (20°C)		30 mΩ
	Max. I_{eff} at 25°C and ΔP = 10 bar		415 A
	V_{max} between coils	(test)	100 V
		(nominal)	40 V
	V_{max} between coils and ground	(test)	5 kV (rms)
		(nominal)	3 kV (max.)
Magnetic properties			
	Magnetic length		195 mm
	$\int G' dl$ at I = 100 A		6.94 T m^{-1}
	Limit of magnetic linearity		720 A
Cooling			
	Coolant		Demineralized water
	Nominal flow for ΔP = 10 bar		3 l/min
	Test pressure		40 bar
References			
	Magnet design		MPS/SR/Spec. 73-6
	Magnetic measurements		–
	Magnet drawings		4C013.3
	Support drawings		4C18.100.2

Appendix E: Characteristics of octupoles

Table E.1: Main parameters of high-energy octupoles type 802

Mechanical properties			
	Magnet structure separable in two halves		
	Diameter inscribed circle	(reduced)	122 mm
	Overall size		
		Vertical	424 mm
		Horizontal	614 mm
		Longitudinal	264 mm
	Weight		200 kg
	Thickness of laminations		1 mm
	Iron length		168 mm
	No. of windings/pole		8
	Cross section of copper conductor		7 mm × 7 mm
	Diameter of cooling hole		4 mm
	Total copper cross section		35.5 mm^2
Electrical properties			
	Inductance	(0–50 Hz)	1.0 mH
		(1000 Hz)	–
	Resistance (20°C)		24.7 mΩ
	Max. I_{eff} at 25°C and ΔP = 10 bar		650 A
	V_{max} between coils	(test)	55 V
		(nominal)	30 V
	V_{max} between coils and ground	(test)	5 kV (rms)
		(nominal)	2 kV (max.)
Magnetic properties			
	Magnetic length		220 mm
	$\int G''dl$ at I = 100 A		433 T m^{-2}
	Limit of magnetic linearity		720 A
Cooling			
	Coolant		Demineralized water
	Nominal flow for ΔP = 10 bar		4.4 l/min
	Test pressure		40 bar
References			
	Magnet design		MPS/SR/Spec 72-4
	Magnetic measurements		MS/SR/Note 74-2
	Magnet drawings		4C07.000.0
	Support drawings		4C08.300.0

Table E.2: Main parameters of SPS octupoles type LOE

Mechanical properties			
	Magnet structure not separable in two halves		
	Diameter inscribed circle	(standard)	134 mm
	Overall size		
		Vertical	784 mm
		Horizontal	754 mm
		Longitudinal	818 mm
	Weight		2082 kg
	Thickness of laminations		–
	Iron length		710 mm
	No. of windings/pole		35
	Cross section of copper conductor		7.5 mm × 7.5 mm
	Diameter of cooling hole		4.5 mm
	Total copper cross section		40 mm^2
Electrical properties			
	Inductance	(0–50 Hz)	30 mH
		(1000 Hz)	–
	Resistance (20°C)		57 mΩ
	Max. I_{eff} at 25°C and ΔP = 10 bar		–
	V_{max} between coils	(test)	–
		(nominal)	–
	V_{max} between coils and ground	(test)	–
		(nominal)	–
Magnetic properties			
	Magnetic length		720 mm
	$\int G''\mathrm{d}l$ at I = 460 A		1320 T m^{-2}
	Limit of magnetic linearity		–
Cooling			
	Coolant		Demineralized water
	Nominal flow for ΔP = 10 bar		3.78 l/min
	Test pressure		–
References			
	Magnet design		MPS/SR/Spec 72-4
	Magnetic measurements		MPS/SR/Note 74-2
	Magnet drawings		–
	Support drawings		–

Appendix F: Kicker system parameters

F.1 KFA13/21

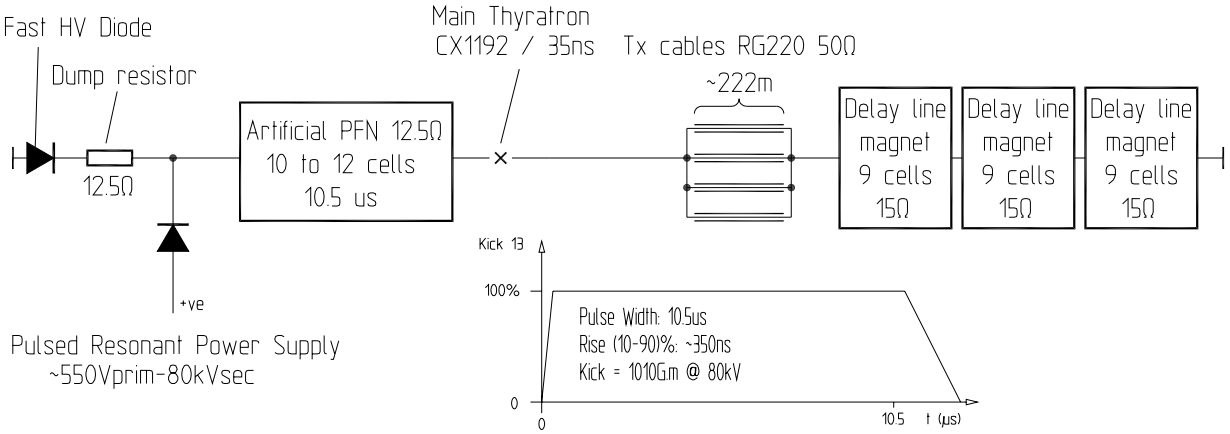

Fig. F.1: Schematic circuit diagram of one module

Table F.1: Main parameters of KFA13/21

Item	Unit	Nominal	Achievable
Deflection angle at 14 GeV/*c*	mrad	1.897	2.16
Magnetic rigidity, *B*ρ at 14 GeV/*c*	T m	46.68	–
$\int B\mathrm{d}l$	T m	0.0886	0.101
Magnet impedance	Ω	15	–
Magnet aperture vertical	mm	53	–
Magnet aperture horizontal	mm	147	–
Magnet effective magnetic length	mm	222	–
Number of magnets (connected in series)		3	–
Vacuum tank length	mm	888	–
Kick duration (5 turns)	μs	10.5	10.5
Kick flat-top stability		±1	–
PFN impedance	Ω	12.5	–
PFN charging voltage	kV	70.3	80
Magnet current	kA	5.62	6.4
Kick rise time (10%–90%)	ns	350	350

F.2 BFA9 (Pedestal kicker)

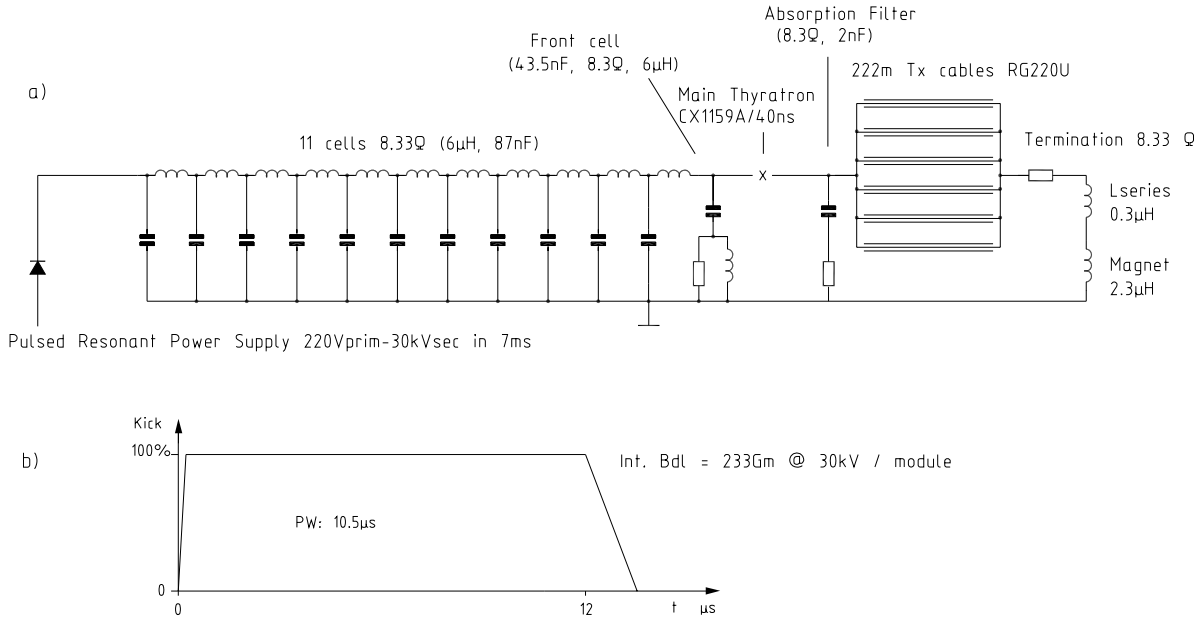

Fig. F.2: Schematic circuit diagram

Table F.2: Main parameters of BFA9

Item	Unit	Nominal	Achievable
Maximum deflection angle at 14 GeV/*c*	mrad	0.120	0.499
Magnetic rigidity, *B*ρ at 14 GeV/*c*	T m	46.68	–
∫*B*d*l* (available)	T m	0.0056	0.0233
Magnet inductance	μH	2.3	–
Magnet aperture vertical	mm	52.5	–
Magnet aperture horizontal	mm	158	–
Magnet effective magnetic length	mm	540	–
Vacuum tank length	mm	1065	–
Kick duration (5 turns)	μs	10.5	10.5
PFN impedance	Ω	8.33	–
PFN charging voltage	kV	7.21	30
Magnet current	kA	0.433	1.8
Kick rise time (10%–90%) (with series inductor)	ns	350	350
Kick rise time (10%–90%) (without series inductor)	ns	305	305

F.3 KFA4

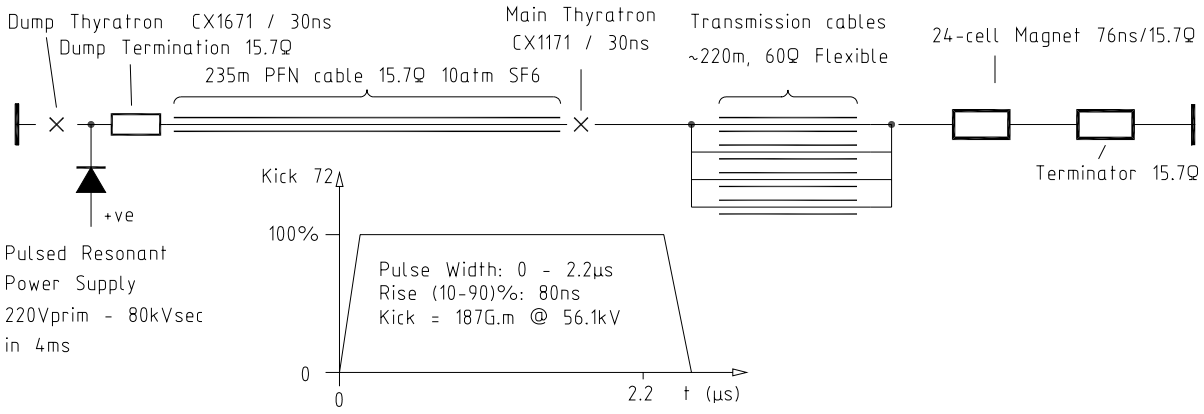

Fig. F.3: Schematic circuit diagram of system

Table F.3: Main parameters of KFA4

Item (per magnet)	Unit	Nominal	Achievable
Deflection angle at 14 GeV/*c*	mrad	0.400	0.571
Magnetic rigidity, $B\rho$ at 14 GeV/*c*	T m	46.68	–
$\int B\mathrm{d}l$	T m	0.0187	0.0267
Magnet impedance	Ω	15.7	–
Magnet aperture vertical	mm	74	–
Magnet aperture horizontal	mm	112	–
Effective magnetic length	mm	615	–
Available straight section length	mm	888	–
Kick duration (1 turn)	μs	2.1	2.1
PFN impedance	Ω	15.7	–
PFN charging voltage	kV	56.1	80
Magnet current	kA	1.788	2.576
Kick rise time (10%–90%)	ns	80	80

F.4 DFA242/243 staircase

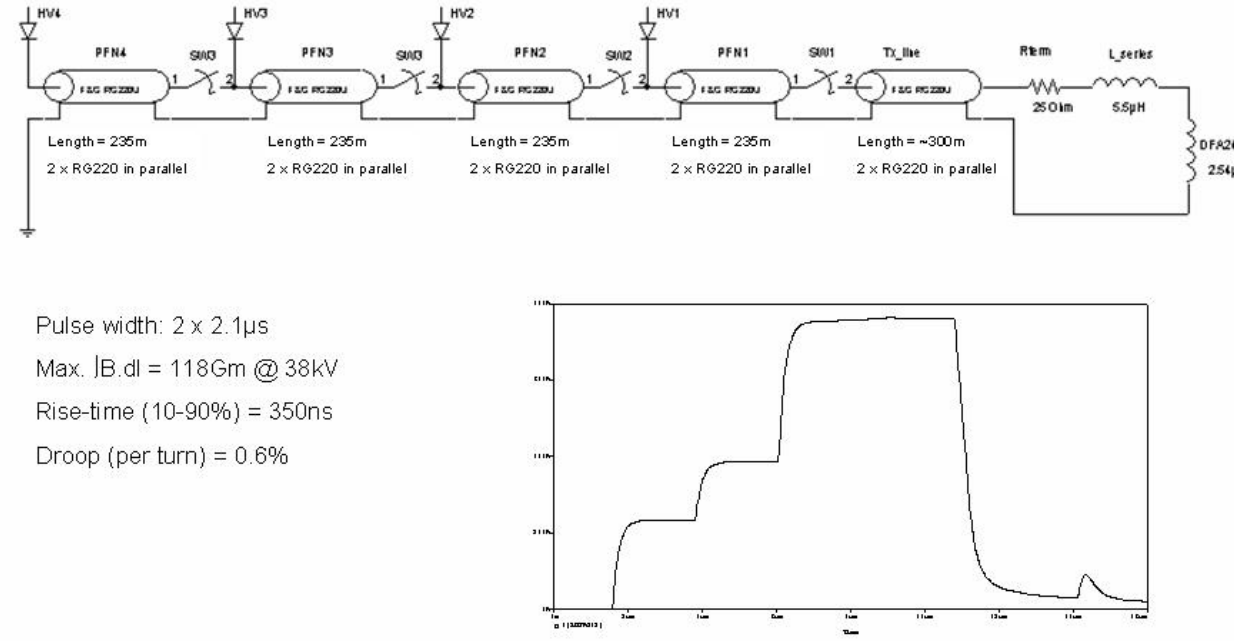

Fig. F.4: Schematic circuit diagram of system

Table F.4: Main parameters of DFA242/243

Item (per magnet)	Unit	Required Nominal	Achievable
Maximum deflection angle at 14 GeV/*c*	mrad	0.155	0.253
Magnetic rigidity, $B\rho$ at 14 GeV/*c*	T m	46.68	–
$\int B\mathrm{d}l$	T m	0.00723	0.0118
Magnet inductance	µH	2.49	–
Magnet aperture vertical	mm	53.5	–
Magnet aperture horizontal	mm	148	–
Effective magnetic length	mm	665	–
Kick duration	µs	4 × 2.1	4 × 2.1
PFN impedance	Ω	25	–
PFN charging voltage	kV	23.2	38
Magnet current	kA	0.463	0.735
Kick rise time (10%–90%) (with series inductor)	ns	350	350
Kick rise time (10%–90%) (without series inductor)	ns	114	114

F.5 Cost breakdown

Table F.5: Material cost breakdown of the new MTE kicker system (kCHF)

KFA13/21		
Magnet and vacuum tank modifications		240
High-voltage pulsed power supply		980
Electronics + controls		435
Oil, SF_6 services		175
	Sub-total	1830
BFA9		
Tank modifications		55
Electronics + controls		220
Oil system upgrade		150
	Sub-total	425
KFA4		
Magnet and vacuum tank modifications		265
High-voltage pulsed power supply		155
Electronics + controls		230
Oil, SF_6 services		150
	Sub-total	800
KFA71/79		
Spare magnet tank replacement		720
Electronics + controls		20
	Sub-total	740
DFA242/243		
Magnet and vacuum tank modifications		175
High-voltage pulsed power supply		625
Electronics + controls		435
Oil, SF_6 services		175
	Sub-total	1410
Infrastructure Building 367		
Electrical distribution		30
Water, networking, fire protection		30
Structural modifications		95
Transport		5
	Sub-total	160
Infrastructure Building 359		
Electrical distribution		30
Water, networking, fire protection		30
Structural modifications (incl. SMH57 dismantling)		70
Transport		5
	Sub-total	135
	Total	5500

Appendix G: Properties of the 8C11 ferrite

Table G.1: Numerical values of the real and imaginary parts of the 8C11 ferrite permeability as a function of frequency

Frequency (MHz)	Real part	Imaginary part	Frequency (MHz)	Real part	Imaginary part
1.000	998.98	160.64	49.288	79.57	152.98
1.162	993.71	212.82	57.259	65.99	140.18
1.350	971.79	269.41	66.520	53.97	127.46
1.568	933.55	325.39	77.278	43.59	114.98
1.821	881.81	373.50	89.777	34.76	102.91
2.116	818.87	410.27	104.296	27.45	91.48
2.458	750.39	433.88	121.164	21.51	80.78
2.856	680.33	445.31	140.760	16.78	70.94
3.318	611.85	445.50	163.525	13.12	62.09
3.854	547.80	436.40	189.973	10.28	54.15
4.478	489.64	420.51	220.697	8.09	47.13
5.202	437.73	399.45	256.390	6.45	40.95
6.043	392.64	375.89	297.857	5.20	35.51
7.021	353.86	351.18	346.029	4.34	30.85
8.156	320.81	327.50	401.993	3.66	26.83
9.475	292.46	305.14	467.007	3.16	23.41
11.007	267.62	285.01	542.536	2.77	20.50
12.788	245.10	267.07	630.281	2.50	18.08
14.856	224.32	251.42	732.217	2.21	16.06
17.259	204.55	237.46	850.639	1.97	14.48
20.050	185.39	224.82	988.213	1.69	13.27
23.292	166.37	213.18	1148.038	1.42	12.35
27.060	147.70	202.00	1333.711	1.18	11.79
31.436	129.09	190.47	1549.412	1.08	11.81
36.520	111.21	178.33	1800.000	1.00	12.64
42.426	94.64	165.77			

Appendix H: Magnetic extraction septum SMH16

The parameters are given for a proton beam at 26 GeV/*c*.

H.1 Existing septum

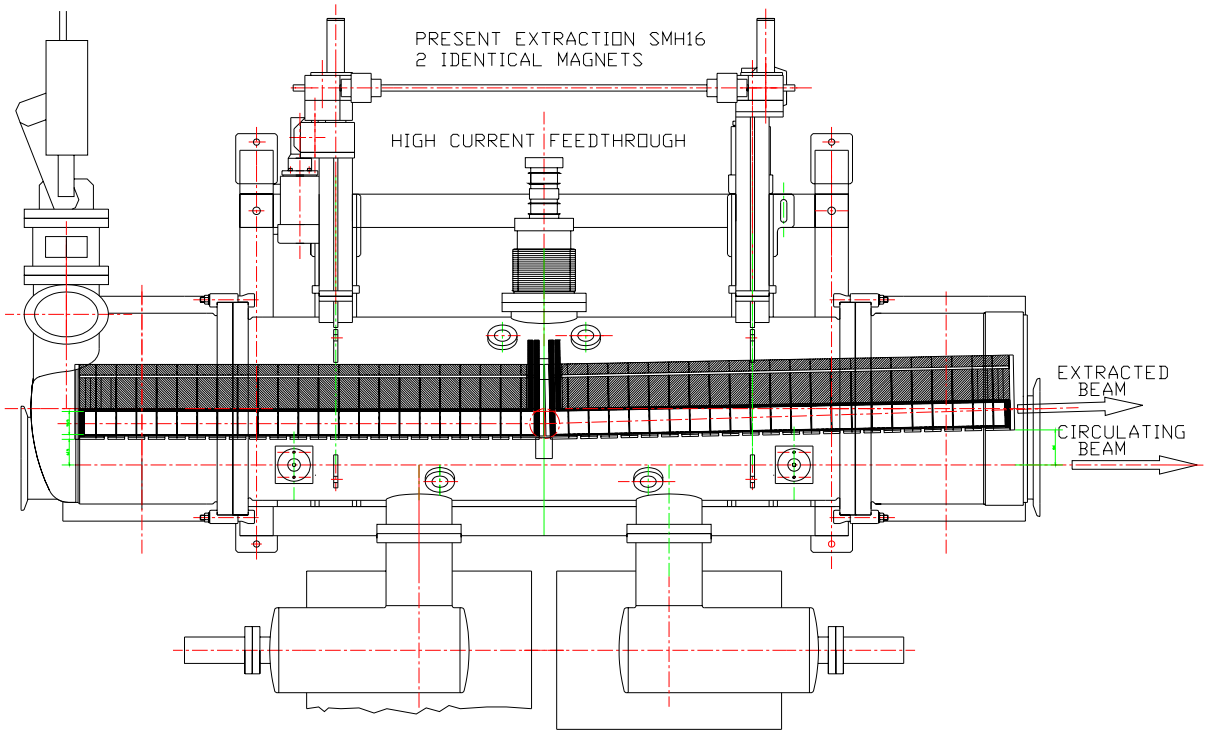

Fig. H.1: Layout of the existing magnets and the common vacuum vessel

Table H.1: Main parameters of the existing system

Physical length	2 × 1125 mm
Septum thickness	3 mm
Gap dimension (width × height)	65 mm × 30 mm
Integrated magnetic field	2.6 T m
Total magnetic length	2174 mm
Peak current	28551 A
Repetition rate	1.2 s
Deflection angle	30 mrad
Rear conductor thickness	6 mm

H.2 New septum

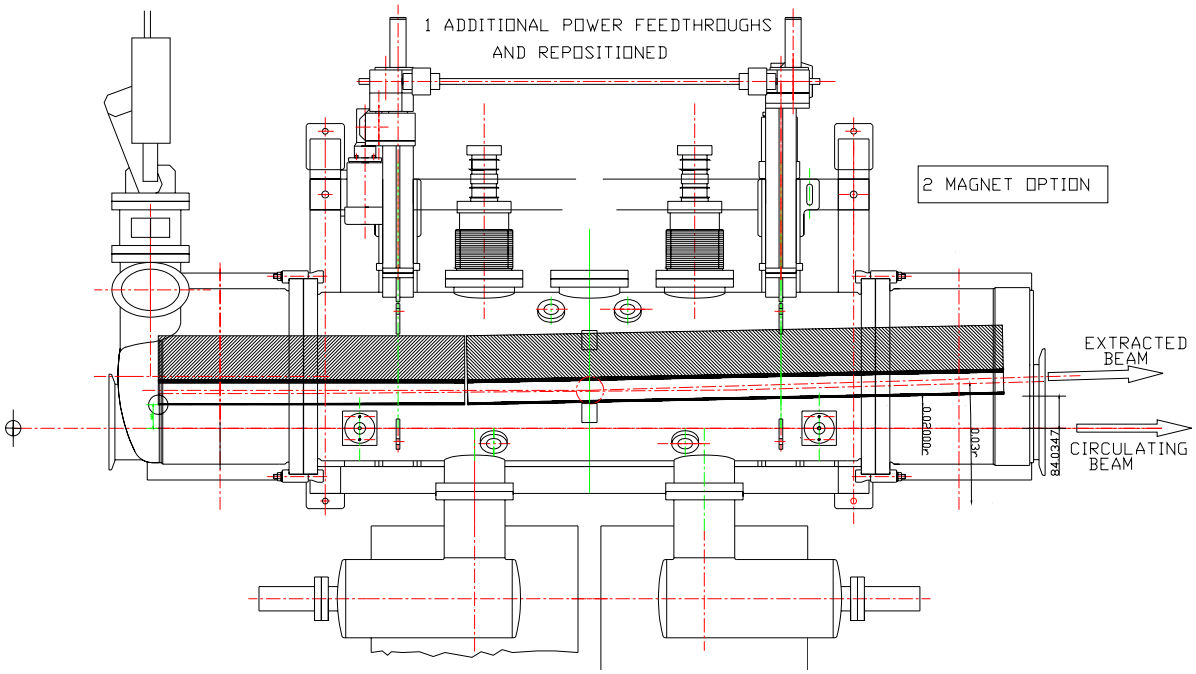

Fig. H.2: Layout of the new magnets and the common vacuum vessel

Table H.2: Main parameters of the new system

	Thin septum (upstream)	Thick septum (downstream)
Physical length (mm)	860	1390
Septum thickness (mm)	1.7	5
Gap dimension (width × height) (mm)	62 × 30	79 × 30
Integrated magnetic field (T m)	0.715	1.885
Magnetic length (mm)	800	1300
Peak current (A)	21337	34616
Repetition rate (s)	0.9	0.9
Deflection angle (mrad)	8.25	21.75
Rear conductor thickness (mm)	9	9
Magnet resistance (mΩ)	0.55	0.26
Magnet inductance (μH)	1.9	3.9
Power dissipation (W)	519	700

H.3 Cost breakdown

Table H.3: Cost breakdown of the new septum (kCHF)

New vacuum vessels (3)	100
Modified movement + support systems inside vacuum tank	120
Magnets (6)	240
Coils (8)	160
Vacuum equipment (unrecoverable due to radiation level)	80
High-current feedthroughs (6)	100
Electrical connections from transformer to magnet	50
Design office	100
Interlock electronics including cabling	50
Total	1000

Appendix I: New sextupoles and octupoles for the MTE

Table I.1: Electrical properties of the octupole (OCT) and sextupoles (XCT) to be used for the MTE

	New OCT		2 XCT	
Magnet	Theoretical	Measured	Theoretical	Measured
Inductance (mH)	30	33	1.5	3.3
Resistance (mΩ)	57	104	30	95
Max current (A)	400		400	
Number of magnets in series	1		2	
Dynamic				
d*I*/d*t* max (kA/s)	15		7.5	
Max. rise time (ms)	100		100	
Estimated rise time (ms)	26.67		53.33	
Round-off time (ms)	10–20		10–20	
Operation				
Current	Unipolar		Unipolar	
PS control	PS standard		PS standard	
TEKELEC power converter	Spare DHZ15		Spare DHZ60	
Type	T7		T7	
Max. current (A)	700		700	
RMS current (A)	450		450	
Max. voltage (V)	650		650	
Minimum current (A)	10		10	
Zero current	Blocking		Blocking	
Voltage bipolar	Yes		Yes	
Current bipolar	Yes with thyristor switch		Yes with thyristor switch	
Max. voltage needed				
$R \cdot I_{max}$ (V)	22.8		24	
$L \cdot \mathrm{d}I/\mathrm{d}t$ (V)	450		22.5	
V_{max} (V)	472.8		46.5	
Remarks	Using a ramp rate of 15 kA/s, the rise time will be around 30 ms.		One choke of 5 mH is placed in series with the magnet.	

Appendix J: Normal and skew air quadrupoles

Table J.1: Main parameters of normal quadrupoles type 401

Mechanical properties			
	Magnet structure separable in two halves. No iron yoke.		
	Elliptical aperture h × v	(standard)	144 mm × 80 mm
	Overall size		
		Vertical	154 mm
		Horizontal	246 mm
		Longitudinal	152 mm
	Weight		15 kg
	Thickness of laminations		–
	Iron length		–
	No. of windings/pole		233
	Cross section of copper conductor		2.95 mm × 1.65 mm
	Diameter of cooling hole		–
	Total copper cross section		4 mm^2
Electrical properties			
	Inductance	(0–50 Hz)	24 mH
		(1000 Hz)	–
	Resistance (20°C)		1.5 Ω
	Max. I_{eff} at 25°C and ΔP = 10 bar		5.6 A
	V_{max} between coils	(test)	5 V
		(nominal)	1 V
	V_{max} between coils and ground	(test)	1 kV (DC)
		(nominal)	0.2 kV (DC)
Magnetic properties			
	Magnetic length		120 mm
	$\int G dl$ at I = 100 A		55.5 mT
	Limit of magnetic linearity		–
Cooling			
	Coolant		Air
	Nominal flow for ΔP = 10 bar		–
	Test pressure		–
References			
	Magnet design		MPS/Int, POW 65-1
	Magnetic measurements		–
	Magnet drawings		4C22.103.1A
	Support drawings		4A30.100.1

Table J.2: Main parameters of normal quadrupoles type 402

Mechanical properties			
	Magnet structure separable in two halves. No iron yoke.		
	Elliptical aperture h × v	(enlarged)	220 mm × 80 mm
	Overall size		
		Vertical	154 mm
		Horizontal	312 mm
		Longitudinal	152 mm
	Weight		–
	Thickness of laminations		–
	Iron length		–
	No. of windings/pole		237
	Cross section of copper conductor		2.95 mm × 1.65 mm
	Diameter of cooling hole		–
	Total copper cross section		4 mm^2
Electrical properties			
	Inductance	(0–50 Hz)	32 mH
		(1000 Hz)	–
	Resistance (20°C)		1.9 Ω
	Max. I_{eff} at 25°C and ΔP = 10 bar		5.6 A
	V_{max} between coils	(test)	5 V
		(nominal)	4 V
	V_{max} between coils and ground	(test)	1 kV (DC)
		(nominal)	0.2 kV (DC)
Magnetic properties			
	Magnetic length		120 mm
	$\int G\mathrm{d}l$ at I = 100 A		55.5 mT
	Limit of magnetic linearity		–
Cooling			
	Coolant		Air
	Nominal flow for ΔP = 10 bar		–
	Test pressure		–
References			
	Magnet design		PS/SM/Spec. 81-1
	Magnetic measurements		–
	Magnet drawings		4C22.102.1A
	Support drawings		4A30.200.1

Table J.3: Main parameters of skew quadrupoles type 403

Mechanical properties			
	Magnet structure separable in two halves. No iron yoke.		
	Elliptical aperture h × v	(standard)	156 mm × 89 mm
	Overall size		
		Vertical	145 mm
		Horizontal	276 mm
		Longitudinal	155 mm
	Weight		15 kg
	Thickness of laminations		–
	Iron length		–
	No. of windings/pole		229
	Cross section of copper conductor		0.9 mm × 3.1 mm
	Diameter of cooling hole		–
	Total copper cross section		2.4 mm^2
Electrical properties			
	Inductance	(0–50 Hz)	–
		(1000 Hz)	–
	Resistance (20°C)		1.6 Ω
	Max. I_{eff} at 25°C and ΔP = 10 bar		3.5 A
	V_{max} between coils	(test)	20 V
		(nominal)	4 V
	V_{max} between coils and ground	(test)	1 kV (DC)
		(nominal)	0.1 kV (DC)
Magnetic properties			
	Magnetic length		–
	$\int G dl$ at I = 100 A		38 mT
	Limit of magnetic linearity		–
Cooling			
	Coolant		Air
	Nominal flow for ΔP = 10 bar		–
	Test pressure		–
References			
	Magnet design		–
	Magnetic measurements		–
	Magnet drawings		–
	Support drawings		4A30.300.1

Table J.4: Main parameters of skew quadrupoles type 404

Mechanical properties			
	Magnet structure separable in four parts. No iron yoke.		
	Elliptical aperture h × v	(enlarged)	144 mm × 80 mm
	Overall size		
		Vertical	120 mm
		Horizontal	288 mm
		Longitudinal	157 mm
	Weight		–
	Thickness of laminations		–
	Iron length		–
	No. of windings/pole		240
	Cross section of copper conductor		0.9 mm × 3.1 mm
	Diameter of cooling hole		–
	Total copper cross section		2.4 mm^2
Electrical properties			
	Inductance	(0–50 Hz)	–
		(1000 Hz)	–
	Resistance (20°C)		2.55 Ω
	Max. I_{eff} at 25°C and ΔP = 10 bar		3.5 A
	V_{max} between coils	(test)	20 V
		(nominal)	4 V
	V_{max} between coils and ground	(test)	1 kV (DC)
		(nominal)	0.1 kV (DC)
Magnetic properties			
	Magnetic length		–
	$\int G dl$ at I = 100 A		–
	Limit of magnetic linearity		–
Cooling			
	Coolant		Air
	Nominal flow for ΔP = 10 bar		–
	Test pressure		–
References			
	Magnet design		–
	Magnetic measurements		–
	Magnet drawings		–
	Support drawings		–

Appendix K: Catalogue of cross sections of replaced vacuum chambers for the implementation of the MTE

In the following the pictures of the cross section of vacuum chambers that need to be replaced are listed (black) as well as the proposed cross section (red).

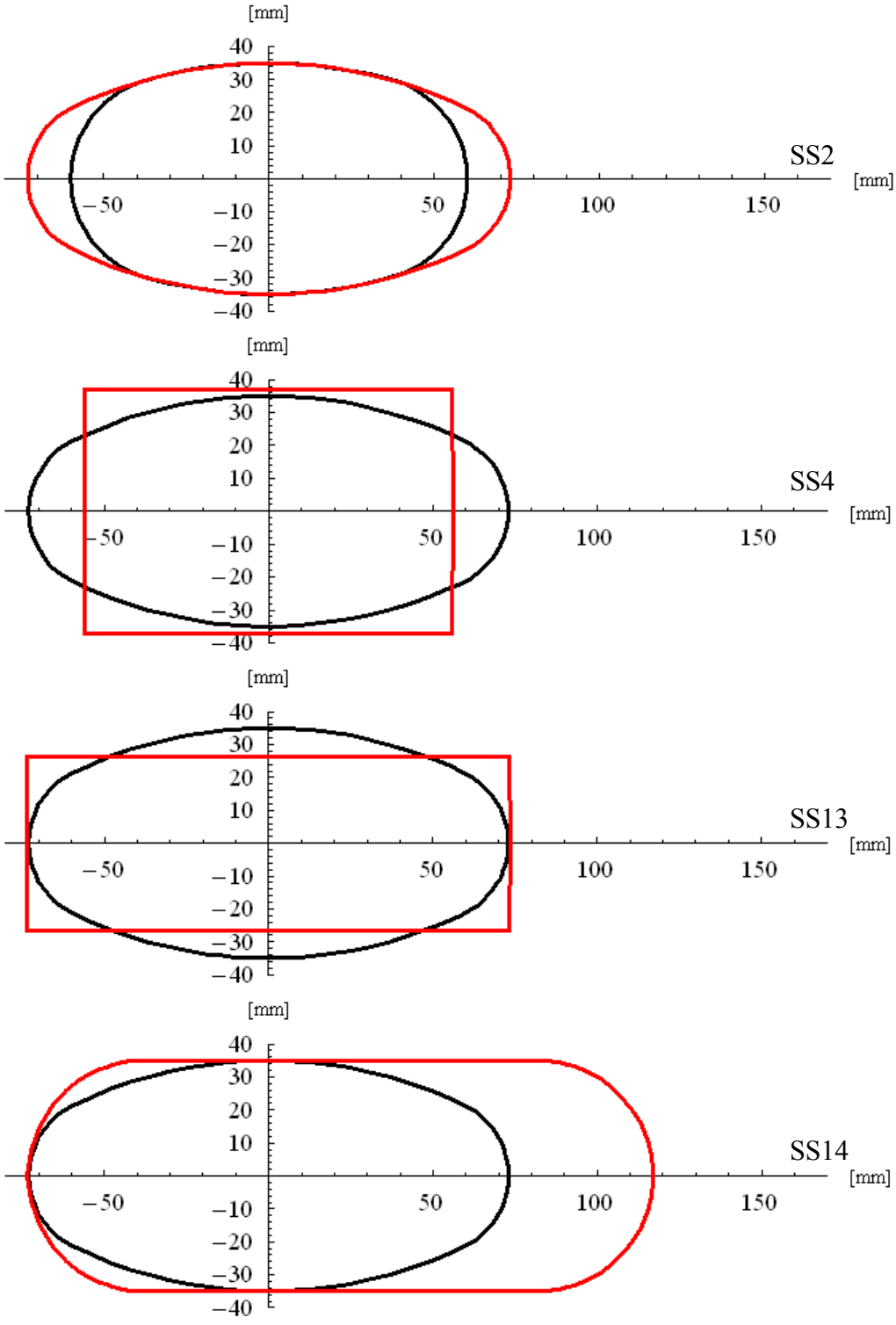

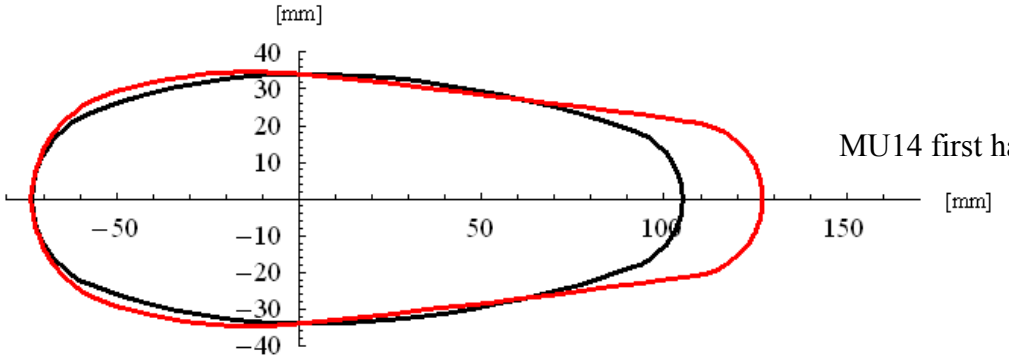

MU14 first half

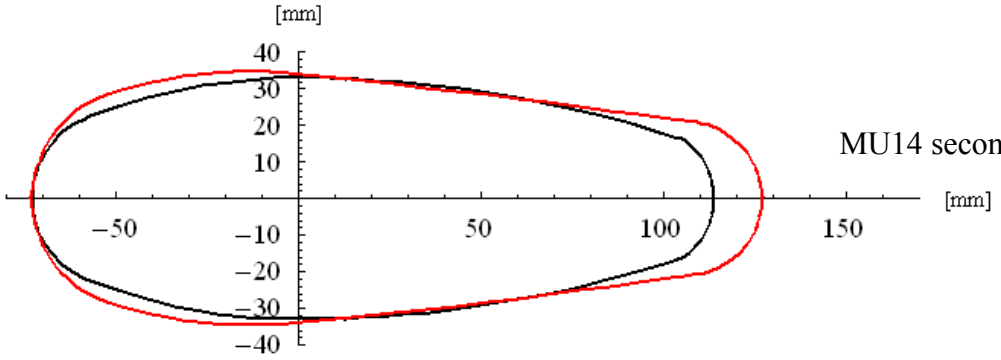

MU14 second half

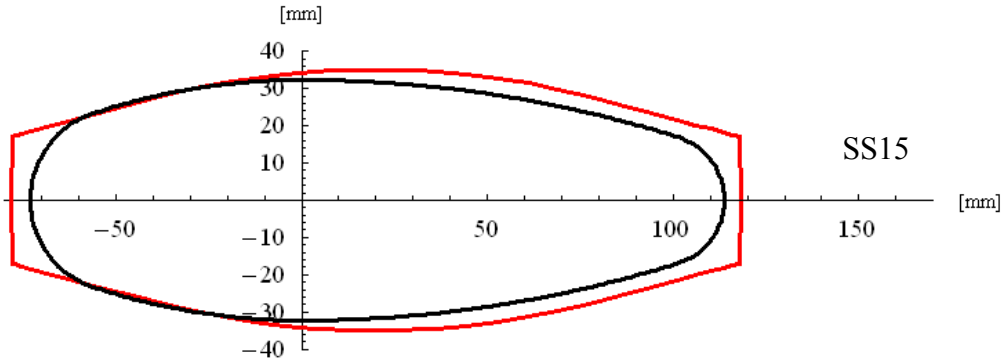

SS15

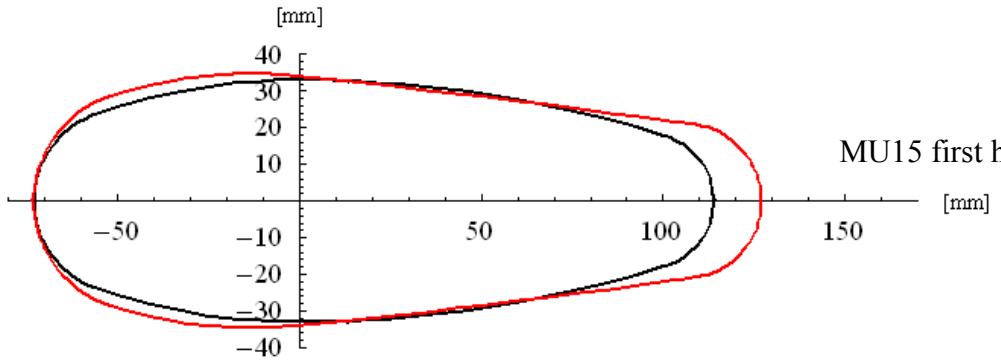

MU15 first half

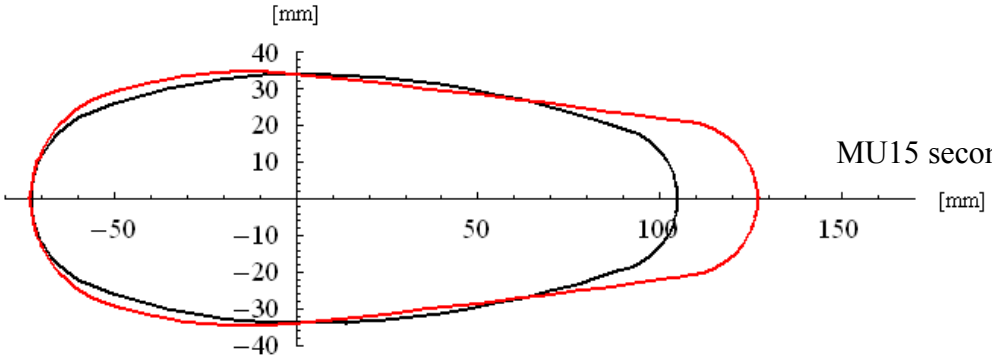

MU15 second half

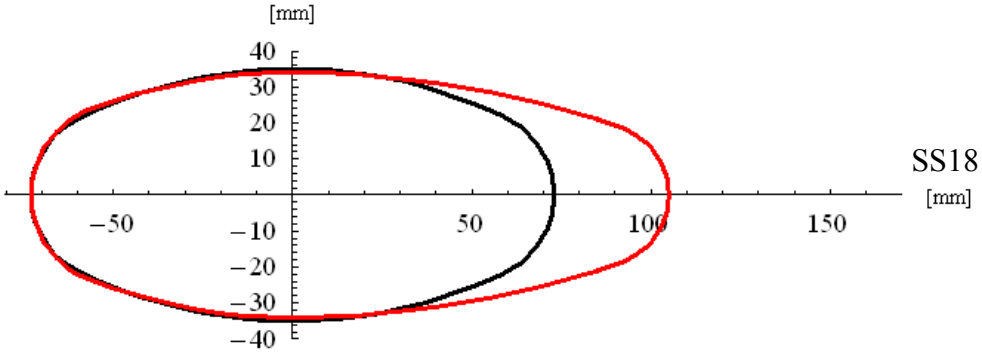

SS18

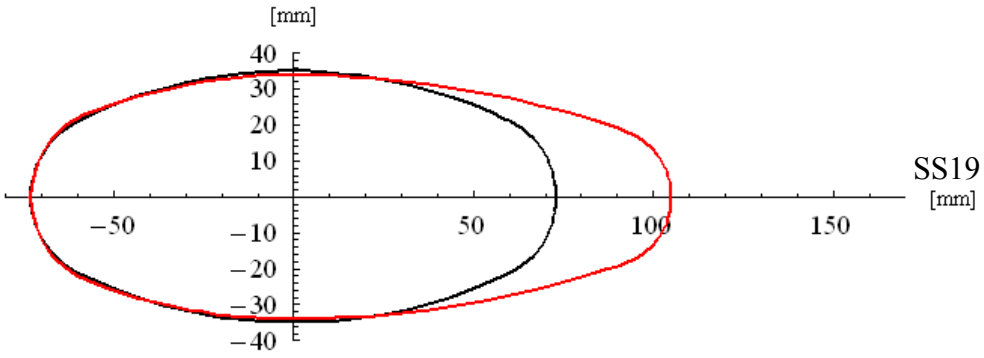

SS19

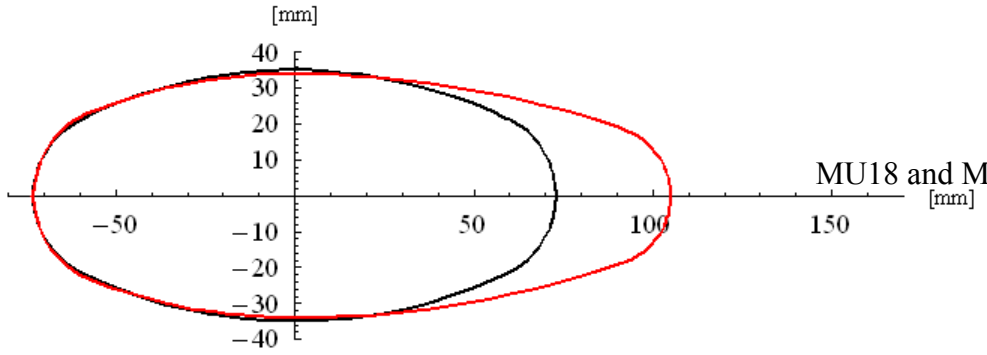

MU18 and MU 19

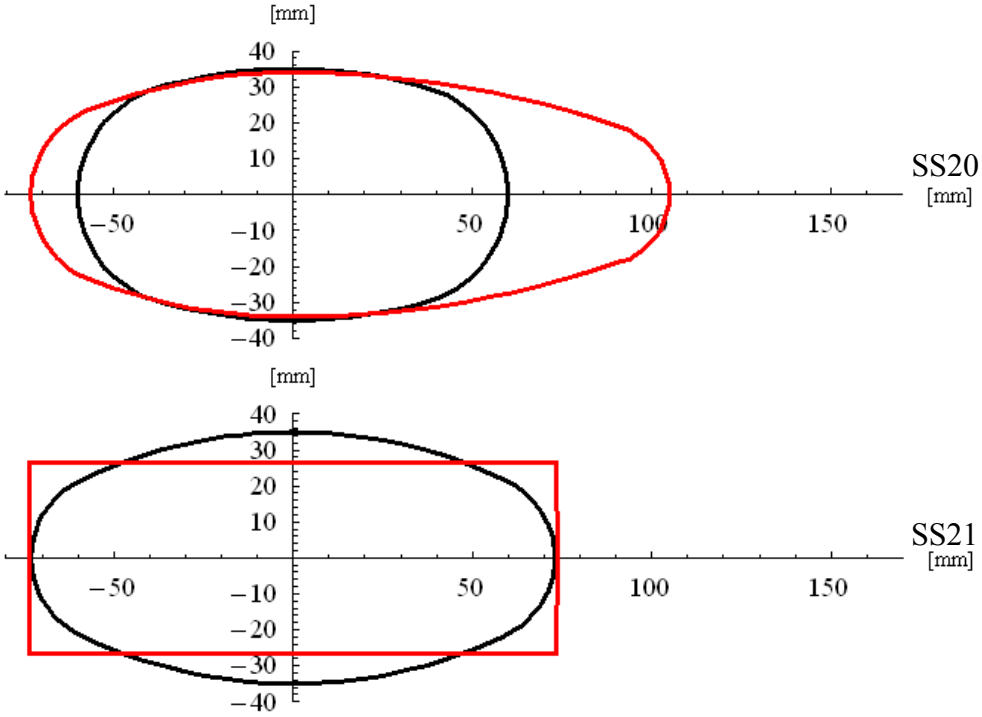
[mm]
40
30
20
10
−50
−10
50
100
150
−20
−30
−40
SS20
[mm]
[mm]
40
30
20
10
−50
−10
50
100
150
−20
−30
−40
SS21
[mm]